

AD-A194 498

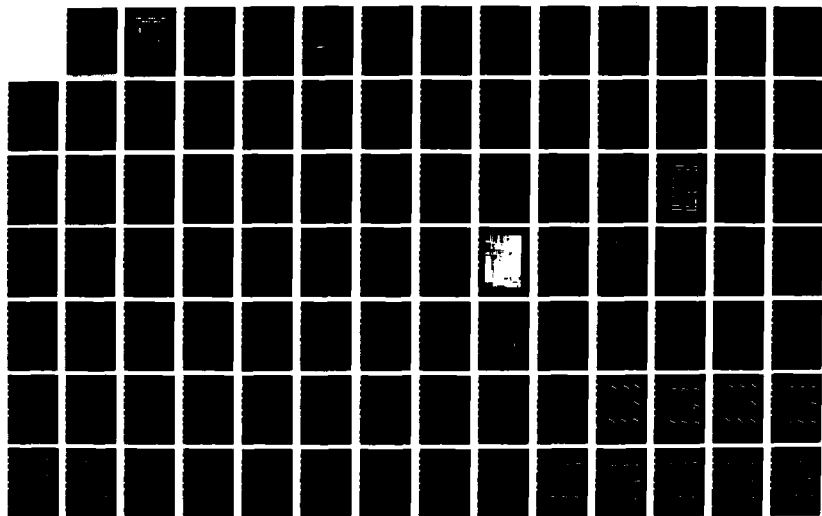
A MAPPING OF THE VISCOUS FLOW BEHAVIOR IN A CONTROLLED
DIFFUSION COMPRESS (U) NAVAL POSTGRADUATE SCHOOL
MONTEREY CA Y ELAZAR MAR 88 NPS67-88-001

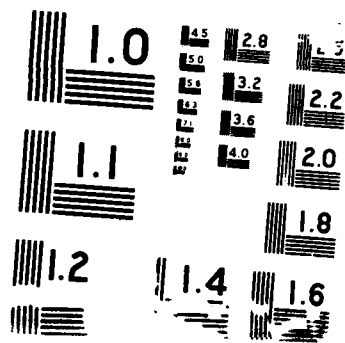
1/3

UNCLASSIFIED

F/G 20/4

NL





NAVAL POSTGRADUATE SCHOOL Monterey, California

AD-A194 490

DTIC
ELECTE
JUN 23 1988

CS D

D



DISSERTATION

A MAPPING OF THE VISCOUS FLOW BEHAVIOR IN A
CONTROLLED DIFFUSION COMPRESSOR CASCADE
USING LASER DOPPLER VELOCIMETRY AND
PRELIMINARY EVALUATION OF CODES
FOR THE PREDICTION OF STALL

by

Yekutiell Elazar

March 1988

Thesis Advisor:

Raymond P. Shreeve

Approved for public release; distribution is unlimited.

Prepared for:

Naval Air Systems Command
Washington, DC 20361

NAVAL POSTGRADUATE SCHOOL
Monterey, California


Rear Admiral Robert C. Austin
Superintendent

Kneale T. Marshall
Acting Provost

This thesis was prepared in conjunction with research initiated by the Naval Air System Command, Washington, DC, under Air Task #A931931E/186A/7R024-03-001, and continued under block funding as part of a program at the Turbo-propulsion Laboratory aimed at the prediction and alleviation of fan and compressor stall.

Reproduction of all or part of this work is authorized.

Released by:



GORDON E. SCHACHER
Dean of Science and
Engineering

UNCLASSIFIED

SECURITY CLASSIFICATION OF THIS PAGE

UNCLASSIFIED			REPORT DOCUMENTATION PAGE			
1a REPORT SECURITY CLASSIFICATION			1b RESTRICTIVE MARKINGS			
2a SECURITY CLASSIFICATION AUTHORITY			3 DISTRIBUTION/AVAILABILITY OF REPORT			
2b DECLASSIFICATION/DOWNGRADING SCHEDULE			Approved for public release; distribution is unlimited.			
4 PERFORMING ORGANIZATION REPORT NUMBER(S) NPS67-88-001			5 MONITORING ORGANIZATION REPORT NUMBER(S)			
6a NAME OF PERFORMING ORGANIZATION Naval Postgraduate School		6b OFFICE SYMBOL (if applicable) Code 67		7a NAME OF MONITORING ORGANIZATION Naval Postgraduate School		
6c ADDRESS (City, State, and ZIP Code) Monterey, California 93943-5000			7b ADDRESS (City, State, and ZIP Code) Monterey, California 93943-5000			
8a NAME OF FUNDING/SPONSORING ORGANIZATION Naval Air Systems Command		8b OFFICE SYMBOL (if applicable)		9 PROCUREMENT INSTRUMENT IDENTIFICATION NUMBER N0001987WR7R048		
8c ADDRESS (City, State, and ZIP Code) Washington, DC 20361		10 SOURCE OF FUNDING NUMBERS				
		PROGRAM ELEMENT NO 61153N		PROJECT NO 7R024		WORK UNIT ACCESSION NO
11 TITLE (Include Security Classification) A MAPPING OF THE VISCOUS FLOW BEHAVIOR IN A CONTROLLED DIFFUSION COMPRESSOR CASCADE USING LASER DOPPLER VELOCIMETRY AND PRELIMINARY EVALUATION OF CODES FOR THE PREDICTION OF STALL						
12 PERSONAL AUTHOR(S) ELAZAR, YEKUTIEL						
13a TYPE OF REPORT DOCTORAL THESIS		13b TIME COVERED FROM _____ TO _____		14 DATE OF REPORT (Year Month Day) 1988 MARCH		15 PAGE COUNT 252
16 SUPPLEMENTARY NOTATION The views expressed in this thesis are those of the author and do not reflect the official policy or position of the Department of Defense or the U.S. Government.						
17 COSATI CODES			18 SUBJECT TERMS (Continue on reverse if necessary and identify by block number)			
FIELD	GROUP	SUB-GROUP	Laser Doppler Velocimeter Measurements; Viscous Cascade Flow; Controlled Diffusion Blading; Code Verification.			
19 ABSTRACT (Continue on reverse if necessary and identify by block number) <i>See C</i> Detailed measurements were made at $M=0.25$ and $Re_c=700000$ of the flow through a linear compressor cascade of controlled diffusion (CD) blading using a two-component argon-ion laser doppler velocimeter system. The measurements included mapping of the inviscid flow in the passage between two adjacent blades, boundary layer surveys, and wake surveys. Viscous flow phenomena such as a laminar separation region with reattachment on the suction surface, and laminar-to-turbulent transition on the pressure surface were resolved, and the viscous growth to the trailing edge was defined for three inlet angles from design incidence to near stall. Numerical calculations to predict the flow were carried out using a fully developed boundary layer code, a strongly interactive viscous-inviscid code and a Navier-Stokes code. It was shown that the common weakness of numerical predictors was in the modelling of transition and turbulence. The documented data can be used generally to calibrate compressor cascade analysis codes and thus enable reliable predictions of stall.						
20 DISTRIBUTION/AVAILABILITY OF ABSTRACT <input checked="" type="checkbox"/> UNCLASSIFIED/UNLIMITED <input type="checkbox"/> SAME AS RPT <input type="checkbox"/> DTIC USERS				21 ABSTRACT SECURITY CLASSIFICATION UNCLASSIFIED		
22a NAME OF RESPONSIBLE INDIVIDUAL Raymond P. Shreeve				22b TELEPHONE (Include Area Code) 408/646-2593		22c OFFICE SYMBOL Code 67Sf

DD FORM 1473, 84 MAR

83 APR edition may be used until exhausted

All other editions are obsolete

SECURITY CLASSIFICATION OF THIS PAGE

UNCLASSIFIED

Approved for public release; distribution is unlimited.

A MAPPING OF THE VISCOUS FLOW BEHAVIOR IN A CONTROLLED
DIFFUSION COMPRESSOR CASCADE USING LASER DOPPLER
VELOCIMETRY AND PRELIMINARY EVALUATION OF
CODES FOR THE PREDICTION OF STALL

by

Yekutiel Elazar
Major, Israeli Air Force
B.S., Technion, Haifa, 1974
M.S., Technion, Haifa, 1983

DOCTOR OF PHILOSOPHY IN AERONAUTICAL ENGINEERING

from the

NAVAL POSTGRADUATE SCHOOL
March 1988

Author: Yekutiel Elazar

Approved by:

S. K. Hebbar

S. K. Hebbar
Professor of Aeronautics
and Astronautics

A. L. Schoenstadt

A. L. Schoenstadt
Professor of Mathematics

M. F. Platz

M. F. PLATZER
Professor of Aeronautics
and Astronautics

R. H. Nunn

R. H. Nunn
Professor of Mechanical
Engineering

Raymond P. Shreeve

R. P. Shreeve
Professor of Aeronautics
and Astronautics
Dissertation Supervisor

Approved by:

M. F. Platz

M. F. Platzter, Chairman, Department of
Aeronautics and Astronautics

Approved by:

Kneale T. Marshall

Kneale T. Marshall, Acting Academic Dean

ABSTRACT

Detailed measurements were made at $M = 0.25$ and $Re_c = 700000$ of the flow through a linear compressor cascade of controlled diffusion (CD) blading using a two-component argon-ion laser doppler velocimeter system. The measurements included mapping of the inviscid flow in the passage between two adjacent blades, boundary layer surveys, and wake surveys. Viscous flow phenomena such as a laminar separation region with reattachment on the suction surface, and laminar-to-turbulent transition on the pressure surface were resolved, and the viscous growth to the trailing edge was defined for three inlet angles from design incidence to near stall.

Numerical calculations to predict the flow were carried out using a fully developed boundary layer code, a strongly interactive viscous-inviscid code and a Navier-Stokes code. It was shown that the common weakness of numerical predictors was in the modelling of transition and turbulence. The documented data can be used generally to calibrate compressor cascade analysis codes and thus enable reliable predictions of stall.



Accession For	
NTIS CRA&I	<input checked="" type="checkbox"/>
DTIC TAB	<input type="checkbox"/>
Unannounced	<input type="checkbox"/>
Justification	
By	
Distribution/	
Availability Codes	
Dist	Avail and/or spread
A-1	

TABLE OF CONTENTS

I.	INTRODUCTION	1
II.	NATURE OF THE PROBLEM	4
	A. CONTROLLED-DIFFUSION (CD) BLADING DESIGN	4
	B. DESCRIPTION OF THE OFF-DESIGN FLOW FIELD	6
	C. CALCULATING THE OFF-DESIGN FLOW BEHAVIOR	8
	D. PREVIOUS EXPERIMENTS	12
III.	TEST FACILITY AND INSTRUMENTATION	18
	A. RECTILINEAR CASCADE	18
	B. CD BLADING AND CASCADE CONFIGURATION	18
	C. INSTRUMENTATION	21
	1. Laser Doppler Velocimeter (LDV)	21
	2. Survey Probe	37
	3. Cascade Wind Tunnel Operating Instrumentation	37
	D. MEASUREMENT UNCERTAINTY	39
IV.	EXPERIMENTAL PROCEDURE	41
	A. OVERVIEW	41
	B. SET-UP PROCEDURES	42
	1. Wind Tunnel Adjustments	42
	2. LDV Optical System Alignment	43
	3. Traverse and Measuring Volume Alignment	48

C.	LDV SURVEY MEASUREMENTS	49
1.	Free Stream Measurements	49
2.	Passage Measurements	49
3.	Boundary Layer Measurements	49
4.	Wake Measurements	50
5.	Two-Dimensionality Checks	50
6.	Non-Dimensionalizing the Data	50
7.	Reynolds Number	54
8.	Data Reduction	54
D.	SURFACE PRESSURE MEASUREMENTS	54
V.	RESULTS AND DISCUSSION	55
A.	INLET FLOW FIELD MEASUREMENTS	55
B.	FLOW FIELD IN THE PASSAGE	56
1.	Velocity Distribution	56
2.	Flow Angle Distribution	72
3.	Surface Pressure Distribution	72
4.	Axial Velocity Density Ratio (AVDR)	83
C.	BOUNDARY LAYER MEASUREMENTS	87
1.	Suction Surface	87
2.	Pressure Surface	110
D.	WAKE MEASUREMENTS	135
1.	Time Averaged Velocity	135
2.	Turbulence	143
VI.	ANALYSIS OF THE RESULTS	151
A.	COMPARISON WITH PREVIOUS EXPERIMENTS	151

B.	COMPARISON WITH CODE PREDICTIONS	164
1.	Non-Interactive Boundary Layer Code	164
2.	Interactive Inviscid-Viscous Boundary Layer Code	167
3.	Navier-Stokes Code	177
C.	SUMMARY ASSESSMENT	183
VII.	CONCLUSIONS AND RECOMMENDATIONS	184
APPENDIX A:	PARTICLE SIZE DISTRIBUTION MEASUREMENTS ...	189
APPENDIX B:	PRELIMINARY MEASUREMENTS OF THE BOUNDARY LAYER ON A FLAT PLATE	198
APPENDIX C:	CALCULATION OF THE INLET FLOW REFERENCE VELOCITY USING PLENUM PRESSURE AND TEMPERATURE MEASUREMENTS	207
APPENDIX D:	LISTING OF SOFTWARE	210
APPENDIX E:	ESTIMATION OF THE UNCERTAINTY IN THE MEASUREMENTS OF BOUNDARY LAYER THICKNESS AND SHAPE FACTOR	220
	LIST OF REFERENCES	222
	INITIAL DISTRIBUTION LIST	227

LIST OF TABLES

1. Test Blade Coordinates	23
2. Geometrical Parameters of the Cascade	24
3. Coordinates of the Test Passage Between Adjacent Blades	26
4. LDV Characteristics	33
5. Measurement Uncertainties	40
6. Suction Surface Boundary Layer Parameters, $\beta_1 = 40^\circ$	111
7. Suction Surface Boundary Layer Parameters, $\beta_1 = 43.4^\circ$	112
8. Suction Surface Boundary Layer Parameters, $\beta_1 = 46^\circ$	113
9. Pressure Surface Boundary Layer Parameters, $\beta_1 = 40^\circ$	126
10. Pressure Surface Boundary Layer Parameters, $\beta_1 = 43.4^\circ$	127
11. Pressure Surface Boundary Layer Parameters, $\beta_1 = 46^\circ$	128
12. Data for Navier-Stokes Code	179
A1. Particle Size Distribution (Seeder Probe Not Included)	193
A2. Particle Size Distribution (With Seeder Probe)	194
A3. Particle Size Distribution in Histogram Format	195

LIST OF FIGURES

Figure 1.	Schematic Description of the Flow Field Around a CD Blade at Typical Inlet Conditions	7
Figure 2.	Cascade Wind Tunnel Test Facility	19
Figure 3.	Cascade Test Section Schematic	20
Figure 4.	Controlled Diffusion Blade Profile	22
Figure 5.	Two Adjacent Blades and Test Passage Geometry, Showing Survey Stations for LDV Measurements	25
Figure 6.	CD Blade Pressure Tap Locations on Pressure and Suction Sides	29
Figure 7.	LDV System Installation	30
Figure 8.	LDV System	32
Figure 9.	Particle Generator	35
Figure 10.	Seeding Probe Installation	36
Figure 11.	Aligning Tool	38
Figure 12.	(a) Inlet Conditions - Velocity	44
Figure 12.	(b) Inlet Conditions - Flow Angle	45
Figure 13.	Periodicity in Adjacent Blade Wakes	46
Figure 14.	Beam Arrangement	47
Figure 15.	Two-Dimensionality Check of the Wake	51
Figure 16.	Two-Dimensionality Check of the Boundary Layer (Suction Surface at $y = 0$)	52

LIST OF FIGURES (CONTINUED)

Figure 17.	Two-Dimensionality Check of the Boundary Layer (Pressure Surface at $y = 0$)	53
Figure 18.	Streamlines in the Passage; $\beta_1 = 40^\circ$, $Re_C = 710000$	57
Figure 19.	Streamlines in the Passage; $\beta_1 = 43.4^\circ$, $Re_C = 740000$	58
Figure 20.	Streamlines in the Passage; $\beta_1 = 46^\circ$, $Re_C = 730000$	59
Figure 21.	Normalized Velocity Distribution in the Passage; $\beta_1 = 40^\circ$, $Re_C = 710000$	60
Figure 22.	Normalized Velocity Distribution in the Passage; $\beta_1 = 43.4^\circ$, $Re_C = 740000$	62
Figure 23.	Normalized Velocity Distribution in the Passage; $\beta_1 = 46^\circ$, $Re_C = 730000$	64
Figure 24.	Passage Inlet (Leading Edge) Velocity Distribution at Three Inlet Air Angles	66
Figure 25.	Passage Outlet Velocity Distribution for Three Inlet Air Angles	67
Figure 26.	Edge Velocity Distribution Over the Blade	68
Figure 27.	Comparison of the Edge Velocity Distribution at Three Inlet Angles	70
Figure 28.	Flow Angle Distribution in the Passage; $\beta_1 = 40^\circ$, $Re_C = 710000$	73

LIST OF FIGURES (CONTINUED)

Figure 29.	Flow Angle Distribution in the Passage; $\beta_1 = 43.4^\circ$, $Re_c = 740000$	75
Figure 30.	Flow Angle Distribution in the Passage; $\beta_1 = 46^\circ$, $Re_c = 730000$	77
Figure 31.	Passage Inlet Flow Angle Distribution for Three Inlet Angles	79
Figure 32.	Passage Outlet Flow Angle Distribution for Three Inlet Angles	80
Figure 33.	Pressure Coefficient Distribution Over the Blade	81
Figure 34.	Comparison Between Edge Velocity Distri- bution Measured with LDV and Derived from Surface Pressure Measurements	84
Figure 35.	Distribution of $\int \frac{v}{V_{ref}} \cdot dx$ Through the Passage for Three Inlet Angles	86
Figure 36.	ADVR Distribution Along the Passage	88
Figure 37.	Suction Surface Boundary Layer Velocity Distributions; $\beta_1 = 40^\circ$, $Re_c = 710000$	90
Figure 38.	Suction Surface Boundary Layer Velocity Distributions; $\beta_1 = 43.4^\circ$, $Re_c = 740000$...	92
Figure 39.	Suction Surface Boundary Layer Velocity Distributions; $\beta_1 = 46^\circ$, $Re_c = 730000$	94

LIST OF FIGURES (CONTINUED)

Figure 40.	Suction Side Boundary Layer Turbulence Level Distributions; $\beta_1 = 40^\circ$, $Re_c = 710000$	98
Figure 41.	Suction Side Boundary Layer Turbulence Level Distributions; $\beta_1 = 43.4^\circ$, $Re_c = 740000$	100
Figure 42.	Suction Side Boundary Layer Turbulence Level Distributions; $\beta_1 = 46^\circ$, $Re_c = 730000$	102
Figure 43.	Boundary Layer Thickness on the Suction Surface	105
Figure 44.	Displacement Thickness on the Suction Surface	106
Figure 45.	Momentum Thickness on the Suction Surface ...	107
Figure 46.	Shape Factor Distribution on the Suction Surface	108
Figure 47.	Pressure Surface Boundary Layer Velocity Distribution; $\beta_1 = 40^\circ$, $Re_c = 710000$	114
Figure 48.	Pressure Surface Boundary Layer Velocity Distribution; $\beta_1 = 43.4^\circ$, $Re_c = 740000$	116
Figure 49.	Pressure Surface Boundary Layer Velocity Distribution; $\beta_1 = 46^\circ$, $Re_c = 730000$	118
Figure 50.	Boundary Layer Thickness on the Pressure Surface	120
Figure 51.	Displacement Thickness on the Pressure Surface	121
Figure 52.	Momentum Thickness on the Pressure Surface	122

LIST OF FIGURES (CONTINUED)

Figure 53.	Shape Factor Distribution on the Pressure Surface	124
Figure 54.	Pressure Side Boundary Layer Turbulence Level Distribution; $\beta_1 = 40^\circ$, $Re_C = 710000$	129
Figure 55.	Pressure Side Boundary Layer Turbulence Level Distribution; $\beta_1 = 43.4^\circ$, $Re_C = 740000$	131
Figure 56.	Pressure Side Boundary Layer Turbulence Level Distribution; $\beta_1 = 46^\circ$, $Re_C = 730000$	133
Figure 57.	Wake Velocity Distributions for Four Downstream Positions; $\beta_1 = 40^\circ$, $Re_C = 710000$...	136
Figure 58.	Wake Velocity Distributions for Four Downstream Positions; $\beta_1 = 43.4^\circ$, $Re_C = 740000$..	138
Figure 59.	Wake Velocity Distributions for Four Downstream positions; $\beta_1 = 46^\circ$, $Re_C = 730000$	140
Figure 60.	Velocity Distributions at $y = 0.678"$ (0.123c from Trailing Edge)	144
Figure 61.	Flow Angle Distributions at $y = 0.678"$ (0.123c from Trailing Edge)	145
Figure 62.	Wake Turbulence Level Distributions; $\beta_1 = 40^\circ$, $Re_C = 710000$	146
Figure 63.	Wake Turbulence Level Distributions; $\beta_1 = 43.4^\circ$, $Re_C = 740000$	147
Figure 64.	Wake Turbulence Level Distributions; $\beta_1 = 46^\circ$, $Re_C = 730000$	148

LIST OF FIGURES (CONTINUED)

Figure 65.	Wake Turbulence Distributions at $y = 0.678''$ (0.123c from Trailing Edge)	150
Figure 66.	Wake Velocity Distribution; $\beta_1 = 40^\circ$	154
Figure 67.	Wake Flow Angle Distribution; $\beta_1 = 40.0^\circ$	155
Figure 68.	Wake Velocity Distribution; $\beta_1 = 43.4^\circ$	156
Figure 69.	Wake Flow Angle Distribution; $\beta_1 = 43.4^\circ$...	157
Figure 70.	Comparison with Hot-Wire Measurements of Velocity	160
Figure 71.	Comparison with Hot-Wire Measurements of Turbulence	162
Figure 72.	Comparison with Suction Surface Boundary Layer Thicknesses Calculated Using BLAYER ...	165
Figure 73.	Comparison with Suction Surface Boundary Layer Velocity Profiles Calculated Using BLAYER	166
Figure 74.	Comparison with Displacement Thickness on the Suction Surface Calculated Using S.I. Code	168
Figure 75.	Comparison with Displacement Thickness on the Pressure Surface Calculated Using S.I. Code	170

LIST OF FIGURES (CONTINUED)

Figure 76.	Comparison with Pressure Surface Boundary Layer Thicknesses Calculated Using S.I. Code with Forced Transition	174
Figure 77.	Comparison with Suction Surface Boundary Layer Thicknesses Calculated Using S.I. Code with Forced Transition	176
Figure 78.	Comparison with Pressure Coefficient Calculated Using Navier-Stokes Code	180
Figure 79.	Comparison with Suction Surface Boundary Layer Velocity Profile Using Navier-Stokes Code	182
Figure A1.	Particle Size Distribution Measurements	191
Figure A2.	Particle Size Distribution	196
Figure B1.	Flat Plate Installed in the Cascade Wind Tunnel	199
Figure B2.	Flat Plate Model	200
Figure B3.	Boundary Layer on a Flat Plate - Velocity Profiles	203
Figure B4.	Boundary Layer on a Flat Plate - Turbulence Profiles	204

LIST OF SYMBOLS

English Letter Symbols

AVDR	-	Axial Velocity Density Ratio ($= \rho_2 v_2 / \rho_1 v_1$)
c	-	Blade chord
C _o	-	Constant
C _p	-	Pressure coefficient
D	-	Distance (locally) from the blade surface
d _f	-	Fringe spacing
H	-	Shape factor
L	-	Focal length
p	-	Pressure
q	-	Dynamic pressure
Re	-	Reynolds number
Re _c	-	Reynolds number based on blade chord
s	-	Blade spacing
T	-	Temperature
t	-	Time
U _∞	-	Edge velocity (parallel to the surface)
u	-	Velocity component in the x direction
V	-	Velocity
V _{ref}	-	Reference velocity
v	-	Velocity component in the y direction
X	-	Dimensionless velocity
x	-	Horizontal displacement (inches)
y	-	Vertical displacement (inches)

LIST OF SYMBOLS (CONTINUED)

z - Spanwise displacement (inches)

Greek Letter Symbols

β - Flow angle with respect to the direction normal
to the line of the blade leading edges

γ - Ratio of specific heats, stagger angle

δ^* - Displacement thickness (inches)

λ - Wavelength

ε - Turbulence (defined as $\sqrt{\frac{u'^2 + v'^2}{2V_{ref}^2}}$)

κ - Half angle between the laser beams

ω - Loss coefficient

θ - Momentum thickness (inches)

ρ - Density

Subscripts

0 - Upstream of the guide vanes

1 - Upstream of the blade row

2 - Downstream of the blade row

atm - Atmospheric

b - Blade row

g - Guide vanes

t - Total (stagnation)

WU - Upper wall

WL - Lower wall

ACKNOWLEDGMENT

I would like to take this opportunity to thank Dr. R. P. Shreeve, Director of the Turbopropulsion Laboratory, for his advice and assistance to make this study an enjoyable learning experience.

Special thanks to Dr. Steven Shamroth for permission to include results obtained with his Navier-Stokes code and to Mr. Andreas Krainer for assistance with the S. I. viscous-inviscid code.

I. INTRODUCTION

Compressor stall and off-design behavior limit the performance attainable in the design of aircraft gas turbine engines. The occurrence of compressor stall in flight can lead to a loss of engine power and, in some circumstances, can lead to the loss of the aircraft. The need to develop higher thrust-to-weight ratio engines for fighter aircraft, and distortion tolerant engines for vertical landing applications, requires that analytical tools be developed to describe the phenomenon of stall, and particularly, its onset. Ideally the compressor flow field should be fully predictable and quantifiable in the design process at all possible operating conditions.

The aerodynamic design of compressor cascades, which is equivalent to designing the blade elements on axisymmetric stream surfaces through the machine, is usually based on simplified but realistic modelling, implemented using Computational Fluid Dynamic (CFD) codes. Design point is analyzed using Euler or potential methods, adding a boundary layer prediction, and using empirical separation criteria to avoid stall. The prediction of the off-design behavior and stall onset however, requires much more sophisticated CFD methods. Such predictions are clearly essential in the selection of optimum designs. Viscous codes based on the

full Navier-Stokes (N-S) equations are becoming increasingly available, but are generally too expensive for routine application in design refinement. In order to overcome the inefficiency of the N-S codes, but to obtain a reasonably accurate description of the flow field containing small regions of separated flow, or simply thick boundary layers, viscous-inviscid strong interaction codes are currently being developed which incorporate either integral or differential boundary layer descriptions. Unfortunately, all computational descriptions of viscous compressor cascade flow fields must rely on empirical models for transition and turbulence. Clearly, the CFD code will only predict the cascade flow well if the empirical models are good ones.

Thus, what is critical to obtaining accurate predictions of the off-design behavior of compressor cascades are carefully controlled experiments in which the viscous code descriptions are, in effect, calibrated. It was found that there were no data available in the open literature from realistic compressor blade geometries which were in sufficient detail to be used for code validation or calibration. Therefore, the present study, in which the emphasis was placed first on obtaining the needed data, was initiated.

What was achieved in the study was

- a. a detailed mapping of the flow field and, in precise detail, the viscous layer development in a modern

- controlled-diffusion compressor cascade at design and two higher incidence angle, off-design conditions;
- b. a comparison of viscous layer growth with predictions obtained using one generally available, non-interactive code, a fully interactive code, and a Navier-Stokes code;
 - c. the identification of limitations and critical needs common to all CFD approaches.

II. NATURE OF THE PROBLEM

A. CONTROLLED-DIFFUSION (CD) BLADING DESIGN

CD bladings have been developed in the last decade to replace the standard series airfoils such as NACA-65 series, Double Circular Arc (DCA), or Multiple Circular Arc (MCA). The CD design was enabled by the evolution of CFD techniques. Such methods, initially based on inviscid flow analysis, could be used to arrive at blade surface shapes having prescribed pressure distributions. By controlling diffusion on the suction surface of the airfoil, boundary layer separation could be avoided at design point, and the flow could be designed to be shock-free in the transonic range.

CD blades are quite different from NACA-65 series or DCA airfoils in that the shapes of the upper and lower surfaces are "arbitrary," resulting from the use of high order polynomials. Also, CD airfoils can be considerably more robust toward the leading and trailing edges, especially compared to the DCA blading. As a result, the trailing edge radius may also be larger in the CD airfoil.

Several organizations have developed methods to design CD airfoils but have reported the results only recently. Dunker et al (Ref. 1) designed and tested CD blade shapes in a redesigned compressor stator and in a plane cascade wind

tunnel at the DFVLR in West Germany. In the U.S., Hobbs and Weingold (Ref. 2) developed a CD blade design system for multistage compressor applications at Pratt & Whitney Aircraft. The design was based on boundary layer calculations incorporating laminar-turbulent transition by Dunham (Ref. 3) and a laminar separation and reattachment criterion by Roberts (Ref. 4). At NASA's Lewis Research Center, Sanger (Ref. 5) used an optimization technique to design CD cascades and applied the method in the redesign of the first stage stator of a two-stage fan. Sanger used a series of computational methods coupled by a numerical optimization procedure. The blade shape, from the mean line shape and thickness distribution, was defined using high order polynomials. Potential flow was calculated by a code developed by Katsanis (Ref. 6) and boundary-layer calculations were carried out using BLAYER by McNally (Ref. 7). The CD test blades and cascade geometry used in the present study were scaled from the midspan section of Sanger's redesigned stator.

All published design methods have used an inviscid flow calculation to predict pressure distribution followed by a boundary layer calculation to predict viscous behavior. The surface contour is generally modified to account for boundary layer displacement thickness and a criterion of some kind is adopted to allow designs to approach but not to exceed the suction side adverse pressure gradient which

would result in separation. For as long as separation is avoided, and the boundary layers are thin compared to the blade spacing, such modelling is appropriate, and gives good results. At well off-design conditions, corresponding to reduced through-flow, thickening boundary layers and the onset of separation make such modelling no longer accurate. To date reliable methods for the prediction of the off-design and, particularly, near-stall behavior of CD blading do not exist.

B. DESCRIPTION OF THE OFF-DESIGN FLOW FIELD

A schematic to illustrate features of the flow field over a CD blade at an incidence angle within its working range is shown in Figure 1. The significant features are labelled from 1 to 8 as follows:

1. The stagnation point, normally within the leading edge curvature.
2. Rapid acceleration of the flow around the leading edge radius. The boundary layer here is laminar.
3. Laminar separation, creating a separation bubble. Transition occurs in the free shear layer with re-attachment usually as a turbulent boundary layer. An enlargement of this region is shown as described by Walker (Ref. 8).
4. Deceleration of the flow in an adverse pressure gradient with a turbulent boundary layer.

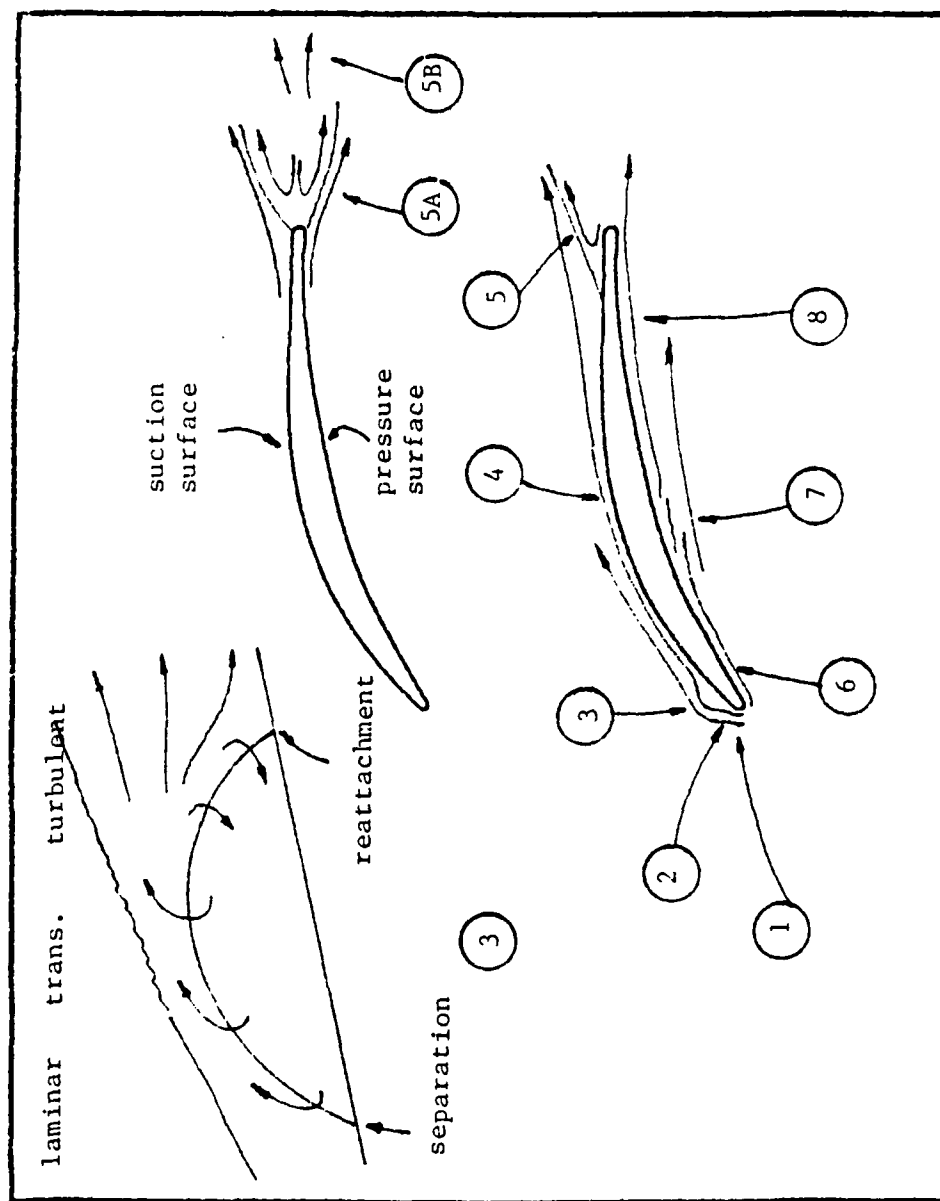


Figure 1. Schematic Description of the Flow Field Around a CD Blade at Typical Inlet Conditions (see Chapter IIB).

5. Separation of the turbulent boundary layer.

5A. When the turbulent boundary-layer remains attached over the suction surface, separation occurs at the curvature of the blunt trailing edge, creating back-flows in the near wake.

5B. Mixing in the far wake.

6. Acceleration of the flow on the leading edge radius of the pressure surface followed by a fairly uniform velocity distribution. The boundary layer here is normally laminar.

7. Boundary layer transition.

8. Turbulent boundary layer under a fairly uniform velocity distribution.

C. CALCULATING THE OFF-DESIGN FLOW BEHAVIOR

During the past twenty-five years, computational techniques for computing flow fields have become increasingly more sophisticated. Inviscid codes are well developed and used extensively in the design process. Viscous codes based on the boundary layer equations are used when the boundary layer is attached and relatively thin and the outer, inviscid flow has been solved. Such an approach is also appropriate for conditions not far from the design point if additional modelling is used for the wake flow. The viscous code BLAYER was developed for the analysis of cascade flow by McNally (Ref. 7). The BLAYER transition is predicted using the Schlichting-Ulrich-Granville method (Ref. 9).

Laminar separation creating a separation bubble is assumed to occur when wall shear stress passes from positive to negative. Turbulent separation is assumed to occur when the magnitude of the incompressible shape factor reaches a specified value.

Calculations based on the solution of the Navier-Stokes equations can, in principle, be used to calculate both on- and off-design conditions and to model, numerically, all the features of the flow field shown in Figure 1. The literature includes papers by Beam and Warming (Ref. 10), Steger (Ref. 11), Rubin and Koshla (Ref. 12) to solve the external flow around airfoils and Shamroth, McDonald, and Briley (Ref. 13), and Shafer et al (Ref. 14) for internal flow and turbomachinery applications.

To overcome the extended computer time and memory requirements of Navier-Stokes codes calculation techniques based on viscous-inviscid interactive procedures have been developed for internal flows in recent years. Johnson and Sockol (Ref. 15) developed an interactive code for a cascade of airfoils. Cebeci, Hess, and Lee (Ref. 16) adopted an external aerodynamic interactive code for cascade applications, and Krainer (Ref. 17) extended the code to calculate the flow in a NACA-65 series airfoil cascade. Viscous-inviscid interaction techniques appear to work when regions of separation are small, and therefore, should be useful in the prediction of stall on-set.

Although very sophisticated, the notable weakness of all viscous codes is that they must rely on empirical models to describe transition and turbulence. Quite complex turbulence models have been developed in the past twenty years. Bradshaw (Ref. 18), Launder and Spalding (Ref. 19), Rotta (Ref. 20), Mellor and Herring (Ref. 21), Launder, Reece, and Rodi (Ref. 22) all introduced complex methods to solve turbulent shear stresses using sets of partial differential equations. Although superior to Prandtl's mixing length theory in their generality, none of these methods results in an adequate quantitative description of the turbulent shear layers in cascades. Shear layer transition has also been widely investigated. Prediction methods for boundary layer transitions were developed by Dunham (Ref. 3), McDonald and Fish (Ref. 23), and Forest (Ref. 24). Abu-Ghannam and Shaw (Ref. 25) measured the transitional boundary layer in a wind tunnel to show the effect of free-stream turbulence, pressure gradient, and flow history. Blair (Ref. 26) measured the effect of free-stream turbulence in favorable pressure gradients as did Wang, Simon, and Buddhavarapu (Ref. 27).

Although the measurements show good agreement with transition onset predictions, transitional length predictions lack good quantitative agreement. Prediction methods for free shear layer transition, such as occurs over laminar bubbles, were developed by Horton (Ref. 28) and Roberts (Ref. 4). Measurements of the separation bubble taken by

Walker (Ref. 8) broadly support Horton's semi-empirical model although some aspects of his theory require significant modifications. A review of the nature of transitional processes in turbomachine blading and existing methods for prediction of the extent of transition was given recently by Walker (Ref. 29).

In summary, inviscid numerical codes work well. Design point conditions in a cascade can be analyzed successfully because the boundary layers are relatively thin and remain attached, and adequate techniques have been developed to model short laminar bubbles and blade wakes. Off-design conditions however, are characterized by thickening boundary layers and, at some threshold, detachment moving forward from the trailing edge. The aerodynamic forces and moments, the exiting average flow angle and the losses, will then depend critically on the thickened boundary layer profile and the location of separation. These, in turn, will depend critically on the correctness of the description used for transition and turbulent growth. Since the physics of transition and turbulence cannot yet be reproduced from fundamental laws using numerical methods, information to complete a numerical simulation must be derived from experiments. Such was the goal of the present investigation.

D. PREVIOUS EXPERIMENTS

In this section some of the earlier experiments that served to influence the present work are briefly reviewed.

NASA SP-36 (Ref. 30) is an early but thorough report on the design of axial compressors. It describes clearly how cascade concepts are used in a compressor "design system." It contains analysis and correlations of the experimentally determined performance of two-dimensional cascades of NACA-65 series, C-series, and DCA bladings. Based on the experimental data, methods to calculate the required blade camber angle, design incidence angle, pressure loss, deviation angle and, consequently, the blade setting angle, to produce specified inlet and outlet velocity vectors, are described. Information gained from many, systematic cascade wind tunnel experiments was reduced to correlating equations and data for blading design. As a result, an axial compressor can be designed successfully using the information given in NASA SP-36. What is not immediately apparent, however, is that all the information given refers strictly to the design point and can be used to predict effects of only very small incidence changes from design point incidence. Also, the great care necessary in the conduct of cascade tests is not evident in SP-36 since the report deals only with the correlation of cascade results. The many difficulties involved in obtaining inlet flow uniformity, blade passage periodicity and span-wise two-dimensionality were encountered and

overcome by the early NASA investigators (e.g., Ref. 31). Only data from strictly two-dimensional flow, requiring side-wall suction to produce an "axial-velocity-density-ratio" (AVDR), equal to unity, were used in the design correlations.

In a compressor, $AVDR \neq 1$ implies stream surface contraction as it passes through the blading. In a cascade wind tunnel, $AVDR \neq 1$ for the center-span stream surface is the result of boundary layers and corner flow on the side-walls at the ends of the blades. Starken, Breugelmans and Schimming (Ref. 32) investigated the effect of ADVR on cascade parameters such as pressure coefficient distribution, exit flow angle, loss coefficient and diffusion factor, by varying boundary layer suction at different inlet angles. They showed the importance of AVDR corrections when comparing prediction with experiment in two-dimensional cascades.

Following the early studies of viscous effects leading to compressor design techniques (Ref. 30), relatively few detailed studies of boundary layers on airfoils in cascades have been reported. Evans (Ref. 33) compared measurements of suction surface boundary layers on cascade airfoils with similar measurements made at the mid-chord of a compressor stator blade using hot-wire instrumentation. He showed that the boundary layer growth on the stator blade was significantly greater than on the cascade blade. Evans explained the phenomenon by invoking the unsteady nature of the

oundary layer development on the stator blade. This information is relevant in applying cascade data to compressor design and in making 2-D CFD codes applicable to the compressor environment. Shama et al (Ref. 34) made hot-film and hot-wire measurements in a wind tunnel simulating the two-dimensional boundary layer on the suction surface of a turbine airfoil, in order to validate computational methods and turbulence models. They showed that the McDonald-Fish turbulence model [Ref. 23] gave reasonable predictions in attached transitional boundary layers. Walker (Ref. 35) made hot-wire measurements of the turbulent boundary layer on the suction surface of an axial compressor stator blade. Walker compared the experimental results with then-current calculational methods to assess their reliability. More recently Deutsch and Zierke (Ref. 36) used a one-dimensional LDV system to measure the boundary layers on the suction and pressure surfaces of a DCA blade in a cascade at 5 degrees incidence angle. Their work served as a useful reference for the present study since it included various other measurements such as surface pressures, flow visualization to determine on-set of transition and separation, near wake measurements using the LDV, and far wake measurements using a five-hole probe.

Several investigators have reported wake measurements made in cascades. Lakshminarayana and Davino (Ref. 37) measured stator blade wakes in an axial flow compressor.

They drew conclusions concerning similarity, decay characteristics, wake width, and pressure distribution in the trailing edge region, near and far wake. They observed substantial enough differences between compressor stator wakes and cascade wakes to warrant the development of a three-dimensional analysis. Ravindranath and Lakshminarayana (Ref. 38) reported similar measurements made in the wakes of a compressor rotor blade. Hobbs et al (Ref. 39) examined the wakes of CD blades in a cascade with the intent of improving the modelling of wake effects then using inviscid analysis. The experiments included measurements of the near and far wakes and of the trailing edge boundary layers using hot-film, Kiel, and five-hole pneumatic probes. An outgrowth of the latter study was an experiment by McCormick and Paterson (Ref. 40) to simulate the CD blade trailing edge and wake flows on a large scale. A single one inch plate was used in a model wind tunnel, the walls of which were adjusted to simulate mid-passage streamlines. Qualitative similarities were found in the wake behavior measured in the present study and McCormick and Peterson's detailed observations for a single, simulated test condition for a specific, but different, CD blade design. In particular, the strong asymmetry in the near-wake velocity profiles was observed in both studies. This asymmetry was previously reported by Dreon (Ref. 41) based on pneumatic, five-hole cone probe measurements of the CD blade wakes in

the present cascade. The present work includes a comparison of the results of LDV measurements with Dreon's calibrated pneumatic probe data.

The program at the Turbopropulsion Laboratory of the Naval Postgraduate School leading to the present study involved experimental measurements in the low speed cascade wind tunnel first with DCA blading, and then with CD blading which was designed to replace the DCA section at the mid-span section of the stator of a NASA transonic stage. Following several preliminary studies, Himes (Ref. 42) reported the blade element performance of the reference DCA cascade design. McGuire (Ref. 43) used flow visualization techniques to examine the transition and boundary layer separation on the DCA blades. Koyuncu (Ref. 44) replaced the DCA blades with the "equivalent" CD blades and evaluated their performance over a wide incidence range. Sanger and Shreeve (Ref. 45) compared the CD cascade results with numerical design and analysis code predictions. The two series of blading tests included surface pressure measurements, calibrated five-hole probe inlet and wake measurements, and surface flow visualization using tufts, oil smear and china clay techniques. A lower loss coefficient and wider range were measured with the CD than with the DCA blading. Measurements compared reasonably well with results of non-interactive numerical codes at the design incidence, except for the pressure distribution and the identification

of separation near the trailing edge. The prediction of losses at off-design incidence angles was extremely poor, and the viscous calculations were found to require the input of boundary layer information which was not resolved adequately in the experiments.

Thus, the present study capitalized on the previous experimental knowledge, but was focused on providing the precise viscous flow field information necessary for the calibration of strong-interaction or fully viscous analysis methods required in the prediction of off-design performance and compressor blade stall.

III. TEST FACILITY AND INSTRUMENTATION

A. RECTILINEAR CASCADE

A schematic diagram of the rectilinear subsonic cascade wind tunnel facility is shown in Figure 2. A more detailed description of its design and operation was given by Rose and Guttormson (Ref. 46). Flow inlet conditions were investigated in detail by McGuire (Ref. 43). While uniform on average, the inlet flow (far upstream) contains periodic wakes due to variable inlet guide vanes which are spaced one inch apart in the blade-to-blade direction. The test section downstream of the guide vanes is shown in Figure 3. The test section dimensions are slightly different from those given by Koyuncu (Ref. 44) and Dreon (Ref. 41). A broken line in Figure 3 represents the optical window used in the present study. The original 7/8" thick plexiglas window was replaced by a 1/4" thick plexiglas window to reduce light transmission energy losses.

B. CD BLADING AND CASCADE CONFIGURATION

The CD test blades and cascade geometry were scaled from the design of the mid-span section of a CD compressor stator blade row (Ref. 5 and Ref. 45). Twenty aluminum blades were machined with a span of ten inches to fit the 60" X 10" test section of the rectilinear cascade. A single blade is

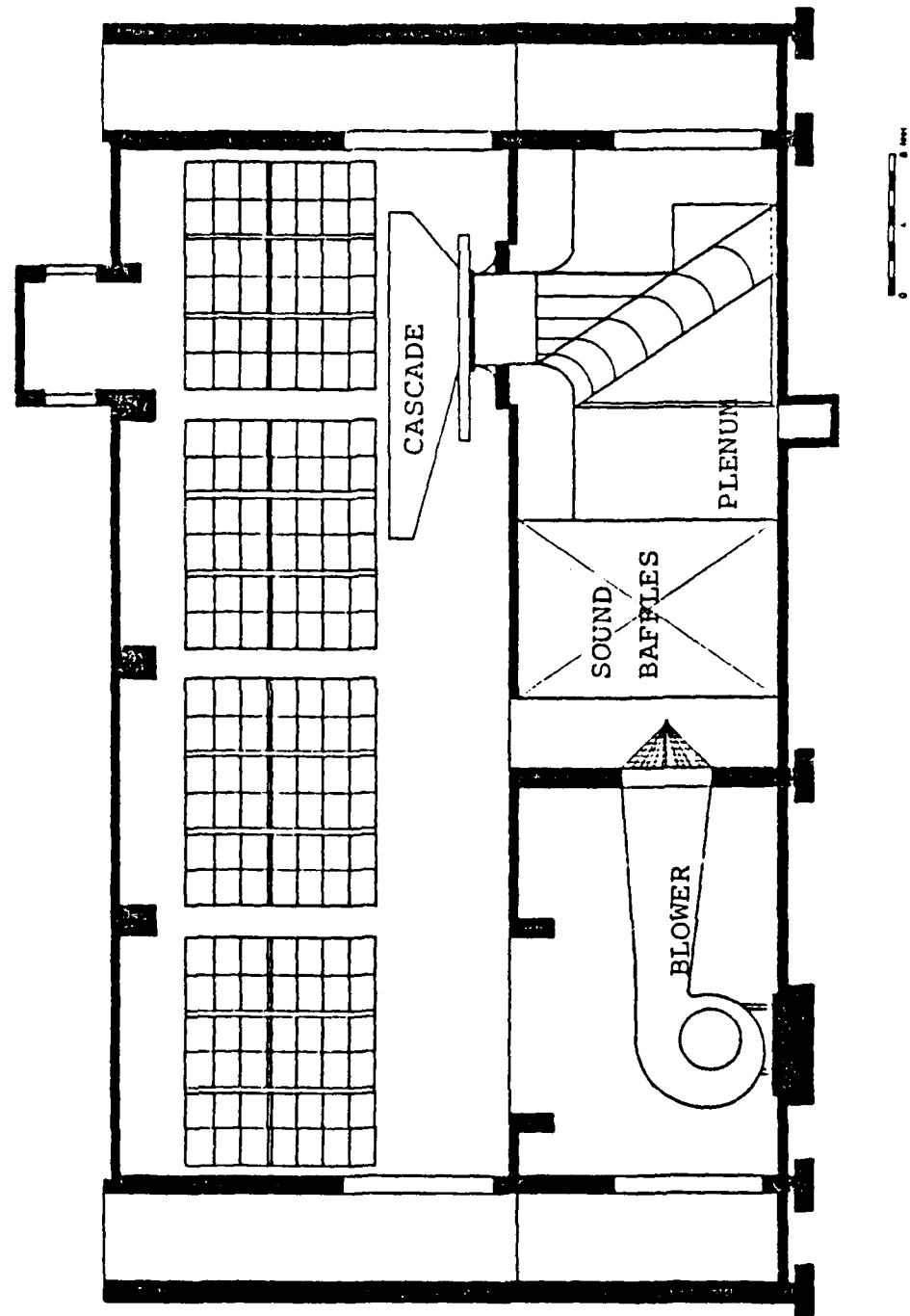


Figure 2. Cascade Wind Tunnel Test Facility.

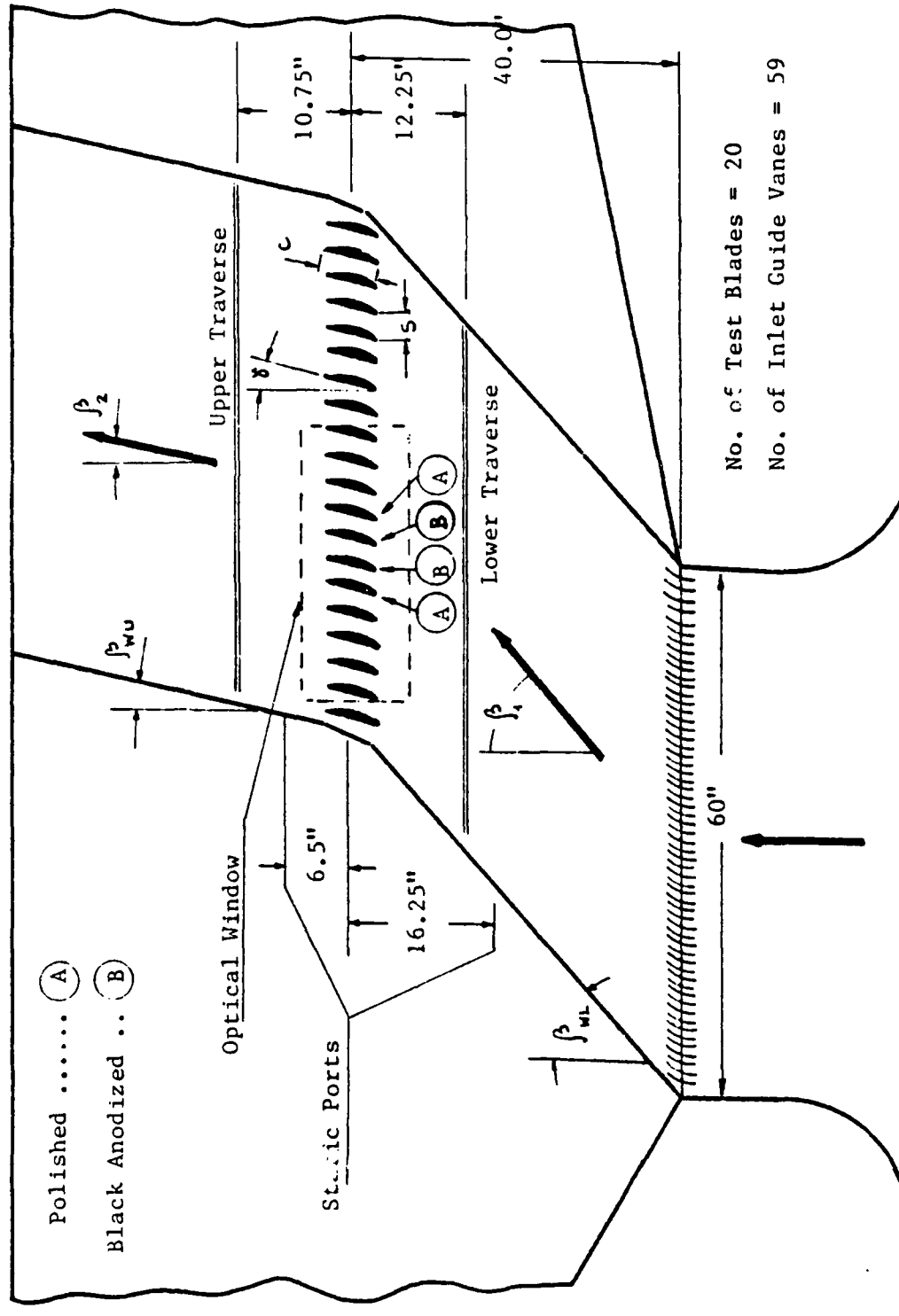


Figure 3. Cascade Test Section Schematic.

shown in Figure 4. The coordinates of the profile are given in Table 1. The geometrical parameters for the cascade are given in Table 2. A single test passage, bounded by two adjacent blades as seen through the optical window is shown in Figure 5. The coordinates of the test passage are given in Table 3 in the coordinate system of Figure 5.

To reduce back reflections from the blade surface four blades were specially treated. Two blades were polished, and the other two were black anodized. The latter allowed flow measurements in the boundary layer closer to the blade surface.

Pressure taps were provided in two other blades. The coordinates of the pressure taps are shown in Figure 6. The locations of the different blades in the cascade are shown in Figure 3. At each setting of the inlet air angle, the blade pair defining the test passage shown in Figure 5 were the 7th and 8th blades from the left in Figure 3.

C. INSTRUMENTATION

1. Laser Doppler Velocimeter (LDV)

The two-dimensional LDV measurement system consisted of four major subsystems: (a) the laser and optics, (b) the data acquisition system, (c) the traverse mechanism, and (d) the seeding probe. A photograph of the LDV equipment is shown in Figure 7.

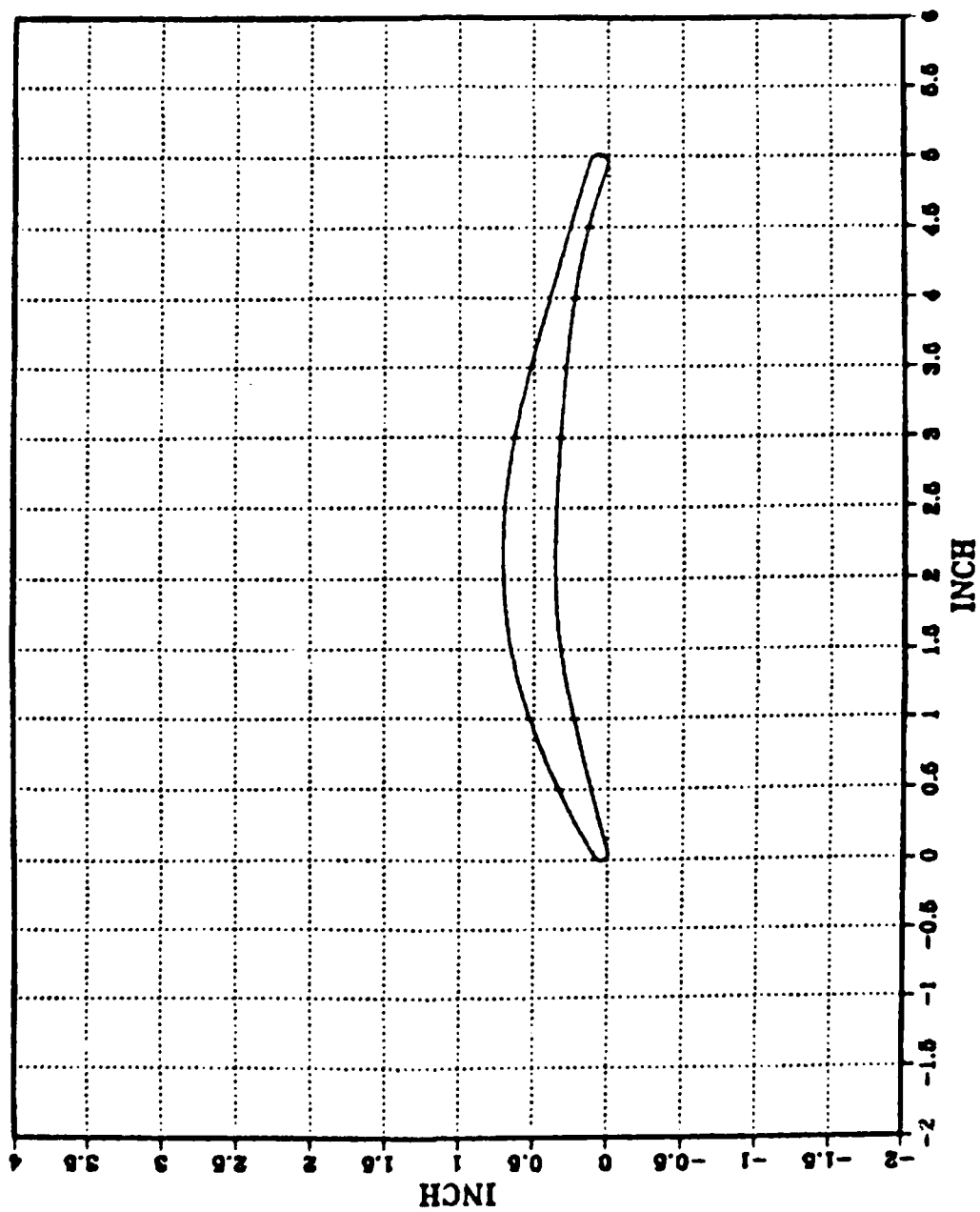


Figure 4. Controlled Diffusion Blade Profile.

TABLE 1.

TEST BLADE COORDINATES (INCHES)		
X	Y (PRESSURE SIDE)	Y (SUCTION SIDE)
0.0	0.045	0.045
0.022	-----	0.084
0.057	0.002	-----
0.222	0.044	0.196
0.444	0.101	0.307
0.666	0.155	0.403
0.888	0.207	0.488
1.110	0.255	0.561
1.332	0.299	0.621
1.554	0.330	0.663
1.776	0.350	0.691
1.998	0.359	0.705
2.220	0.359	0.708
2.442	0.352	0.701
2.664	0.342	0.681
2.886	0.331	0.650
3.108	0.317	0.610
3.330	0.301	0.563
3.552	0.281	0.510
3.774	0.257	0.453
3.996	0.227	0.393
4.218	0.191	0.332
4.440	0.146	0.270
4.662	0.089	0.208
4.884	0.019	0.145
4.925	0.004	-----
4.964	-----	0.122
5.010	0.062	0.062

(Coordinate System as in Figure 4)

TABLE 2
GEOMETRICAL PARAMETERS OF THE CASCADE

Number of Blades	20
Blade Spacing	3.0"
Chord	5.01"
Solidity	1.67
Leading Edge Radius	0.045"
Trailing Edge Radius	0.062"
Thickness	7% Chord
Setting Angle	14.2 ± 0.1 deg.
Stagger Angle	14.4 ± 0.1 deg.
Span	10.0"

NOMINAL TEST CONDITIONS

T_{t1}	530	°R
P_{t1}	1.032	Atmos.
P_2	1.00	Atmos.
M_1	0.25	
Re_c	700,000	

#	1	2	3	4	5	6	7	8			
y(")	-6.292	-4.792	-4.542	-4.292	-4.042	-3.792	-3.292	-2.792			
9	10	11	12	13	14	15	16	17	18	19	
	-2.292	-1.792	-1.292	-0.792	-0.5	-0.25	0.0	0.262	0.362	0.678	1.062

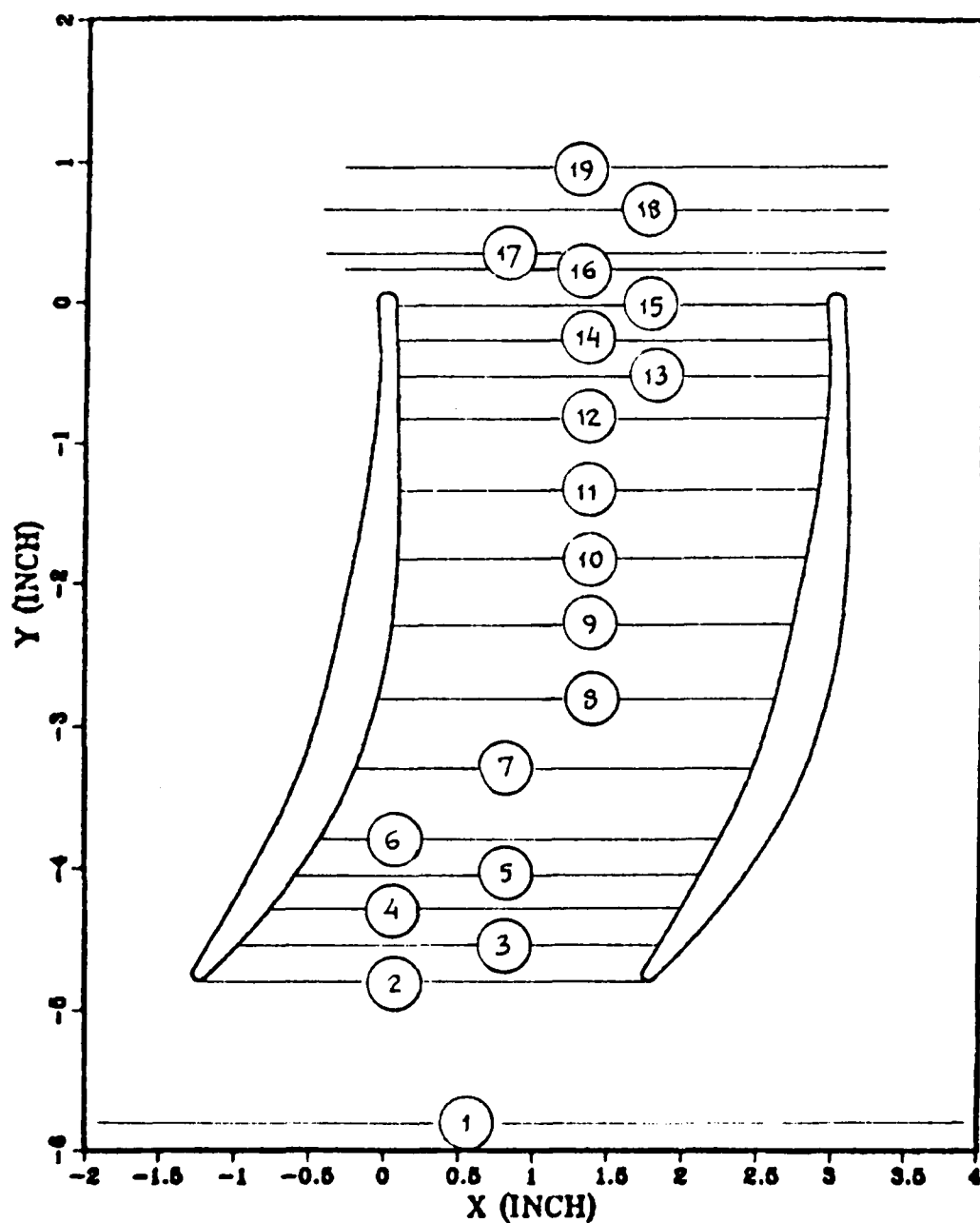


Figure 5. Two Adjacent Blades and Test Passage Geometry, Showing Survey Stations for LDV Measurements.

TABLE 3
COORDINATES OF THE TEST PASSAGE BETWEEN ADJACENT BLADES

	VERTICAL	HORIZONTAL	HORIZONTAL
1.	-4.7905	-1.2386	1.7614
2.	-4.7806	-1.2574	1.7426
3.	-4.7738	-1.2636	1.7364
4.	-4.7677	-1.2674	1.7326
5.	-4.7619	-1.2699	1.7301
6.	-4.7596	-1.2707	1.7293
7.	-4.7509	-1.2723	1.7277
8.	-4.7407	-1.2721	1.7279
9.	-4.7358	-1.2711	1.7289
10.	-4.7310	-1.2696	1.7304
11.	-4.7245	-1.2666	1.7334
12.	-4.5751	-1.1848	1.8152
13.	-4.3741	-1.0747	1.9253
14.	-4.1723	-0.9675	2.0325
15.	-3.9700	-0.8623	2.1377
16.	-3.7668	-0.7610	2.2390
17.	-3.5625	-0.6635	2.3365
18.	-3.3550	-0.5786	2.4214
19.	-3.1449	-0.5044	2.4956
20.	-2.9320	-0.4409	2.5591
21.	-2.7168	-0.3860	2.6140
22.	-2.5000	-0.3380	2.6620
23.	-2.2824	-0.2928	2.7072
24.	-2.0646	-0.2486	2.7514
25.	-1.8460	-0.2074	2.7926

TABLE 3 (CONTINUED)

COORDINATES OF THE TEST PASSAGE BETWEEN ADJACENT BLADES

	VERTICAL	HORIZONTAL	HORIZONTAL
26.	-1.6269	-0.1681	2.8319
27.	-1.4068	-0.1326	2.8674
28.	-1.1858	-0.1010	2.8990
29.	-0.9633	-0.0753	2.9247
30.	-0.7392	-0.0553	2.9447
31.	-0.5130	-0.0441	2.9559
32.	-0.2838	-0.0445	2.9555
33.	-0.0514	-0.0575	2.9425
34.	-0.0080	-0.0619	2.9381
35.	-0.0028	-0.0619	2.9381
36.	0.0074	-0.0616	2.9384
37.	0.0153	-0.0601	2.9399
38.	0.0220	-0.0580	2.9420
39.	0.0303	-0.0541	2.9459
40.	0.0441	-0.0436	2.9564
41.	0.0520	-0.0338	2.9662
42.	0.0587	-0.0199	2.9801
43.	0.0601	0.0153	3.0153
44.	0.0420	0.0456	3.0456
45.	0.0294	0.0546	3.0546
46.	0.0179	0.0593	3.0593
47.	0.0007	0.0621	3.0621
48.	-0.0825	0.0646	3.0646
49.	-0.3132	0.0708	3.0708
50.	-0.5436	0.0761	3.0761

TABLE 3 (CONTINUED)

COORDINATES OF THE TEST PASSAGE BETWEEN ADJACENT BLADES

	VERTICAL	HORIZONTAL	HORIZONTAL
51.	-0.7741	0.0813	3.0813
52.	-1.0043	0.0856	3.0856
53.	-1.2342	0.0889	3.0889
54.	-1.4634	0.0893	3.0893
55.	-1.6916	0.0858	3.0858
56.	-2.9183	0.0765	3.0765
57.	-2.1433	0.0605	3.0605
58.	-2.3661	0.0357	3.0357
59.	-2.5862	0.0002	3.0002
60.	-2.8030	-0.0478	2.9522
61.	-3.0174	-0.1056	2.8944
62.	-3.2291	-0.1740	2.8260
63.	-3.4373	-0.2559	2.7441
64.	-3.6420	-0.3515	2.6485
65.	-3.8423	-0.4644	2.5356
66.	-4.0394	-0.5900	2.4100
67.	-4.2336	-0.7272	2.2728
68.	-4.4250	-0.8751	2.1249
69.	-4.6127	-1.0375	1.9625
70.	-4.7787	-1.1957	1.8043
71.	-4.7803	-1.1974	1.8026
72.	-4.7842	-1.2025	1.7975
73.	-4.7878	-1.2087	1.7913
74.	-4.7907	-1.2174	1.7826
75.	-4.7905	-1.2386	1.7614

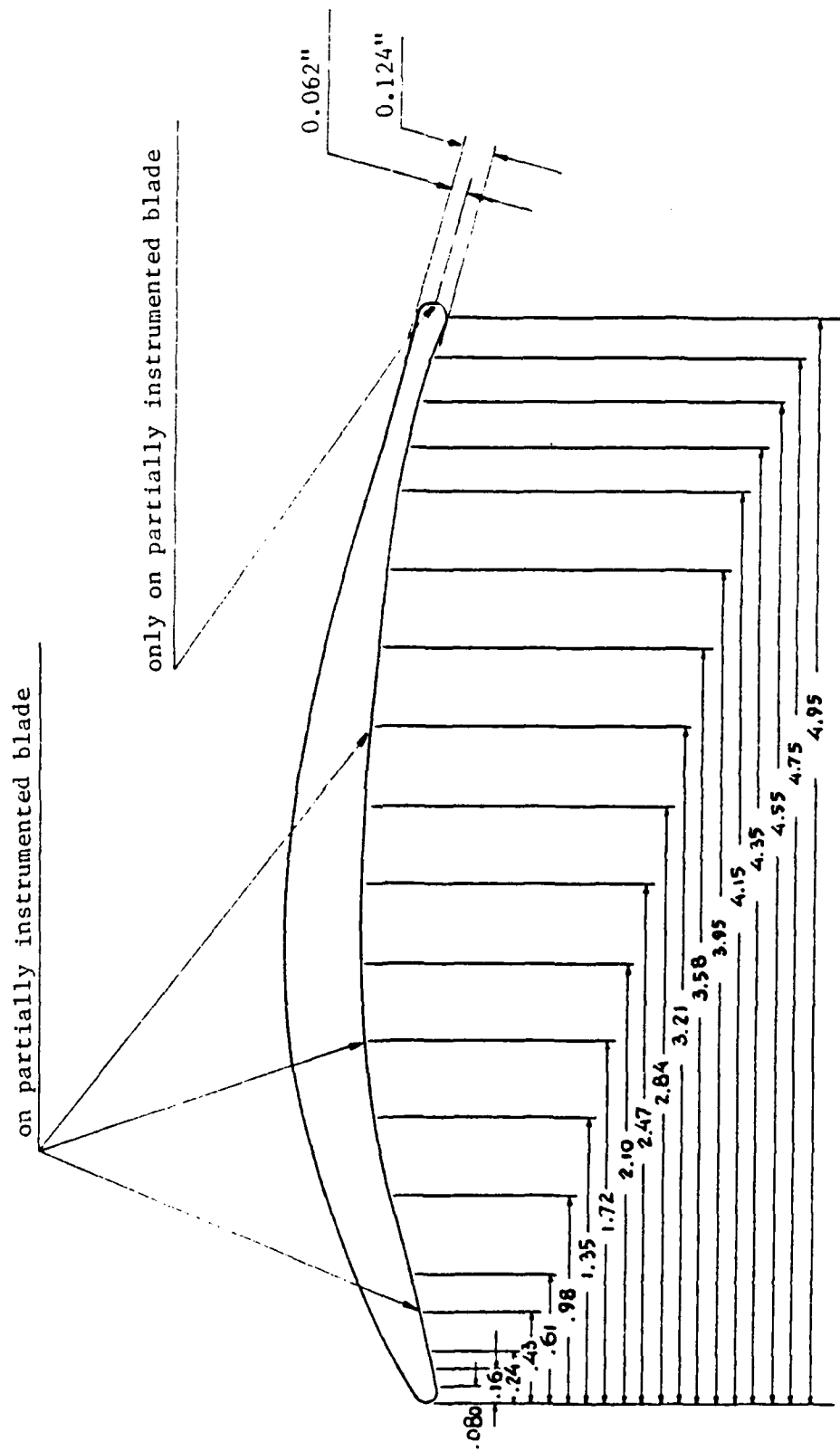


Figure 6. CD Blade Pressure Tap Locations on Pressure and Suction Sides.



Figure 7. LDV System Installation.

a. Laser and Optics

A TSI Model 9100-7 (backscatter) LDV system was used. A top view of the system is shown in Figure 8. The laser was a Laxell five-watt argon-ion laser. A prism separated the laser output beam into different colors. Two colors, green (514.5 nm) and blue (488 nm) were selected by the optical components. The two beams were centered and split into a four beam arrangement to measure two velocity components at right angles to each other. Two Bragg cells shifted the frequency of one beam in each pair to allow measurements of reversed flows. The four beams then passed through a divergence section which improved the dimensions of the measuring volume. The end lens produced a focal length of 762 mm for the four beams. Two photo-detectors collected the scattered light after it passed through the same optics. Table 4 contains a summary of the characteristics of the LDV system.

b. Data Acquisition

The data acquisition system consisted of two TSI Model 1990 counter-type signal processors in which the signals from the photo-detectors were processed and transformed into voltages proportional to the Doppler frequencies. An interface unit mounted on one of the counters transferred the information to a Hewlett-Packard 1000 series computer that controlled the data acquisition and performed

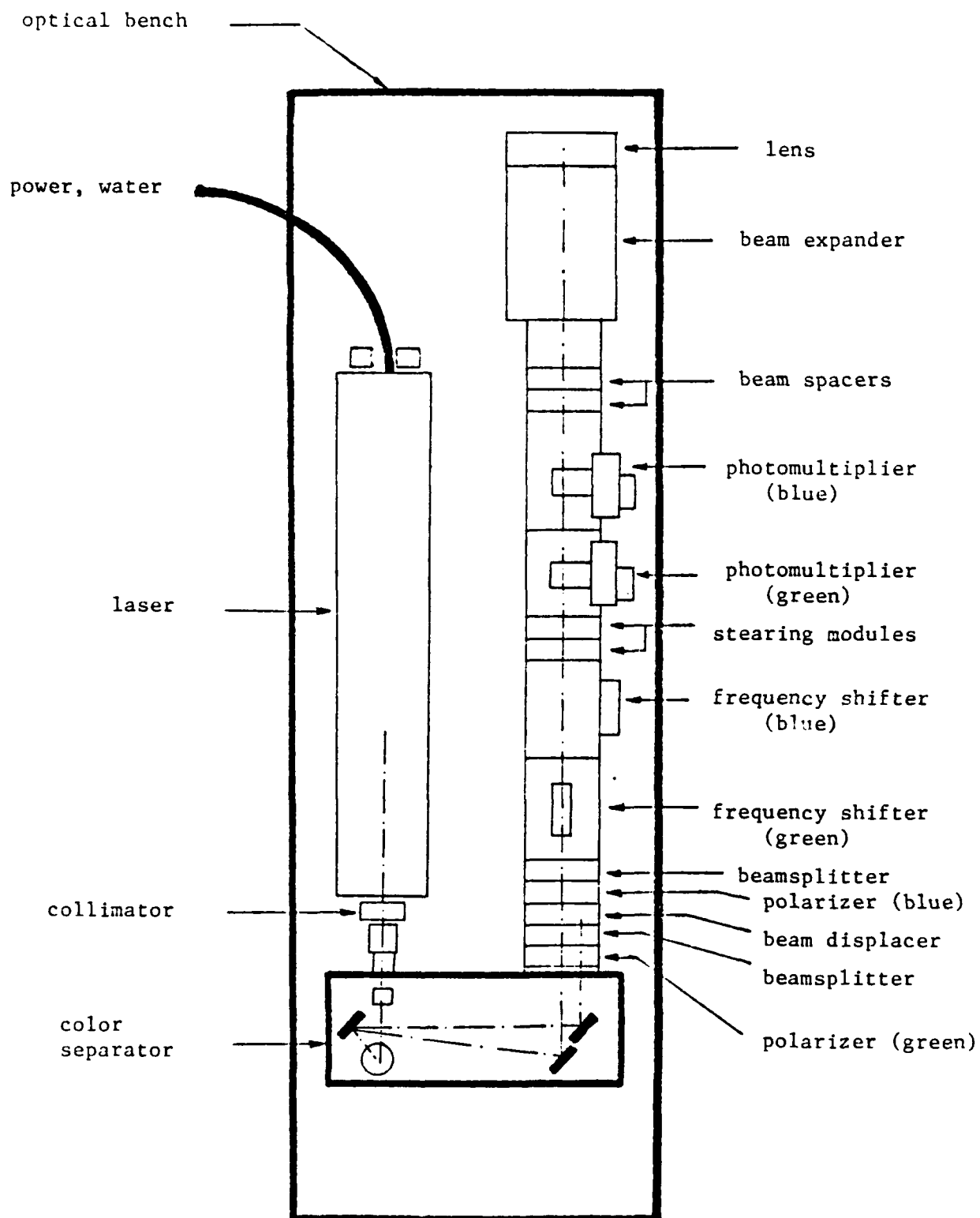


Figure 8. LDV System.

TABLE 4
LDV CHARACTERISTICS

WAVELENGTH	: Blue - 488 nm, Green - 514.5 nm
FRINGE SPACING	: Blue - 4.51 μm , Green - 4.76 μm
FOCAL LENGTH	: 762 mm
NUMBER OF FRINGES	: 28
HALF ANGLE	: 3.10°
MEASURING VOLUME DIAMETER:	133 μm
MEASURING VOLUME LENGTH :	2.5 mm
FREQUENCY SHIFT	: 2kHz to 40 MHz in 1,2,5, sequence to 10 MHz
SIGNAL PROCESSOR	: Counter Type (TSI Model 1990)
COUNTER SETTINGS	: Filters - As Required Gain - As Required Single Measurement per Burst 8 Cycles per Burst 4% Comparison Coincidence Mode

preliminary analysis of the data. The software "DRP3" was provided by TSI.

c. Traverse Mechanism

The laser and optics, mounted on an optical bench, were installed on the bed of a milling machine modified to serve as a traversing mechanism. The bed was manually traversed in x,y, and z directions, and the x and z coordinates were recorded manually using digital-electronic readouts.

d. Seeding

The flow was seeded with commercial olive-oil droplets. The seeding system consisted of the particle generator and the seeding probe. The particle generator is shown in Figure 9. The geometry and dimensions of the seeding probe are shown in Figure 10. The probe was installed upstream of the guide vanes to seed the required streamlines such that there was minimum disturbance to the flow and minimum oil contamination on the optical window. The particle size distribution was measured in preliminary tests as a function of the feed air pressure as described in Appendix A. An air pressure of 40 psi was selected to give an average particle size of 0.9 microns with a standard deviation of 0.45 microns. Ninety-five percent of the particles were smaller than 1.8 microns in diameter. These characteristics were considered to be satisfactory by the

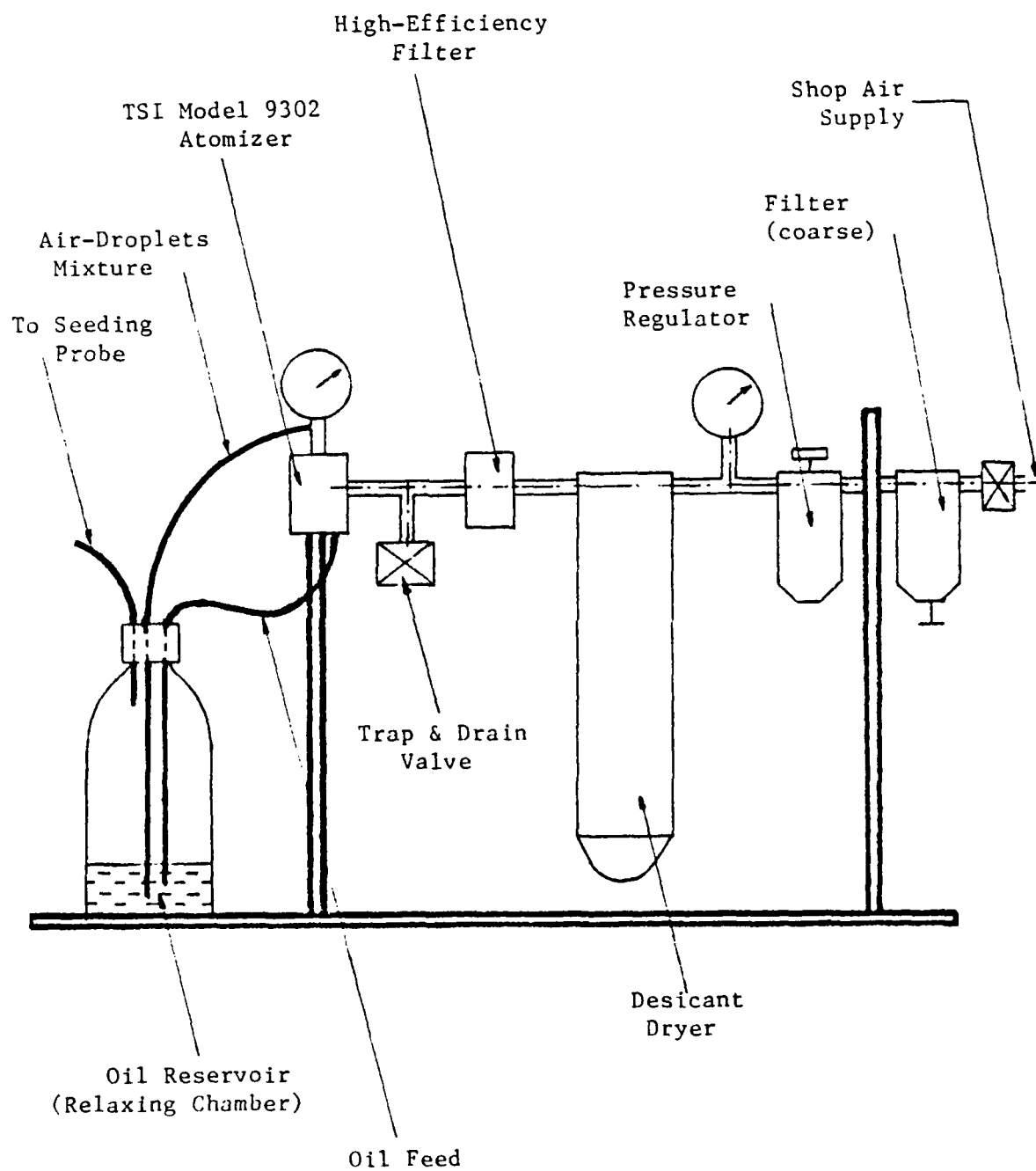


Figure 9. Particle Generator.

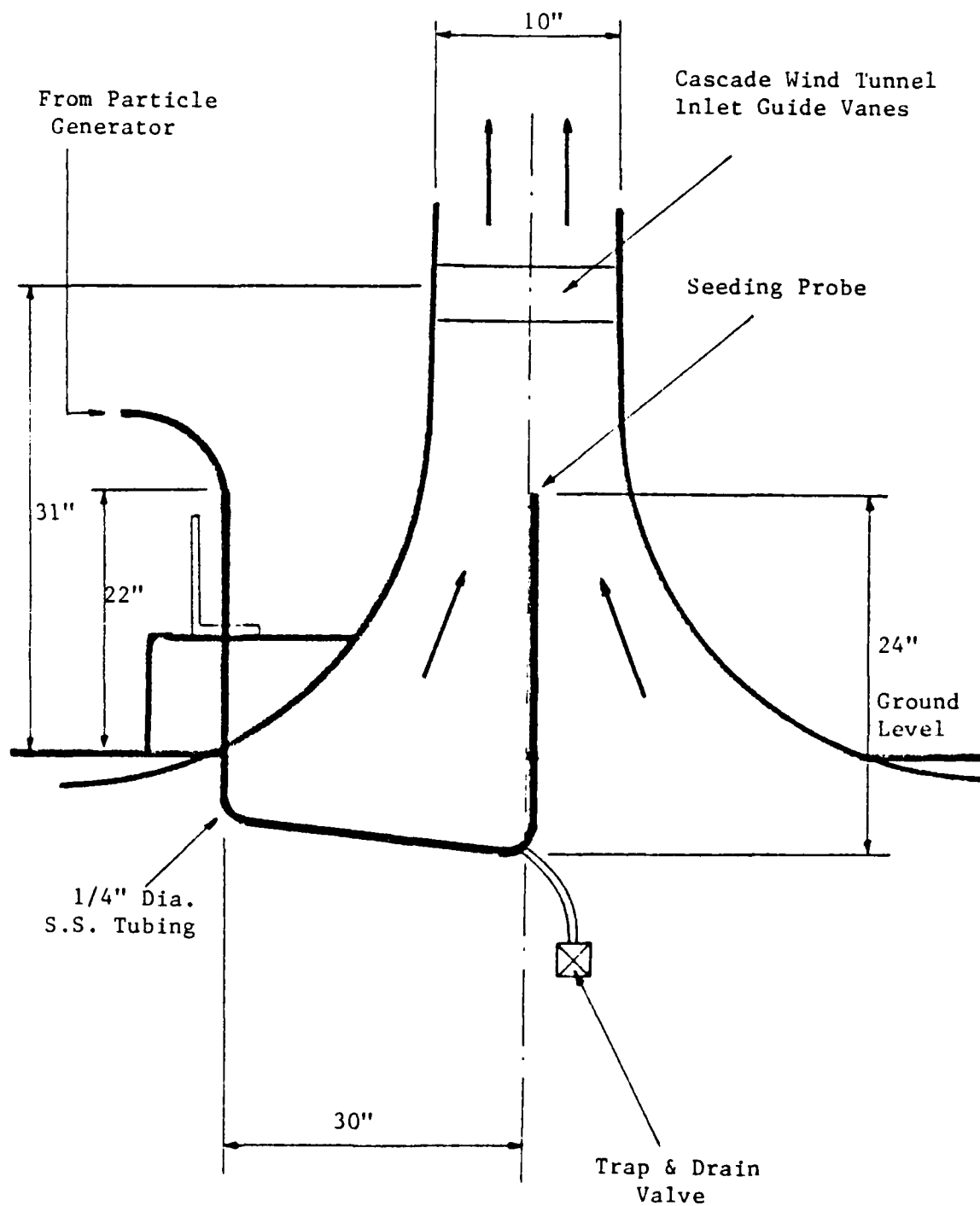


Figure 10. Seeding Probe Installation

criteria described by Durst, Melling, and Whitelaw [Ref. 47], pp. 275-285, or Dring (Ref. 48).

e. Aligning Tool

An aligning tool was designed to position the LDV system measuring volume with respect to the blades in the test section. Figure 11 shows the aligning tool installed between two blades. When the measuring volume was positioned at one of the 0.013" diameter holes the four beams were clearly visible on the far side-wall.

2. Survey Probe

A United Sensor Model 5711 cylindrical pneumatic five-hole probe was used to measure the inlet conditions (velocity and flow angle) to the test section. the probe was located 1.8 chord lengths (1.8c) axially upstream of the blade row. A Hewlett-Packard Data Acquisition System (HP-3032) and an HP Interface Bus (HP-98034 HP-IB) were used to collect data from pressure probes and surface pressure taps, through two 48-port Scanivalves. The system was controlled by an HP-9845A computer.

3. Cascade Wind Tunnel Operating Instrumentation

Tunnel (plenum) stagnation pressure was measured using a tube suspended in the plenum chamber below the wind tunnel. An iron-constantan thermocouple, similarly suspended in the plenum, measured stagnation temperature. Two rows of static taps (Fig. 3) were connected to water manometers, and used to monitor the static pressure

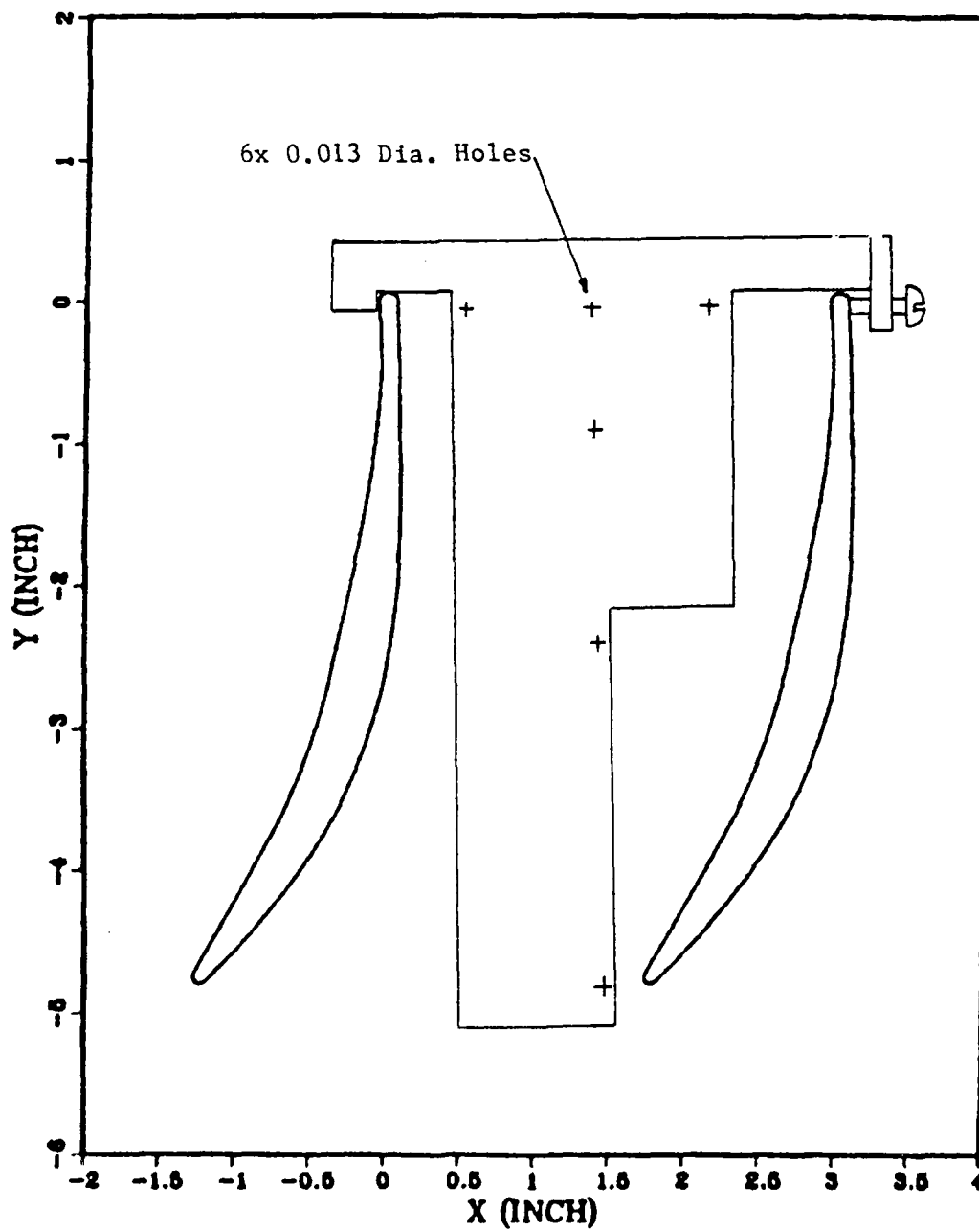


Figure 11. Aligning Tool

distribution into and out of the test cascade. At each inlet air angle, the inlet guide vanes and outlet tailboards were adjusted to produce nearly uniform static pressure in the blade-to-blade direction both upstream and downstream of the test blading.

D. MEASUREMENT UNCERTAINTY

Table 5 summarizes the measurement uncertainties. The uncertainties of the LDV parameters (K , L , λ) were supplied by TSI. Fringe spacing was calculated using (Ref. 47)

$$d_f = \frac{\lambda}{2 \sin K}$$

The particle velocity uncertainty was calculated using

$$\frac{\Delta V}{V} = \frac{\Delta d_f}{d_f} + \frac{\Delta t}{t} = \frac{\Delta d_f}{d_f} + \frac{V \Delta t}{8 d_f}$$

where Δt = clock accuracy = 1 n-sec.

$$t = \text{time to cross 8 fringes} = 8 d_f / V$$

Since the particles do not follow the flow precisely, the flow velocity uncertainty is always than the particle velocity uncertainty.

TABLE 5
MEASUREMENT UNCERTAINTIES

<u>ITEM</u>	<u>DESCRIPTION</u>	<u>METHOD</u>	<u>UNCERTAINTY</u>
x	Blade-to-Blade (Passage)	Milling Machine Elec. Readout	0.01"
x	Distance from Blade Surface	Milling Machine Elec. Readout	0.002"
y	Vertical	Milling Machine Scale	0.01"
y	Distance from Blade Surface	Milling Machine Scale	0.002"
z	Spanwise	Milling Machine Elec. Readout	0.05"
	Pitch, Roll, Yaw of LDV System	Electronic Precision Level Sperry Model 45	0.1 deg.
Pt	Plenum Pressure	Water Manometer	0.10" H ₂ O
p	Pressure	Scanivalve Transducer	0.05" H ₂ O
Patm	Atm. Pressure	Mercury Barometer	0.01" Hg
Tt	Plenum Temperature	Iron Constantan Thermocouple	0.25 deg. F
	LDV Counter Clock		1 n-sec.
K	Beam Half Angle		20 arcsec. (0.2%)
L	Focal Length		7.6 mm (1%)
λ	Wavelength		0.1%
d_f	Fringe Spacing		0.3%
V	Particle Velocity	(for V=10 m/sec.) (for V=100 m/sec.)	0.33% 0.65%

IV. EXPERIMENTAL PROCEDURE

A. OVERVIEW

First, in order to exercise and verify all aspects of the LDV measurement system, an experiment was conducted in the cascade wind tunnel to measure the boundary layer on a flat plate and to compare the results with analytical solutions and other published data. A detailed description of the flat plate experiment is given in Appendix B. The velocity measurements which were obtained at low Reynolds number showed very good agreement with the Blasius solution for a laminar boundary layer on a flat plate. The turbulence distribution measurements also showed good agreement with other published data.

The CD blading was then installed, as shown in Figure 3 and detailed flow measurements were made for three different inlet air angles, namely;

1. $\beta_1 = 40^\circ$ - the design condition,
2. $\beta_1 = 43.4^\circ$ - a moderate positive incidence angle, and
3. $\beta_1 = 46^\circ$ - a high incidence angle, near to stall.

At each inlet air angle measurements were made covering four regions of the flow field, namely;

1. the inlet flow field 0.3 chords upstream of the blade leading edge,

2. the passage between the 7th and 8th blades, to map the inviscid field,
3. the 7th blade pressure and suction surface boundary layers, to map their growth, and
4. the wake downstream of the 7th blade.

B. SET-UP PROCEDURES

1. Wind Tunnel Adjustments

At each inlet angle, special attention was given to setting the tunnel to obtain a uniform and correct inlet flow angle. The inlet side-walls were first set to the required angle. Then the guide vanes were set approximately based on previous experience. The flow angle distribution at the inlet was measured with a five-hole probe and then, for the test passage only, with the LDV. The guide vanes were then adjusted to give the correct flow angle distribution guided by the probe and LDV measurements. Static pressure distributions were observed using water manometers to verify uniformity of pressures at the inlet and outlet of the test section.

(a) Inlet Flow Quality

For conditions similar to those in the present study, McGuire (Ref. 43) and Dreon (Ref. 41) made probe measurements of the inlet velocity field 1.8 chords upstream of the test blades and obtained acceptably uniform distributions of the velocity and the flow angle. In the

present study the LDV system was used to measure the inlet conditions to the test passage (between the 7th and 8th blades) 0.3 chords upstream of the test blading. (This was as far upstream as the window would allow.) The results, plotted in Figure 12, showed nearly uniform velocity and flow angle at each of the three inlet air angles. The deviation from total uniformity is likely to be the upstream influence of the blades.

(b) Periodicity

At similar conditions to those in the present study, Koyuncu (Ref. 44) and Dreon (Ref. 41) made probe measurements of the far wake to verify periodic behavior of the cascade. LDV measurements presented in Figure 13 showed similar results for the 7th and 8th blade wakes.

2. LDV Optical System Alignment

Periodic LDV alignments were carried out regularly to ensure proper beam crossing and fringe patterns. Special optical configurations were set for different parts of the experiment. Usually it was preferred to orient the beams such that the velocity vector lay at about 45 degrees to the blue and green beams. Thus, as shown in Figure 14, when testing in the lower section of the cascade (stations 1-5 in Figure 5) the beams were arranged in a vertical-horizontal arrangement, whereas in the upper part of the cascade (stations 6-19 in Figure 5) the beams were rotated by 45 degrees. Most measurements were taken with the Bragg cells

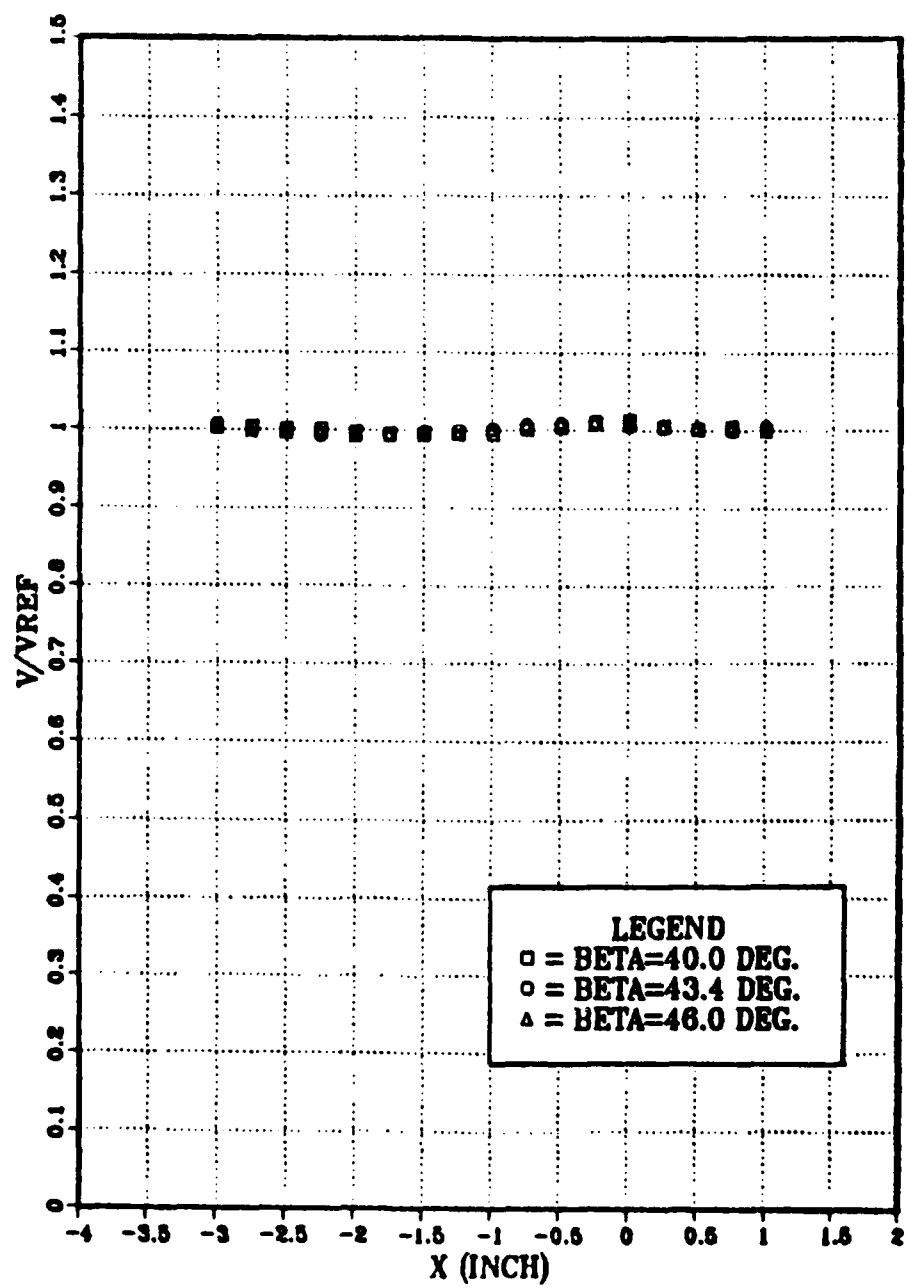


Figure 12(a). Inlet Conditions - Velocity.

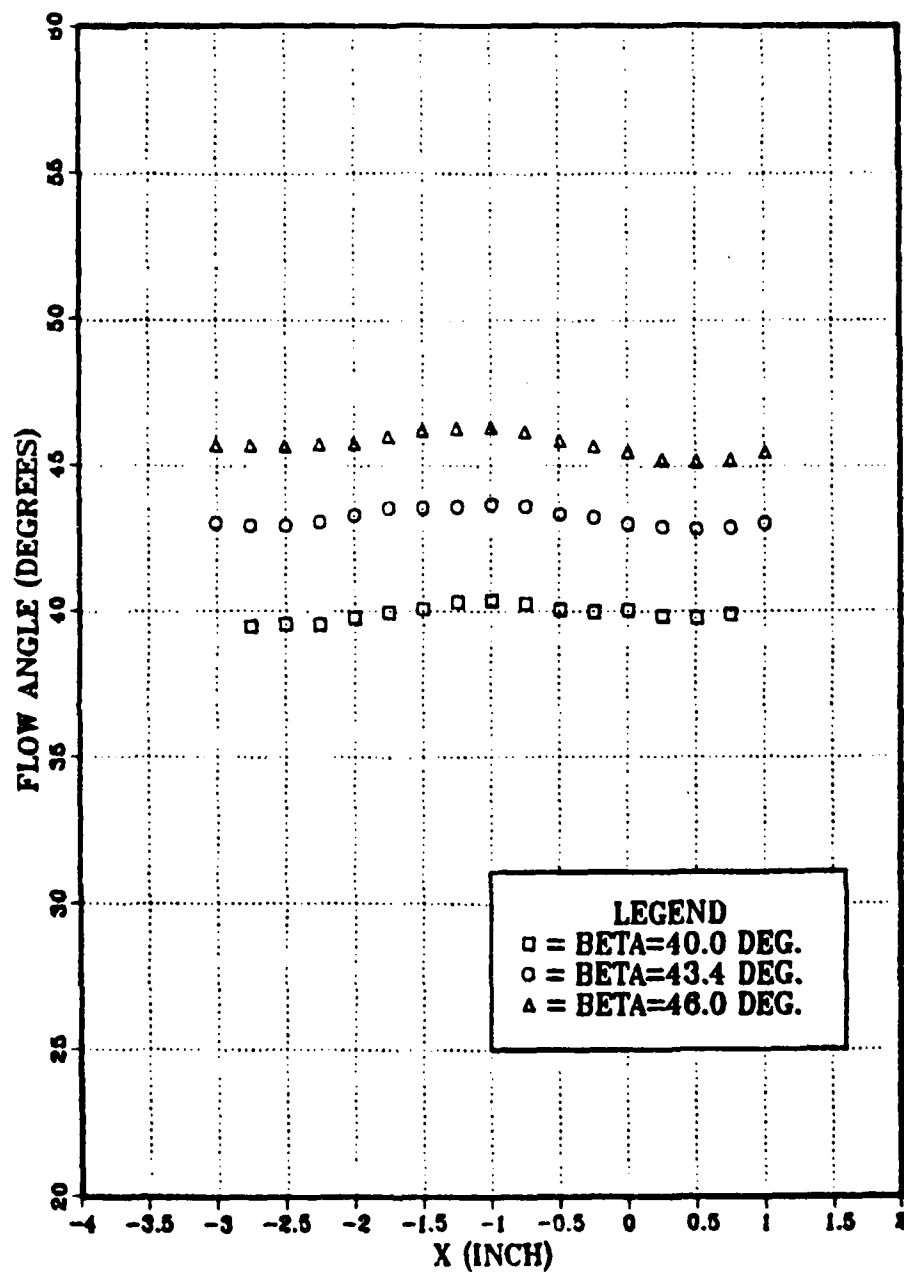
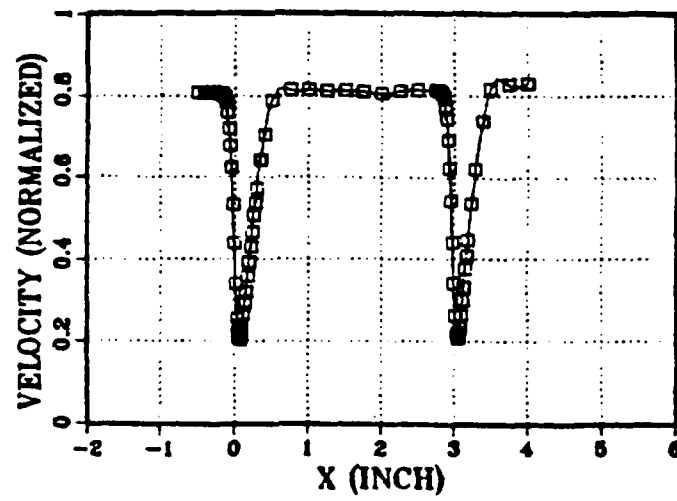


Figure 12(b). Inlet Conditions - Flow Angle.

BETA = 43.4 DEG.



BETA = 46 DEG.

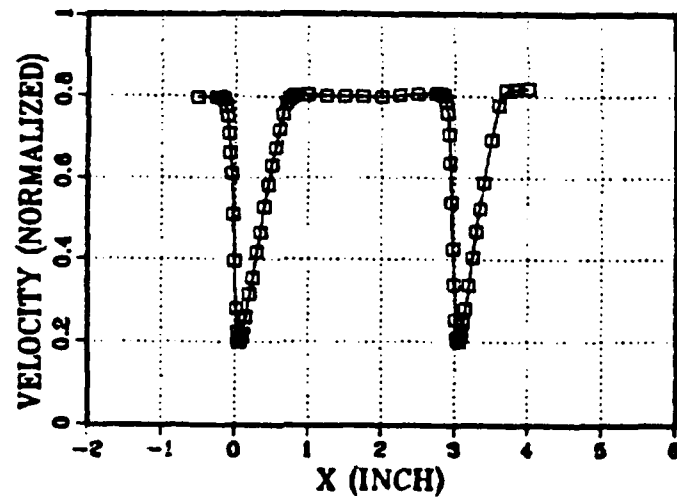
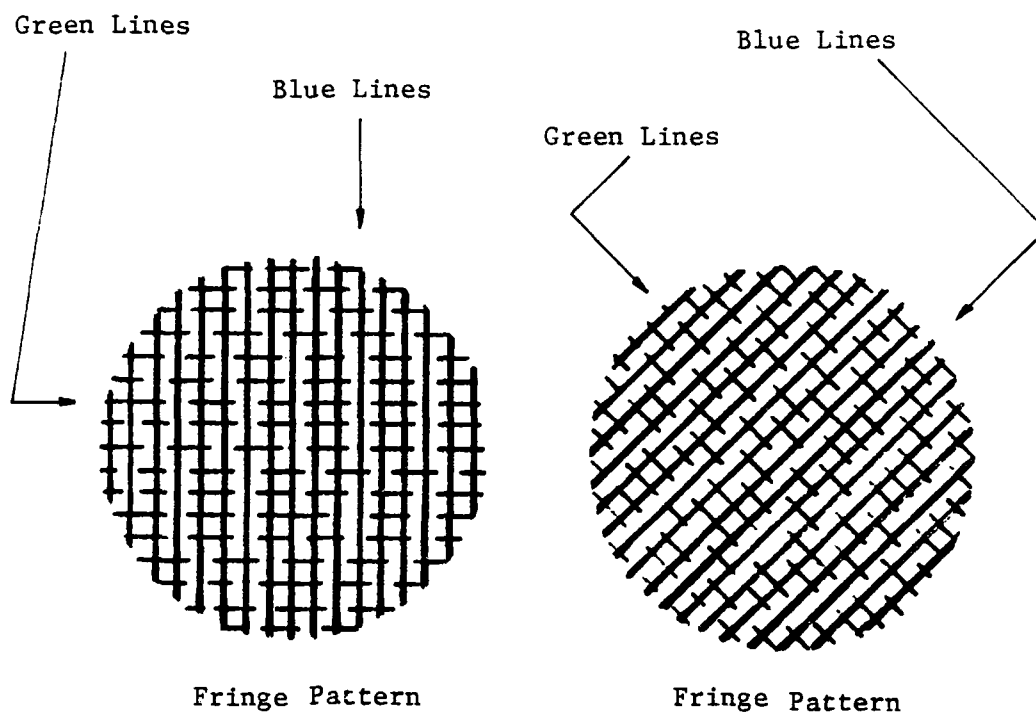


Figure 13. Periodicity.



BEAMS VERTICAL/HORIZONTAL

BEAMS ROTATED BY 45 DEGREES

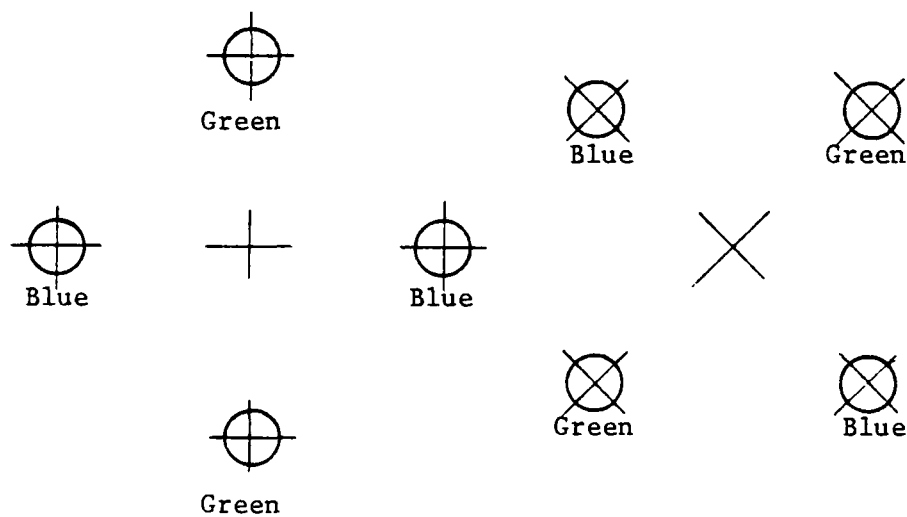


Figure 14. Beam Arrangement.

installed, applying proper frequency shifting. However, where no reversed flows could be present, frequency shifting was not needed. The inlet flow field (reference velocity field) and the lower section of the passage were measured without the Bragg cells installed.

3. Traverse and Measuring Volume Alignment

A rectangular coordinate system was chosen where the origin lay on the center-of-radius of the 7th blade trailing-edge. Figure 5 shows the test passage and the coordinate system. Aligning the measuring volume in the coordinate system for the passage flow measurements was carried out using the special tool shown in Figure 11. The table was adjusted such that the four beams crossed at a specific hole, and the image was clearly visible on the rear wall of the tunnel. The hole coordinates were then set on the traverse mechanism digital electronic readouts. The measuring volume was aligned for wake measurements in the same way. For boundary layer measurements the procedure was different. First, the optical bench was yawed on the milling table, 3.5 degrees with respect to the span-wise direction. Then the measuring volume was positioned at the proper level (y axis) using the aligning tool. Finally, the measuring volume was traversed horizontally (x direction) until the four beams crossed on the blade surface. The crossing was observed with the naked eye and an accuracy of 0.002" in the adjustment was achieved with ease.

C. LDV SURVEY MEASUREMENTS

1. Free Stream Measurements

Free stream measurements were taken 0.3 chords upstream of the blade row leading edge (station 1 in Figure 5). The velocity and flow angle distribution (in Figure 12) were uniform within $\pm 1\%$ and $\pm 0.75^\circ$ respectively, despite the proximity of the survey station to the blades. These measurements provided the reference velocity and reference turbulence level for subsequent surveys at the same test condition, as described in Appendix C.

2. Passage Measurements

Passage measurements were taken at 14 levels through the passage (stations 2-15 in Figure 5) to measure the inviscid behavior of the flow field.

3. Boundary Layer Measurements

Boundary layer measurements were taken at several stations on the suction and pressure surfaces. The stations were coincident with those of the passage measurements. The first survey was made at the trailing-edge center-of-radius. The surveys were then moved progressively upstream towards the leading-edge until the boundary layers were too thin to be measured accurately with the LDV. The procedure for surveying the boundary layer was first to position the measuring volume on the blade surface at the required level. The LDV was then traversed normal to the surface (using both x and y traversing mechanisms) and data were acquired at predetermined intervals.

4. Wake Measurements

Wake measurements were made at four different levels downstream of the 7th blade trailing-edge (stations 16-19 in Figure 5).

5. Two-Dimensionality Checks

Special attention was given to the question of whether the flow field at mid-span was two-dimensional. Verification checks included the following:

- a. Surveying the wake at $y = 0.678''$ ($0.123c$) at two different spanwise locations and comparing the distributions with the mid-span distribution.
- b. Surveying the suction surface boundary layer at two different spanwise locations and comparing the distributions with the midspan distribution.
- c. Surveying the pressure surface boundary layer in the same manner as the suction surface boundary layer.

The results of these measurements at each inlet air angle are plotted in Figures 15-17. It was concluded that the flow was two-dimensional at mid-span to within acceptable error.

6. Non-Dimensionalizing the Data

The LDV data were non-dimensionalized by dividing the reference velocity at the time of recording. The reference velocity was calculated using the plenum pressure and temperature as described in Appendix C. The plenum

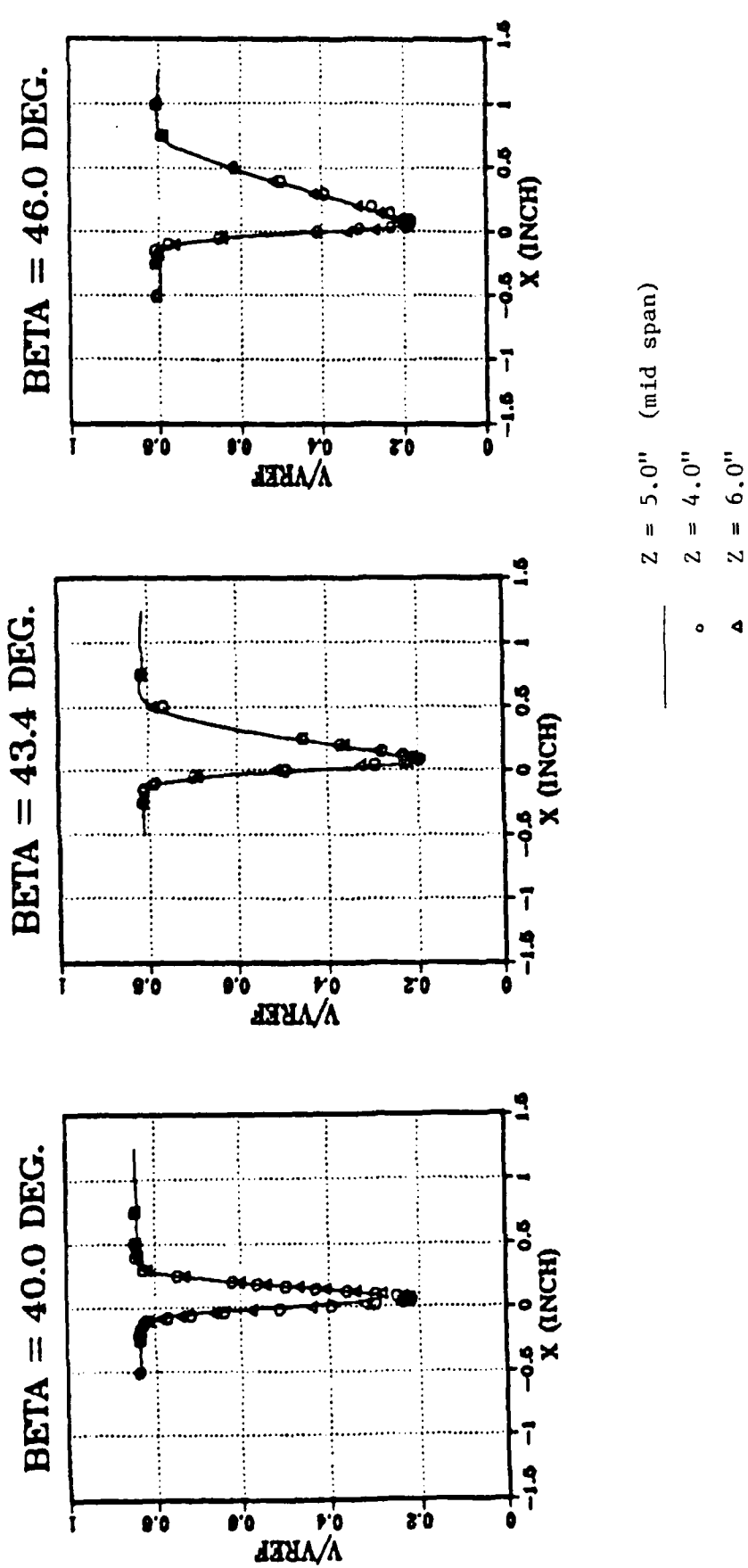


Figure 15. Two-Dimensionality Check of the Wake.
(y = 0.678")

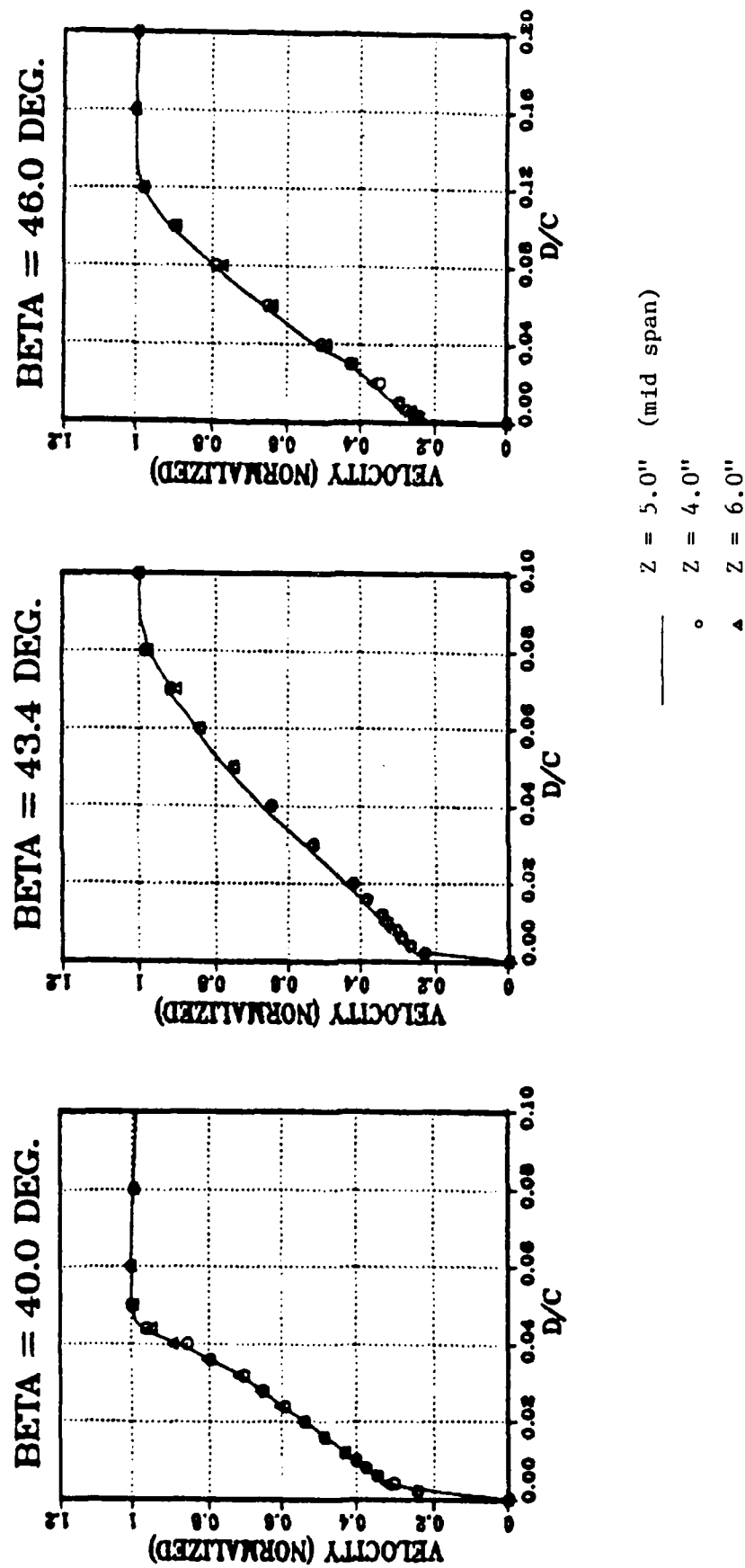


Figure 16. Two-Dimensionality Check of the Boundary Layer.
(Suction Surface at $y = 0.0$)

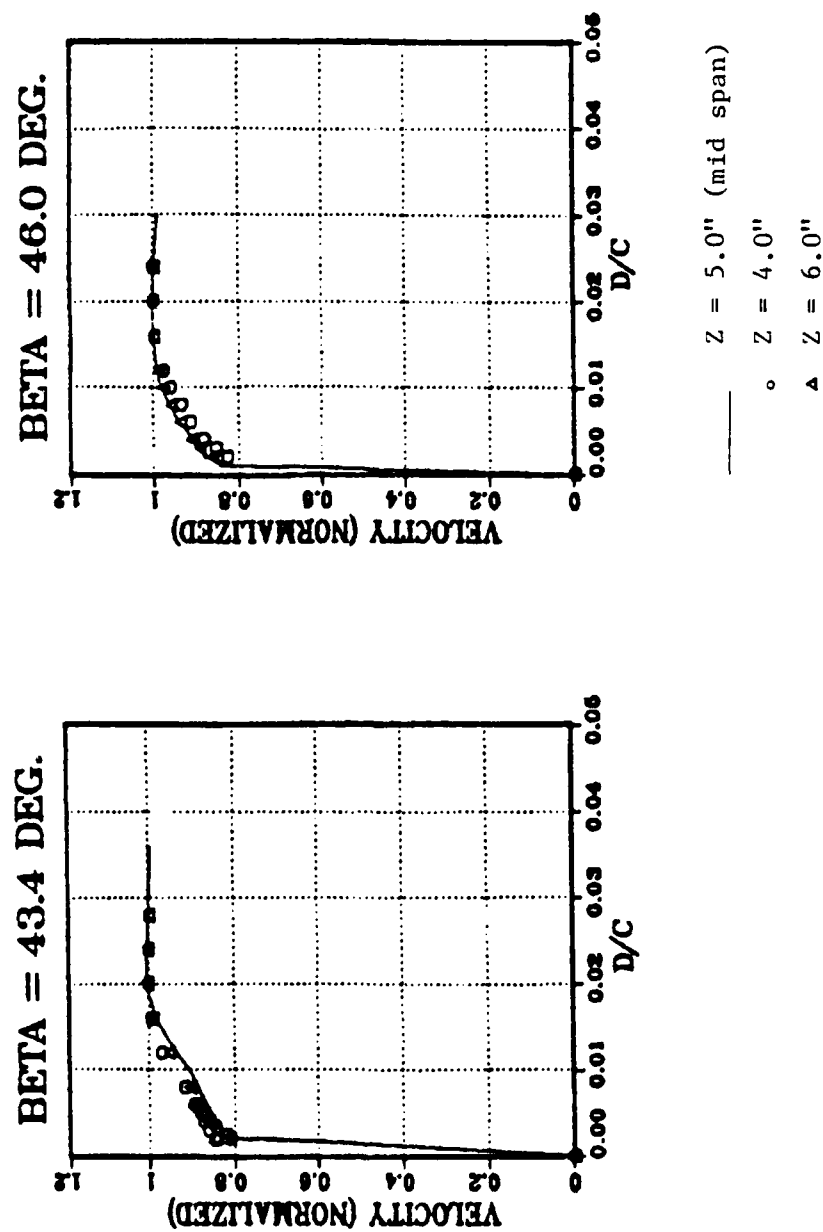


Figure 17. Two-Dimensionality Check of the Boundary Layer.
(Pressure Surface at $\gamma = 0.0^\circ$)

pressure and temperature were constantly monitored and recorded throughout the experiment.

7. Reynolds Number

The chord length Reynolds number of the experiment was nearly constant ($Re_c = 740000 \pm 40000$). The variation were the result of variations in the plenum pressure and day-to-day variations in atmospheric conditions.

8. Data Reduction

The data were acquired using the HP-1000 series computer, stored on floppy disks and thereby transferred to an IBM 3033 (main frame) for analysis. Three Fortran programs were written to analyze the data. A listing of the software can be found in Appendix D. The programs include;

- i. CASCADE FORTRAN - Analyzes the data from passage measurements.
- ii. BLAYER FORTRAN - Analyzes the data from boundary layer measurements.
- iii. WAKE FORTRAN - Analyzes the data from wake measurements.

D. SURFACE PRESSURE MEASUREMENTS

Surface static pressure measurements were taken using the partially-and fully-instrumented blades. The partially-instrumented blade was used to measure the trailing-edge static pressure. The fully-instrumented blade was used to measure the pressure distribution over the blade at the highest incidence angle for which previous data were not available.

V. RESULTS AND DISCUSSION

In this chapter the measured data are presented, and discussed, dealing with the different regions in the flow field one at a time.

A. INLET FLOW FIELD MEASUREMENTS

The following parameters were measured for each inlet air angle; two velocity components, u , v , turbulence level ϵ , plenum pressure and temperature P_{to} , T_{to} and atmospheric pressure P_{atm} . The velocity measurements throughout the flow field were subsequently normalized with respect to the inlet reference velocity at corresponding inlet air angle. The inlet reference velocity for each individual LDV measurement was derived from the inlet flow field measurements and local plenum conditions as shown in Appendix C. This procedure removed the effects of varying supply conditions while surveys were conducted, and gave results in a form suitable for comparison with code predictions.

Inlet mach number was about 0.25. Inlet velocity was about 85 m/sec.

The free stream turbulence level was measured to be $\epsilon = 1.4 \pm 0.2\%$ at each test condition. (Free stream turbulence level was calculated using only u' and v' as defined in the list of symbols.)

B. FLOW FIELD IN THE PASSAGE

Streamlines of the flow in the passage for the three inlet angles are shown in Figures 18-20. The streamlines were generated in the following manner. Volumetric flow was calculated for each level by spline interpolation and integration of the vertical component of the velocity (v). The field was marked every $1/6$ of the volumetric flow (to generate five streamlines). The flow angle was drawn at each mark using the local velocity components (u , v) obtained by interpolation. The flow field was seen to be smooth throughout the range of angles. While the streamline closest to the blade suction surface moved progressively away from the surface as the inlet angle increased, there was no obvious indication of significant separation.

1. Velocity Distribution

Normalized velocity distributions in the passage for three inlet angles are shown in Figures 21-23. A comparison between the passage inlet (leading edge station) velocity distributions at three inlet angles is shown in Figure 24. A comparison of the outlet velocity distributions is shown in Figure 25. The distributions of the edge velocity (defined as the velocity where it reaches its maximum value or where turbulence level reaches free stream values) for the three angles are shown in Figures 26 and 27. There seemed to be similar trends at the three inlet angles, namely;

- a. a velocity peak at the suction surface leading edge,

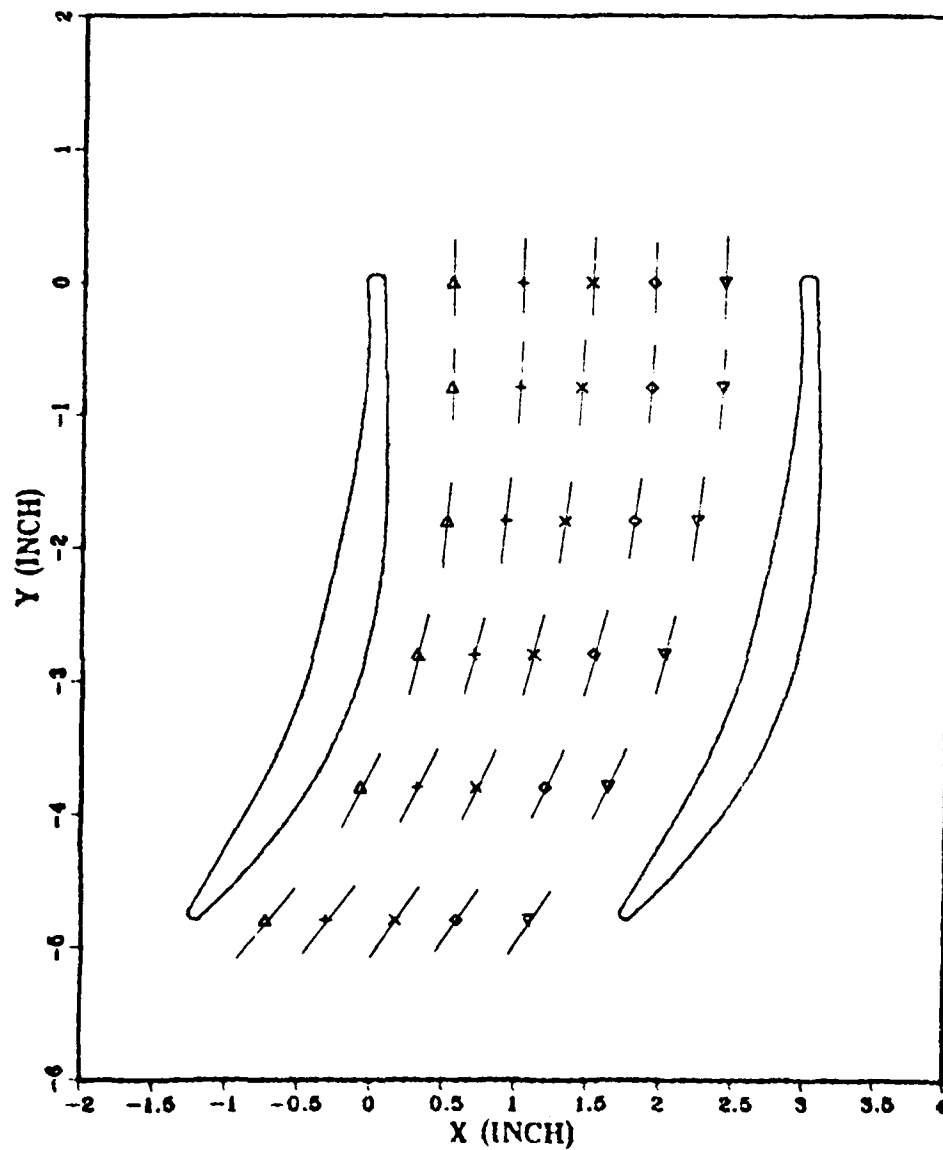


Figure 18. Streamlines in the Passage;
 $\beta_1 = 40^\circ$, $Re = 710000$.

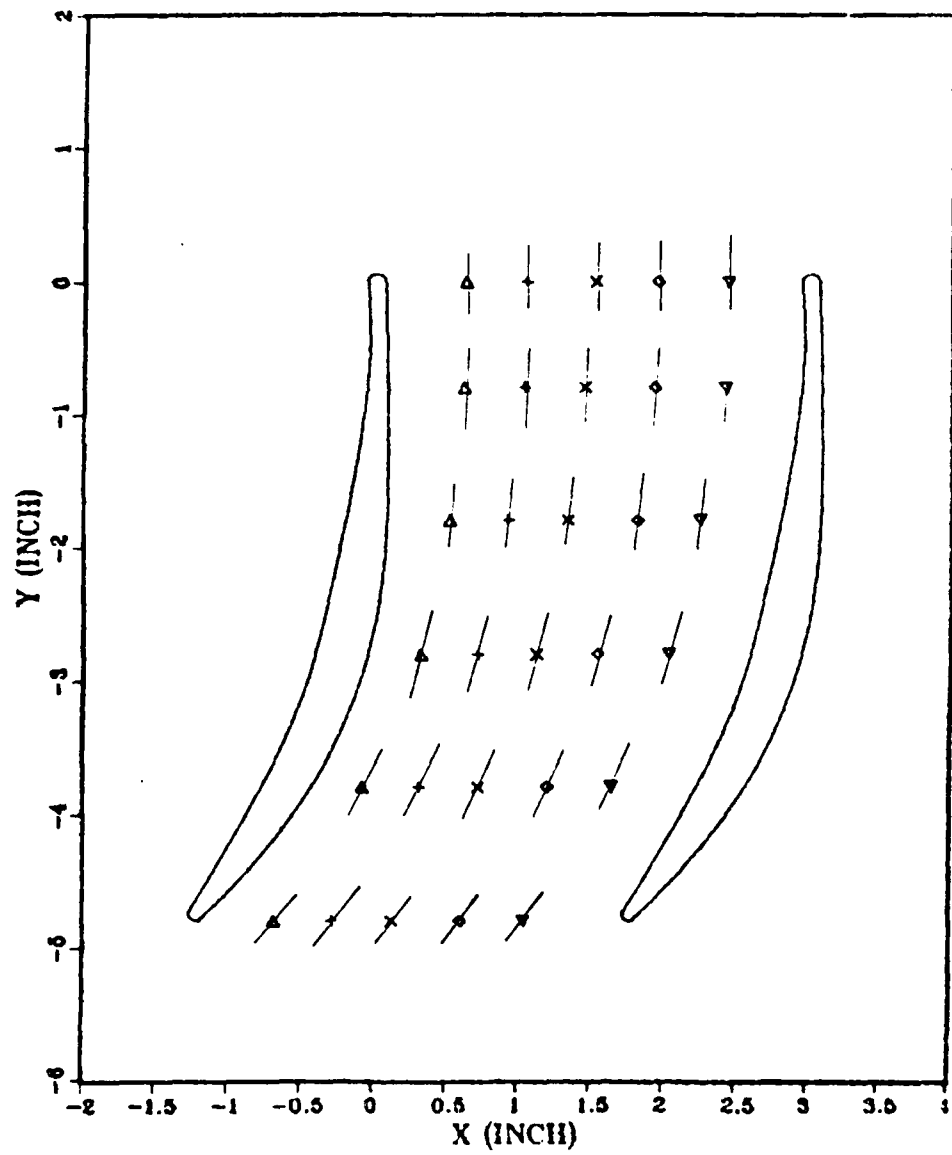


Figure 19. Streamlines in the Passage;
 $\beta_1 = 43.4^\circ$, $Re = 740000$.

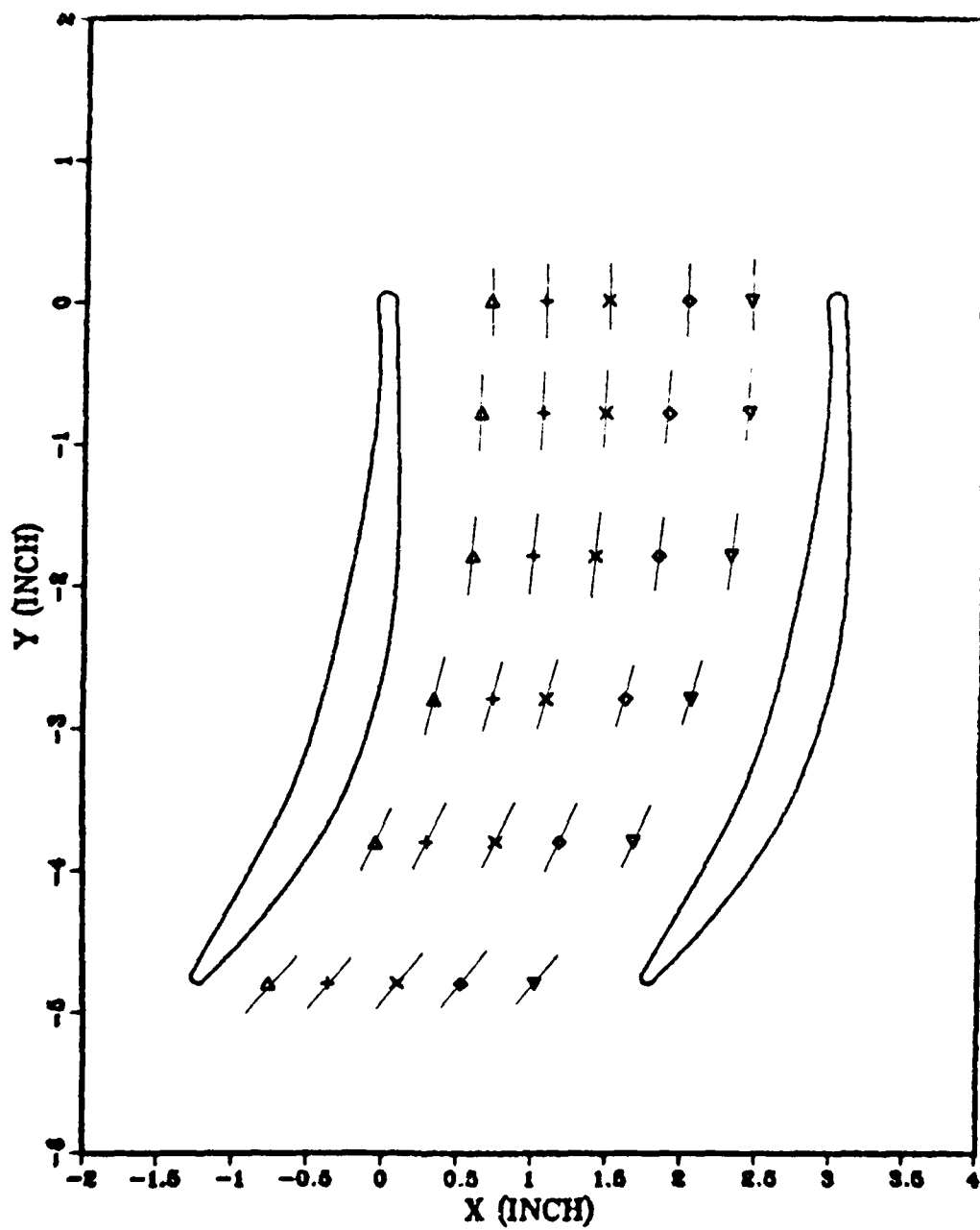


Figure 20. Streamlines in the Passage;
 $\beta_1 = 46^\circ$, $Re = 730000$.

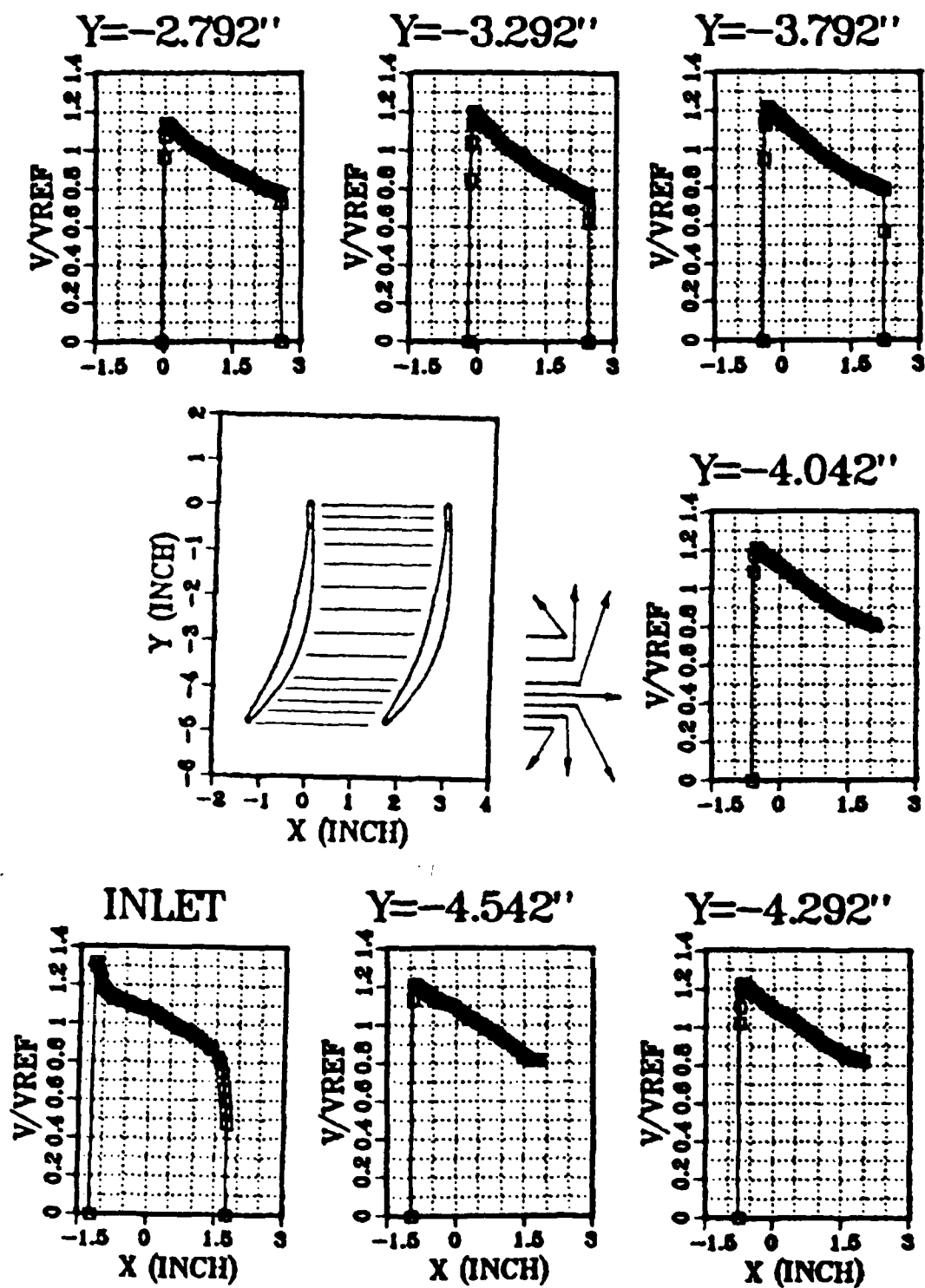


Figure 21. Normalized Velocity Distribution in the Passage
 $\beta_1 = 40^\circ$, $Re = 710000$.

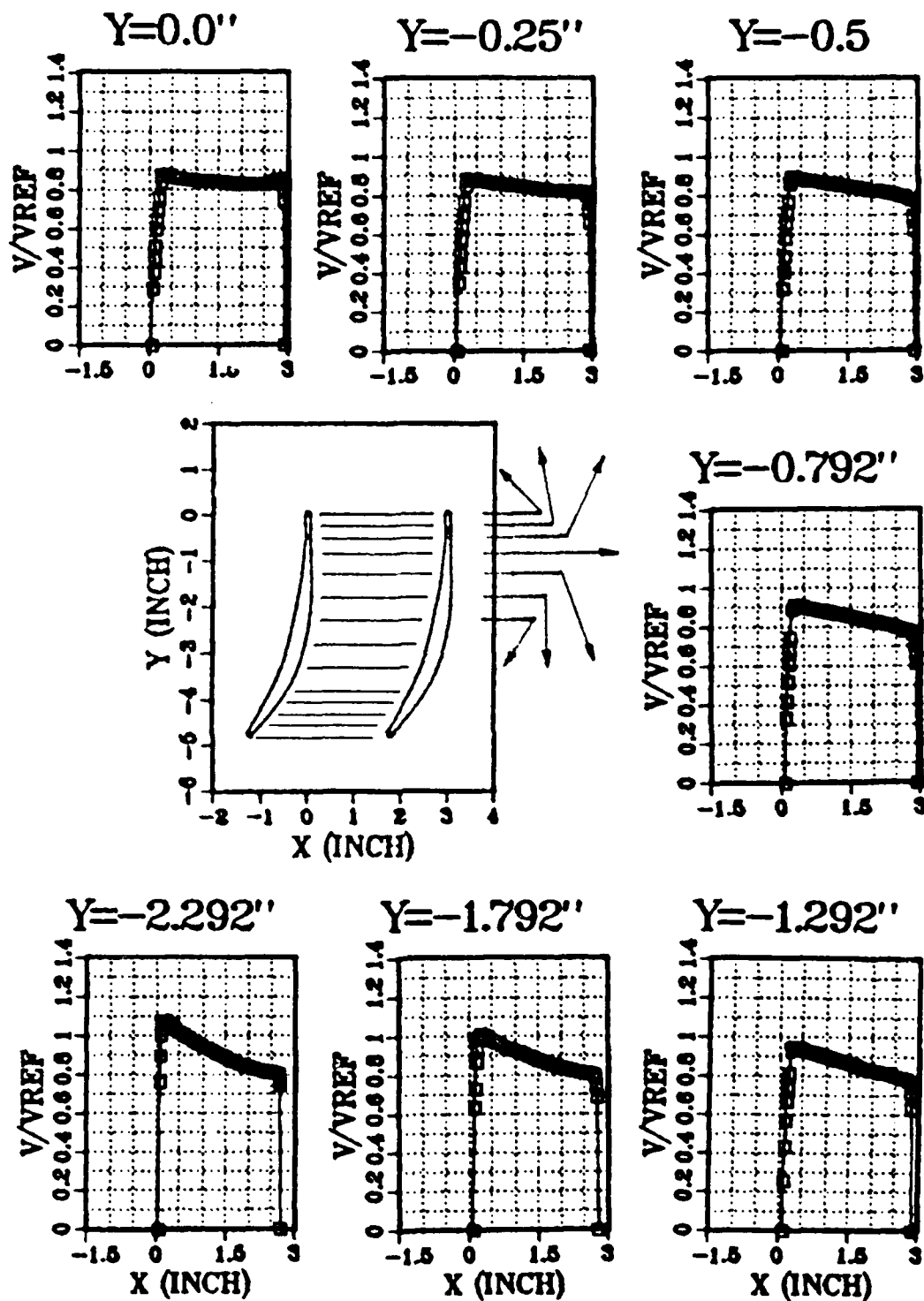


Figure 21. (cont.) Normalized Velocity Distribution in the Passage; $\beta_1 = 40.0^\circ$, $Re = 710000$.

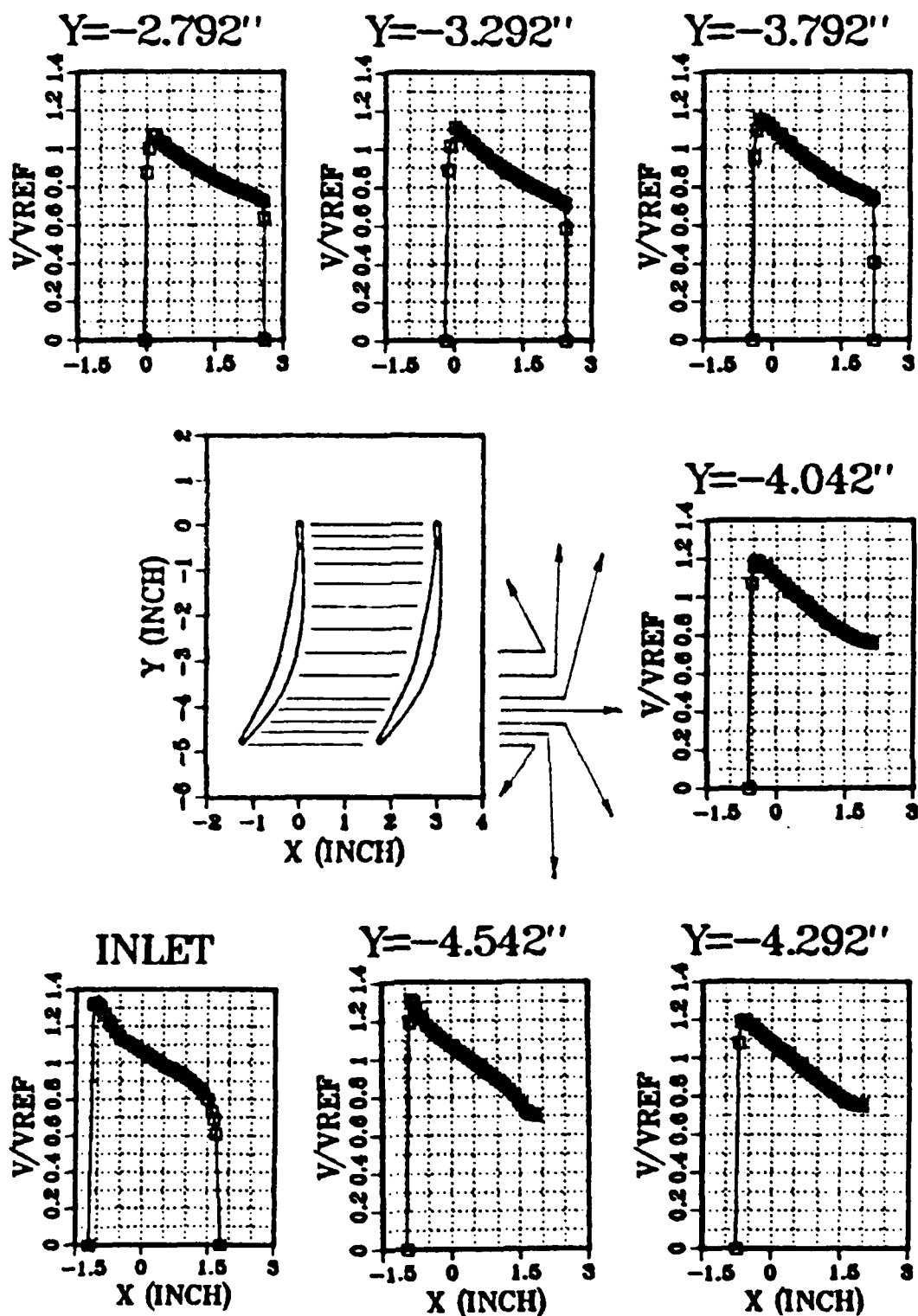


Figure 22. Normalized Velocity Distribution in the Passage; $\beta_1 = 43.4^\circ$, $Re = 740000$.

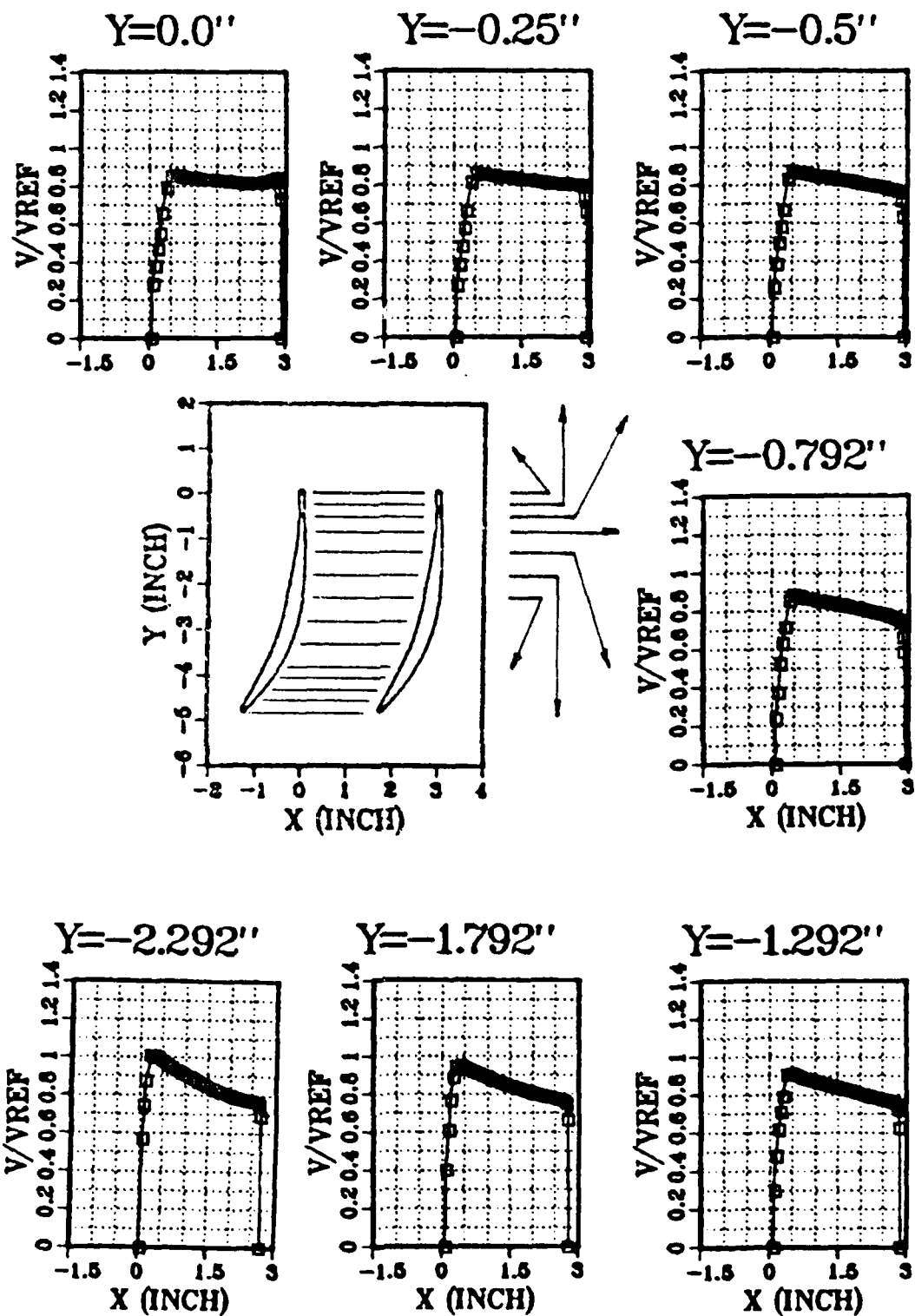


Figure 22. (cont.) Normalized Velocity Distribution in the Passage; $\beta = 43.4^\circ$, $Re = 740000$.

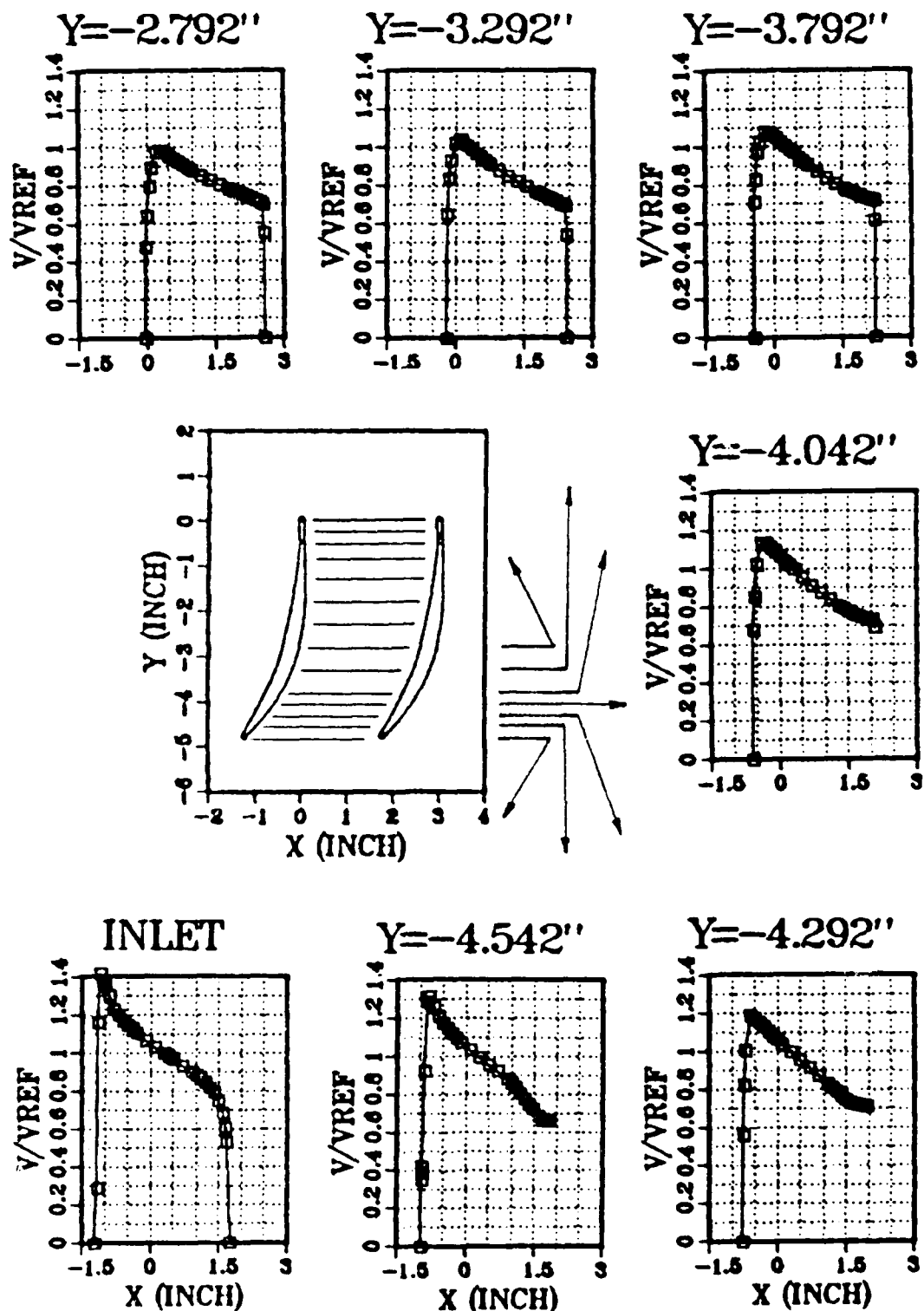


Figure 23. Normalized Velocity Distribution in the Passage; $\beta_1 = 46^\circ$, $Re = 730000$.

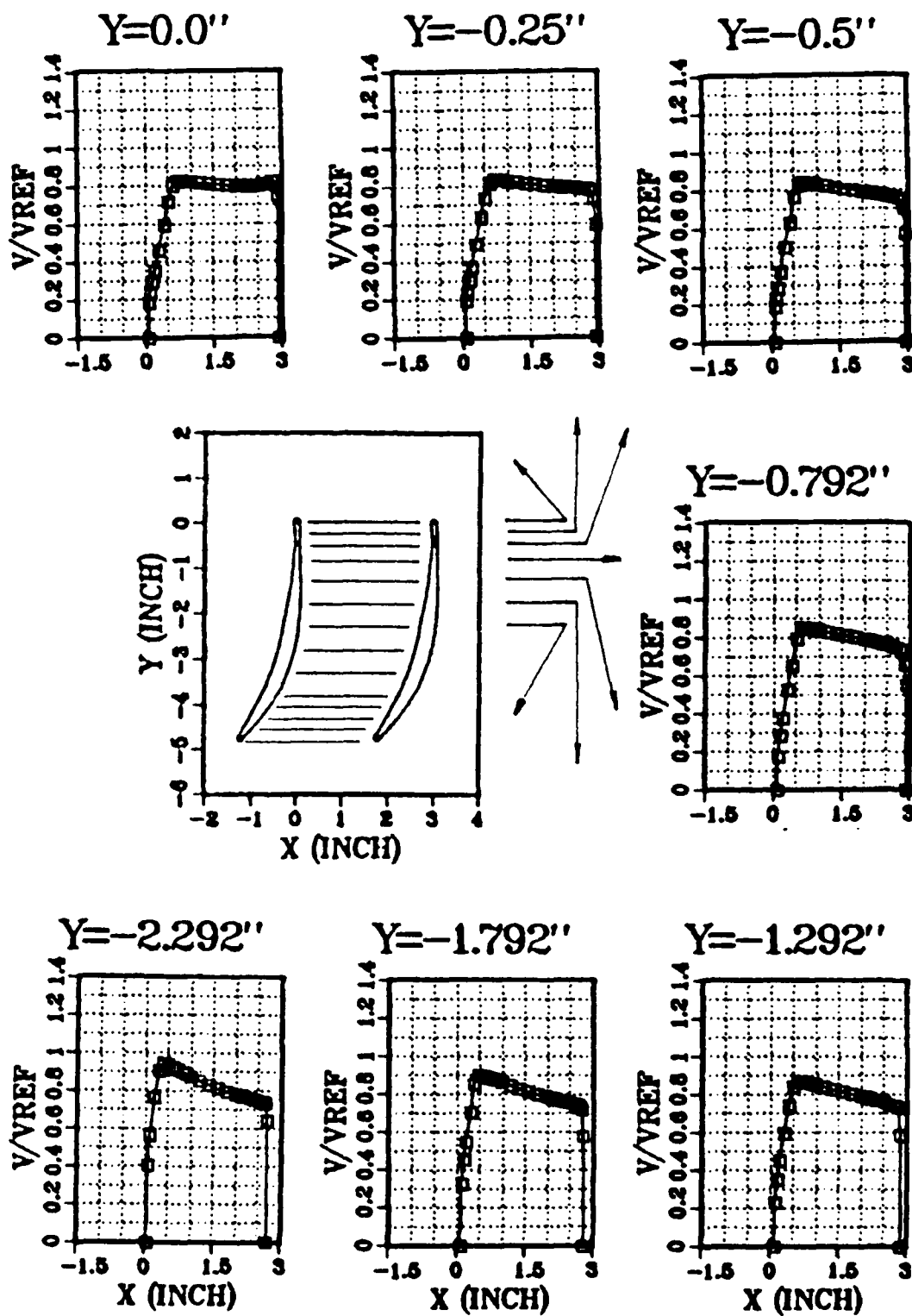


Figure 23. (cont.) Normalized Velocity Distribution in the Passage; $\beta = 46^\circ$, $Re = 730000$.

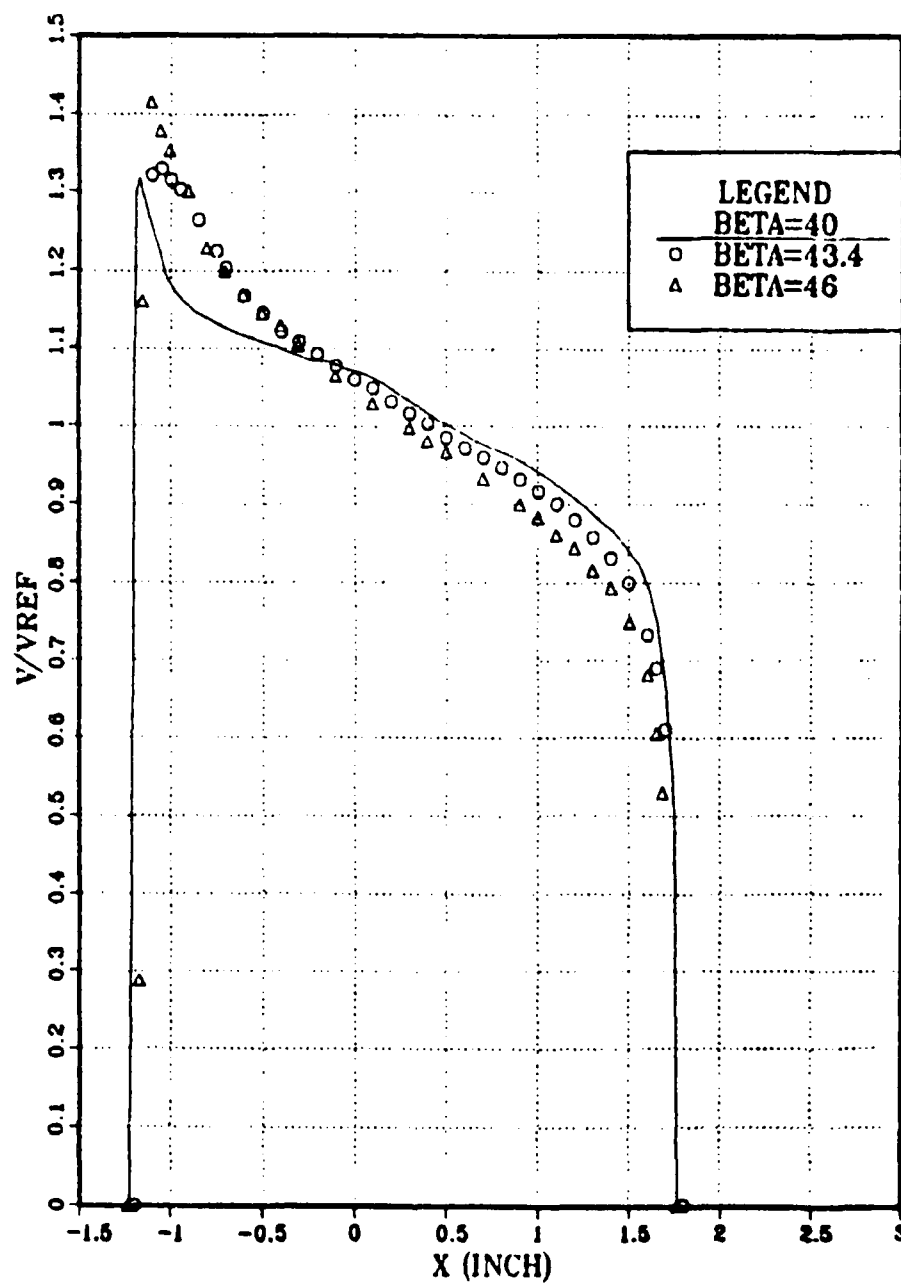


Figure 24. Passage Inlet (Leading Edge) Velocity Distribution at Three Inlet Air Angles.

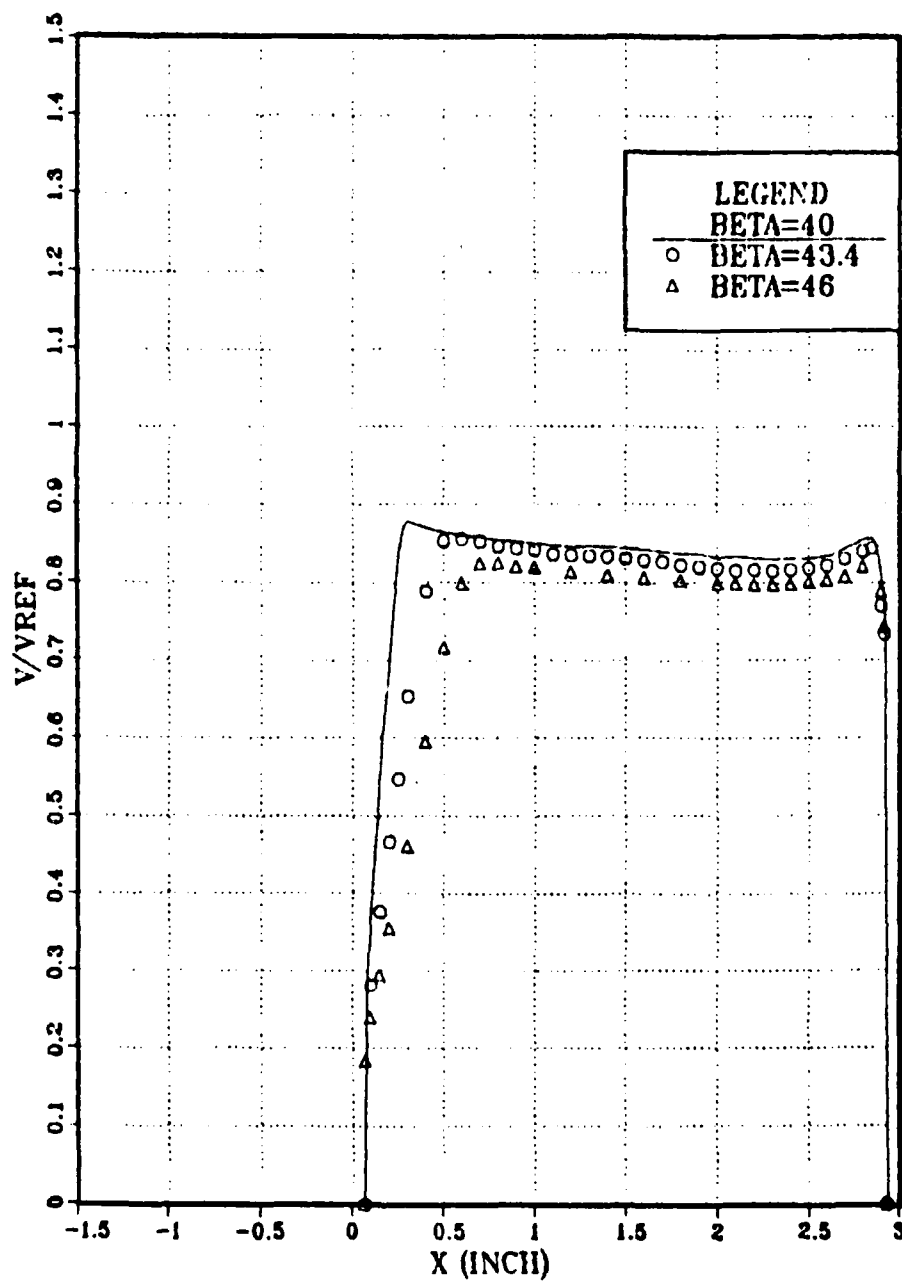
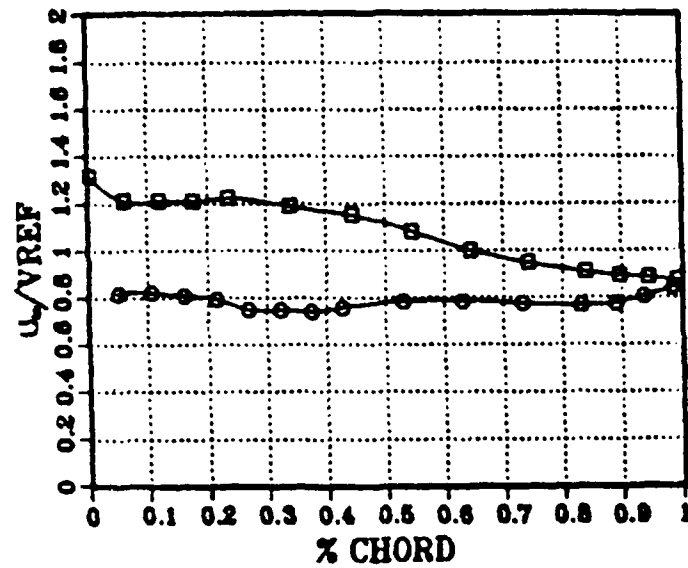


Figure 25. Passage Outlet Velocity Distribution for Three Inlet Angles.

BETA = 40 DEG.



BETA=43.4 DEG.

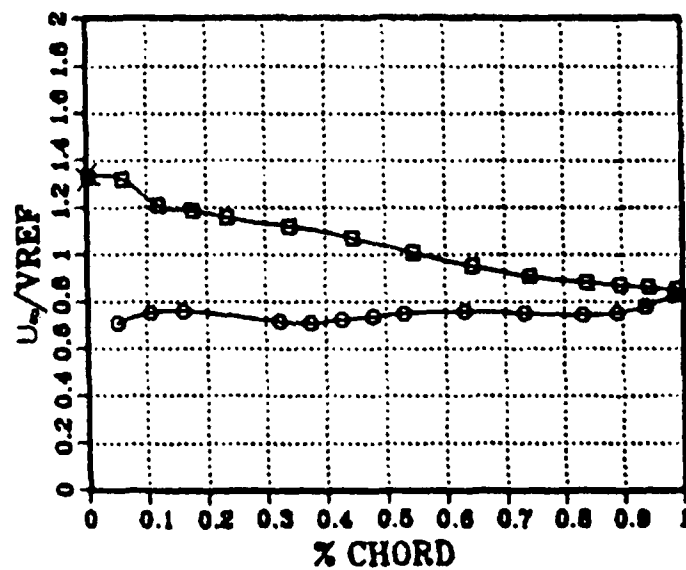


Figure 26. Edge Velocity Distribution Over the Blade.

BETA = 46 DEG.

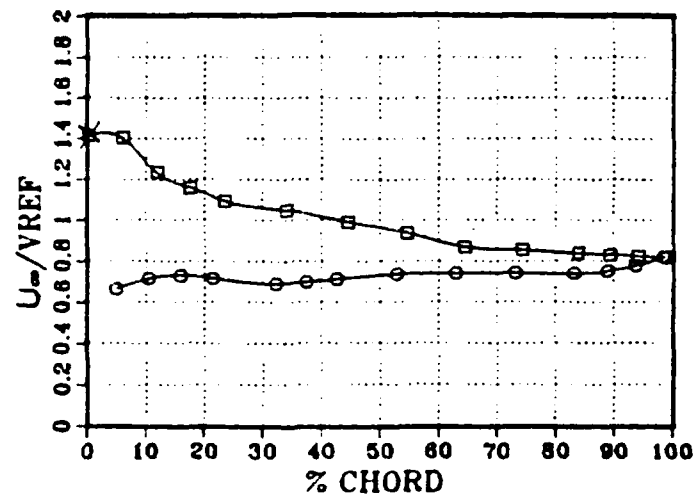


Figure 26. (cont.) Edge Velocity Distribution Over the Blade.

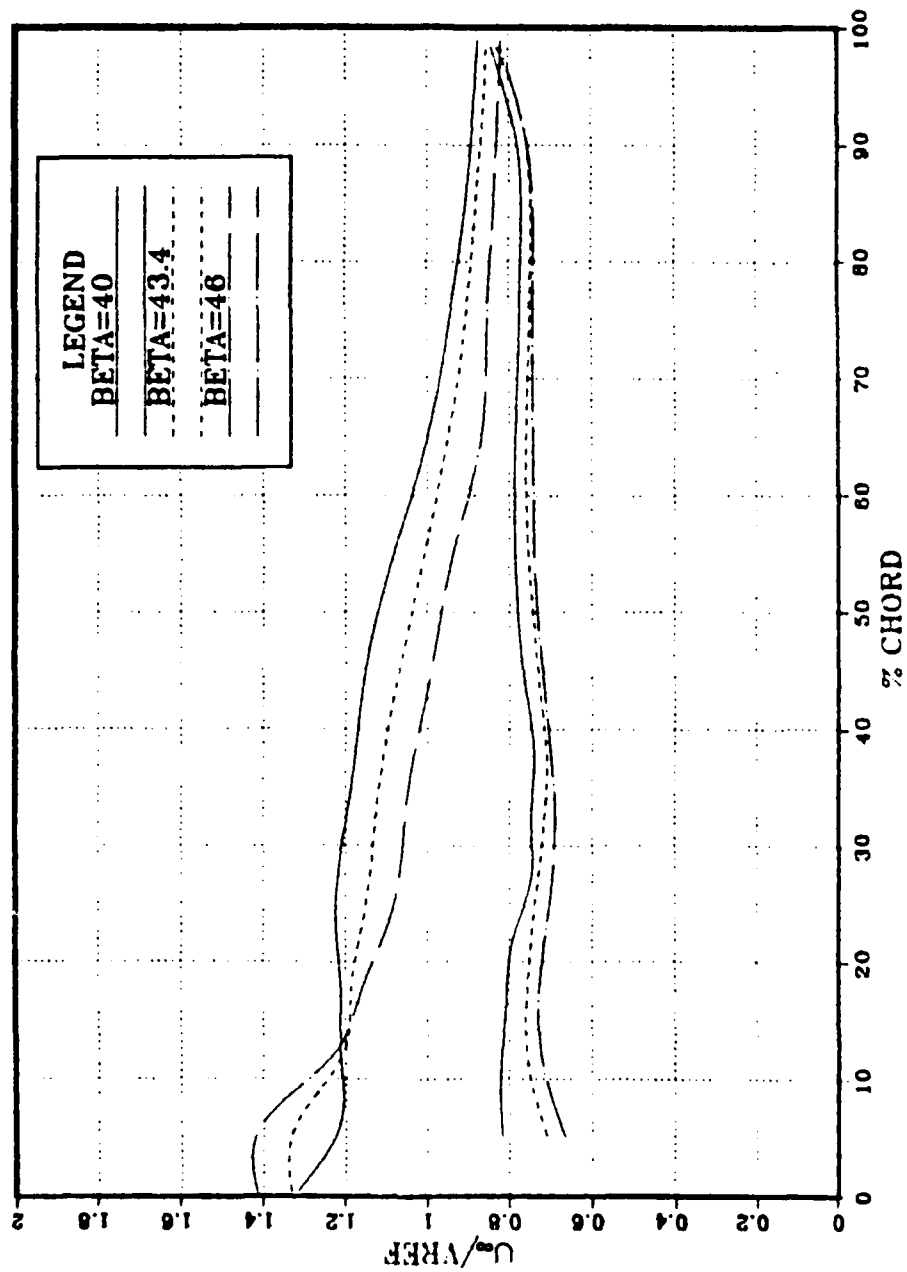


Figure 27. Comparison of the Edge Velocity Distribution at Three Inlet Angles.

- b. a significant velocity difference between the suction side and the pressure side near the leading edges (passage inlet) which decreases downstream and becomes almost flat over the aft 15% of the passage,
- c. an almost flat velocity distribution over the pressure surface and a slight acceleration towards the trailing edge.

Other observations were as follows:

- a. The maximum velocity at the suction side inlet increased as the inlet flow angle increased. Downstream of 15% chord the edge velocity on the suction surface decreased as inlet flow angle increased.
- b. The magnitude of the velocity over the pressure side decreased as the inlet flow angle increased, as did the nearly common magnitude of the suction and pressure side edge velocities at the trailing edges. The distribution of the edge velocity over the pressure side surface varied very little as the inlet angle was changed.
- c. At the two largest inlet angles (43.4° , 46°) the first two stations (2 and 3 in Figure 5) on the suction surface gave a nearly constant edge velocity. This flatness in the edge velocity distribution was not consistent with the measured surface pressure distribution as is discussed later. It is suspected that the seed particles could not follow the high

acceleration around the blade leading edge, creating a velocity lag. Thus, the leading edge data points on the suction surface for the higher inlet angles were plotted in Figure 26, but marked out.

- d. At the outlet the boundary layer was very thick compared to the passage width. For the high inlet angle ($\beta_1 = 46^\circ$) the boundary layer thickness was more than 20% of the passage width and 12% of the chord.

2. Flow Angle Distribution

Flow angle distribution in the passage for three inlet angles are shown in Figures 28-30. A comparison between the flow angle distributions across the passage at the blade row leading edge (Station 2 in Figure 5) for three inlet angles, is shown in Figure 31. A comparison of the passage outlet (Station 15 in Figure 5) flow angle distributions is shown in Figure 32. The following were concluded from the figures:

- a. Most of the flow turning took place in the forward half of the cascade.
- b. The outlet flow angle distribution was almost identical at all three inlet angles. Deviation angle did not vary significantly with inlet angle throughout the inlet angle range.

3. Surface Pressure Distribution

Pressure coefficient distributions over the airfoil for the three inlet angles are shown in Figure 33. The

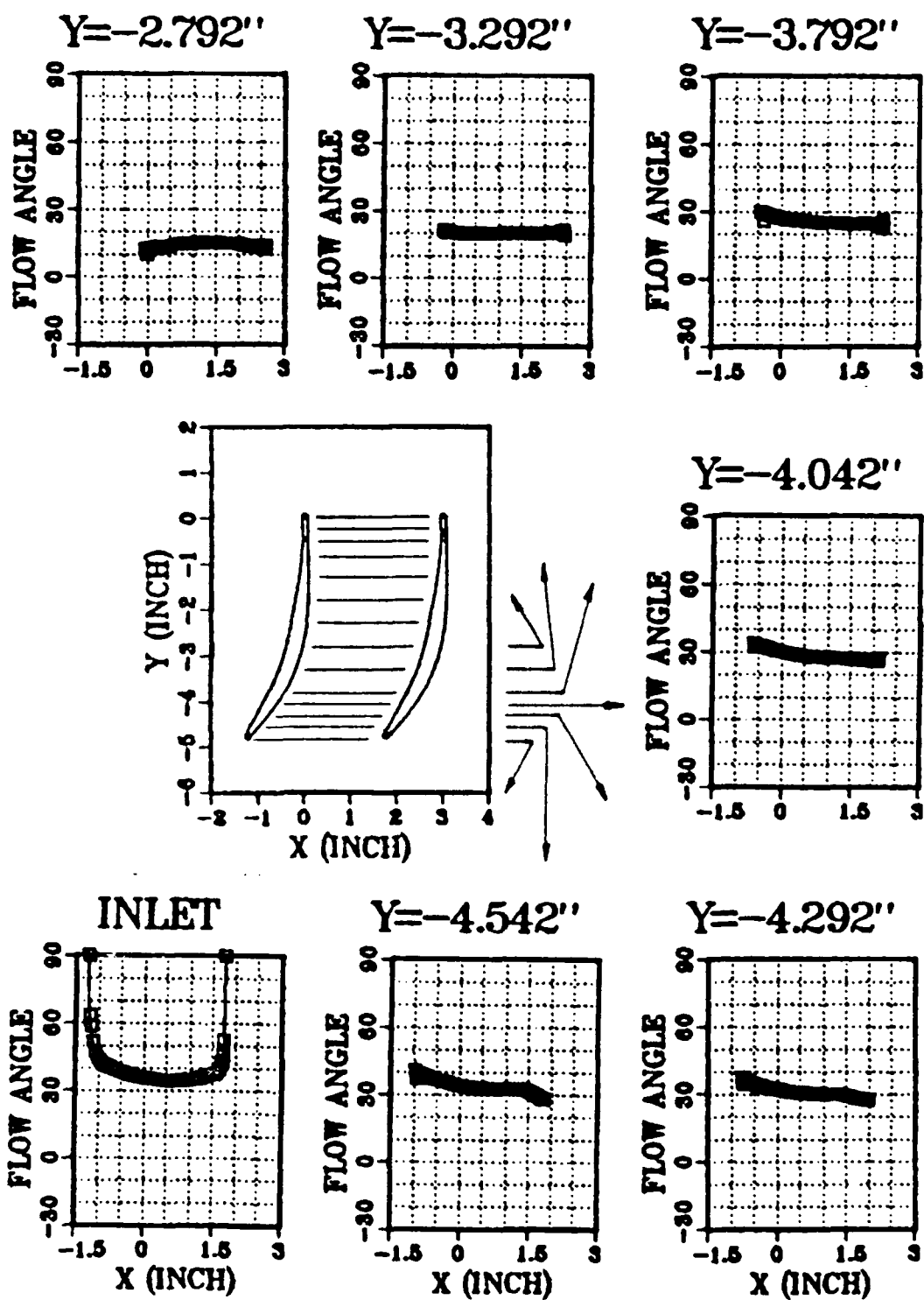


Figure 28. Flow Angle Distribution in the Passage;
 $\beta_1 = 40^\circ$, $Re = 710000$.

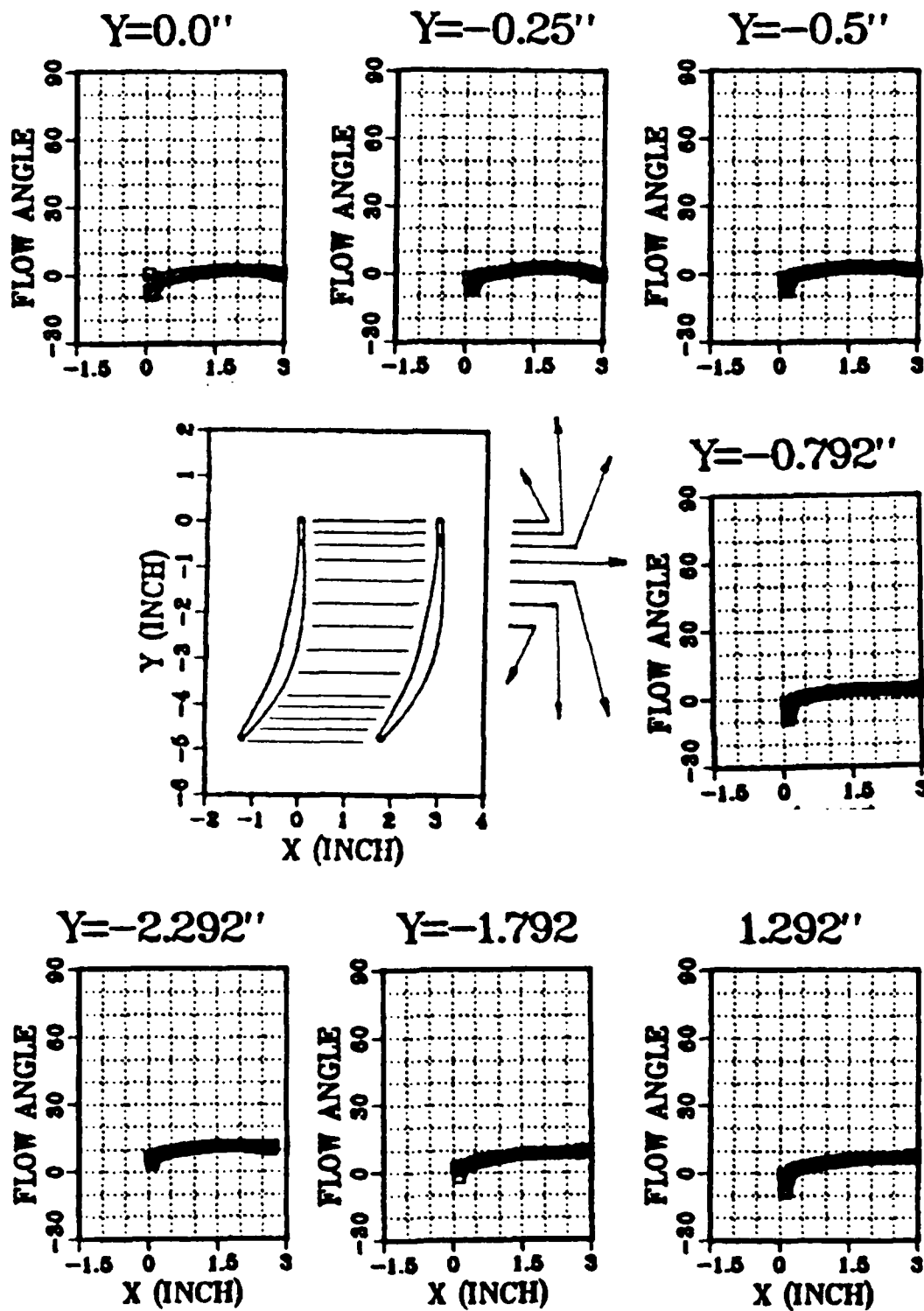


Figure 28. (cont.) Flow Angle Distribution in the Passage; $\beta_1 = 40^\circ$, $Re = 710000$.

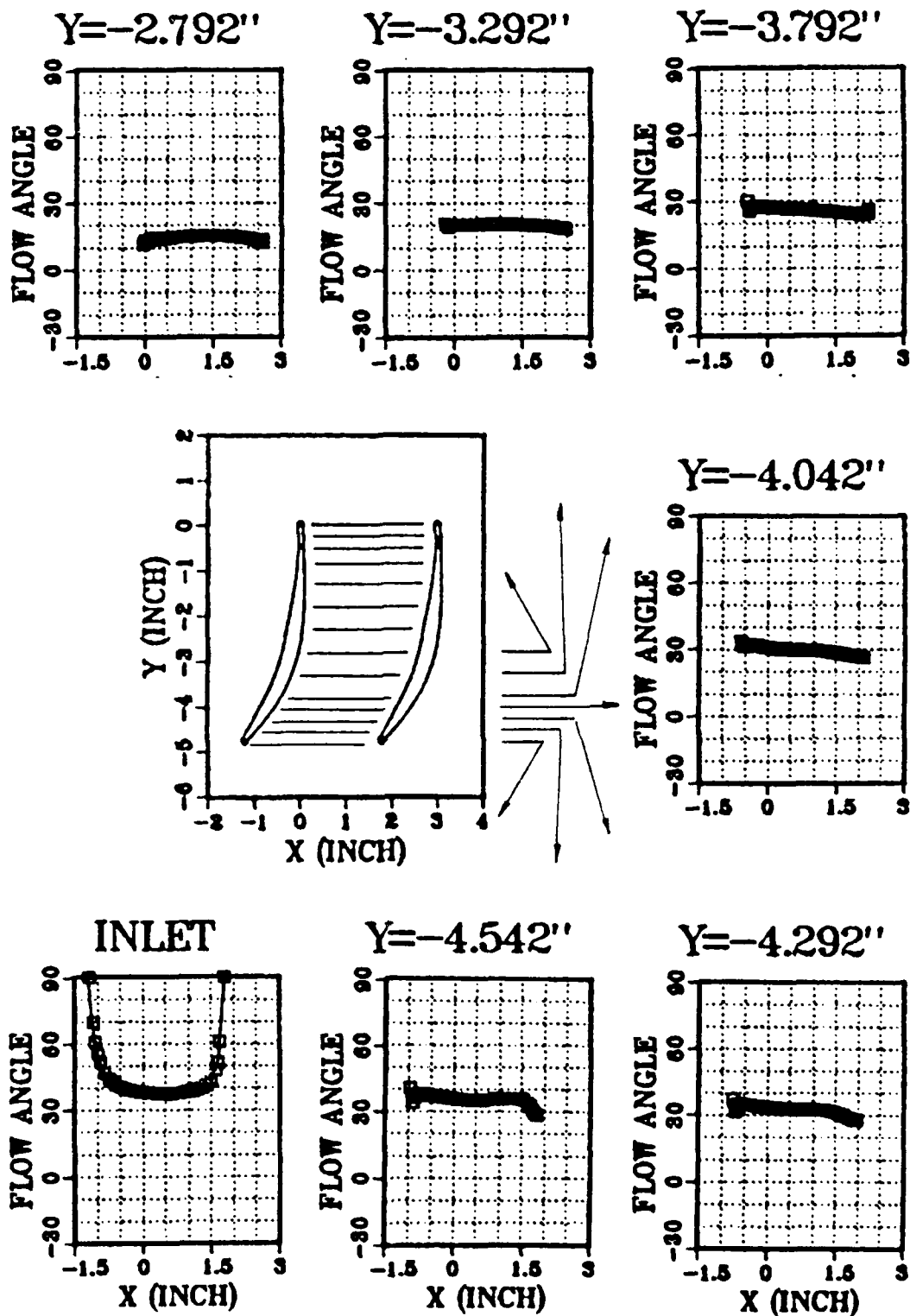


Figure 29. Flow Angle Distribution in the Passage; $\beta_1 = 43.4^\circ$, $Re = 740000$.

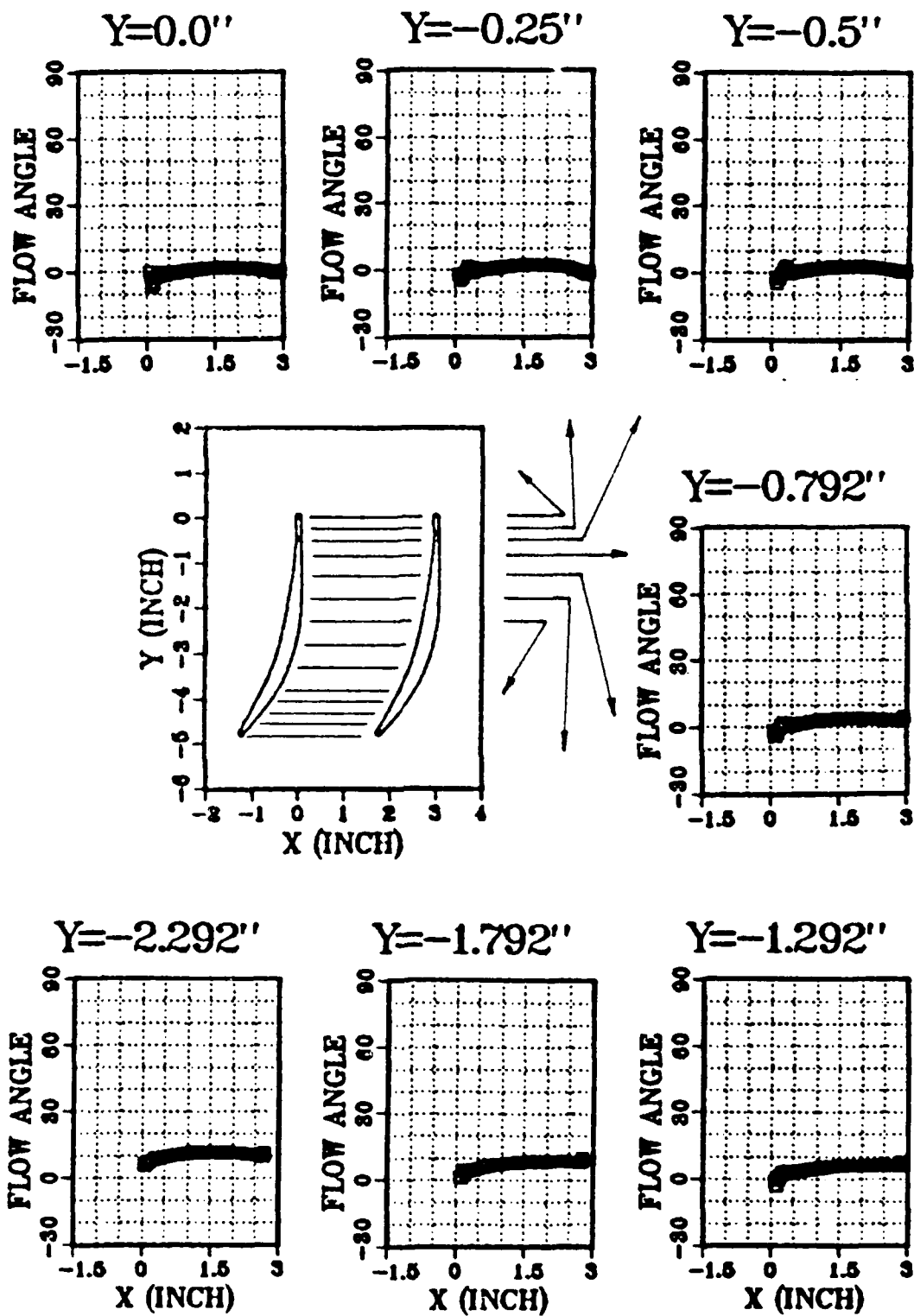


Figure 29. (cont.) Flow Angle Distribution in the Passage; $\beta_1 = 43.4^\circ$, $Re = 740000$.

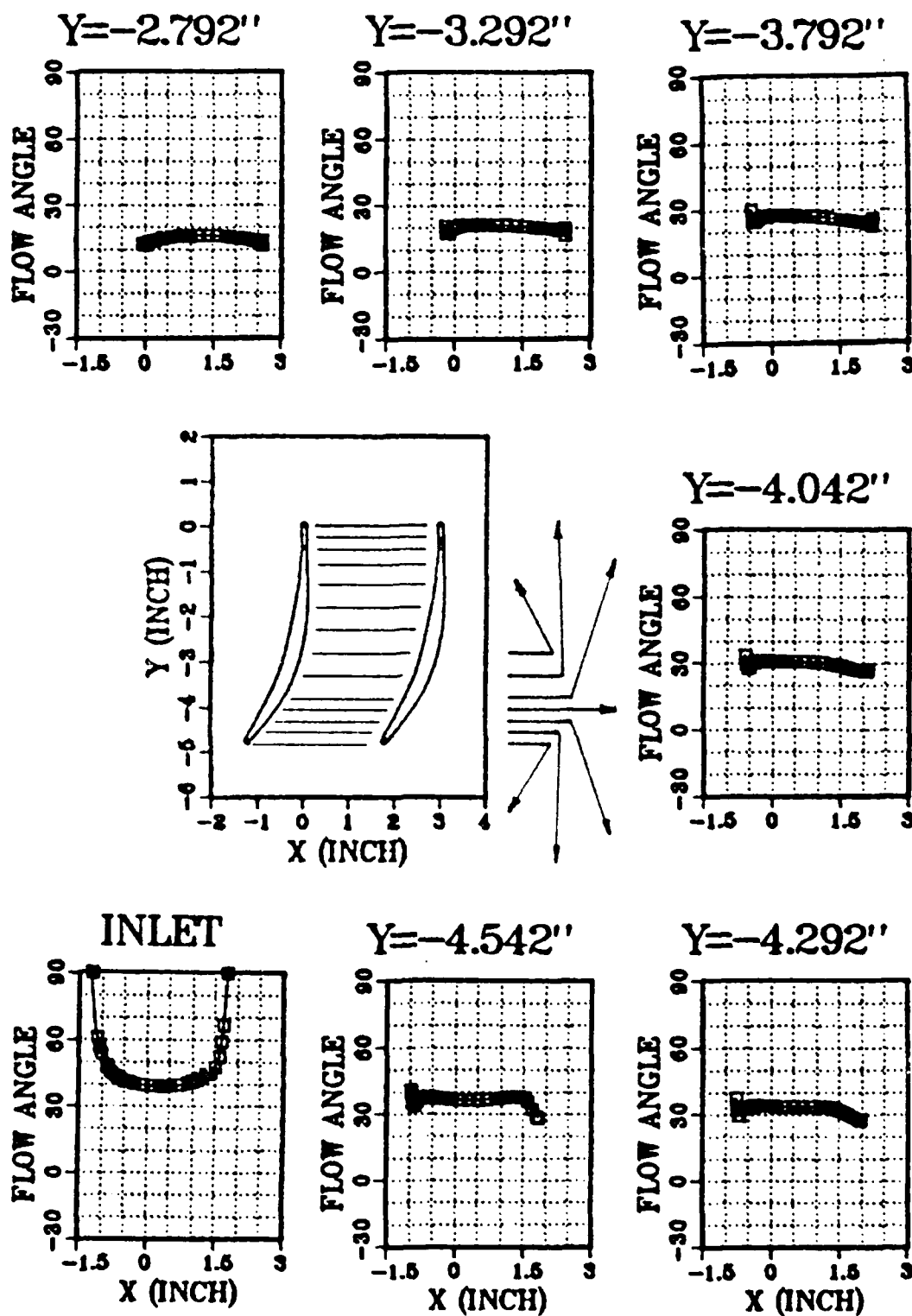


Figure 30. Flow Angle Distribution in the Passage;
 $\beta_1 = 46^\circ$, $Re = 730000$.

AD-A194 498

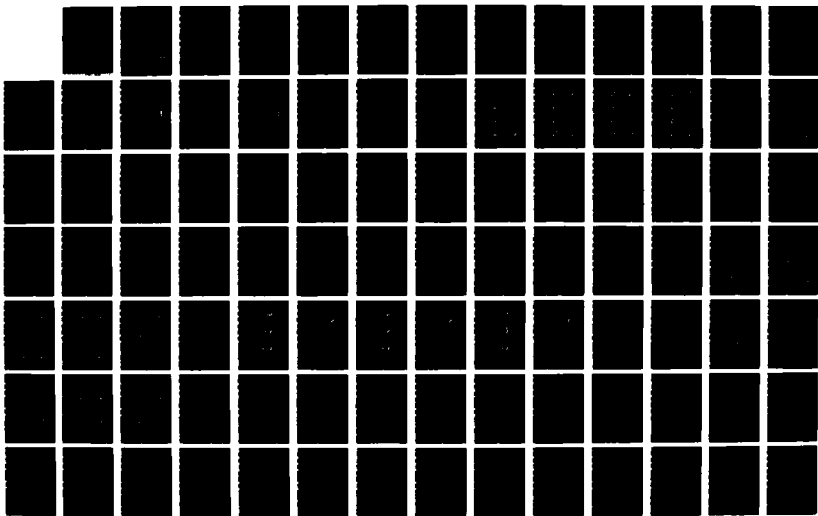
A MAPPING OF THE VISCOUS FLOW BEHAVIOR IN A CONTROLLED
DIFFUSION COMPRESS (U) NAVAL POSTGRADUATE SCHOOL
MONTEREY CA Y ELAZAR MAR 88 NPS67-88-001

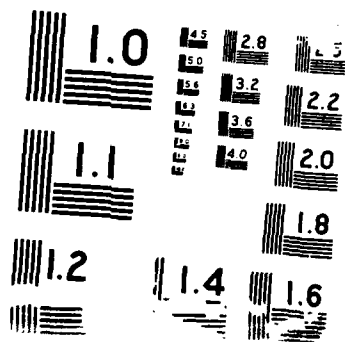
2/3

UNCLASSIFIED

F/G 20/4

NL





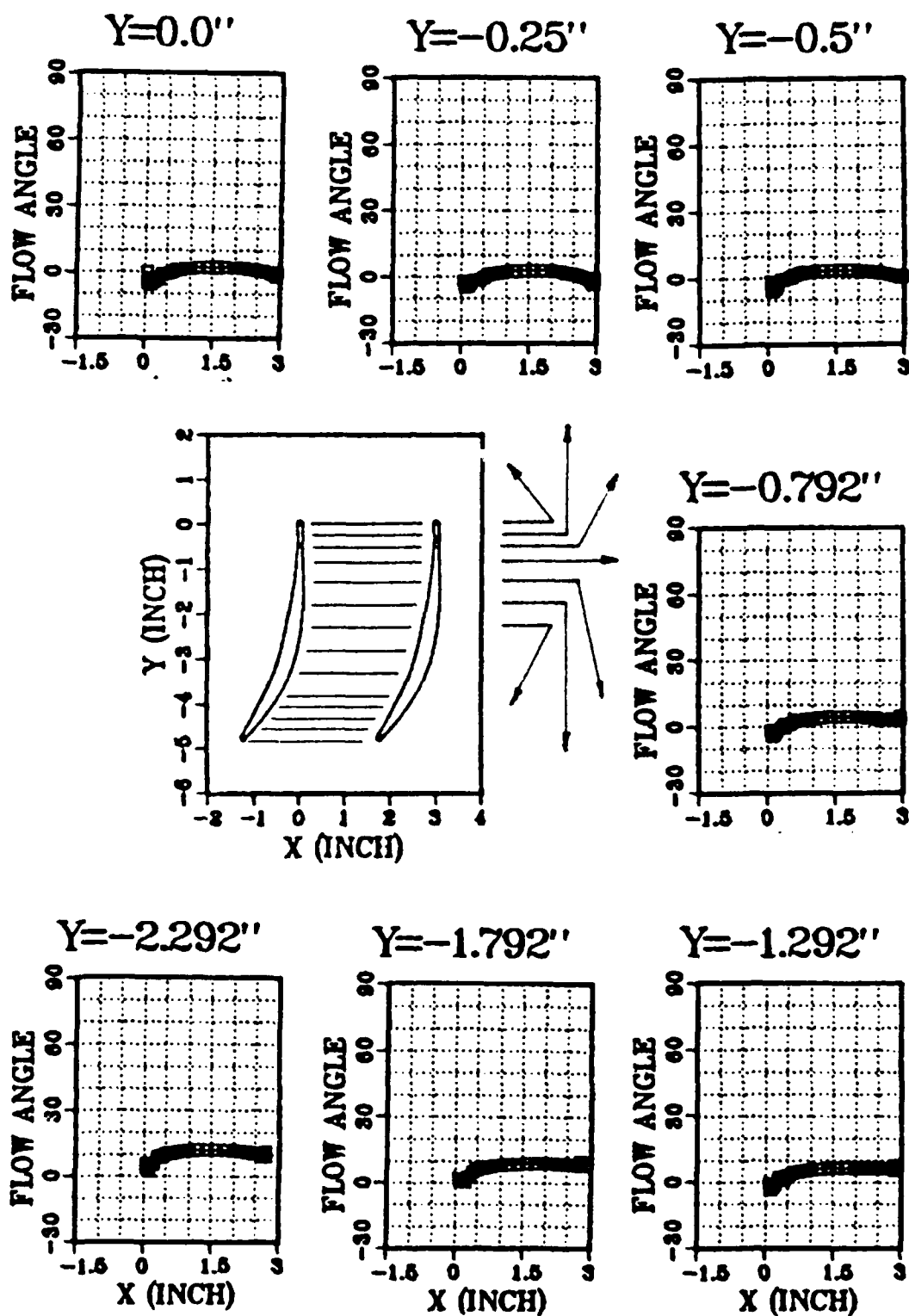


Figure 30. (cont.) Flow Angle Distribution in the Passage; $\beta_1 = 46^\circ$, $Re = 730000$.

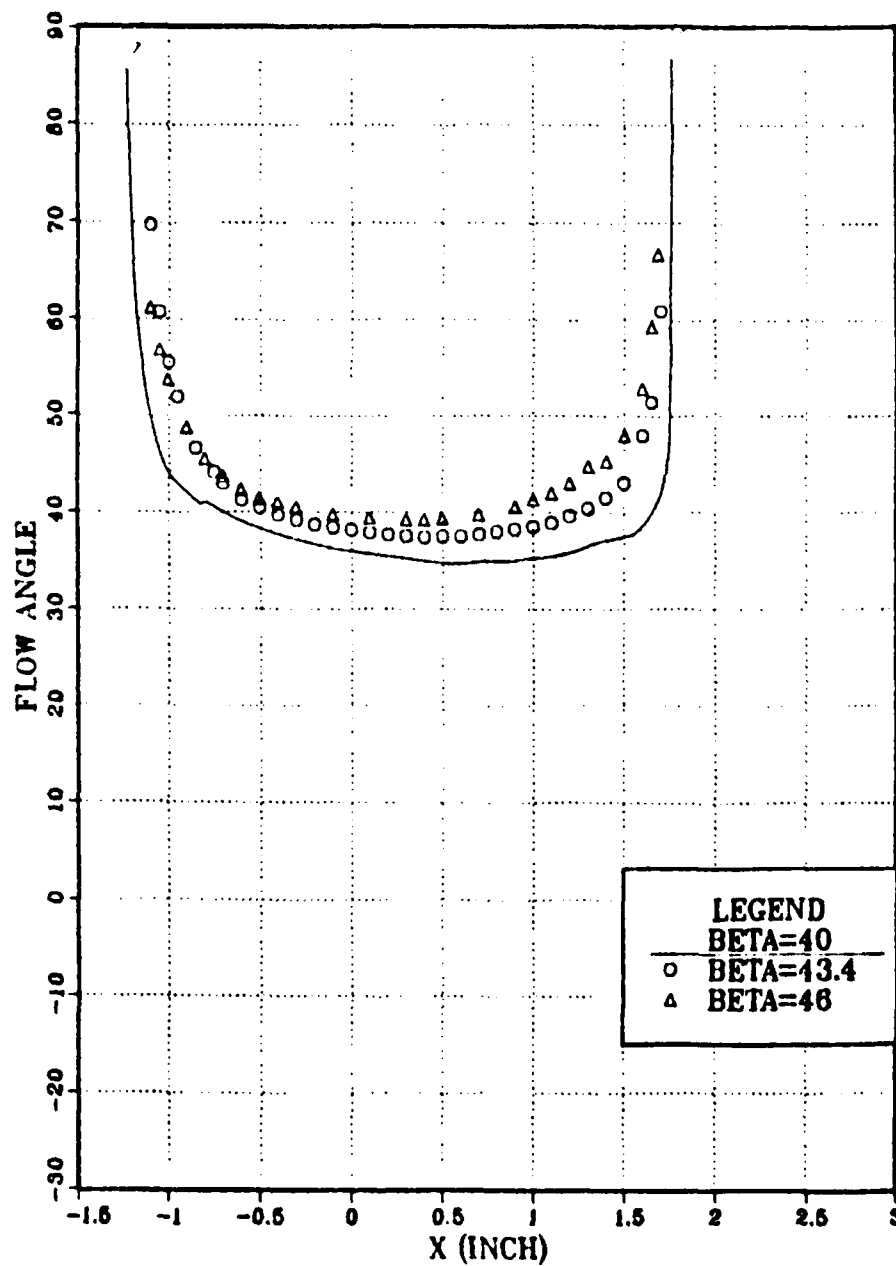


Figure 31. Passage Inlet Flow Angle Distribution for Three Inlet Angles.

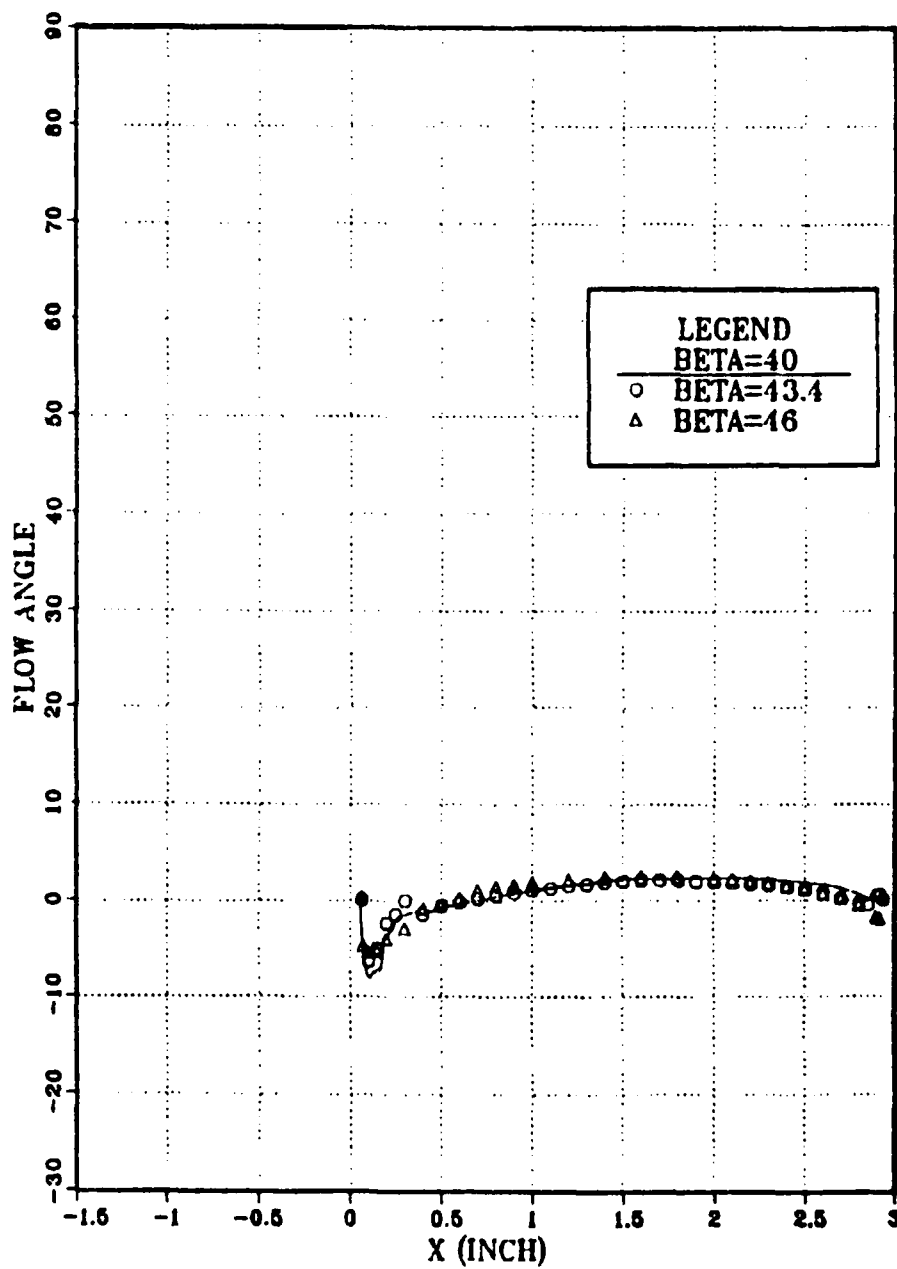
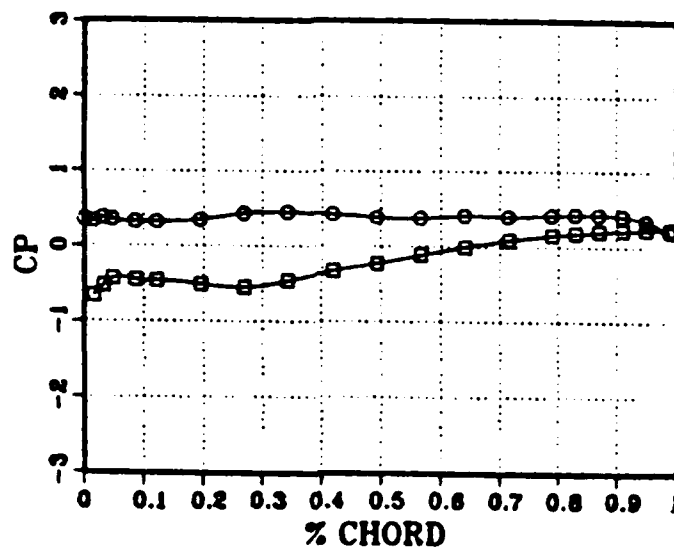


Figure 32. Passage Outlet Flow Angle Distribution for Three Inlet Angles.

BETA=40



BETA=43.4

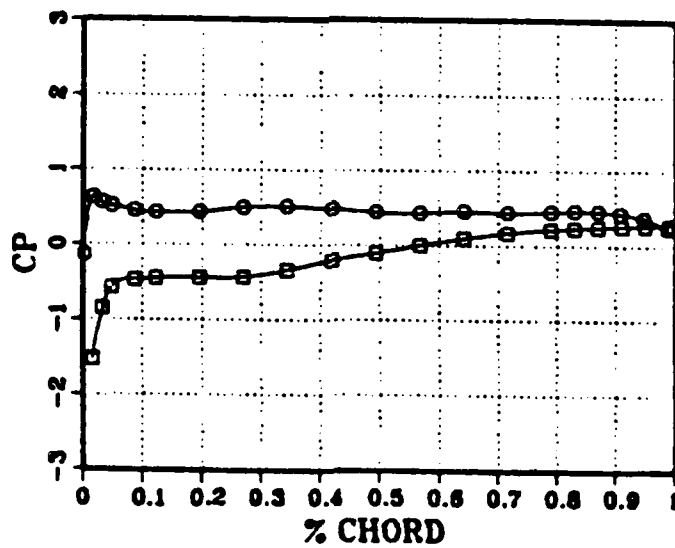


Figure 33. Pressure Coefficient Distribution Over the Blade.

BETA = 46 DEG.

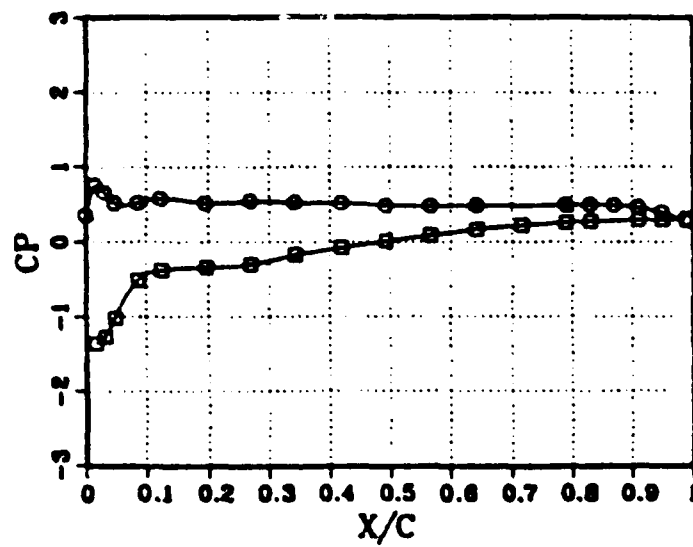


Figure 33. (cont.) Pressure Coefficient Distribution Over the Blade.

distributions follow the same general trends as the edge velocity distributions in Figure 26, except at the suction surface for the higher inlet angles (43.4°, 46°). If the boundary layer is thin the edge velocity and surface pressure are related using the inviscid, incompressible expression

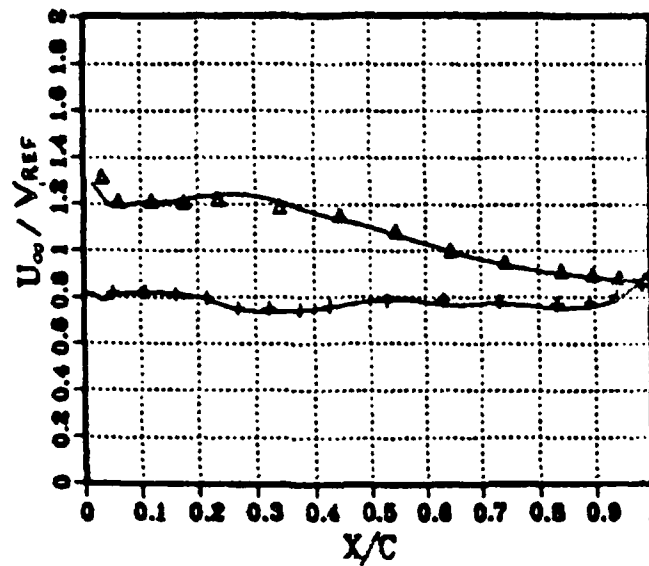
$$\left(\frac{U_m}{V_{ref}}\right)^2 = 1 - C_p$$

A comparison between the edge velocity calculated using this expression and the measured edge velocity is shown in Figure 34. Since, as suggested earlier, the seed particles cannot handle the high acceleration of the flow at the suction surface leading edge, the leading edge velocity data points were omitted as in Figure 26. The slight acceleration of the flow on the pressure surface towards the trailing edge shows as a slight decrease of the pressure coefficient, to satisfy the Kutta condition within the base flow.

4. Axial Velocity Density Ratio (AVDR)

The "referred" passage volumetric flow rate, calculated at each station by numerically integrating the distribution of v/V_{ref} from one side of the passage to the other, is shown in Figure 35. Eighteen data points are shown plotted corresponding to the levels in Figure 5 but excluding the near wake, station 16 at $y = 0.262$ ". The broken lines are a least-squares fit to the data. The calculated

BETA = 40 DEG.



Δ , + LDV — Surface Pressure Measurements

BETA = 43.4 DEG.

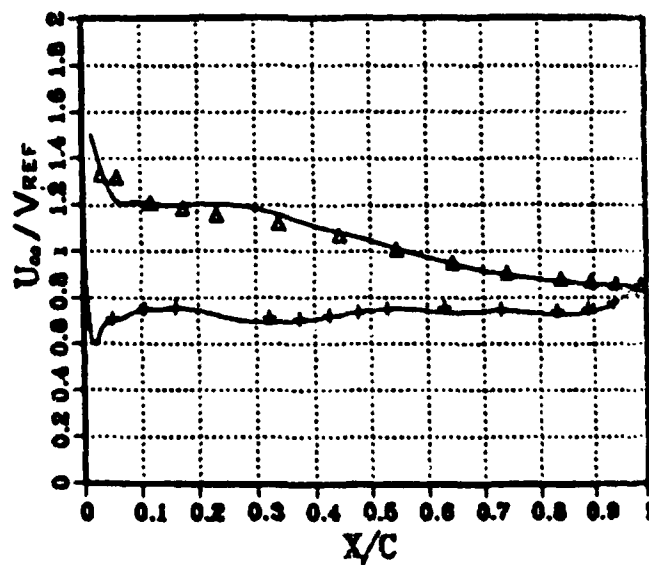
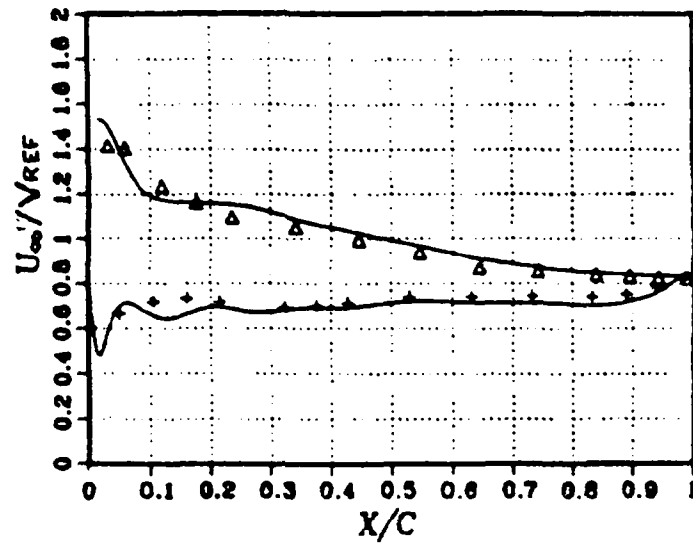


Figure 34. Comparison Between Edge Velocity Distribution Measured with LDV and Derived from Surface Pressure Measurements.

BETA = 46 DEG.



$\Delta, +$ LDV — Surface Pressure Measurements

Figure 34. (cont.) Comparison Between Edge Velocity Distribution Measured with LDV and Derived from Surface Pressure Measurements.

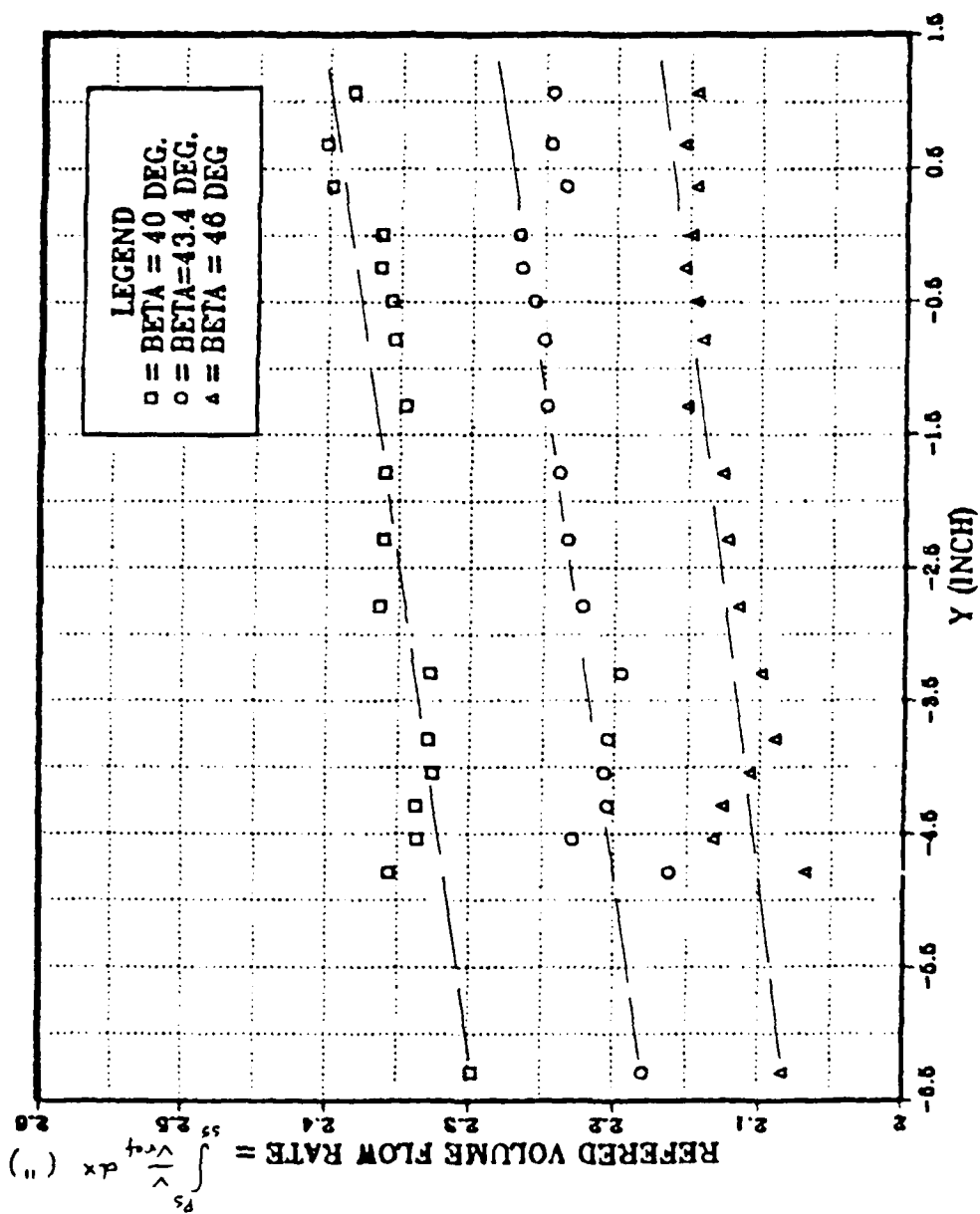


Figure 35. Distribution of $\int \frac{v}{v_{ref}} dx$ Through the Passage for Three Inlet Angles.

Volumetric flow is seen to fluctuate close to the passage inlet since the velocities near the suction surface were not easily resolved and the velocity (including flow reversals) within the suspected separation bubble could not be measured at all. Fluctuations away from the leading edge have no obvious trends nor interpretation. The magnitude of the uncertainty in the result can be gauged from an examination of the AVDR.

The AVDR at each station was calculated by normalizing the volumetric flow rate to the reference inlet volumetric flow rate and assuming that the flow is incompressible throughout. The results are shown in Figure 36. The data away from the leading edge are seen to be within 1% of the linear distribution shown within the passage. The AVDR of the test passage was 1.025 ± 0.002 for the three inlet angles.

C. BOUNDARY LAYER MEASUREMENTS

1. Suction Surface

The suction surface velocity distributions obtained at the three inlet angles are shown plotted in Figures 37-39. The velocity is shown normalized with respect to the edge velocity. Both velocity components, normal and parallel to the wall, are shown. The following is a discussion of the results:

- a. Measurements inside the suspected laminar separation bubble were impossible to obtain since seed particles

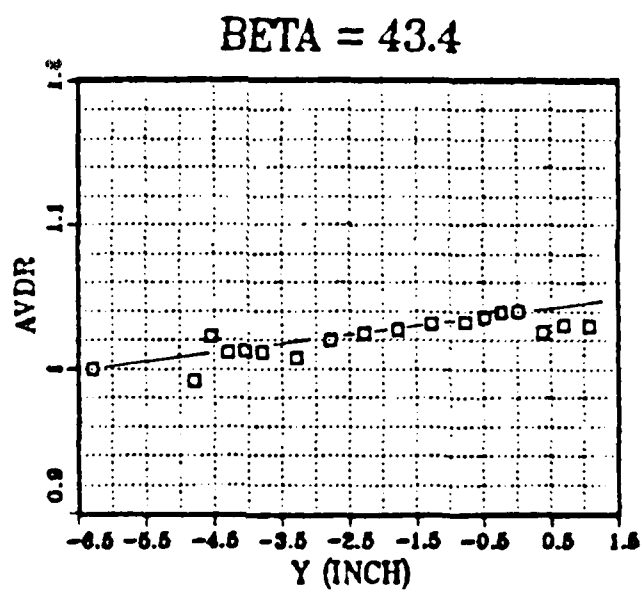
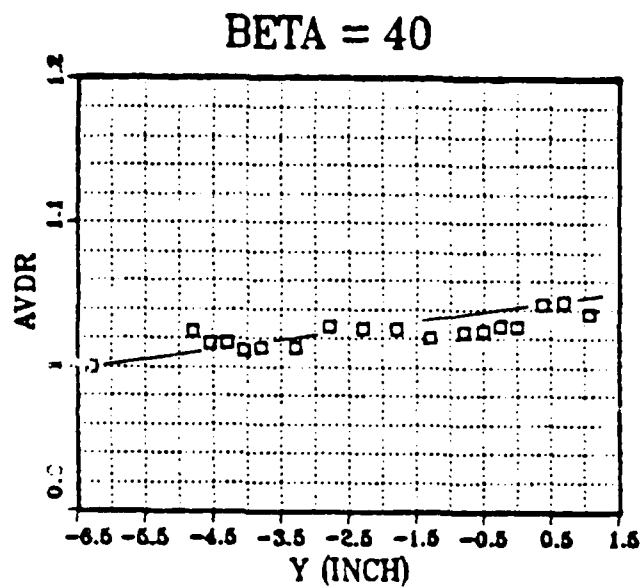


Figure 36. AVDR Distribution Along the Passage.

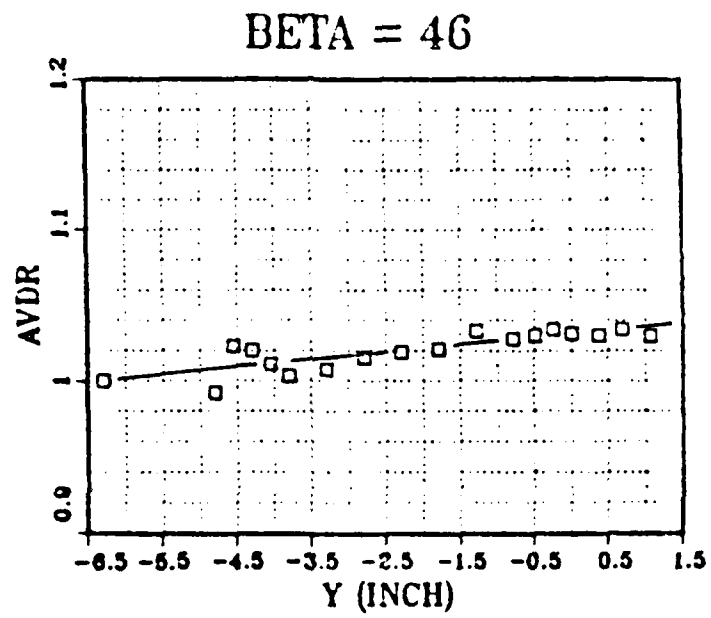


Figure 36. (cont.) AVDR Distribution Along the Passage.

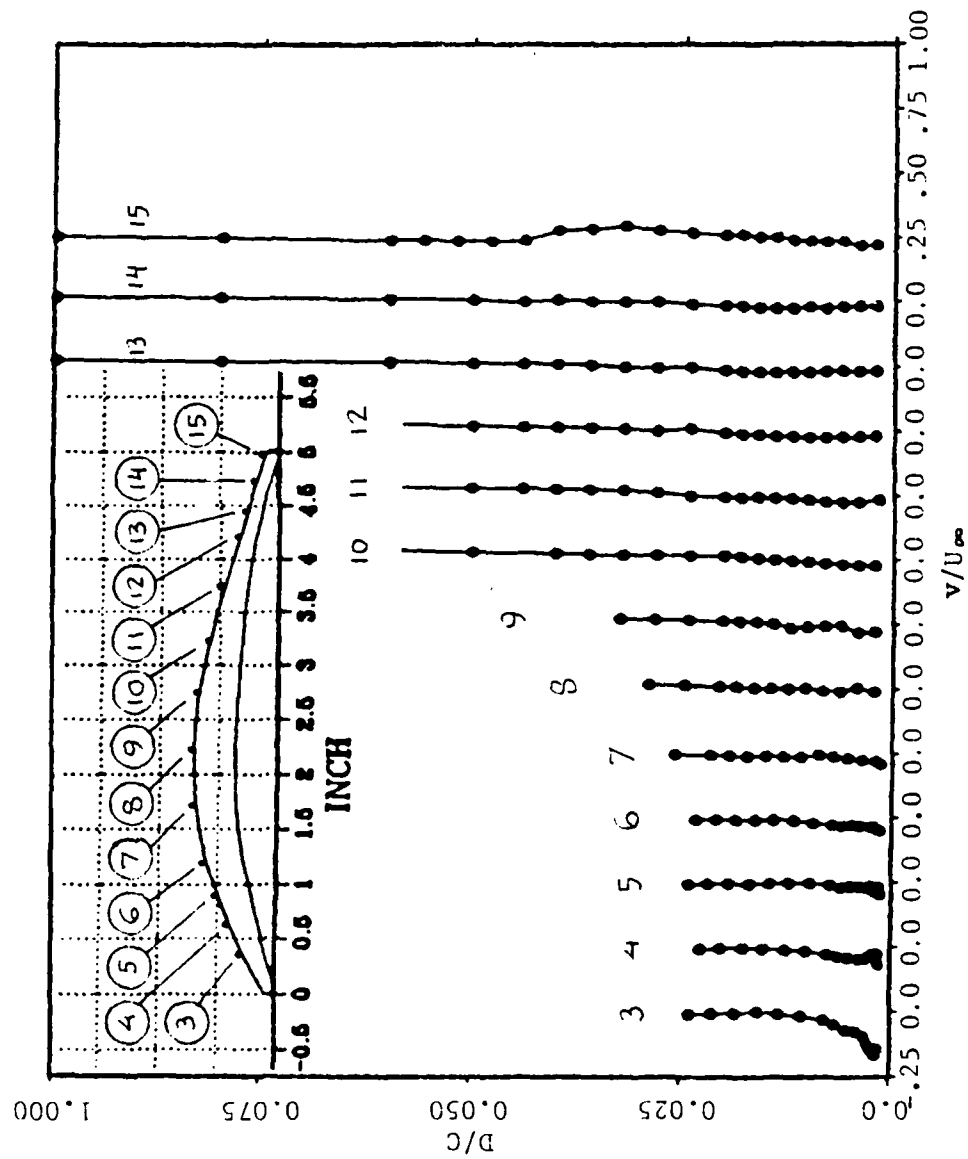


Figure 37(b). Boundary Layer Velocity Distributions; $\epsilon_1 = 40^\circ$, $Re = 710000$.
Velocity Normal to Wall

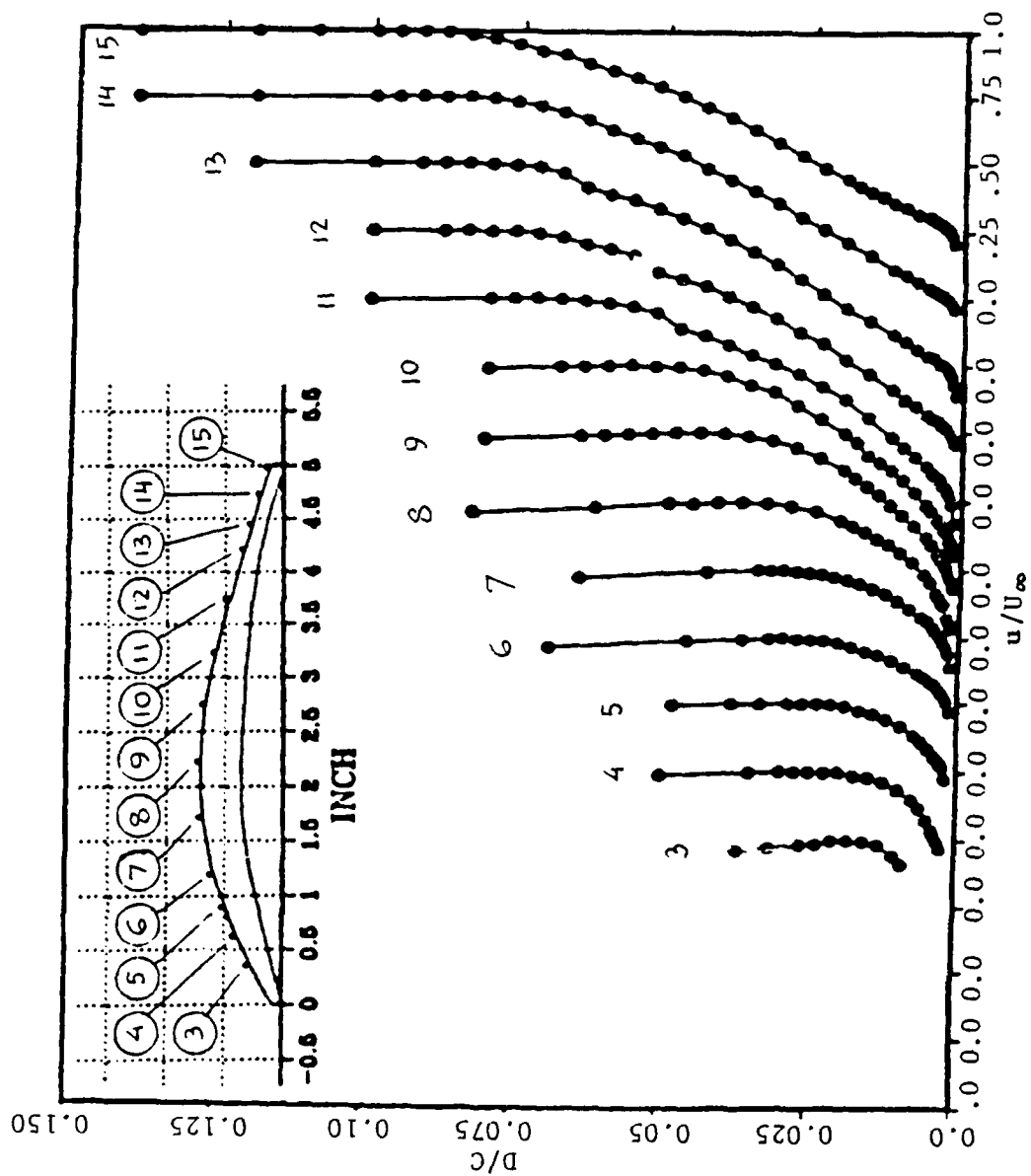


Figure 38(a). Boundary Layer Velocity Distributions;
 $\beta_1 = 43.4^\circ$, $Re = 740000$.

Velocity Parallel to Wall

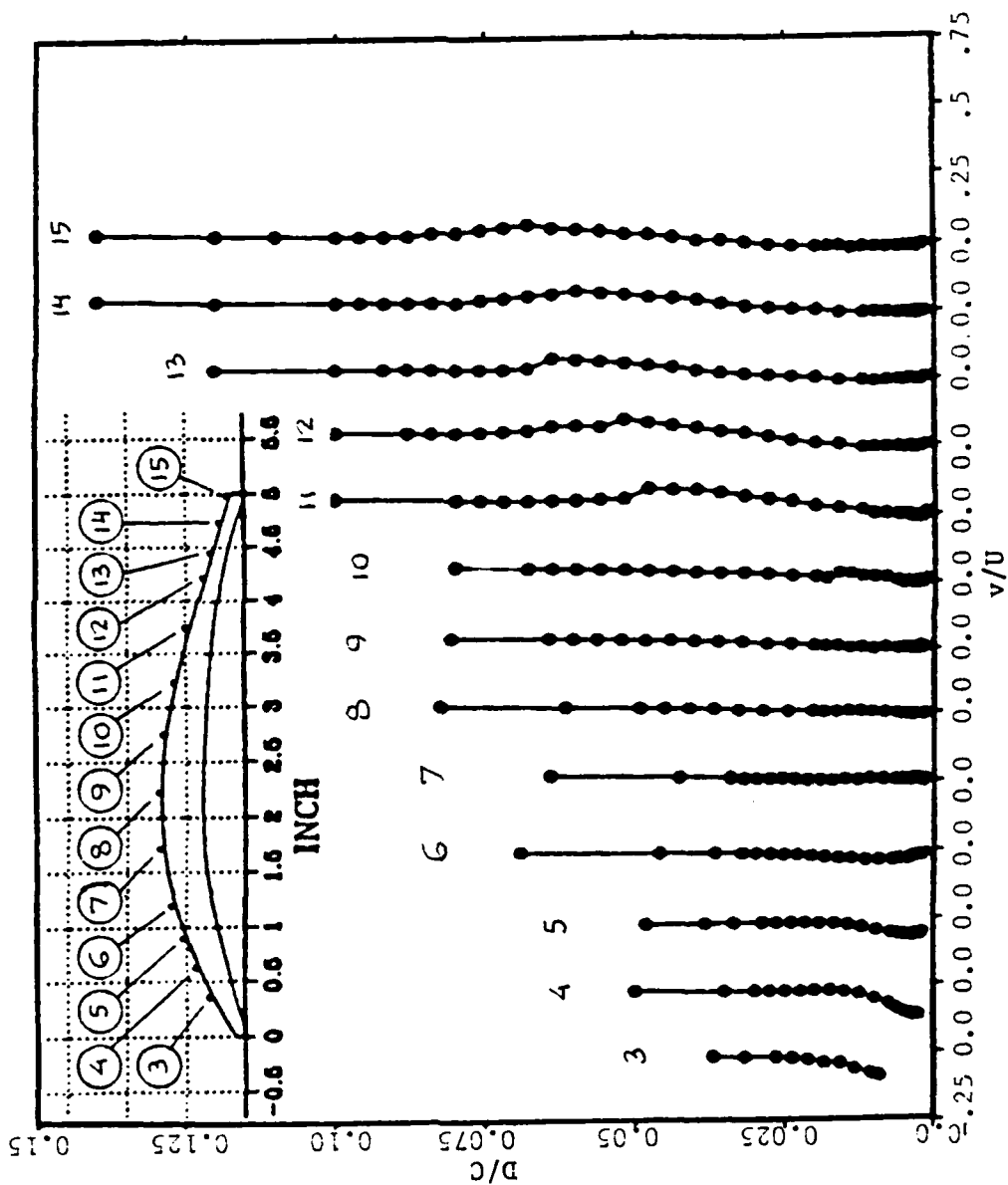


Figure 38(b). Boundary Layer Velocity Distributions;
 $\beta_1 = 43.4^\circ$, $Re = 740000$.
 Velocity Normal to Wall

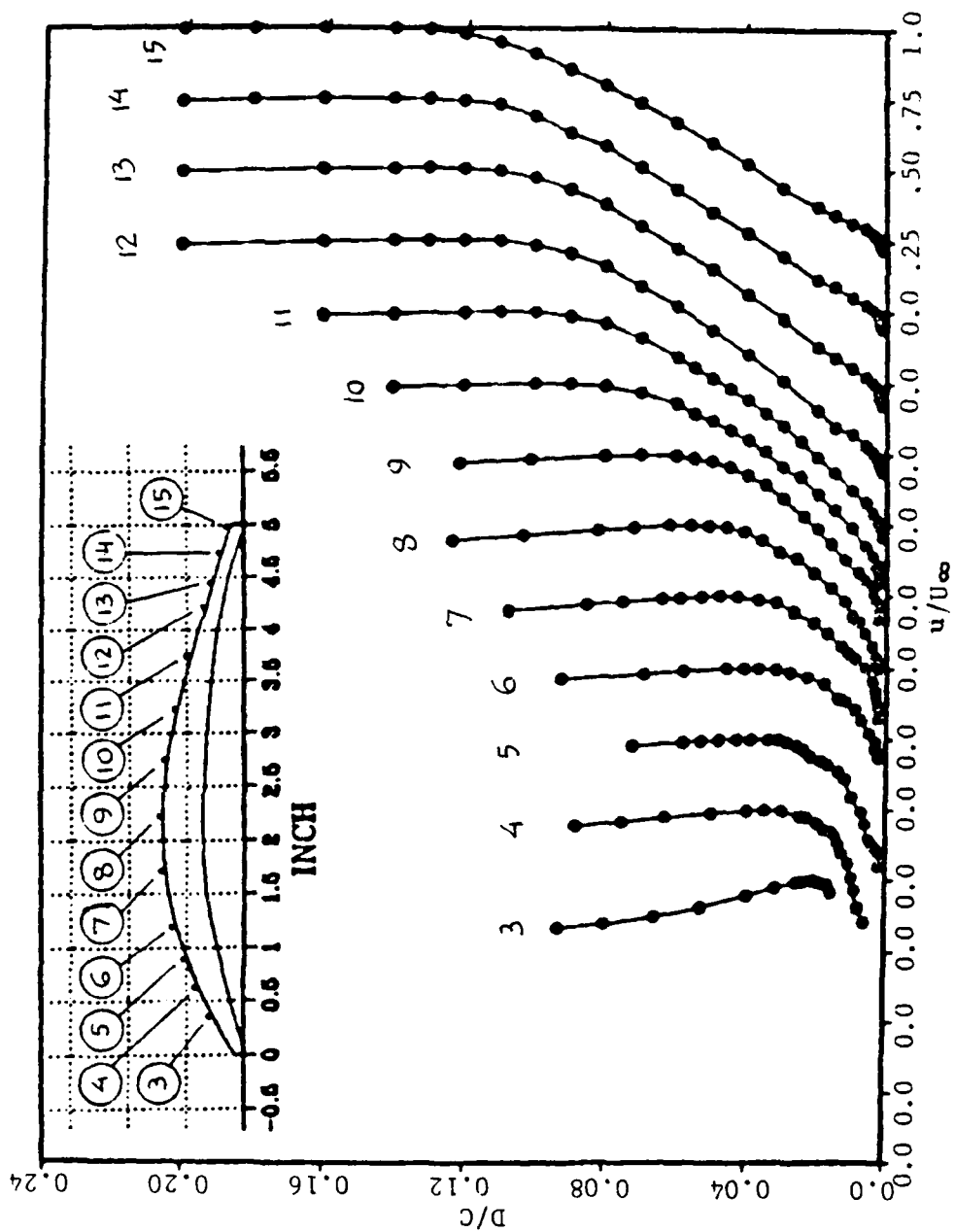


Figure 39(a). Boundary Layer Velocity Distributions; $\beta_1 = 46^\circ$, $Re = 730000$.
Velocity Parallel to Wall

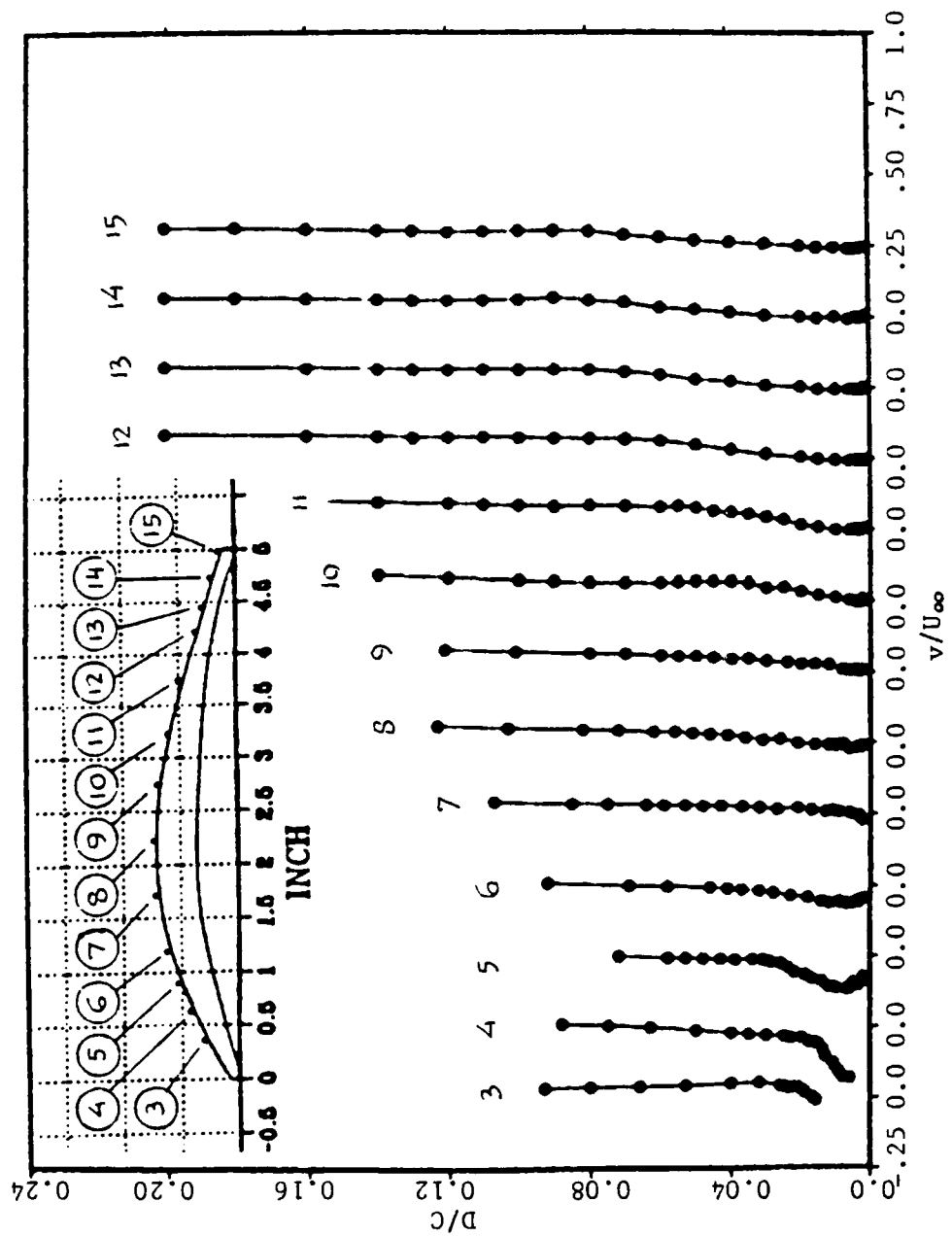


Figure 39(b). Boundary Layer Velocity Distributions; $\beta_1 = 46^\circ$, $Re = 730000$.
Velocity Normal to Wall

seed particles apparently did not penetrate into the separated region. The presence of the bubble, however, was evident in the measurements. At the design condition, ($\beta_1 = 40^\circ$, Figure 37) at Station 3, a negative velocity component normal to the wall (velocity towards the wall) indicates that the flow was approaching reattachment. The fact that measurements could not be achieved close to the wall at that station, as was possible at other stations, was taken to indicate that the station was slightly upstream of the reattachment point. Further downstream, at Station 4, the two component velocity profiles in Figure 37 indicate that the station was slightly downstream of the reattachment point. At $\beta_1 = 43.4^\circ$, at Station 3 the velocity profiles in Figure 38 indicate that this same station was now above the bubble. The following profile, at the same angle, indicates that Station 4 was slightly upstream of reattachment. Further downstream, at Station 5, the flow was slightly downstream of reattachment. At $\beta_1 = 46^\circ$, shown in Figure 39, the measurements exhibited the same qualitative behavior. Station 3 was above the bubble. Station 4 was also above the bubble. Station 5 was close to reattachment and Station 6 was close but downstream of reattachment. The data suggest that as the inlet angle was increased the separation bubble

bubble moved or extended further downstream. It is noted that the component of velocity normal to the surface was negligibly small at all stations downstream of the indicated reattachment.

b. Distributions of the turbulence level through the suction side boundary layer are shown plotted in Figures 40-42. The following observations are made:

- (1) High levels of unsteadiness were recorded above the bubble. At the design condition ($\beta_1 = 40^\circ$, Figure 40) turbulence there was 10-12%. At higher angles the unsteadiness progressively increased, with $\epsilon = 12-13\%$ at $\beta_1 = 43.4^\circ$ and 16-17% at $\beta_1 = 46^\circ$.
- (2) The turbulence level dropped to 8% and lower after reattachment.
- (3) The peak in the turbulence level profile moved away from the wall as the station moved downstream.
- (4) Very close to the wall, where the velocity gradient was high, high turbulence levels were recorded, but were due to velocity broadening (significant velocity variations in the measuring volume at the LDV focal point). Those data points were, therefore, shown in the plots with a cross.

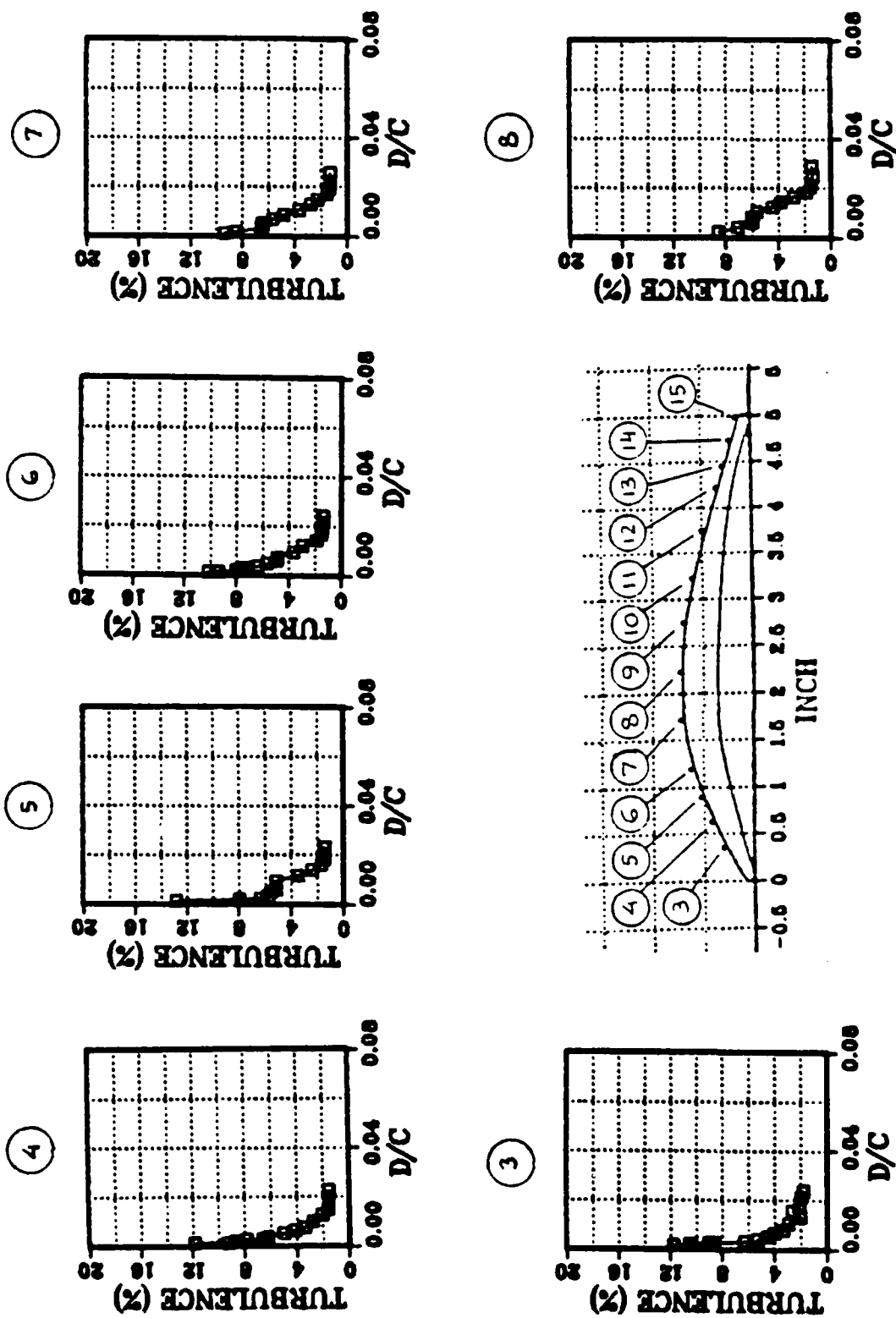


Figure 40. Suction Side Boundary Layer Turbulence Level Distributions;
 $\beta_1 = 40^\circ$, $Re = 710000$.

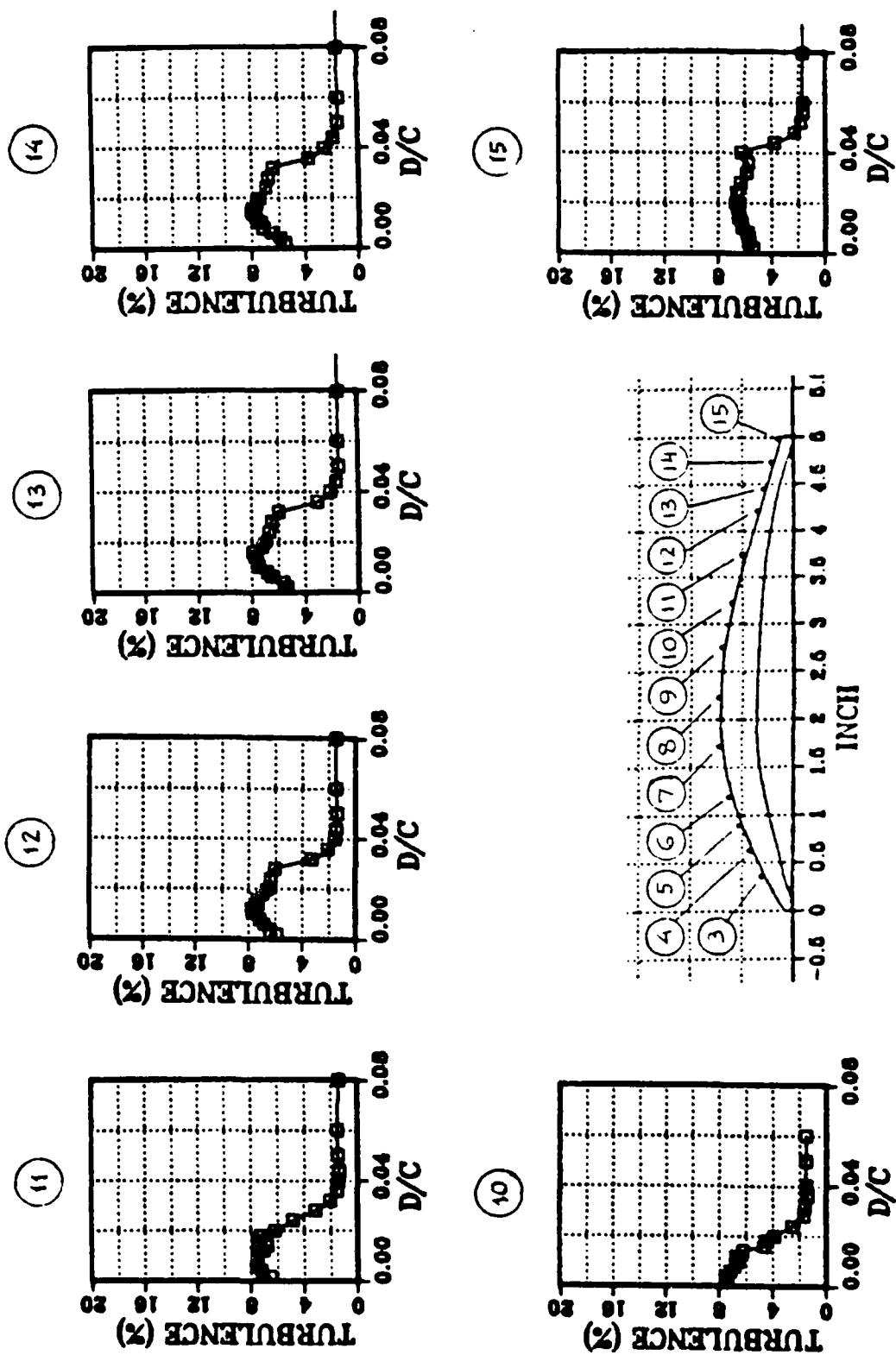


Figure 40. (cont.) Suction Side Boundary Layer Turbulence Level Distributions; $\delta_1 = 40^\circ$, $Re = 710000$.

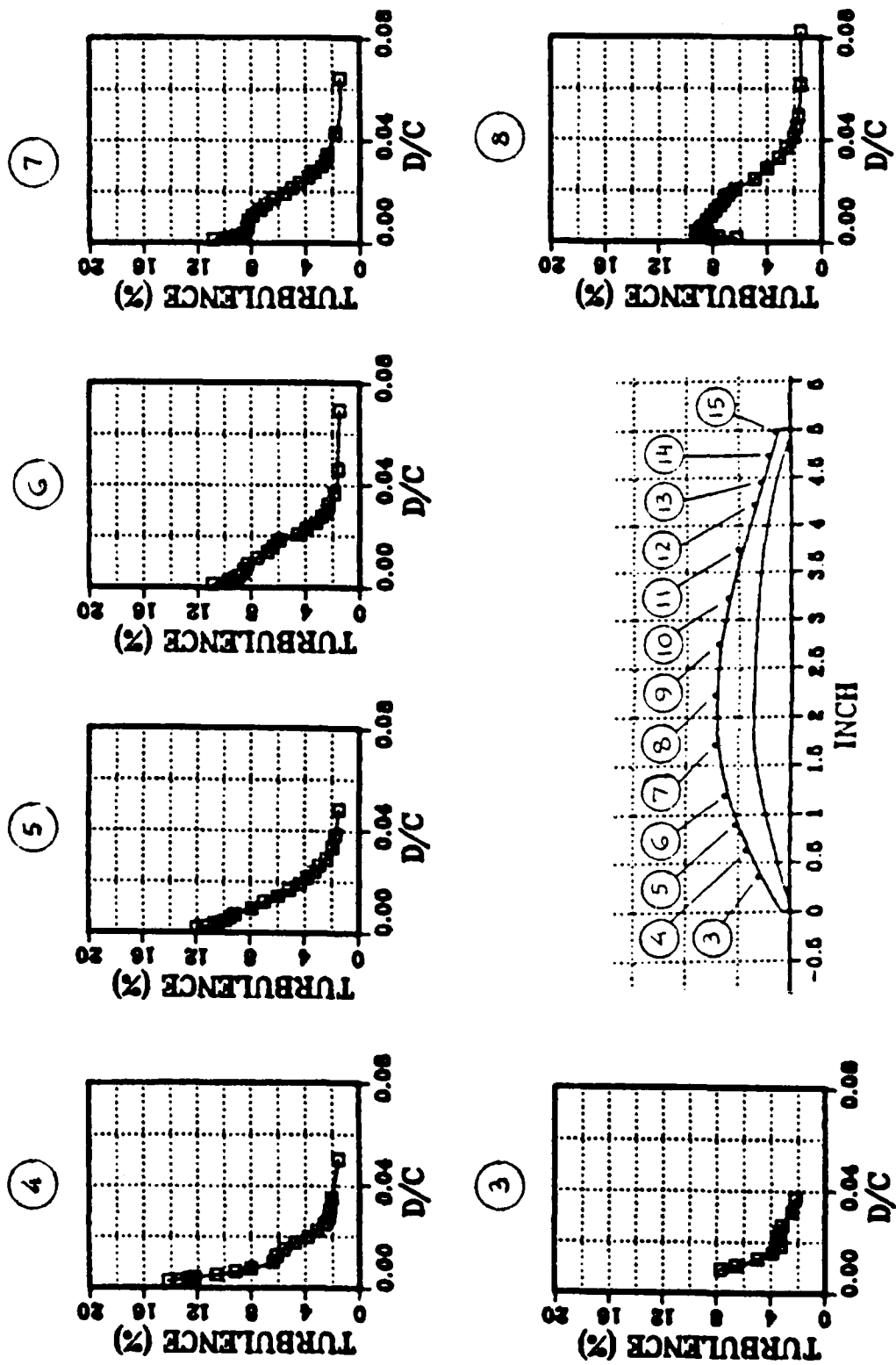


Figure 41. Suction Side Boundary Layer Turbulence Level Distributions;
 $\beta_1 = 43.4^\circ$, $Re = 740000$.

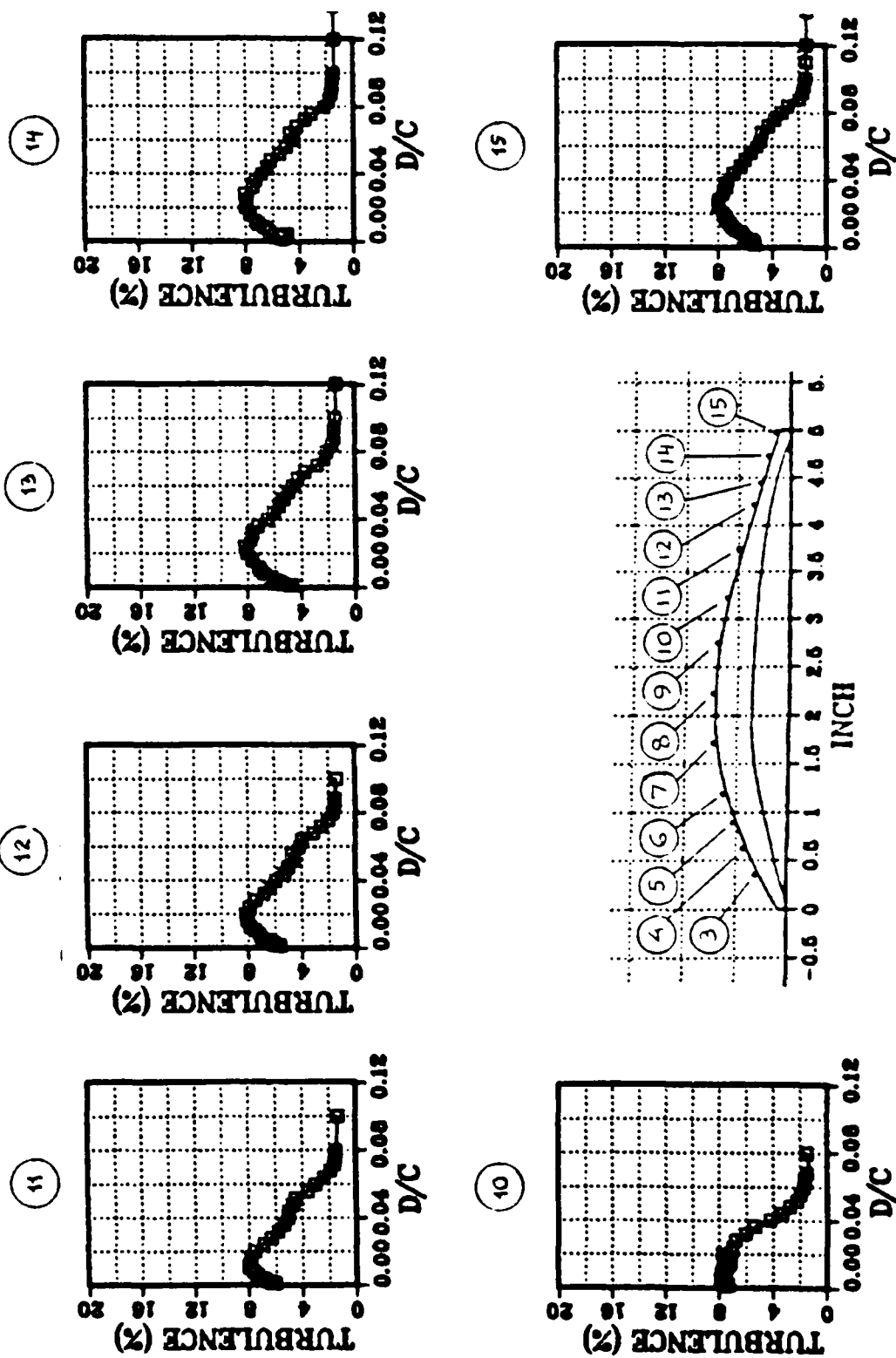


Figure 41. (cont.) Suction Side Boundary Layer Turbulence Level Distributions; $\beta_1 = 43.4^\circ$, $Re = 740000$.

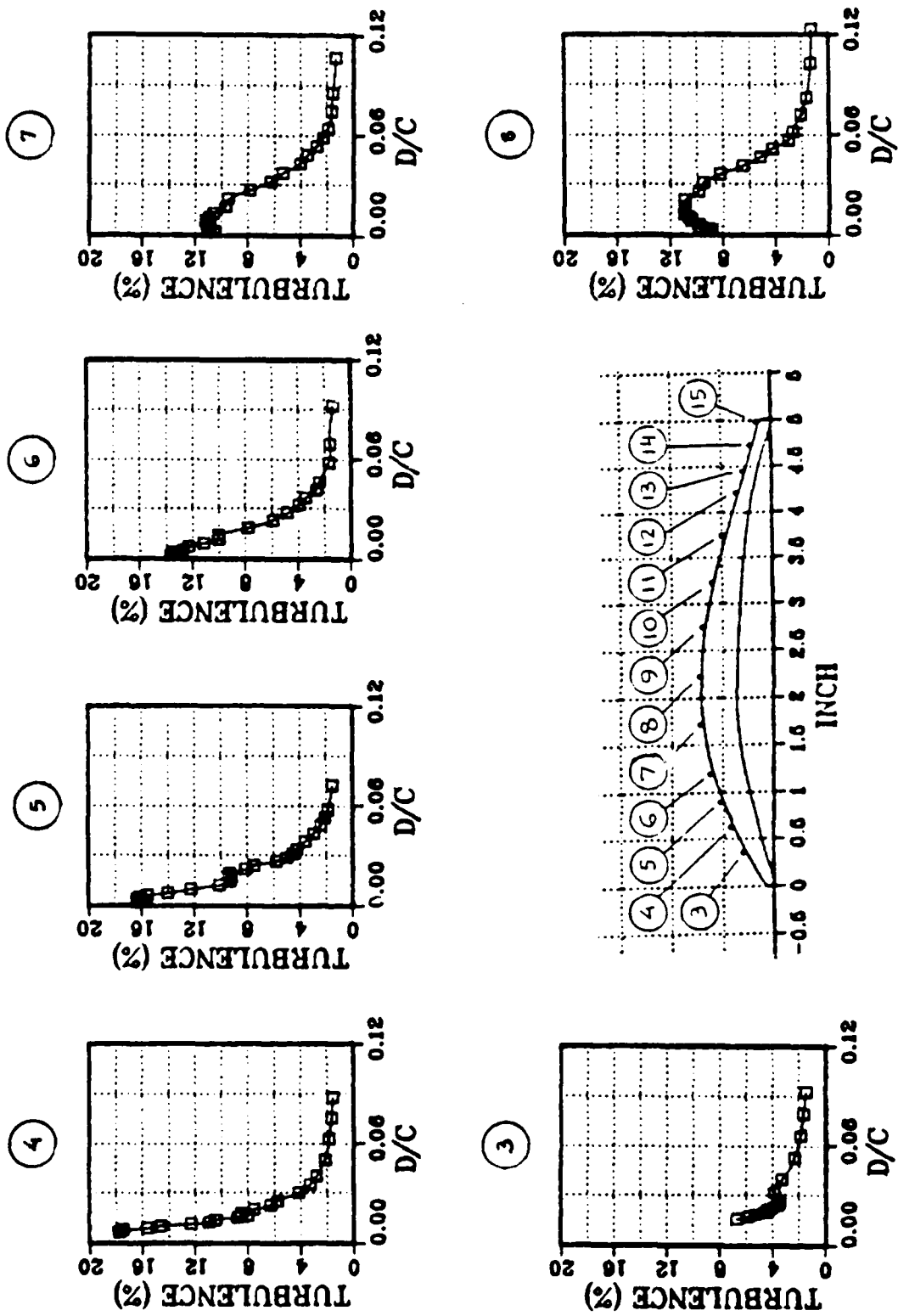


Figure 42. Suction Side Boundary Layer Turbulence Level Distributions;
 $\delta_1 = 46^\circ$, $Re = 730000$.

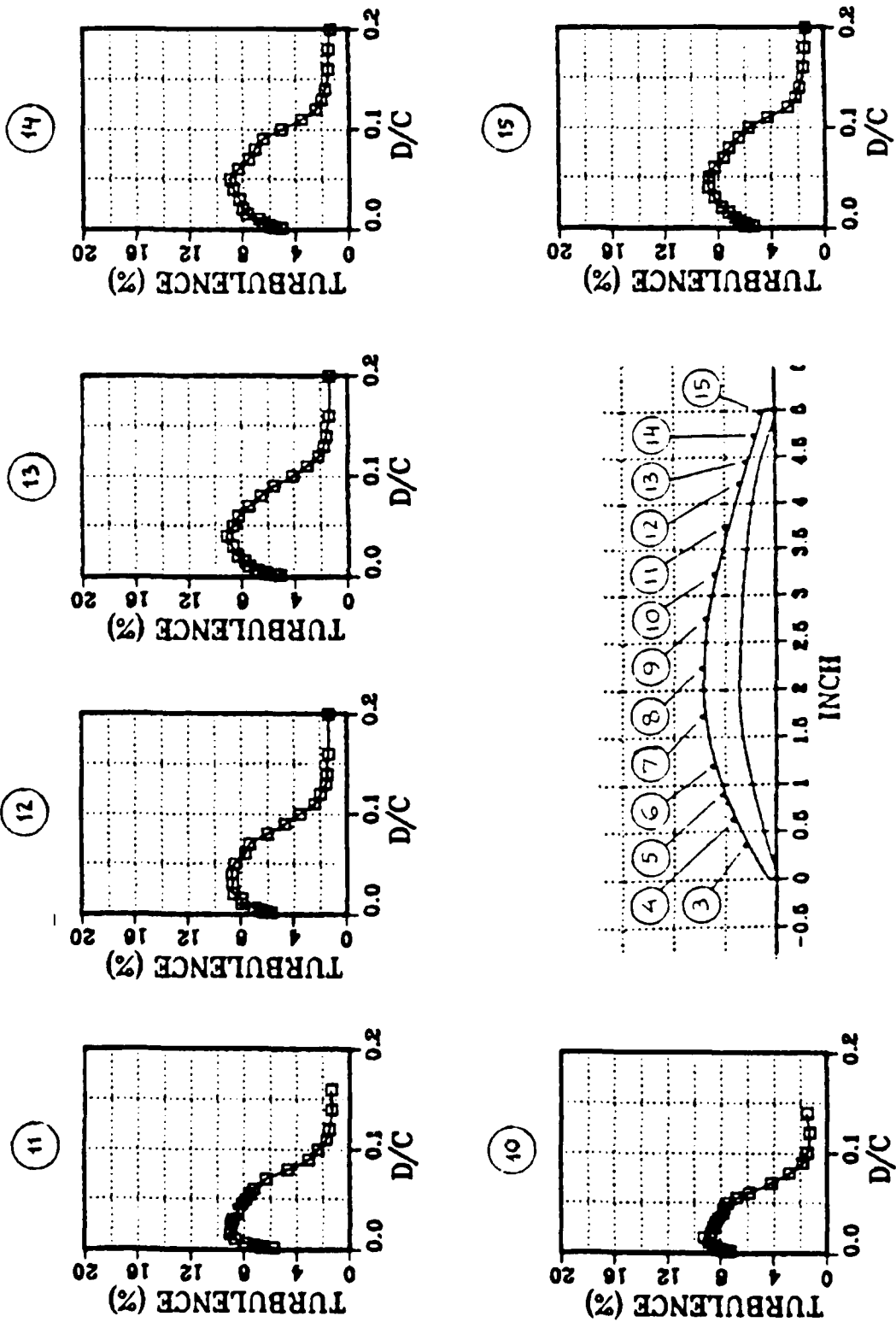


Figure 42. (cont.) Suction Side Boundary Layer Turbulence Level Distributions; $\beta_1 = 46^\circ$, $Re = 730000$.

From the high levels of turbulence above the bubble and the observation that all profiles downstream of reattachment were clearly not laminar it was concluded that transition occurred as a result of the bubble.

- c. The boundary layer growth is shown in Figures 43-45. Figure 43 shows the growth in the thickness of the boundary layer along the suction surface of the blade. The boundary layer thickness was defined as the distance from the wall where the component of the velocity parallel to the wall was 99% of the edge velocity. Figure 44 shows the displacement thickness distributions and Figure 45 the momentum thickness distributions, calculated by spline interpolation and integration of the boundary layer data.

At the trailing edge, as the incidence was increased, the suction side boundary layer became very thick although no separation was detected. For the highest inlet angle ($\beta_1 = 46^\circ$) the displacement thickness was about 6.5% of the passage width and the boundary layer thickness was more than 20% of the passage width.

The distribution of the shape factor along the suction surface is shown in Figure 46. After reattachment, the shape factor at first decreased until a minimum value was reached, and then increased as the turbulent boundary layer thickened. The

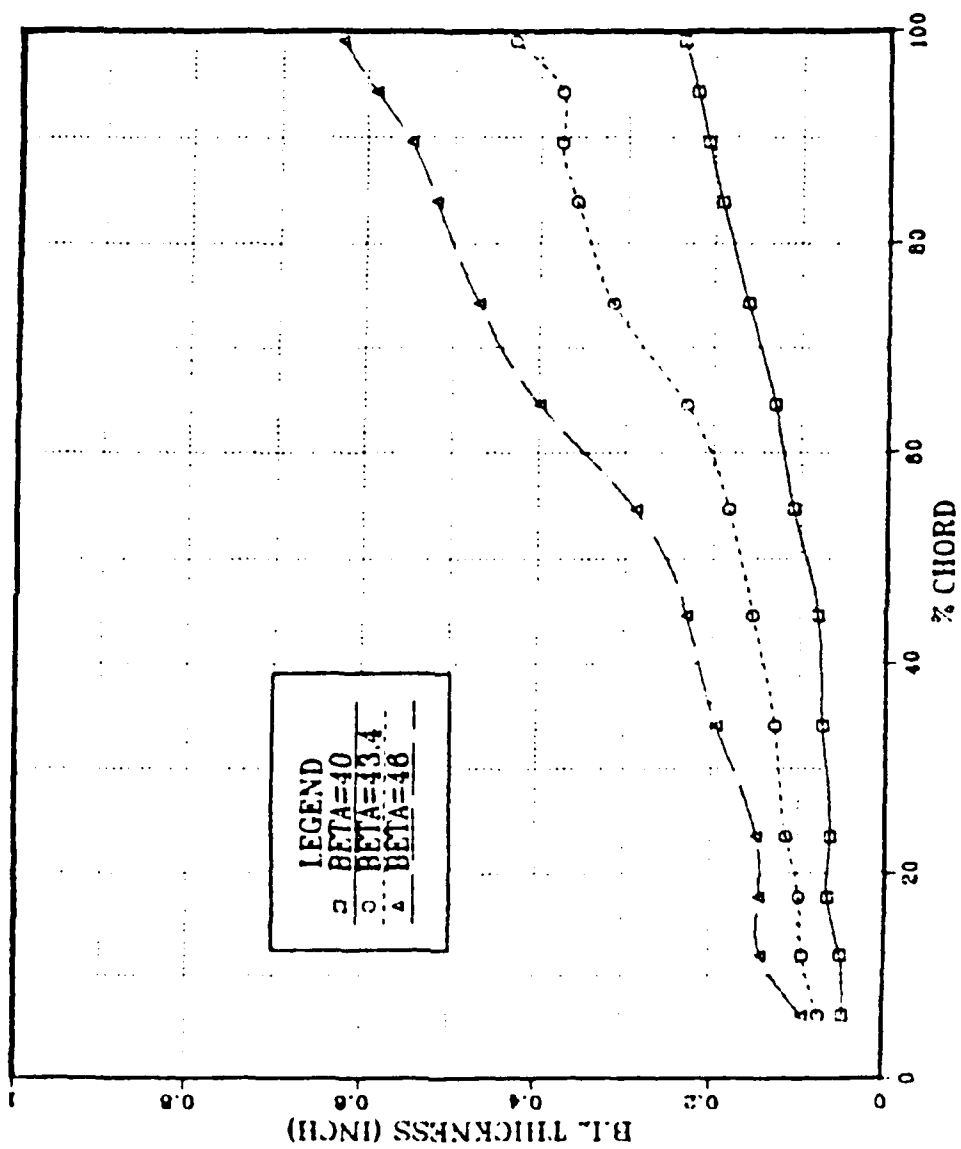


Figure 43. Boundary Layer Thickness on the Suction Surface.

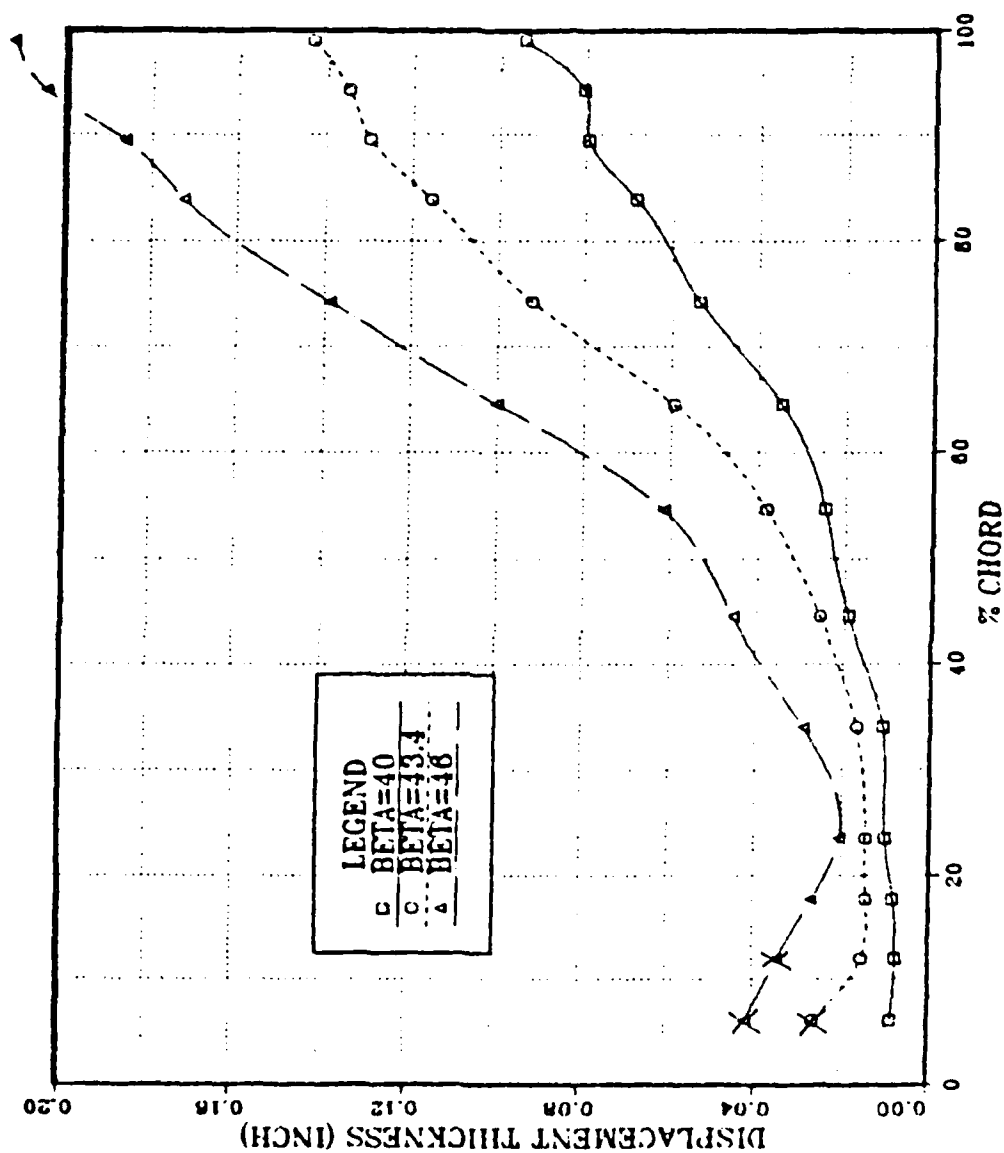


Figure 44. Displacement Thickness on the Suction Surface.

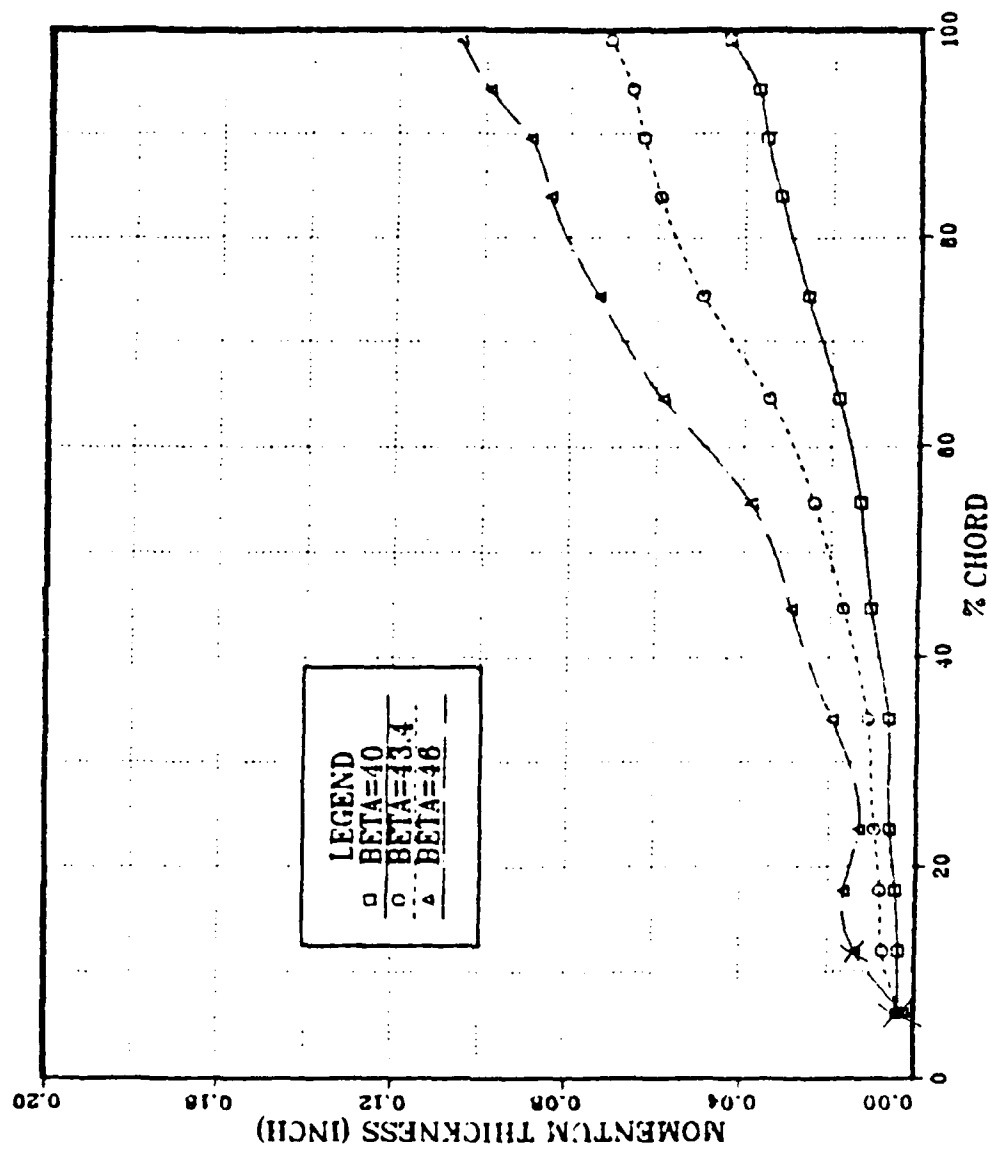


Figure 45. Momentum Thickness on the Suction Surface.

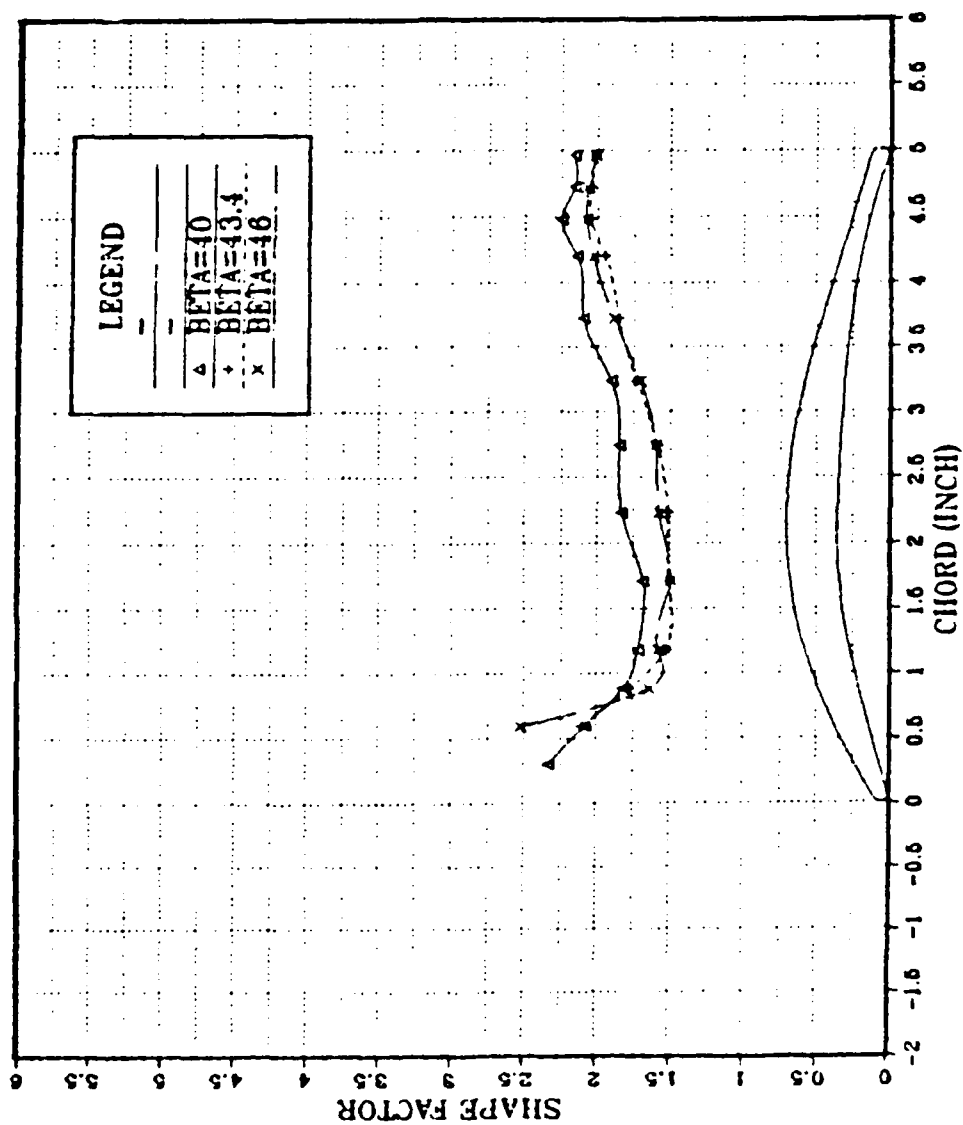


Figure 46. Shape Factor Distribution on the Suction Surface.

minimum shape factor was at approximately 30% chord. The value at the minimum was approximately 1.7 for the design condition ($\beta_1 = 40^\circ$) and approximately 1.5 for the higher angles ($\beta_1 = 43.4^\circ, 46^\circ$).

The similarity in the shape factor distribution at the two largest inlet angles but clear departure from the results obtained at the design inlet angle implies a nonlinear behavior in the boundary layer development. This would not be expected simply by looking at the results in Figures 44 and 45 for the displacement and momentum thicknesses respectively. Each of the thicknesses, and the overall thickness shown in Figure 43, increased steadily as the inlet angle was increased. However, Figure 24 and Figure 27 show that the velocity distribution near the leading edge on the suction side behaved somewhat differently at the design angle compared with the two higher angles. Also, it can be seen in Figure 33 that no strong leading edge suction peak was detected at the design angle, but one did occur at the two larger angles. Unfortunately, the differences in the early development of the boundary layer, particularly the presence, structure, and effects of the leading edge bubble, could not be resolved in the experiment.

It is noted that the magnitude of the shape factor at the design angle increased to 2.2 at the trailing

edge, without sign of separation. Fortuitously, the magnitude of the shape factor was less at the off-design, higher incidence angles.

Tables 6-8 summarize the thickness data and their uncertainties. The method for calculating the uncertainty is described in Appendix E.

2. Pressure Surface

Pressure surface boundary layer profiles are shown plotted in Figures 47-49. Transition from a typical laminar velocity distribution to a typical turbulent distribution is seen, at each angle, as the survey station moves downstream. The pressure surface boundary layers are clearly much thinner than the suction surface boundary layers, especially at the highest inlet angle.

The growth in the boundary layer thickness on the pressure surface is shown in Figure 50. The calculated displacement thickness distribution is shown in Figure 51 and the momentum thickness distribution is shown in Figure 52. The following observations are made with references to Figures 50-52.

- a. The inlet angle had a negligible effect on the measured boundary layer thickness. However, the higher the inlet angle, the smaller became the displacement and momentum thicknesses. The very small changes and the trend were due to the fact that the edge velocity on the pressure surface changed slightly from one

TABLE 6

SUCTION SURFACE BOUNDARY LAYER PARAMETERS, $\beta_1 = 40^\circ$

y	u_1/U_∞	δ^*	$\Delta\delta^*$	θ	$\Delta\theta$	H	ΔH
0.0	0.202	0.0945	0.0018	0.0438	0.00017	2.156	0.05
-0.25	0.261	0.0807	0.0018	0.0374	0.00021	2.158	0.06
-0.5	0.222	0.0795	0.0018	0.0353	0.00022	2.251	0.06
-0.792	0.267	0.0685	0.0017	0.0320	0.00022	2.141	0.07
-1.292	0.259	0.0538	0.0017	0.0256	0.00021	2.101	0.08
-1.792	0.405	0.0349	0.0016	0.0183	0.0003	1.905	0.12
-2.292	0.488	0.0249	0.0015	0.0134	0.00033	1.848	0.16
-2.792	0.601	0.0192	0.0014	0.0105	0.00036	1.831	0.2
-3.292	0.633	0.0108	0.0014	0.0064	0.00037	1.685	0.31
-3.792	0.674	0.0101	0.0013	0.0059	0.00037	1.720	0.33
-4.042	0.751	0.0080	0.0012	0.0044	0.00037	1.819	0.42
-4.292	0.766	0.0073	0.0012	0.0035	0.00037	2.081	0.56

TABLE 7

SUCTION SURFACE BOUNDARY LAYER PARAMETERS, $\beta_1 = 43.4^\circ$

y	u_1/U_∞	δ^*	$\Delta\delta^*$	θ	$\Delta\theta$	H	ΔH
0.0	0.21	0.1433	0.0018	0.0709	0.00018	2.021	0.03
-0.25	0.217	0.1349	0.0018	0.0661	0.00019	2.043	0.03
-0.5	0.139	0.1299	0.0019	0.0634	0.00013	2.050	0.03
-0.792	0.21	0.1156	0.0018	0.0594	0.00018	1.948	0.04
-1.292	0.172	0.0922	0.0018	0.0496	0.00015	1.859	0.04
-1.792	0.309	0.0594	0.0017	0.0343	0.00024	1.733	0.06
-2.292	0.438	0.0382	0.0016	0.0241	0.00031	1.587	0.09
-2.792	0.536	0.0257	0.0015	0.0170	0.00034	1.517	0.12
-3.292	0.640	0.0169	0.0014	0.0112	0.00037	1.509	0.17
-3.792	0.720	0.0145	0.0013	0.0095	0.00037	1.530	0.20
-4.042	0.724	0.0143	0.0013	0.0080	0.00037	1.777	0.24
-4.292	0.718	0.0151	0.0013	0.0072	0.00037	2.106	0.29

TABLE 8
SUCTION SURFACE BOUNDARY LAYER PARAMETERS, $\beta_1 = 46^\circ$

y	u_1/U_∞	δ^*	$\Delta\delta^*$	θ	$\Delta\theta$	H	ΔH
0.0	0.22	0.2127	0.0018	0.1058	0.00019	2.01	0.02
-0.25	0.194	0.2050	0.0018	0.0992	0.00017	2.067	0.02
-0.5	0.174	0.1863	0.0018	0.0896	0.00015	2.079	0.02
-0.792	0.188	0.1723	0.0018	0.0848	0.00016	2.032	0.02
-1.292	0.209	0.1387	0.0018	0.0734	0.00018	1.89	0.03
-1.792	0.297	0.1000	0.0017	0.0586	0.00024	1.707	0.04
-2.292	0.42	0.0617	0.0016	0.0386	0.0003	1.599	0.05
-2.792	0.498	0.0457	0.0015	0.0290	0.00033	1.576	0.07
-3.292	0.573	0.0292	0.0014	0.0195	0.00035	1.5	0.1
-3.792	0.684	0.0205	0.0013	0.0130	0.00037	1.582	0.14
-4.042	0.549	0.0269	0.0014	0.0164	0.00035	1.642	0.12

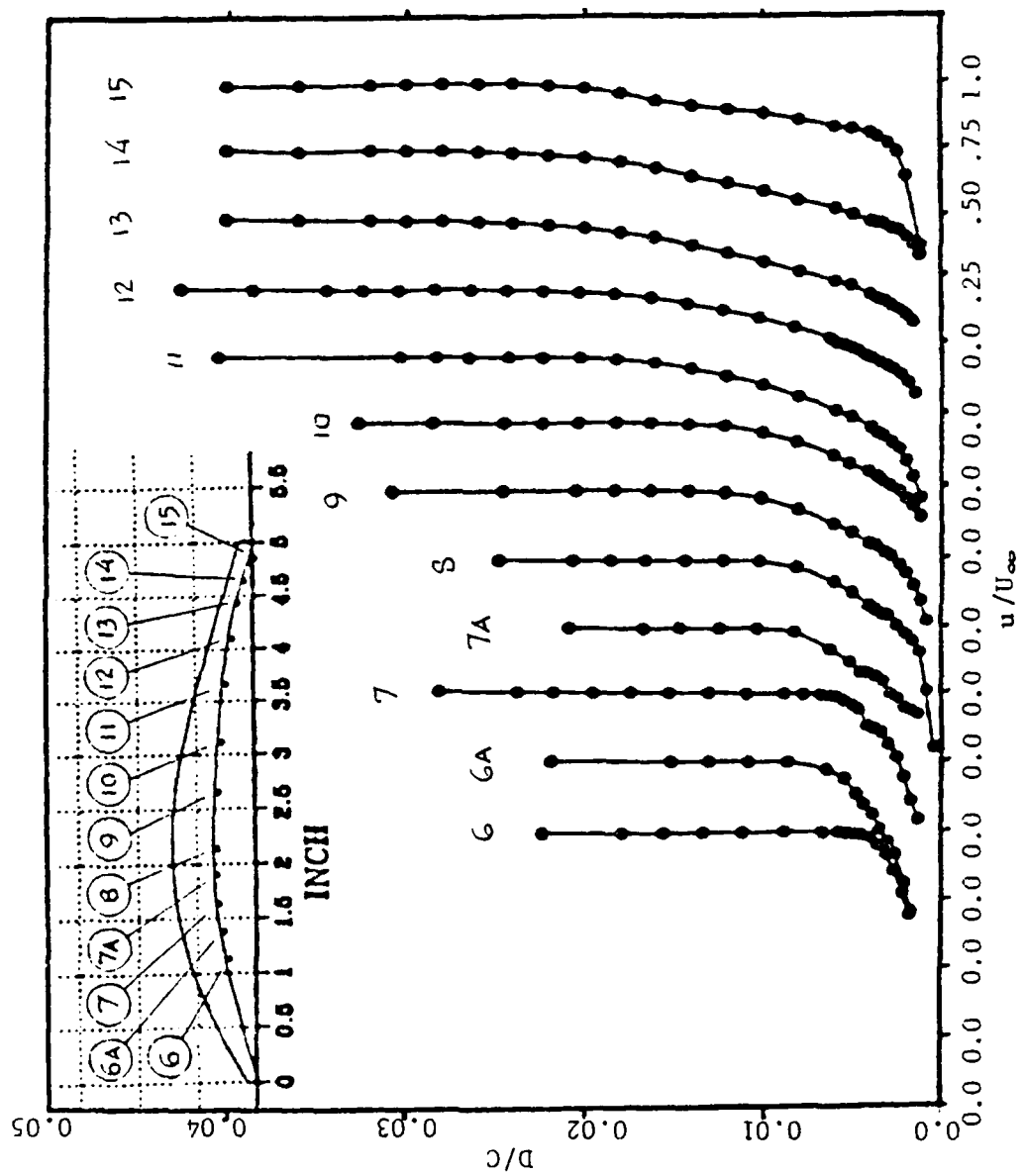


Figure 47(a). Pressure Surface Boundary Layer Velocity Distribution ;
 $\beta = 40^\circ$, $Re = 710000$.
 Velocity Parallel to Wall

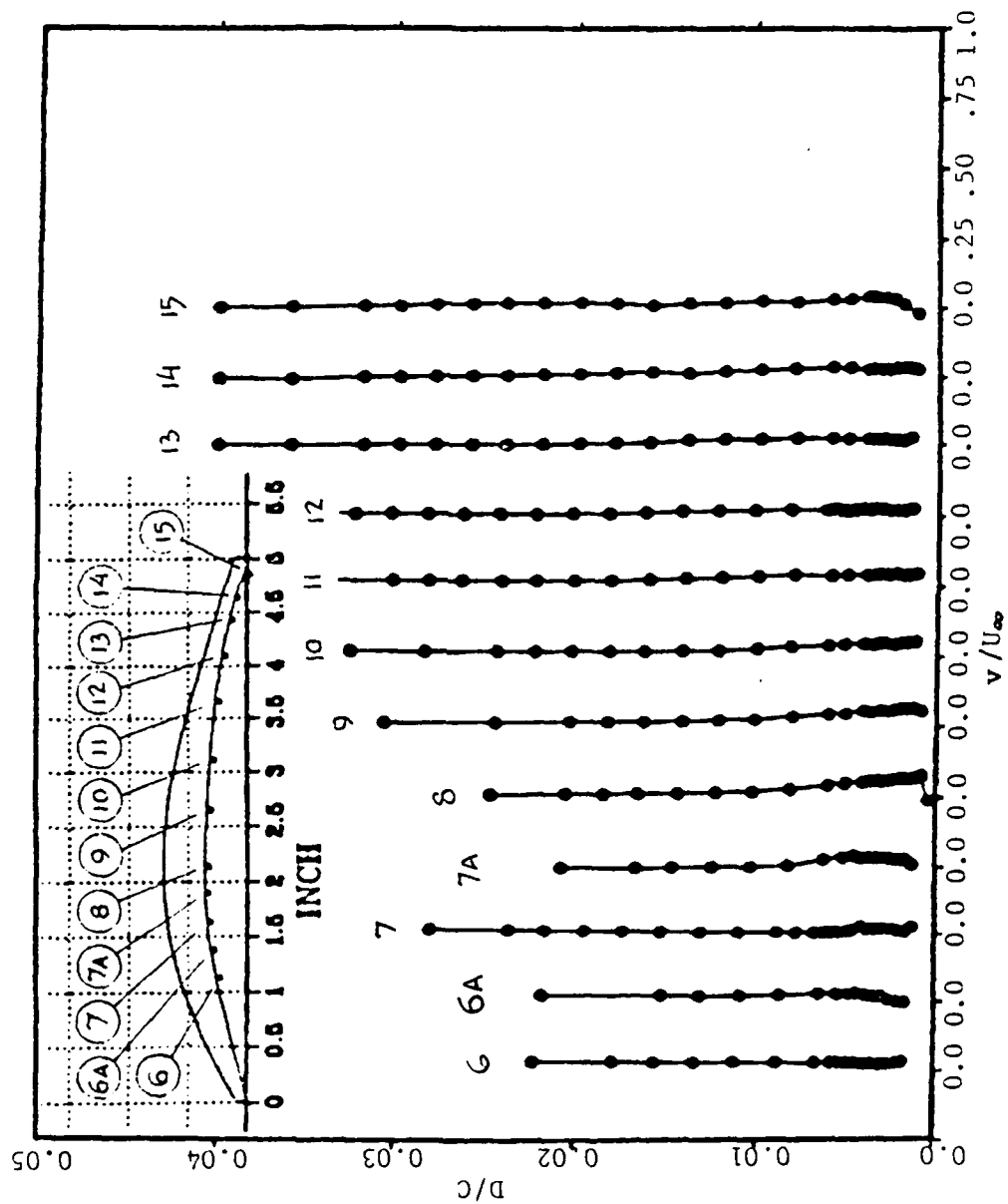


Figure 47(b). Pressure Surface Boundary Layer Velocity Distribution ;
 $\beta = 40^\circ$, $Re = 710000$.
 Velocity Normal to Wall

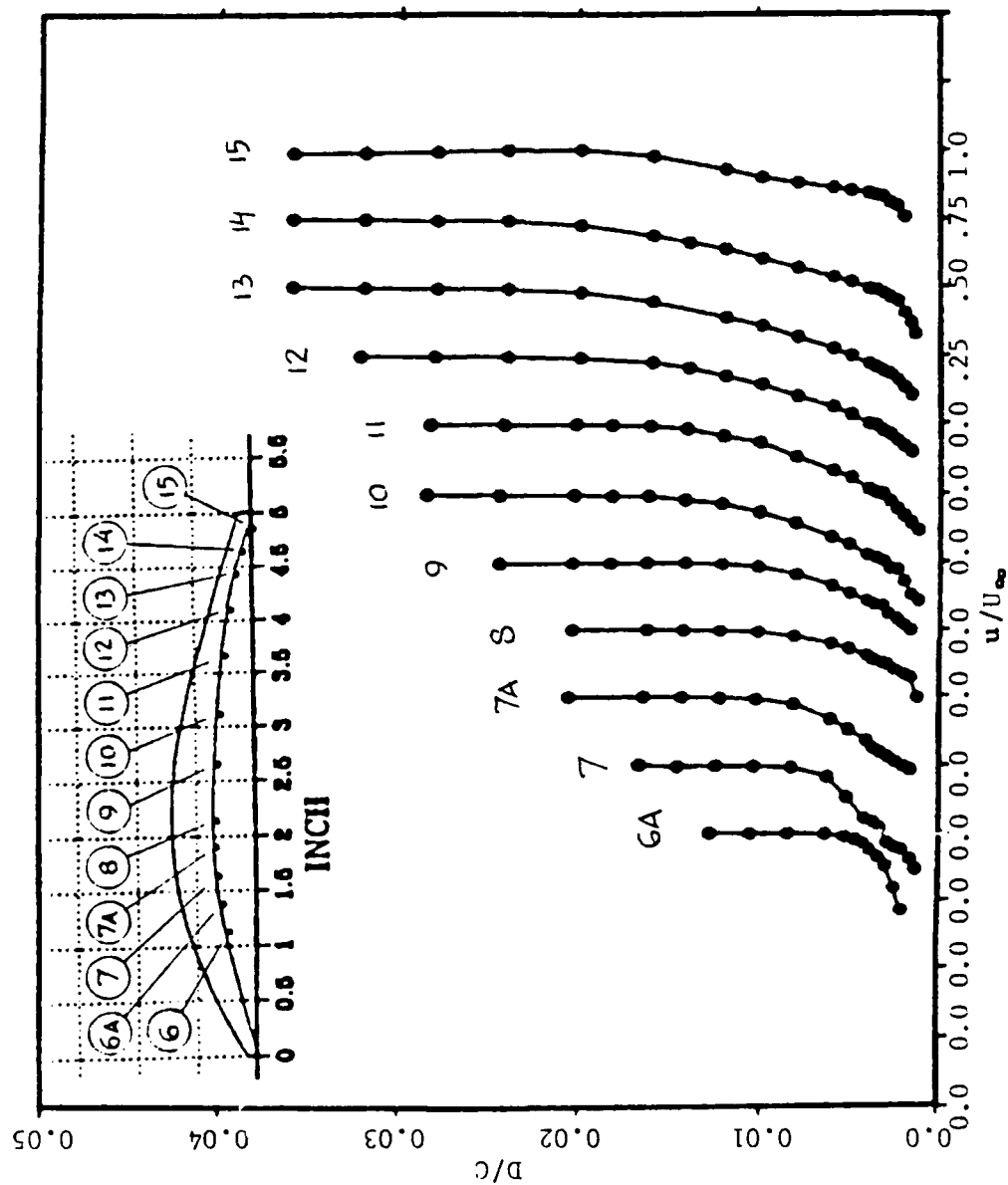


Figure 48(a). Pressure Surface Boundary Layer Velocity Distribution ;
 $\beta = 43.4^\circ$, $Re = 740000$.
 Velocity Parallel to Wall

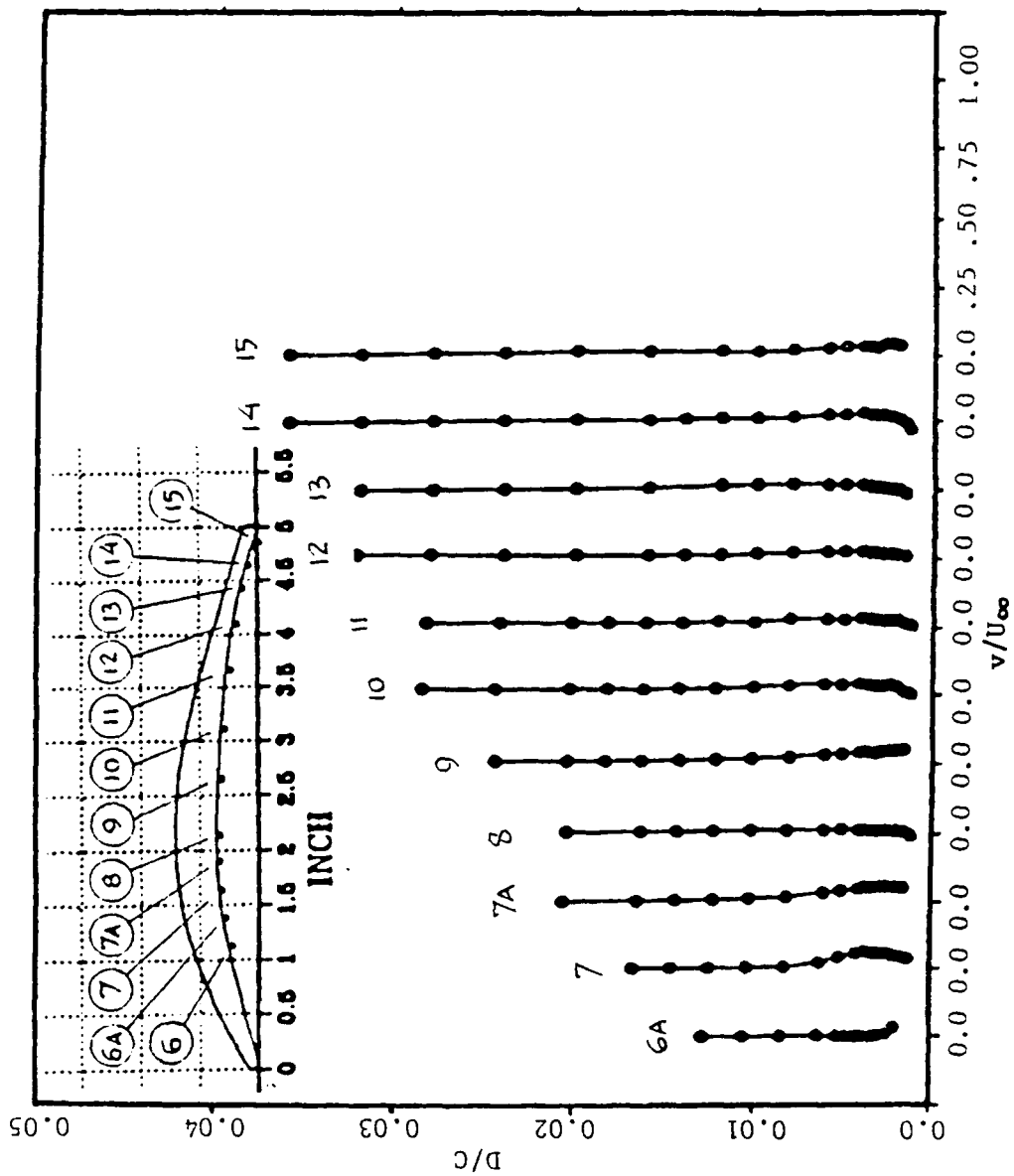


Figure 48(b). Pressure Surface Boundary Layer Velocity Distribution ;
 $\beta = 43.4^\circ$, $Re = 740000$.
 Velocity Normal to Wall

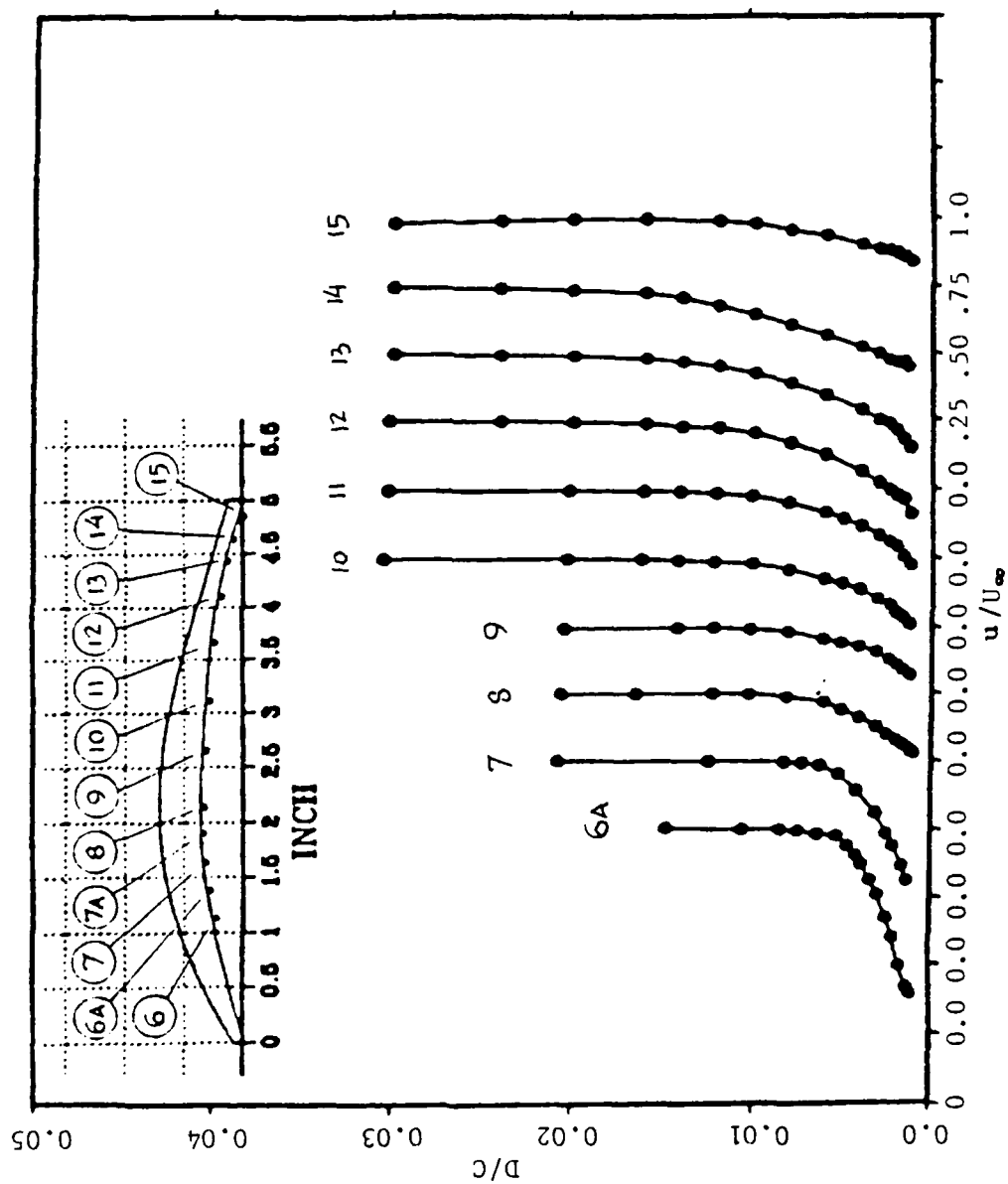


Figure 49(a). Pressure Surface Boundary Layer Velocity Distribution ;
 $\beta = 46^\circ$, $Re = 730000$.
 Velocity Parallel to Wall

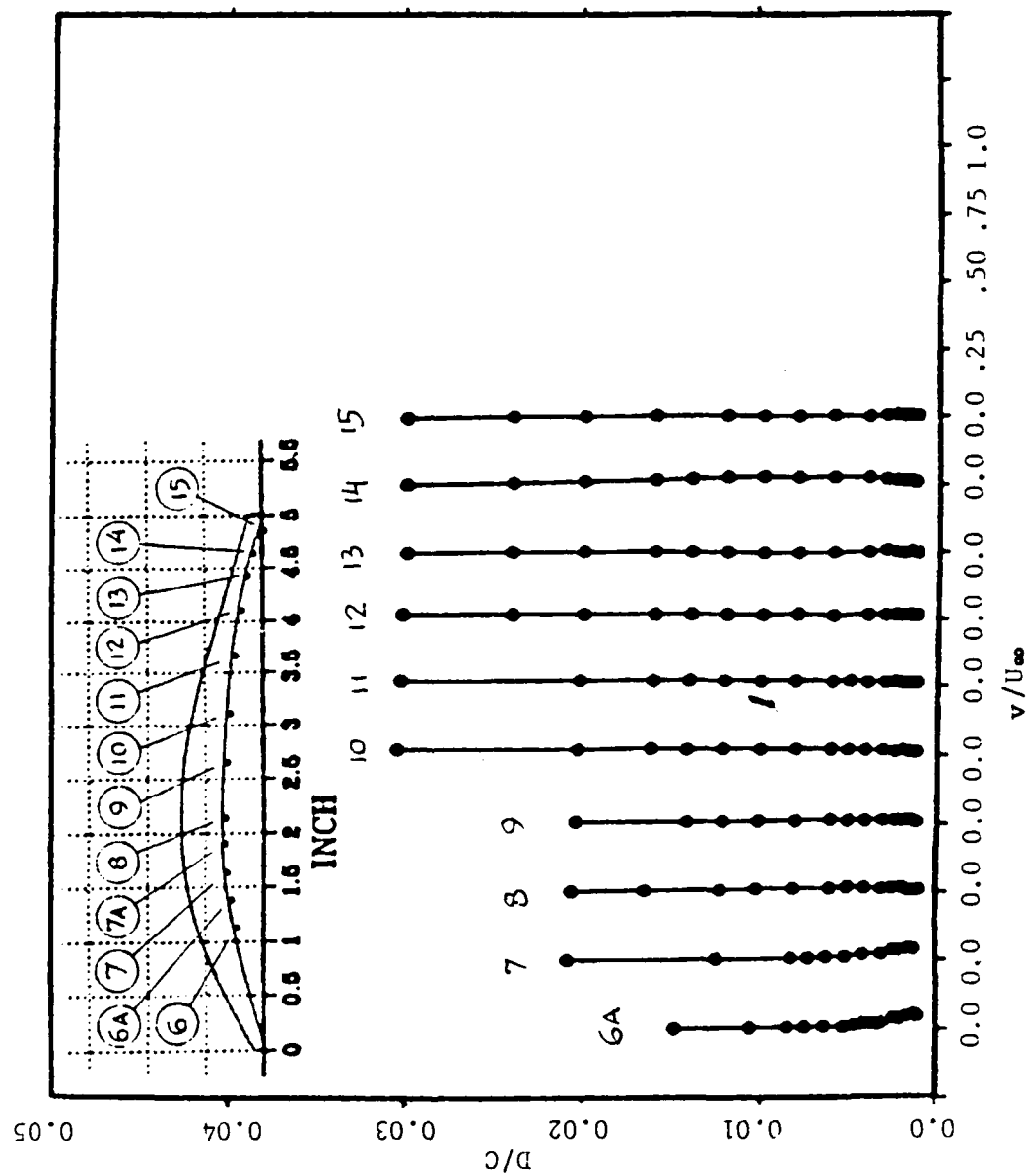


Figure 49(b). Pressure Surface Boundary Layer Velocity Distribution ;
 $\beta = 46^\circ$, $Re = 730000$.
 Velocity Normal to Wall

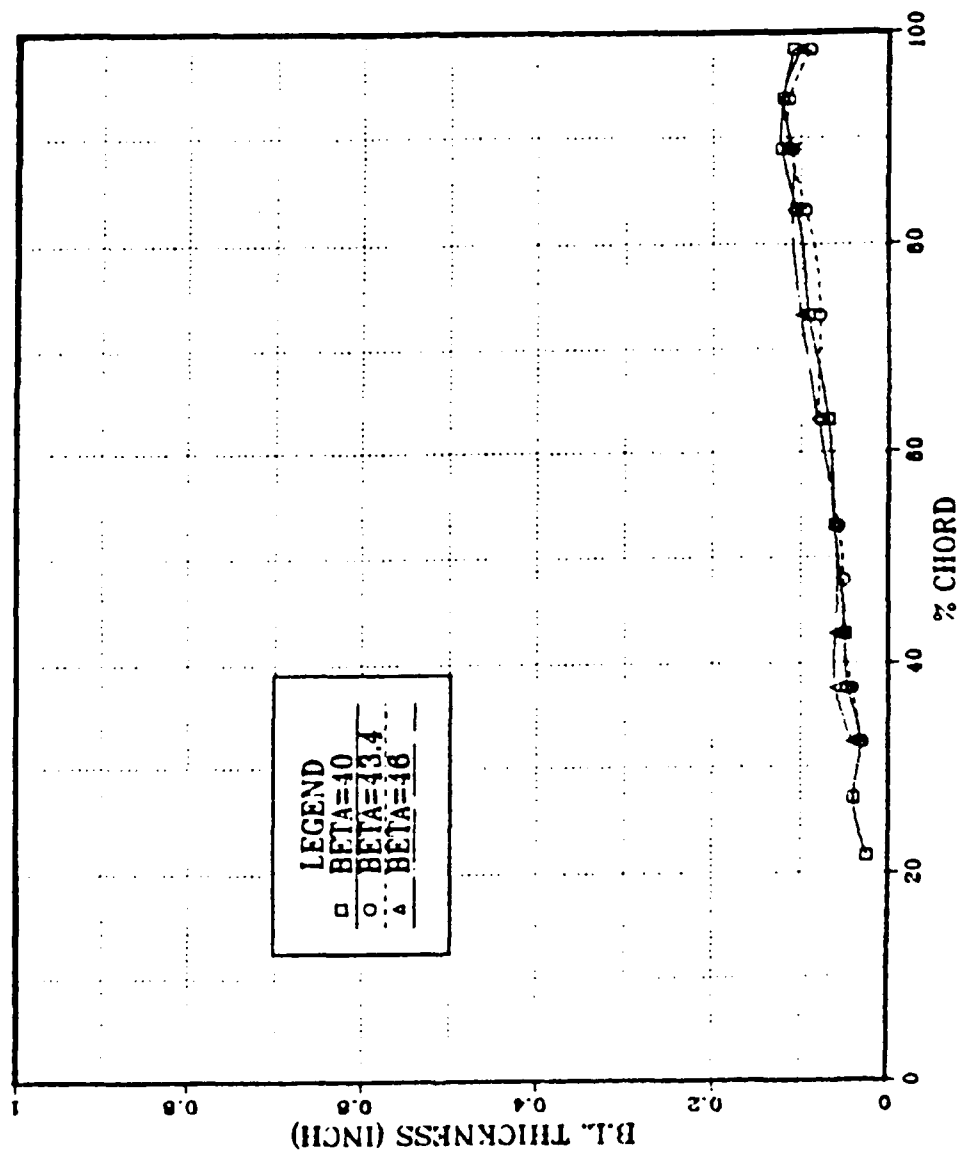


Figure 50. Boundary Layer Thickness on the Pressure Surface.

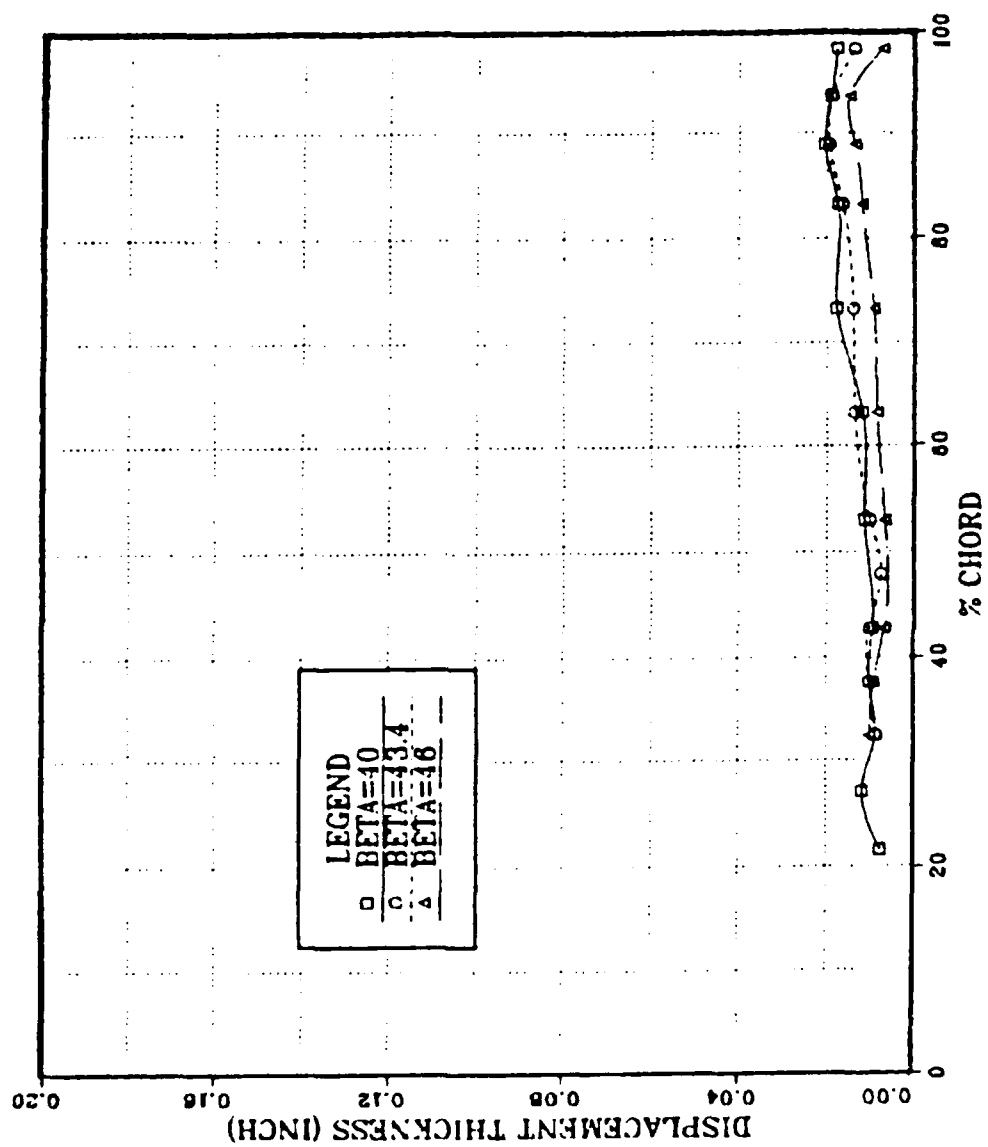


Figure 51. Displacement Thickness on the Pressure Surface.

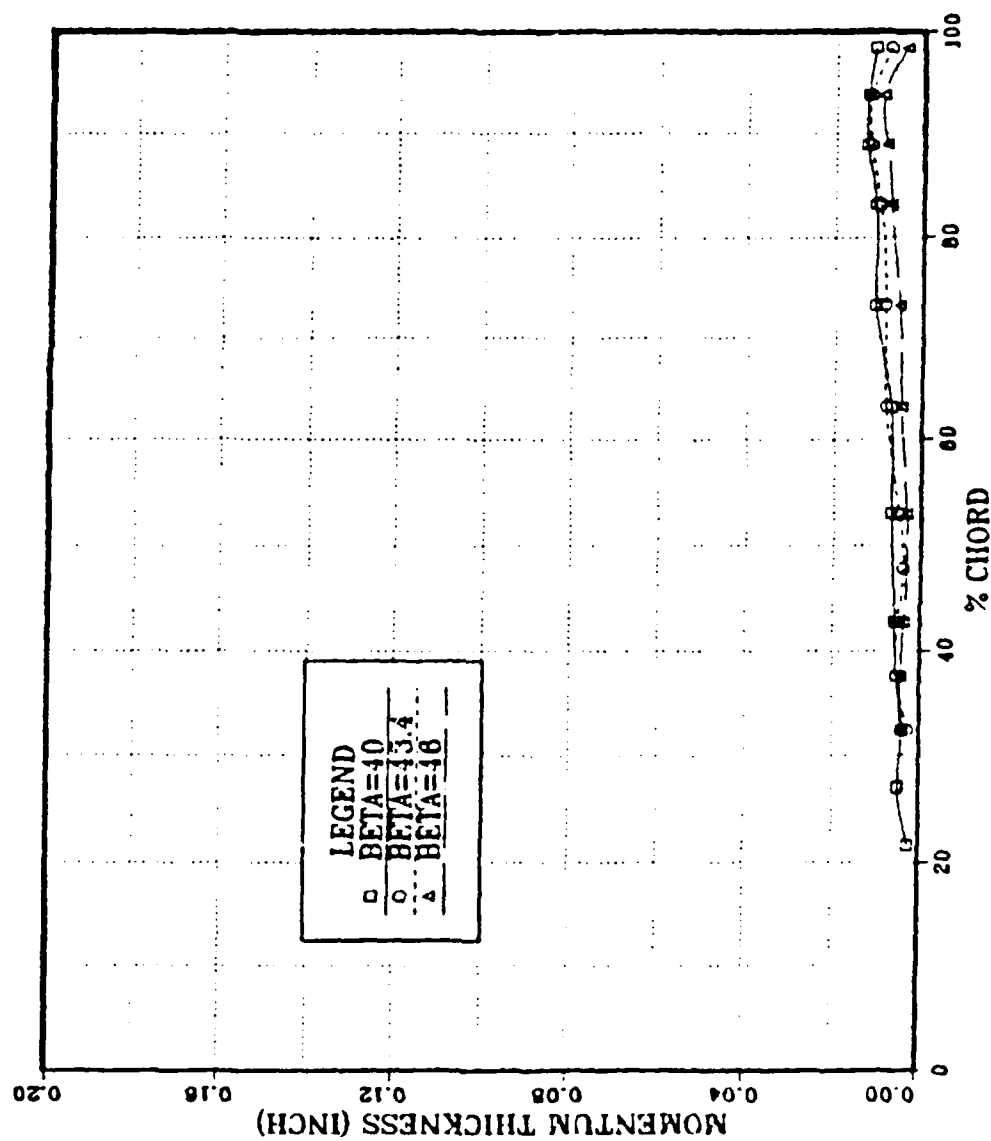


Figure 52. Momentum Thickness on the Pressure Surface.

inlet angle to the other, and the higher the inlet angle the lower was the edge velocity. (See Section B.1.)

- b. A typical transitional boundary layer on a flat plate is characterized by a progressive reduction of the displacement thickness until the boundary layer has become turbulent (Ref. 49). This trend is seen in Figure 51 at the two highest inlet angles (43.4° , 46°), and the minimum is seen to occur at about 50% chord. At the design angle (40°), the displacement thickness grew steadily from about 30% chord.
- c. The momentum thickness, although smaller in magnitude, behaved very similarly to the displacement thickness.
- d. All thicknesses decreased slightly over the aft 5% of chord. This was the result of the local acceleration of the outer flow over the pressure surface near the trailing edge, which is clearly seen in Figure 27.

The shape factor distribution is shown plotted in Figure 53. Three regions are clearly evident at each inlet angle. The forward region, where the shape factor decreases sharply, is indicative of a transitional boundary layer. The central region, with a nearly flat distribution at $H = 1.7 - 1.8$, is typical of an attached turbulent boundary layer. The aft region where the shape factor is seen to increase

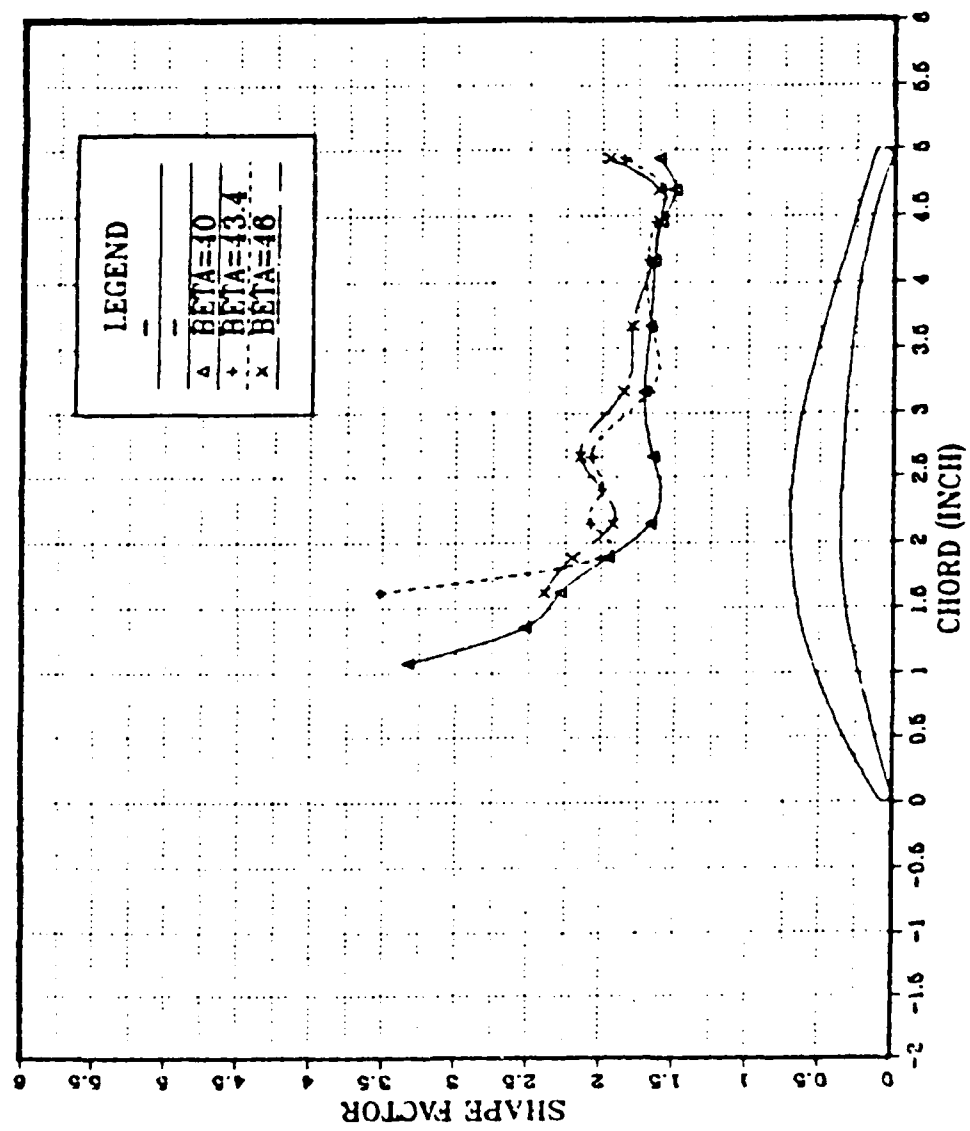


Figure 53. Shape Factor Distribution on the Pressure Surface.

quite suddenly indicates that the flow is about to separate over the trailing edge curvature.

Data for the calculated thicknesses and the uncertainties resulting from the positioning of the probe volume at the pressure surface, are summarized in Tables 9-11. A further uncertainty is caused by the need to interpolate in the integration between the measurements and zero velocity at the surface. A larger fraction of the layer is involved in the interpolation when the layer is thin, as is the case on the pressure side.

The onset of transition also could not be resolved in the pressure side measurements since the laminar boundary layers were simply too thin to be measured properly by the LDV system. The edge of the transitional zone, however, could be roughly estimated after an examination of the turbulence intensities. The boundary layer turbulence level distributions are shown plotted in Figures 54-56. As was the case on the suction surface, high instability was evident in the transitional boundary layer region covering at least 30% of the chord ($\epsilon = 10\%-12\%$). For the design angle ($\beta_1 = 40^\circ$) the boundary layer was fully turbulent at 40%-50% chord. For the higher angles ($\beta_1 = 43.4^\circ, 46^\circ$) the boundary layer was fully turbulent at 60% chord. Full transition at the higher angles

TABLE 9

PRESSURE SURFACE BOUNDARY LAYER PARAMETERS, $\beta_1 = 40^\circ$

y	u_1/U_∞	δ^*	$\Delta\delta^*$	θ	$\Delta\theta$	H	ΔH
0.0	0.4	0.0177	0.0016	0.011	0.00029	1.613	0.19
-0.25	0.616	0.01912	0.0014	0.0127	0.00036	1.507	0.15
-0.5	0.622	0.0204	0.0014	0.0128	0.00036	1.599	0.15
-0.792	0.602	0.0174	0.0014	0.0106	0.00036	1.644	0.19
-1.292	0.471	0.0177	0.0015	0.0106	0.00032	1.677	0.19
-1.792	0.652	0.0116	0.0013	0.0068	0.00037	1.711	0.28
-2.292	0.524	0.0112	0.0015	0.0067	0.00034	1.652	0.3
-2.792	0.298	0.0093	0.0017	0.0056	0.00024	1.665	0.37
-3.042	0.671	0.01	0.0013	0.0051	0.00037	1.957	0.4
-3.292	0.542	0.0087	0.0015	0.0038	0.00035	2.288	0.60
-3.542	0.458	0.0116	0.0015	0.0046	0.00032	2.528	0.50
-3.792	0.698	0.0074	0.0013	0.0022	0.00037	3.326	0.14

TABLE 10
PRESSURE SURFACE BOUNDARY LAYER PARAMETERS, $\beta_1 = 43.4^\circ$

y	u_1/U_∞	δ^*	$\Delta\delta^*$	θ	$\Delta\theta$	H	ΔH
0.0	0.759	0.0136	0.0012	0.0073	0.00037	1.85	0.26
-0.25	0.58	0.0188	0.0014	0.0119	0.00035	1.577	0.16
-0.5	0.604	0.0194	0.0014	0.0119	0.00036	1.638	0.17
-0.792	0.648	0.0163	0.0013	0.0096	0.00037	1.693	0.20
-1.292	0.617	0.0138	0.0014	0.0083	0.00036	1.666	0.24
-1.792	0.605	0.0134	0.0014	0.0080	0.00036	1.676	0.25
-2.292	0.746	0.0098	0.0012	0.0047	0.00037	2.071	0.42
-2.542	0.742	0.0073	0.0012	0.0037	0.00037	1.997	0.53
-2.792	0.73	0.0101	0.0012	0.0049	0.00037	2.078	0.4
-3.042	0.611	0.0101	0.0014	0.005	0.00036	2.003	0.42
-3.292	0.71	0.0085	0.0013	0.0024	0.00037	3.521	1.08

TABLE 11
PRESSURE SURFACE BOUNDARY LAYER PARAMETERS, $\beta_1 = 46^\circ$

y	u_1/U_∞	δ^*	$\Delta\delta^*$	θ	$\Delta\theta$	H	ΔH
0.0	0.844	0.0069	0.0012	0.0036	0.00037	1.951	0.54
-0.25	0.701	0.0148	0.0013	0.0091	0.00037	1.617	0.21
-0.5	0.646	0.0134	0.0013	0.0083	0.00037	1.615	0.23
-0.792	0.662	0.0117	0.0013	0.0071	0.00037	1.662	0.27
-1.292	0.725	0.0090	0.0013	0.0050	0.00037	1.799	0.39
-1.792	0.758	0.0082	0.0012	0.0044	0.00037	1.853	0.43
-2.292	0.816	0.0064	0.0012	0.0030	0.00037	2.152	0.67
-2.792	0.773	0.0065	0.0012	0.0034	0.00037	1.925	0.56
-3.042	0.558	0.009	0.0014	0.0041	0.00035	2.204	0.53
-3.292	0.391	0.01	0.0016	0.0042	0.00029	2.396	0.55

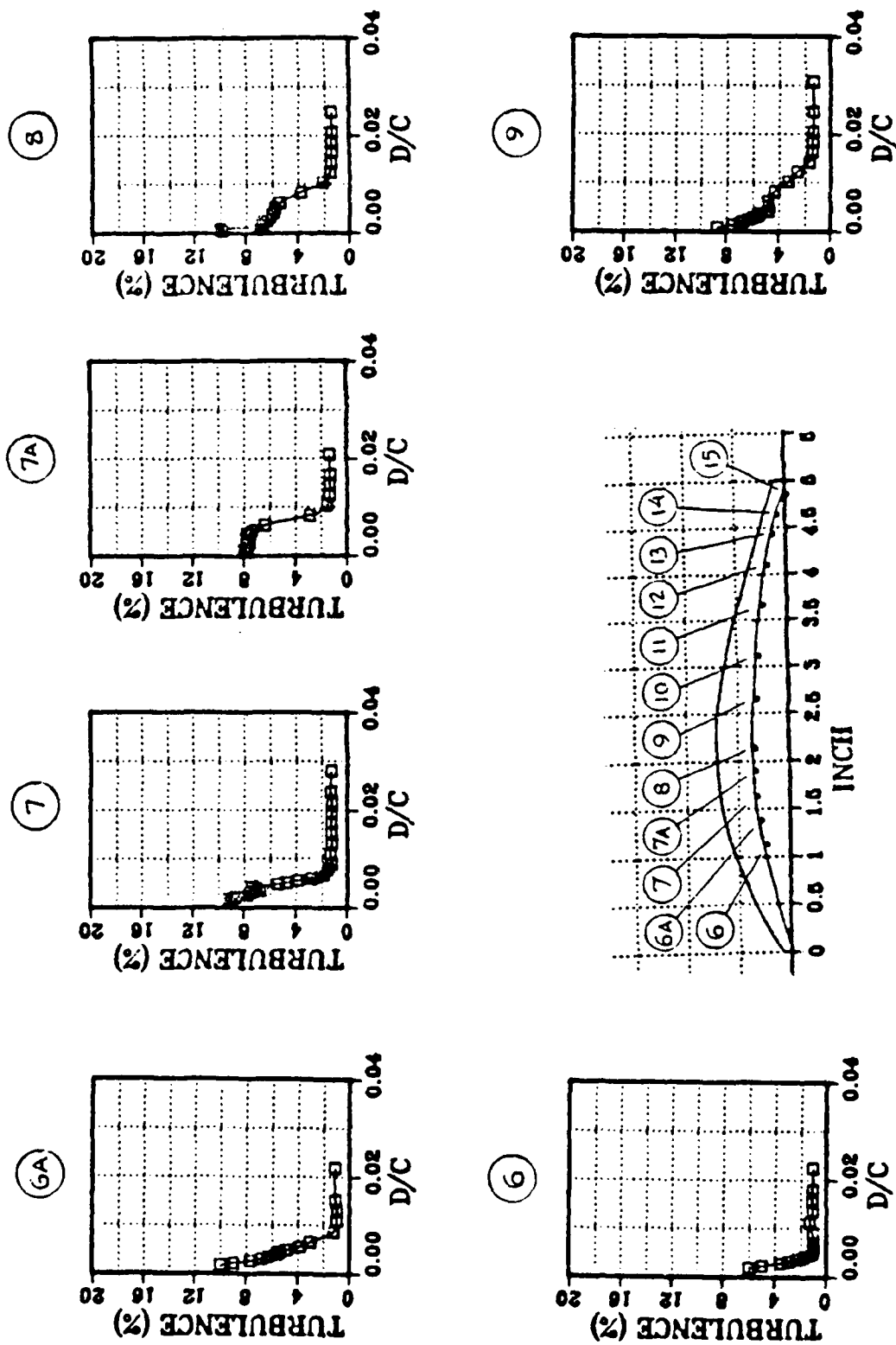


Figure 54. Boundary Layer Turbulence Level Distribution ;
 $\beta_1 = 40^\circ$, $Re = 710000$.

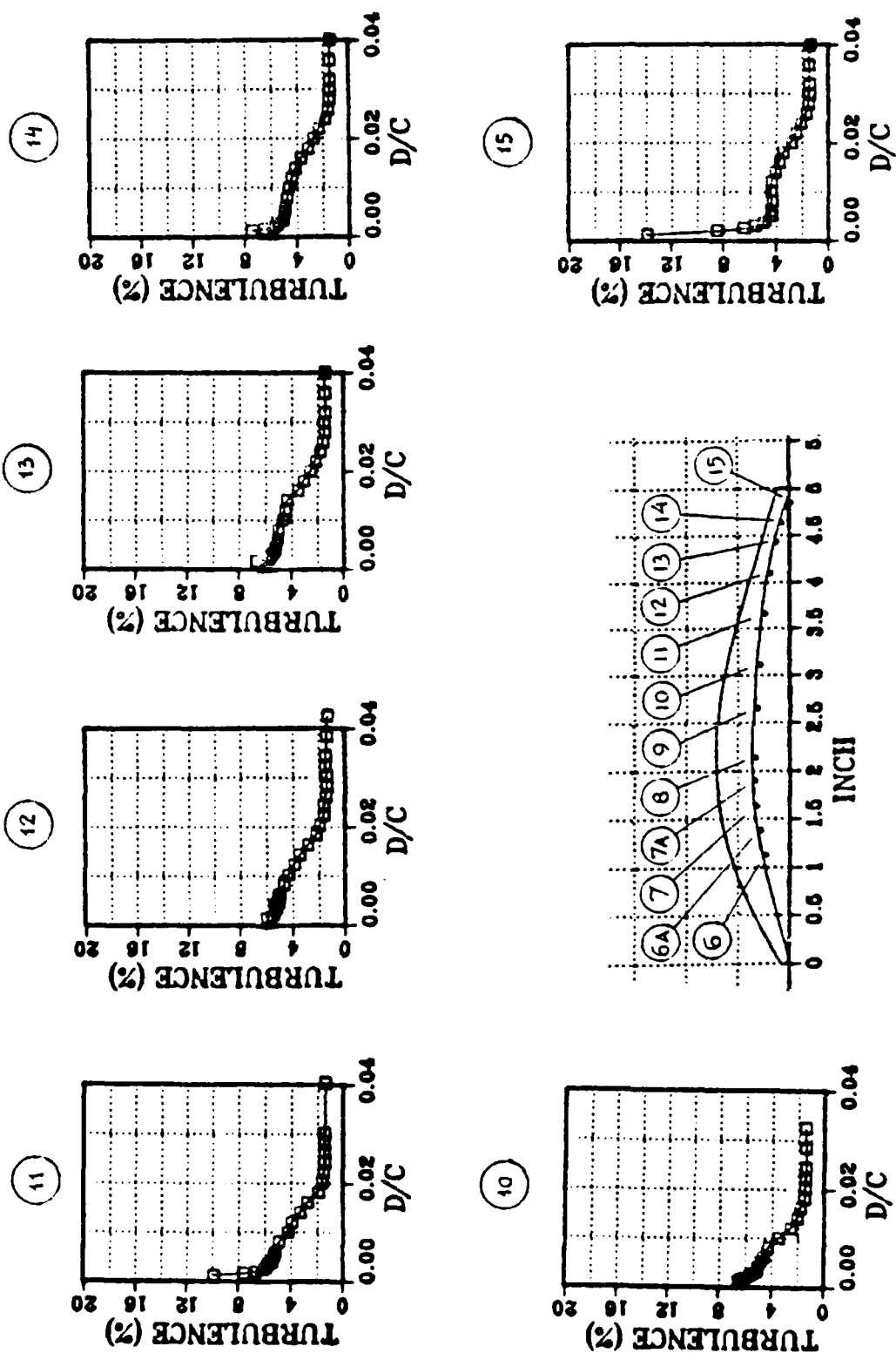


Figure 54. (cont.) Boundary Layer Turbulence Level Distribution ; $\beta_1 = 40^\circ$, $Re = 710000$.

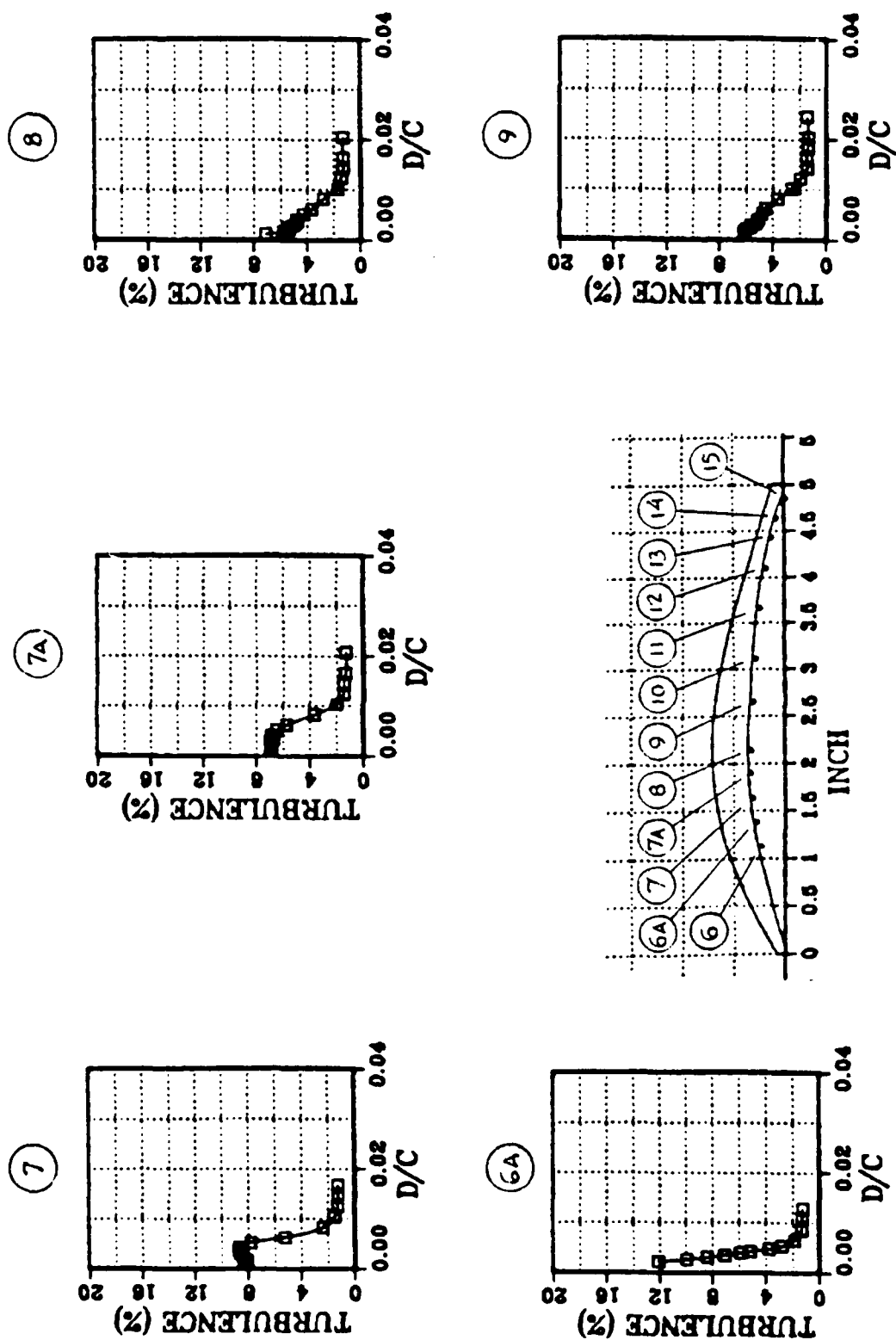


Figure 55. Boundary Layer Turbulence Level Distribution ;
 $\beta_1 = 43.4^\circ$, $Re = 740000$.

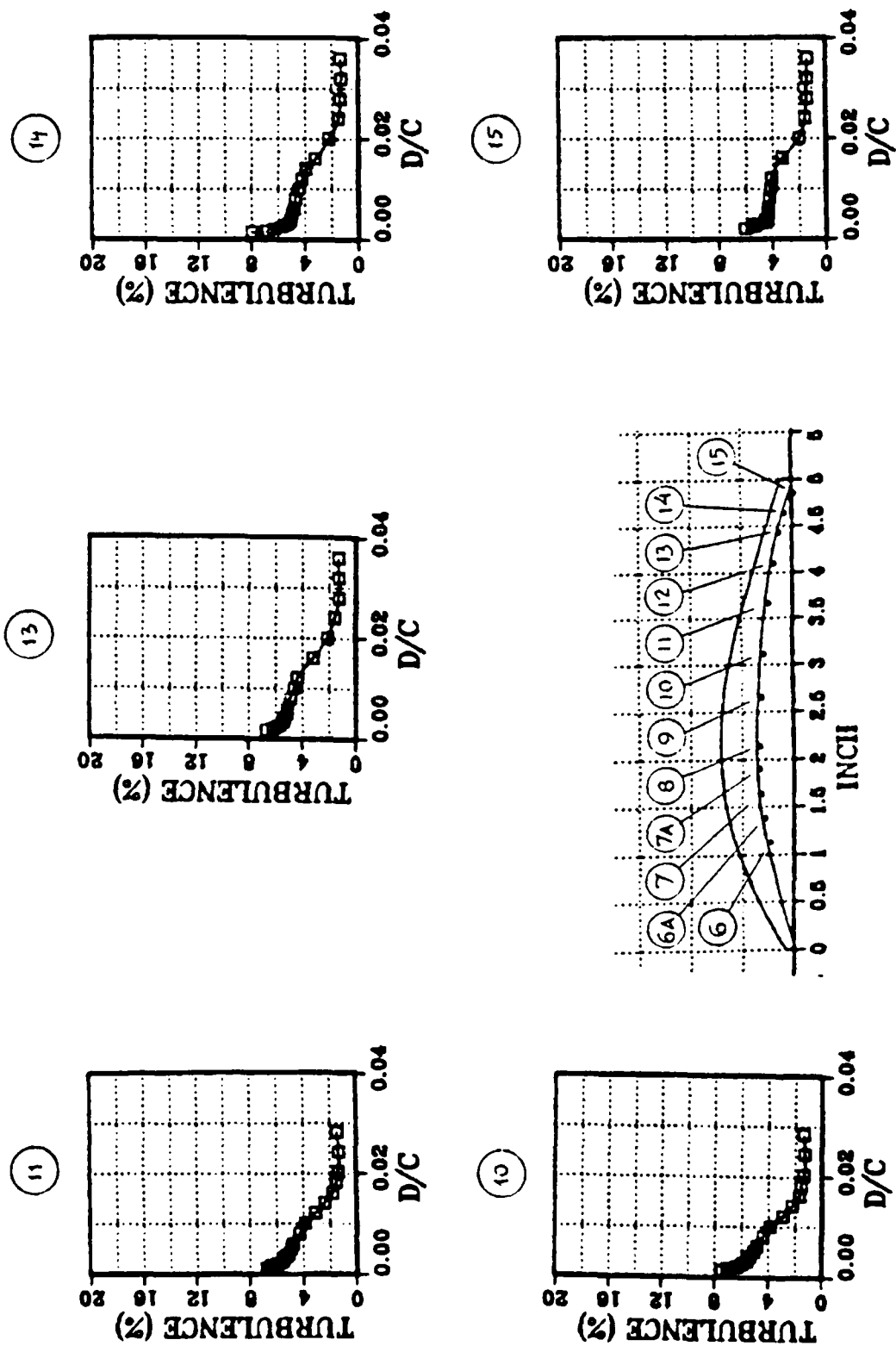


Figure 55. (cont.) Boundary Layer Turbulence Level Distribution ;
 $\beta_1 = 43.4^\circ$, $Re = 740000$.

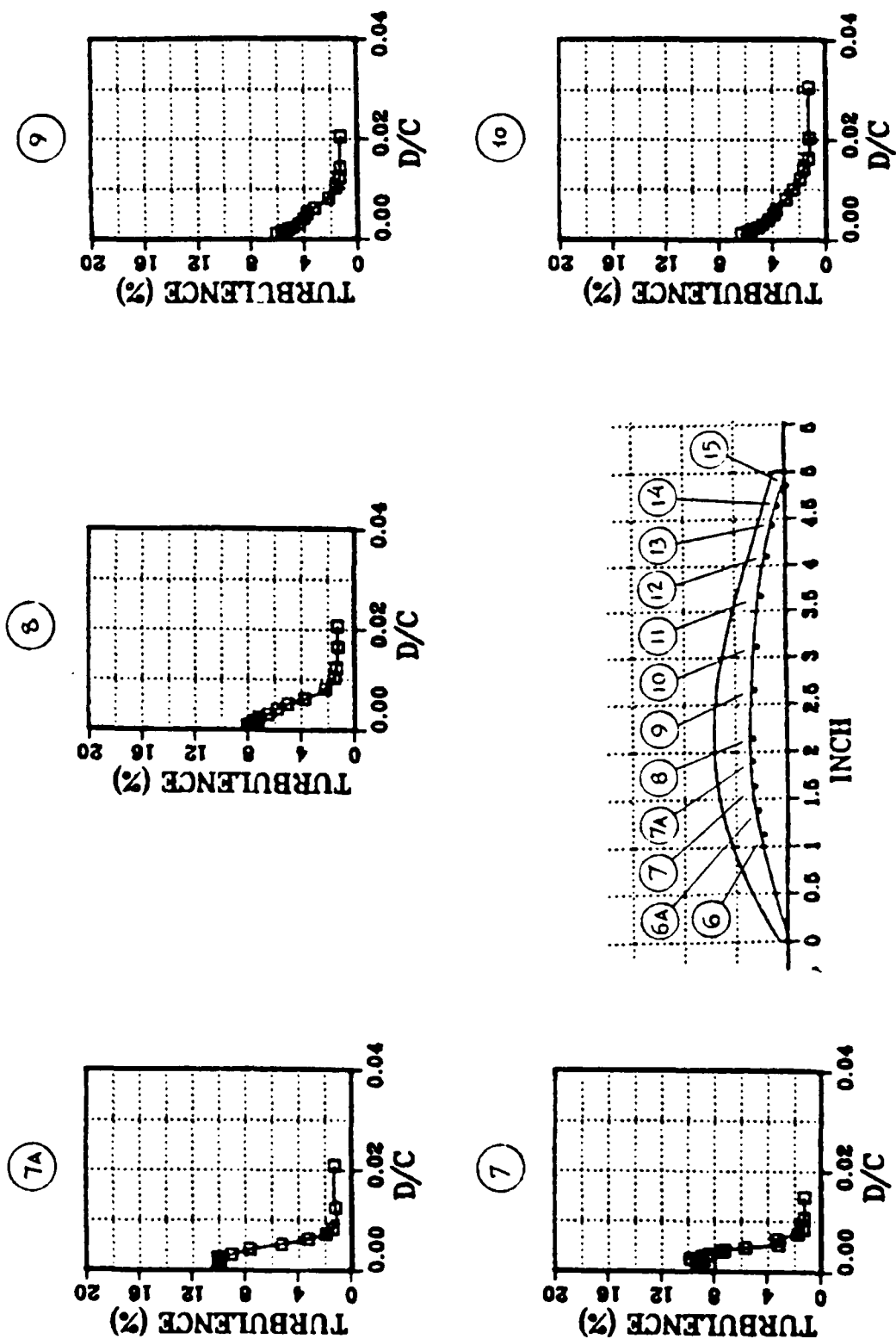


Figure 56. Boundary Layer Turbulence Level Distribution ;
 $\beta_1 = 46^\circ$, $Re = 730000$.

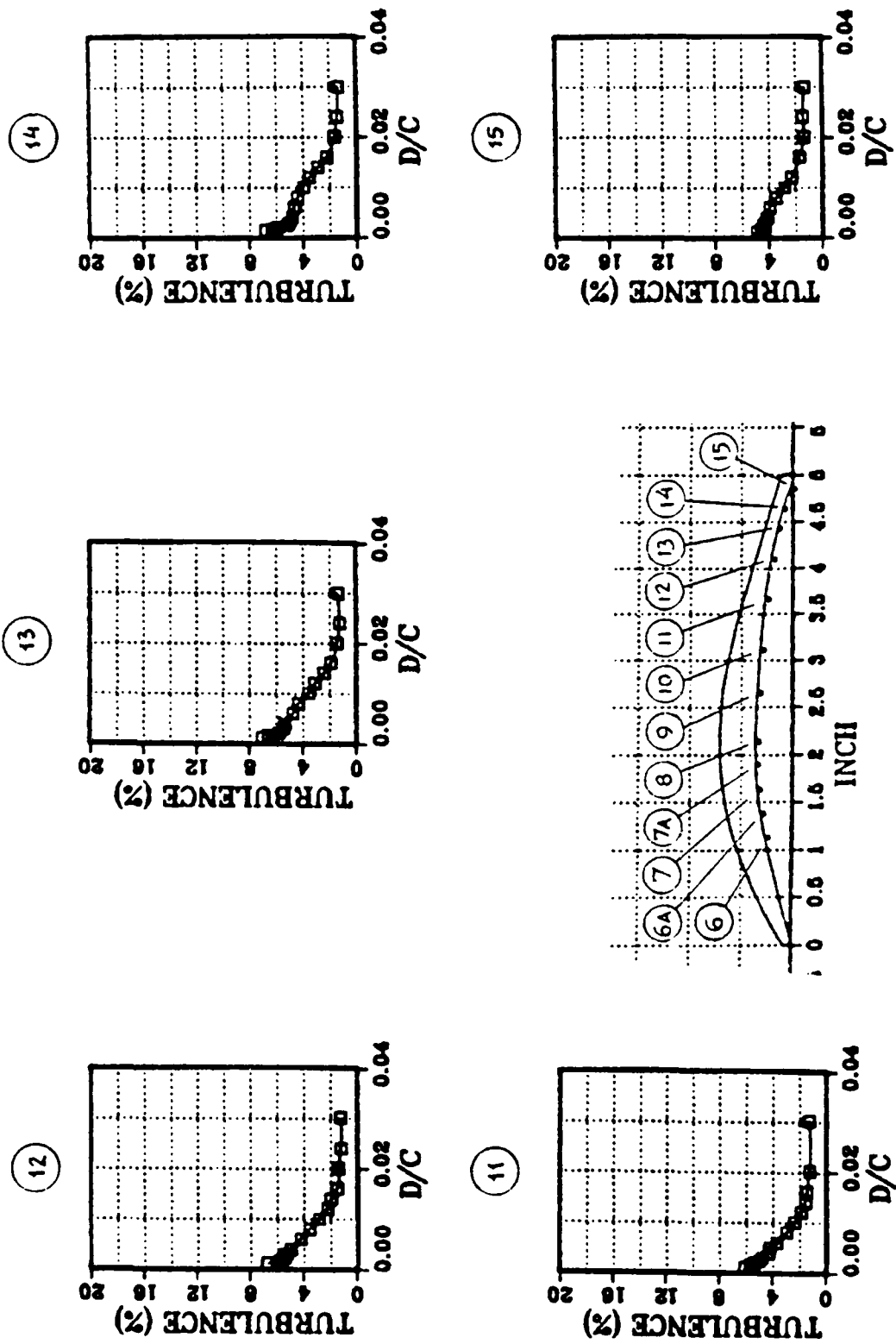


Figure 56. (cont.) Boundary Layer Turbulence Level Distribution ;
 $\beta_1 = 46^\circ$, $Re = 730000$.

was delayed due to the fact that the edge velocity over the pressure side of the airfoil was lower than at the design angle.

The fully turbulent boundary layer (beyond 70% chord) had a lower peak turbulence level ($\epsilon = 6\%$). The distribution of the turbulence level in the fully turbulent boundary layer on the pressure side was different than that on the suction surface since the peak in the turbulence level occurred closer to the wall.

D. WAKE MEASUREMENTS

1. Time Averaged Velocity

Wake velocity distributions are shown plotted in Figures 57-59. The following observations are made with reference to the Figures:

- a. The variation of the minimum of the vertical component of the velocity (which is in the direction of the intended downstream flow at the design condition) as a function of the distance from the trailing edge, is seen to be typical of wake decay. At design condition ($\beta_1 = 40^\circ$), for $y = 0.262"$ the minimum velocity was negative, i.e., the flow was reversed due to separation and recirculation in the base of the trailing edge curvature. For $y = 0.362"$ the average minimum velocity was positive, but small. For $y = 0.678"$ the minimum velocity was about 28% and for $y = 1.062"$ about 40% of the inlet reference velocity.

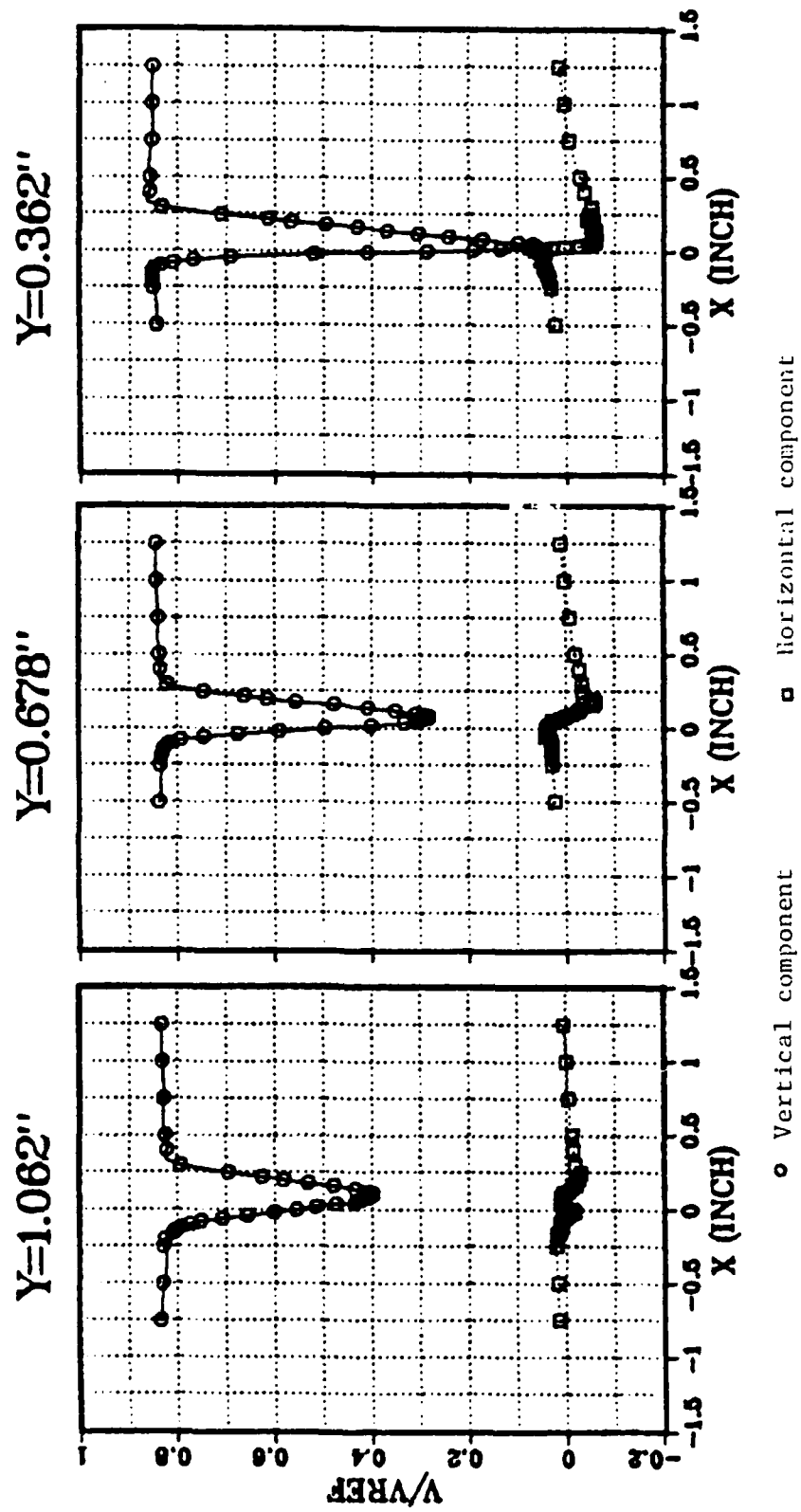


Figure 57. Wake Velocity Distributions for Four Downstream Positions;
 $\beta_1 = 40^\circ$, $Re = 710000$.

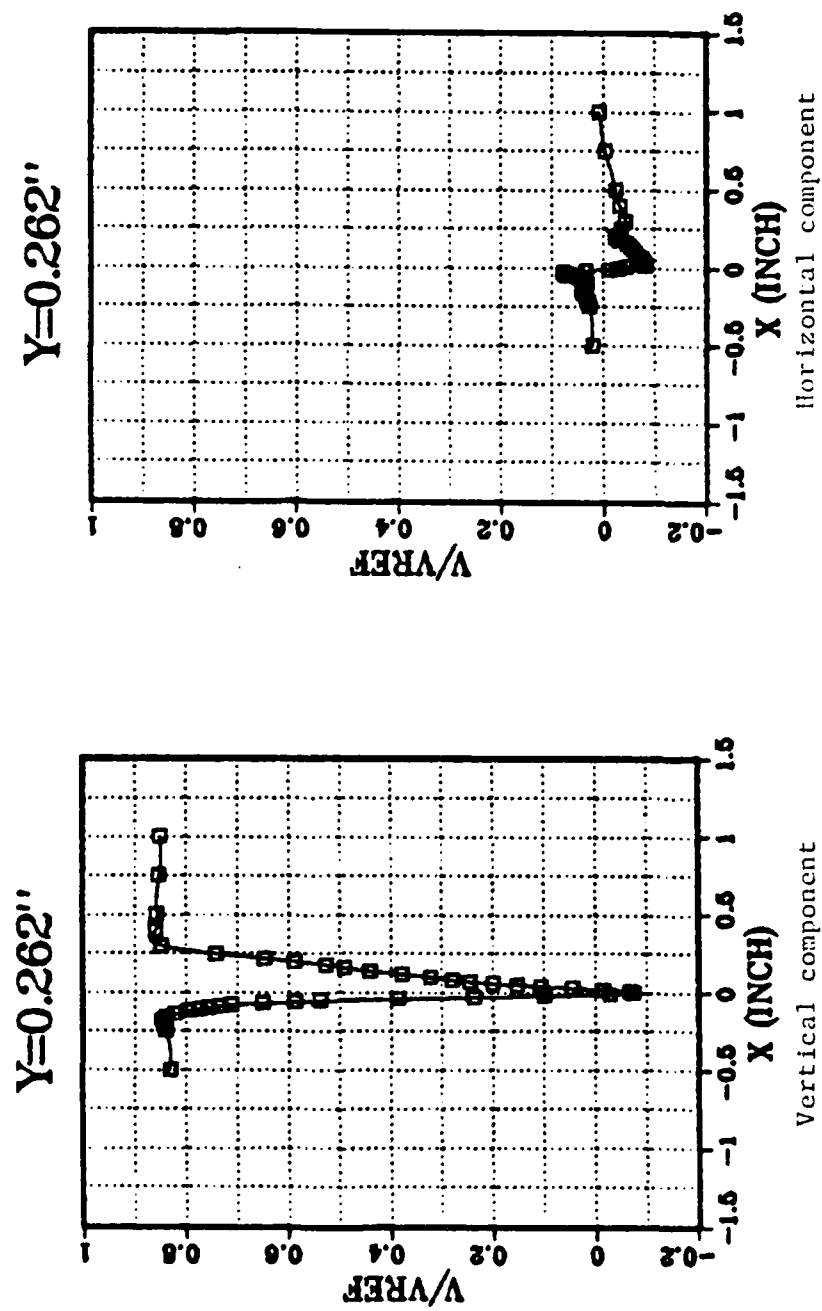


Figure 57. (cont.) Wake Velocity Distributions for Four Downstream Positions; $\beta_1 = 40^\circ$, $Re = 710000$.

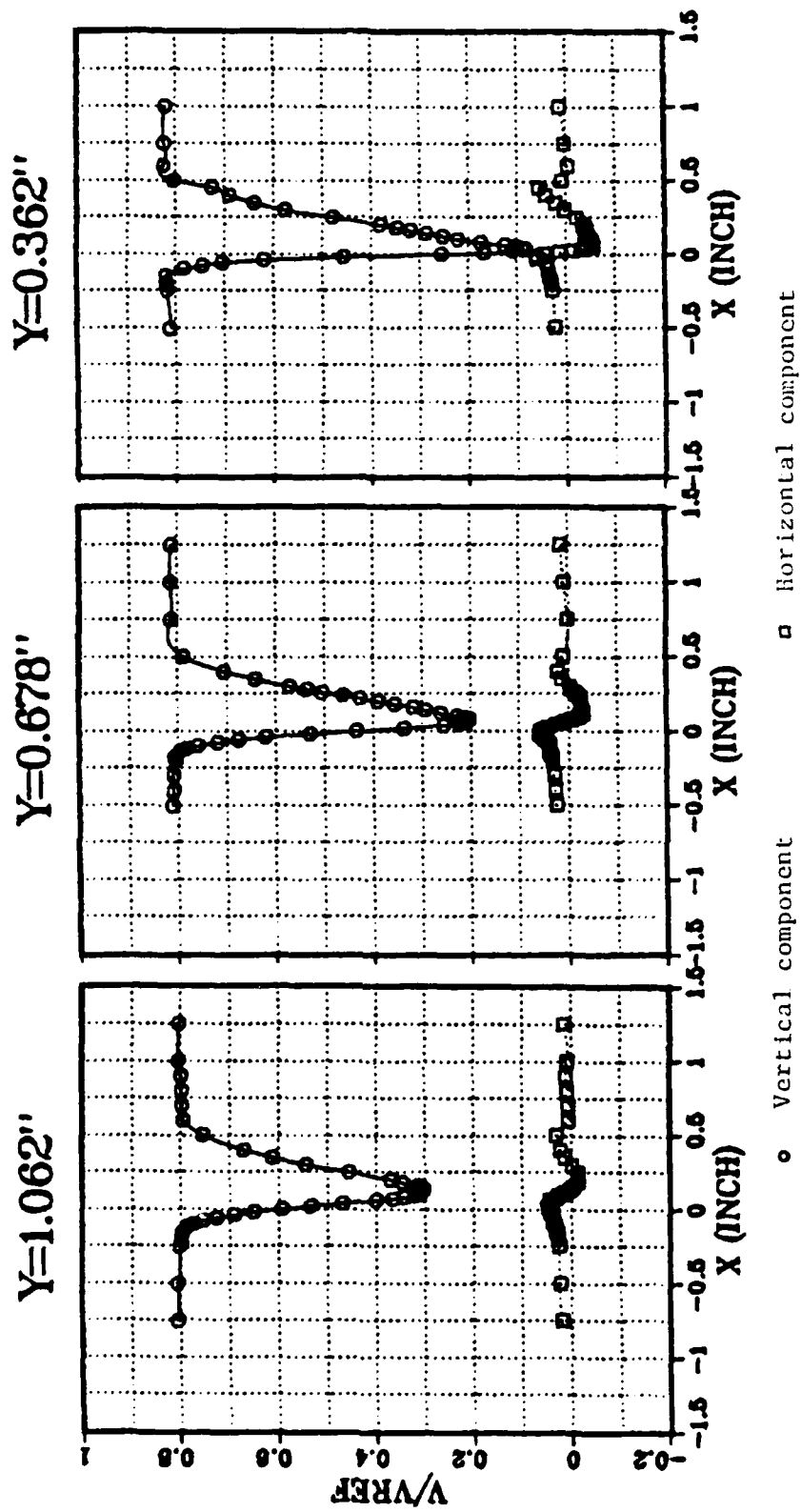


Figure 58. Wake Velocity Distributions for Four Downstream Positions;
 $\beta_1 = 43.4^\circ$, $Re = 740000$.

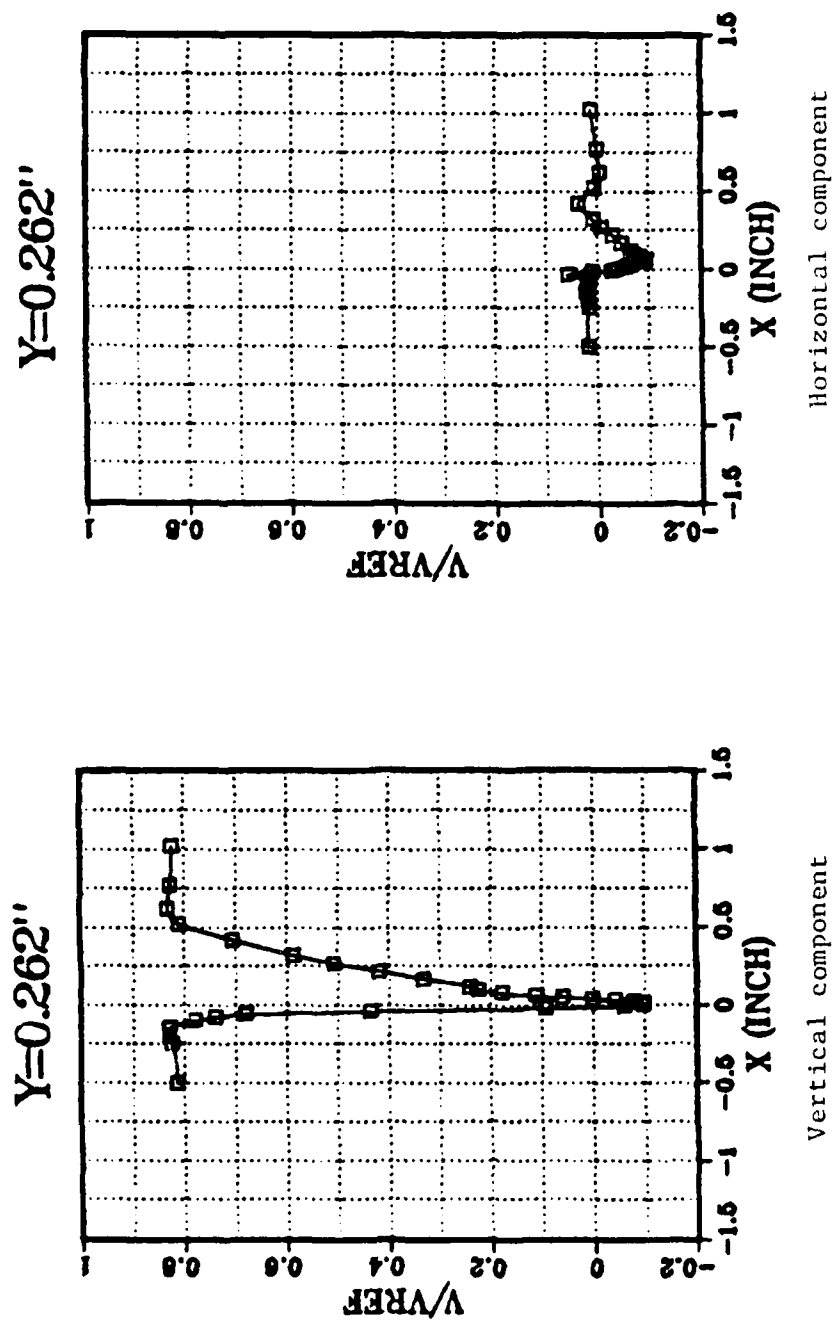


Figure 58. (cont.) Wake Velocity Distributions for Four Downstream Positions; $\beta_1 = 43.4^\circ$, $Re = 740000$.

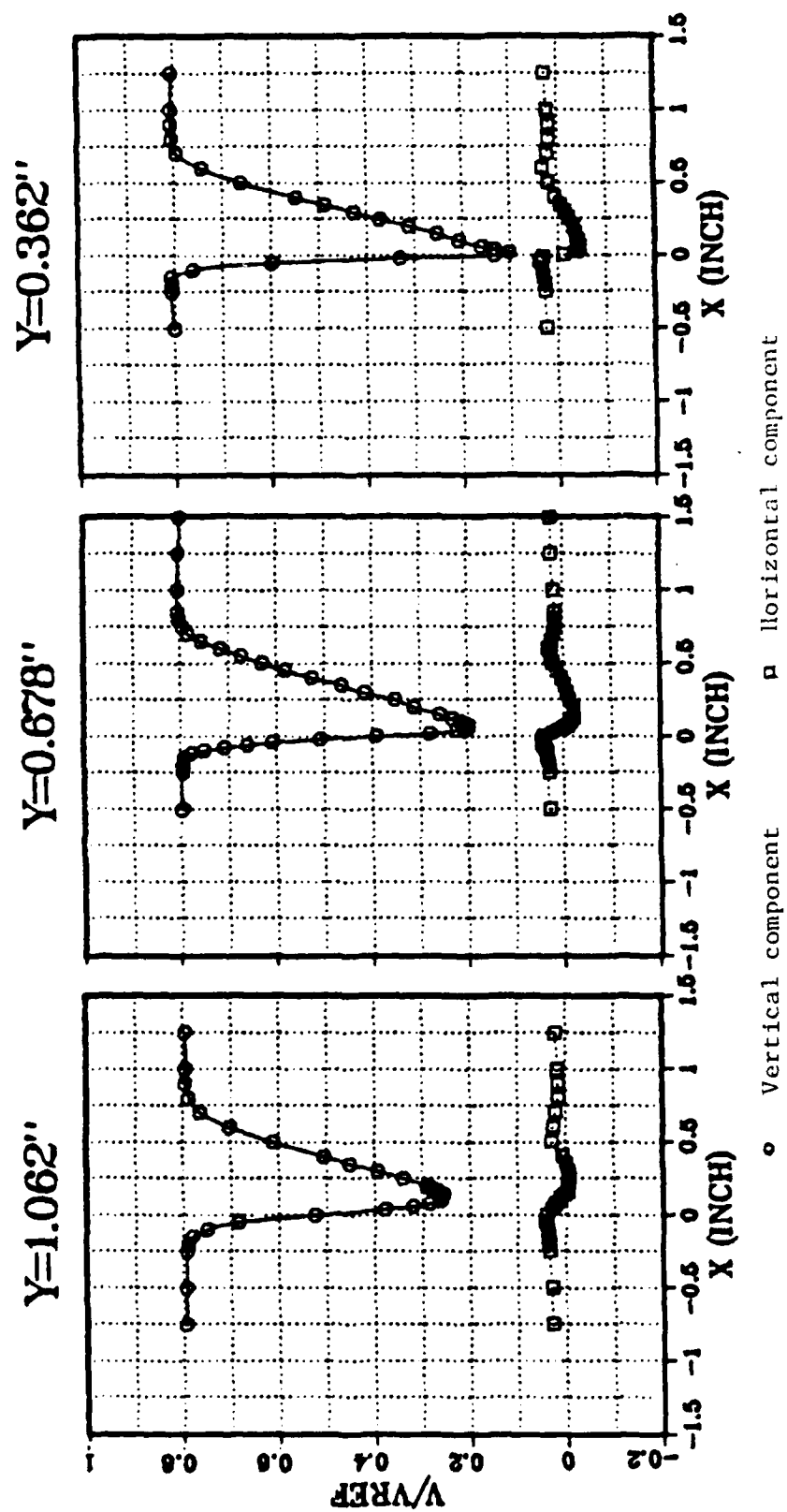


Figure 59. Wake Velocity Distributions for Four Downstream Positions;
 $\beta_1 = 46^\circ$, $Re = 730000$.

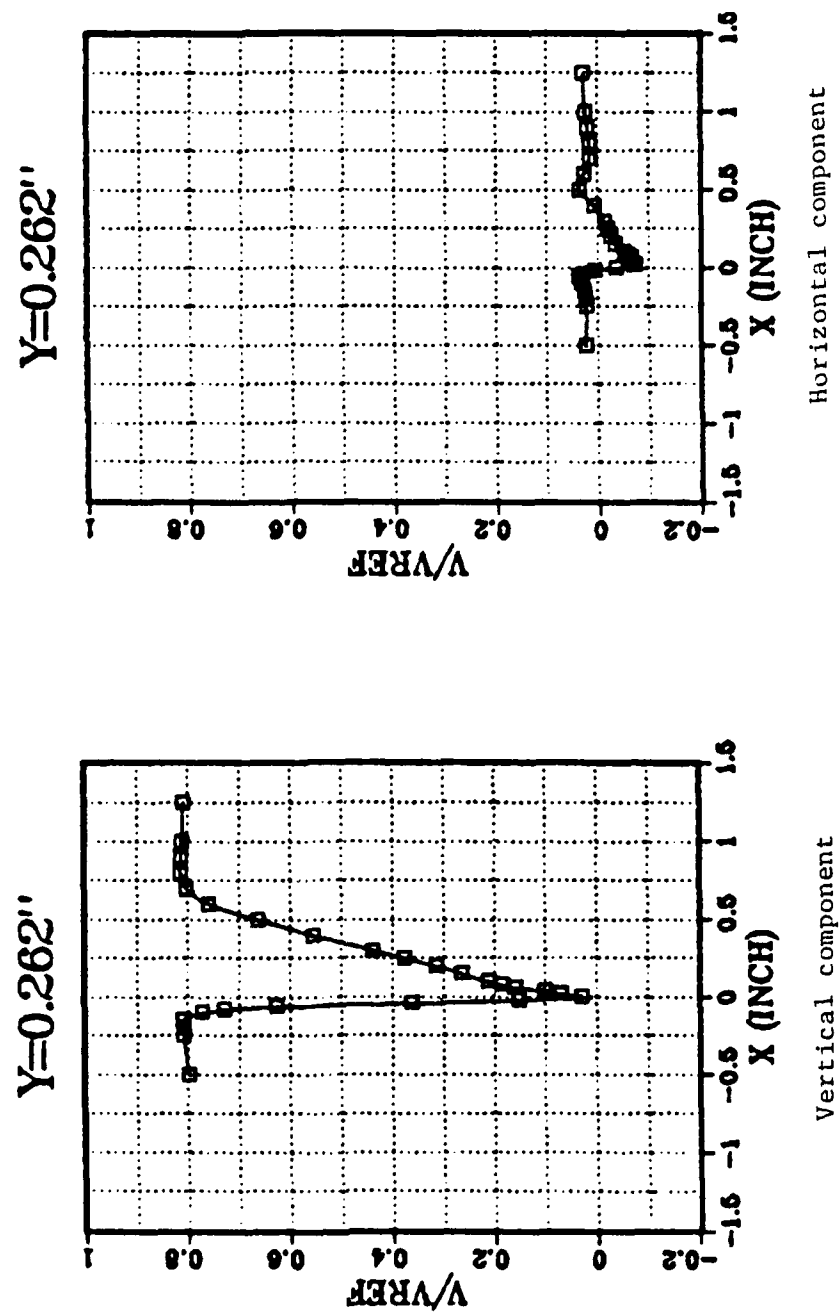


Figure 59. (cont.) Wake Velocity Distributions for Four Downstream Positions; $\beta_1 = 46^\circ$, $Re = 730000$.

At the higher inlet angle ($\beta_1 = 43.4^\circ$) the same trends were seen but the magnitude of the minima were lower. At the highest inlet angle ($\beta_1 = 46^\circ$) the results were somewhat different. At $y = 1.062$ " the minimum was again lower than at $\beta_1 = 43.4^\circ$ and for $y = 0.678$ " the minimum was the same. But the near wakes at $\beta_1 = 46^\circ$ showed higher minimum velocities than at the lower inlet angles. Although, some data samples showed negative velocities in the near wake at $\beta_1 = 46^\circ$ the time averaged mean velocity was everywhere positive.

- b. At design inlet angle ($\beta_1 = 40^\circ$) the wake profile was almost symmetric. The suction surface side of the wake was slightly thicker than the pressure side. At higher inlet angle ($\beta_1 = 43.4^\circ$) the wakes were clearly not symmetric, the suction side being much thicker than the pressure side. At the highest inlet angle, the wake profile had pronounced asymmetry.
- c. The distribution of the horizontal component of the the velocity through the wake is seen to follow a wave shape. Traversing from the pressure side towards the center of the wake resulted in a gradual increase of the horizontal velocity component until a maximum was reached. From there, there was a sharp decrease to negative values, passing through the center of the wake. Traversing further, the horizontal velocity

component gradually increased to small positive values. This wave shape was found through all measured wakes except at the design angle in the most far wake where the profile was somewhat smeared.

A comparison of the wakes at $y = 0.678"$ at three inlet angles is shown in Figure 60. The decrease of the minimum of the vertical component as the inlet angle increased is clearly evident. The pressure surface side of the wake is seen to have changed only slightly with inlet angle. In contrast, the suction surface side of the wake is seen to have thickened significantly as the inlet angle was increased.

The corresponding distributions at $y = 0.678"$ of the flow angle, derived from the two components of velocity, are shown in Figure 61. The flow angle exhibits the same qualitative behavior as the horizontal component of the velocity. The pressure surface side of the wake did not change significantly with inlet angle, whereas the suction surface side was changed significantly.

2. Turbulence

Distributions of the turbulence level measured in the wakes are shown plotted in Figures 62-64. The following observations are made with reference to the Figures.

- a. The pressure surface side of the wake was characterized by higher levels of turbulence. The peak

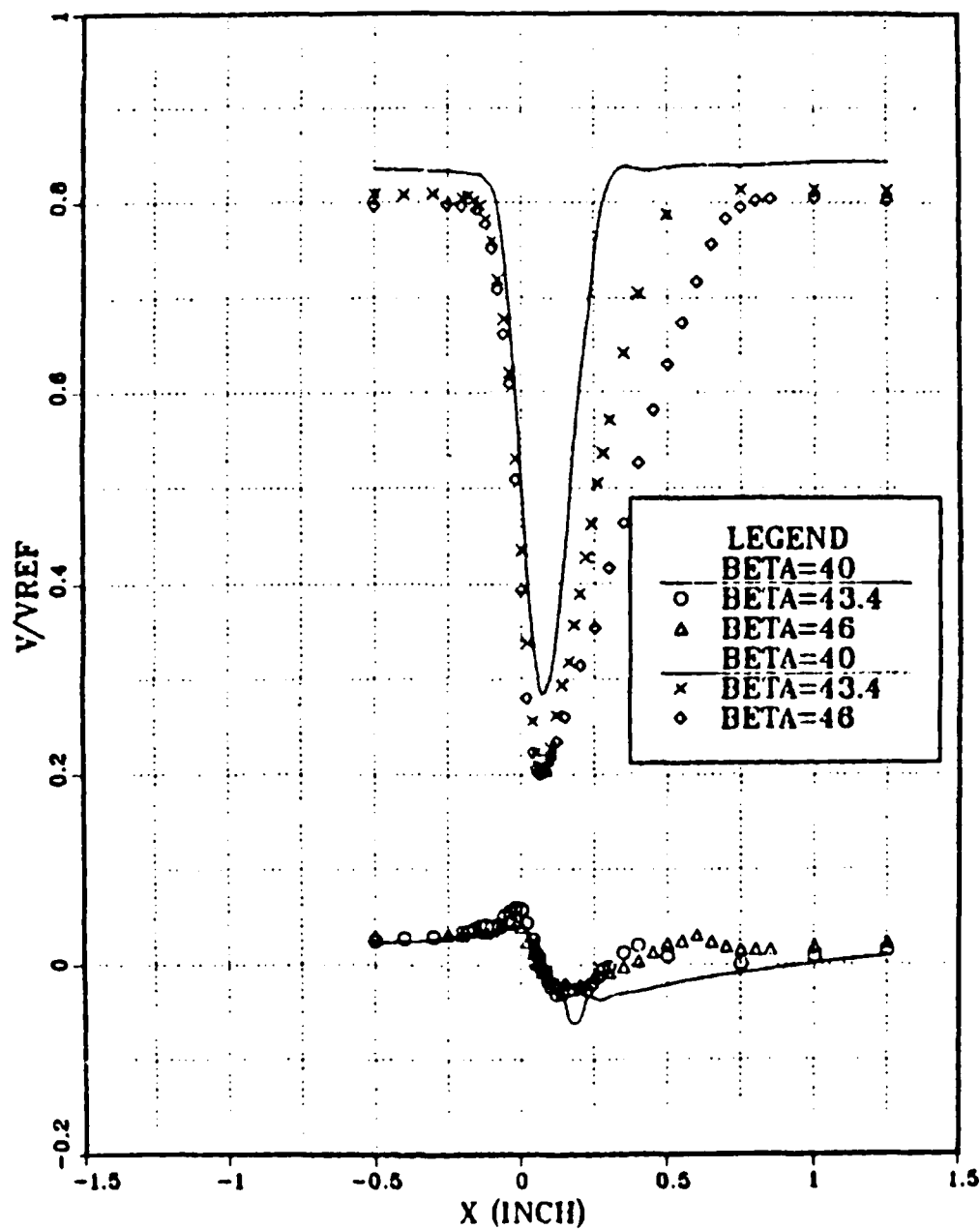


Figure 60. Velocity Distributions at $y = 0.678''$
(0.123c from Trailing Edge).

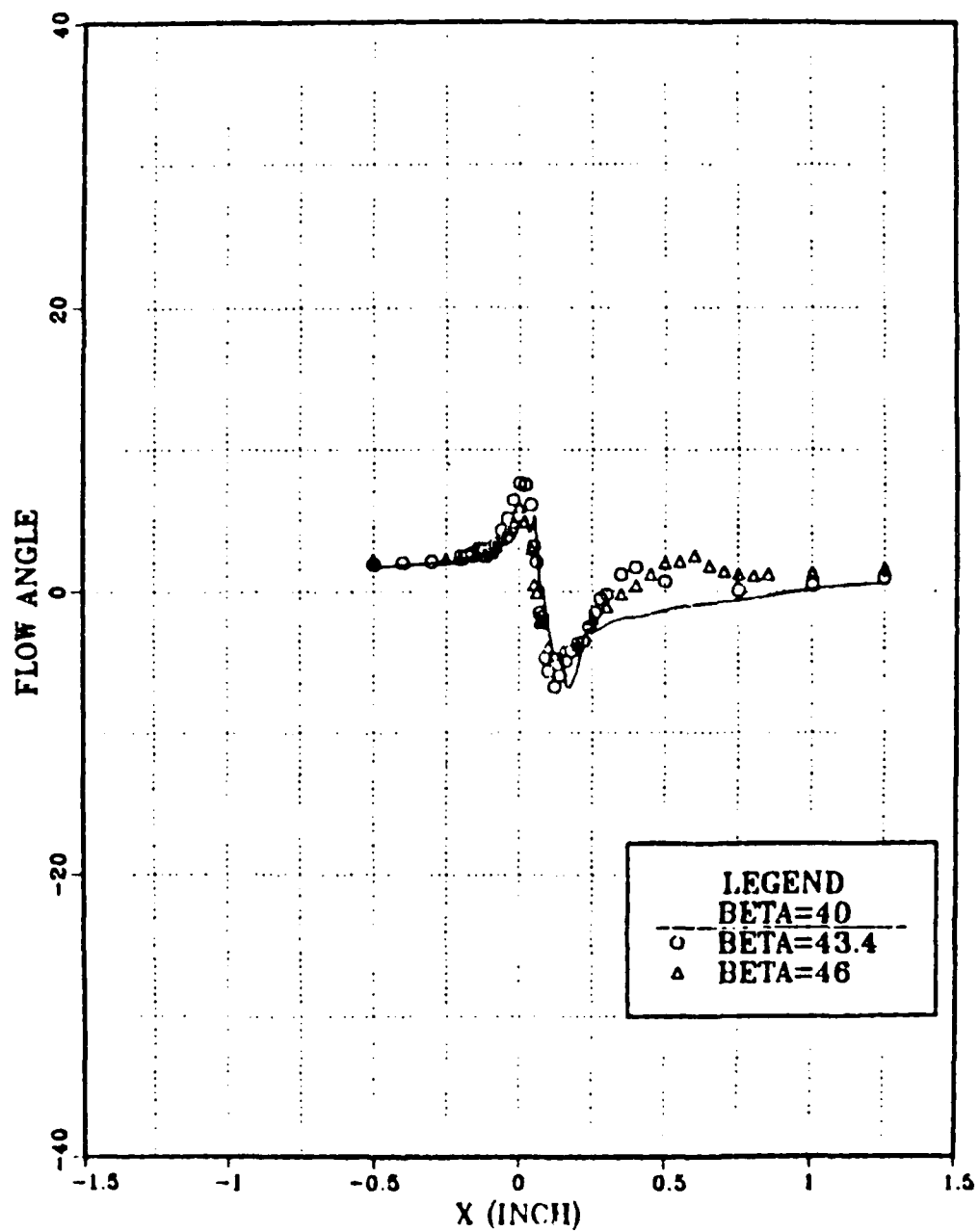


Figure 61. Flow Angle Distributions at $y = 0.678''$ ($0.123c$ from Trailing Edge).

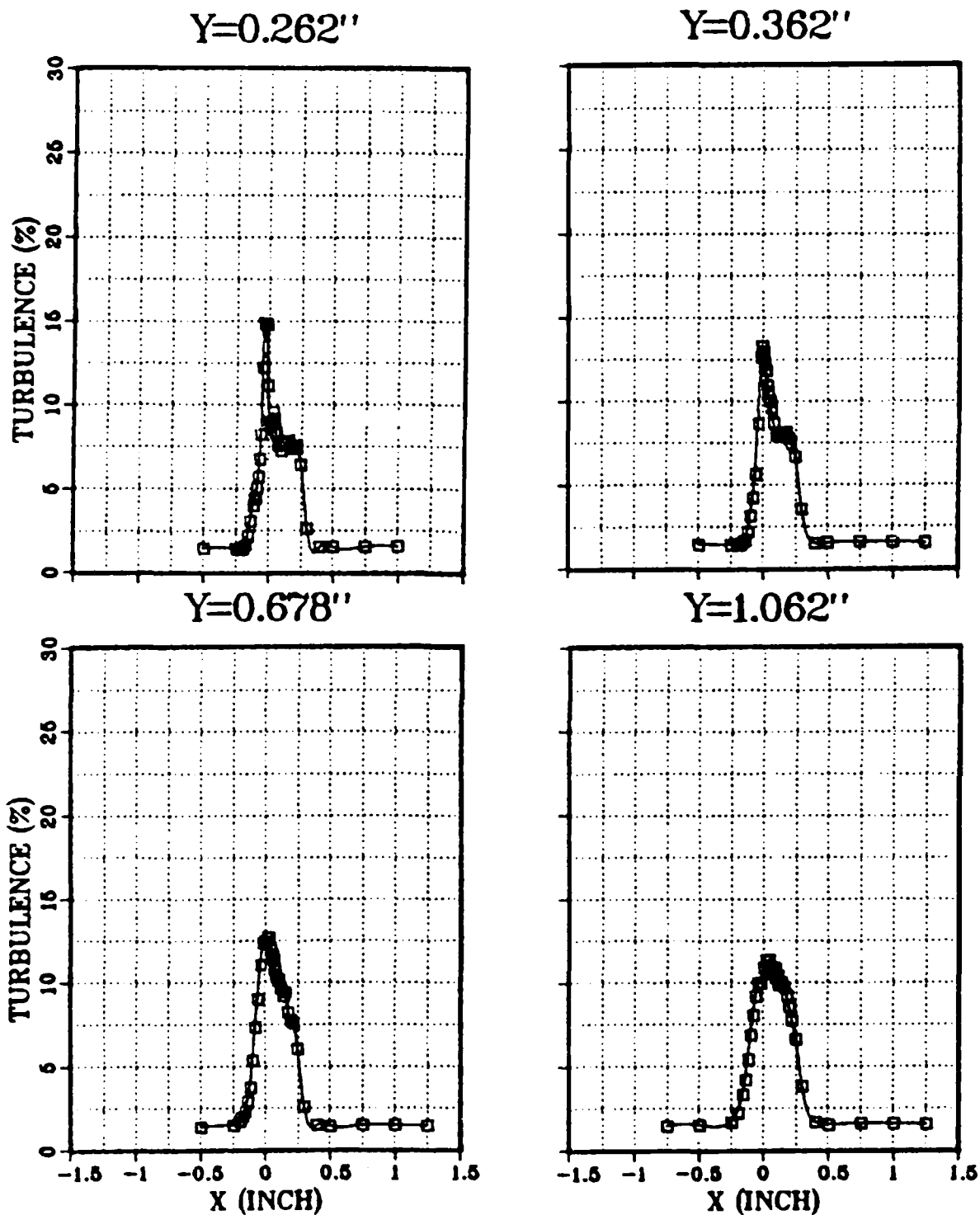


Figure 62. Wake Turbulence Level Distributions;
 $\beta_1 = 40^\circ$, $Re = 710000$.

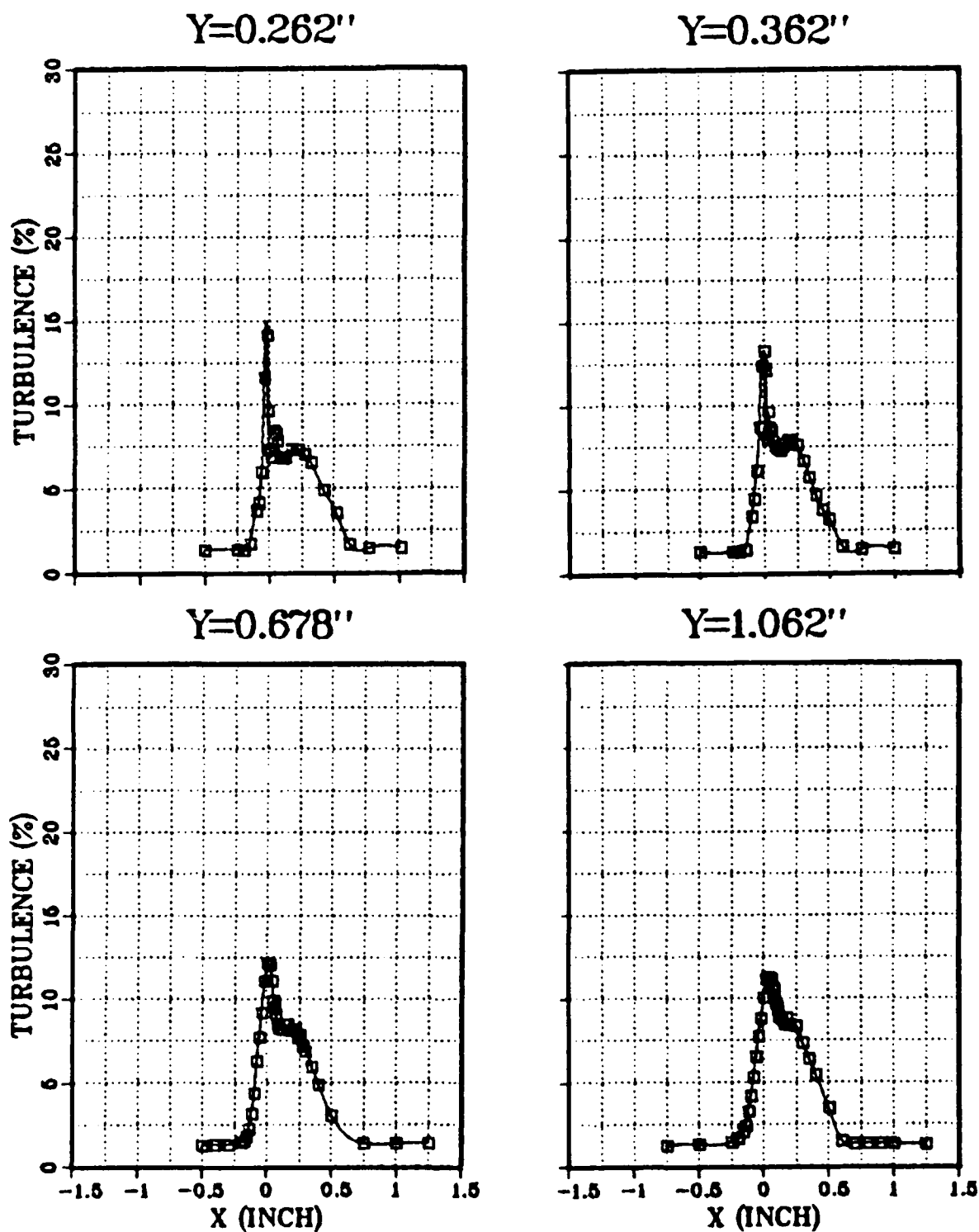


Figure 63. Wake Turbulence Level Distributions;
 $\beta_1 = 43.4^\circ$, $Re = 740000$.

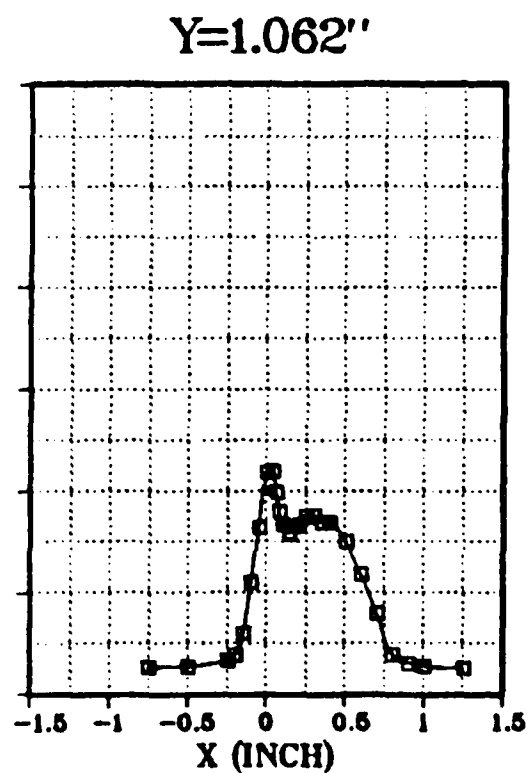
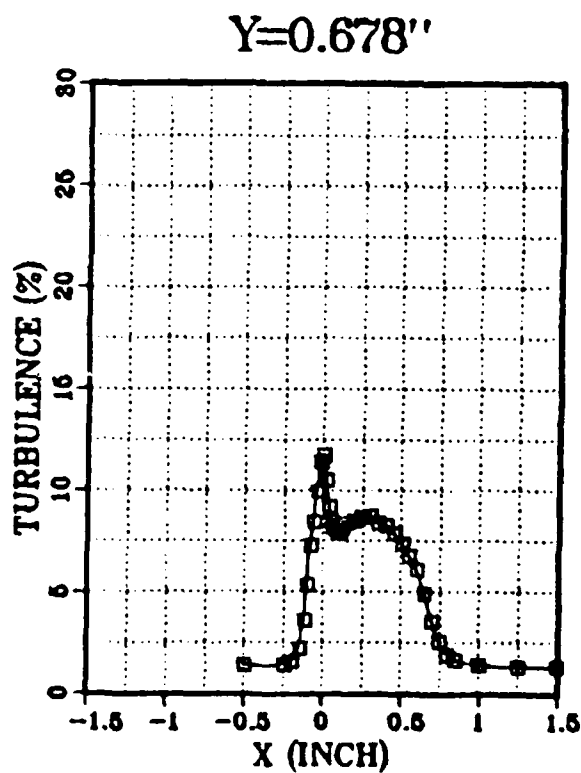
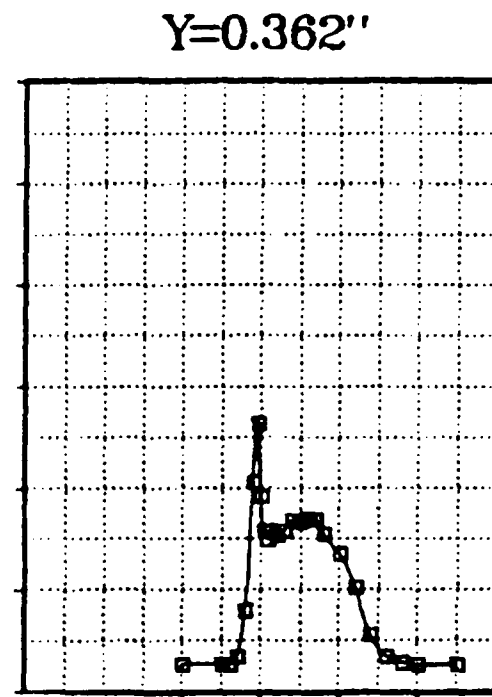
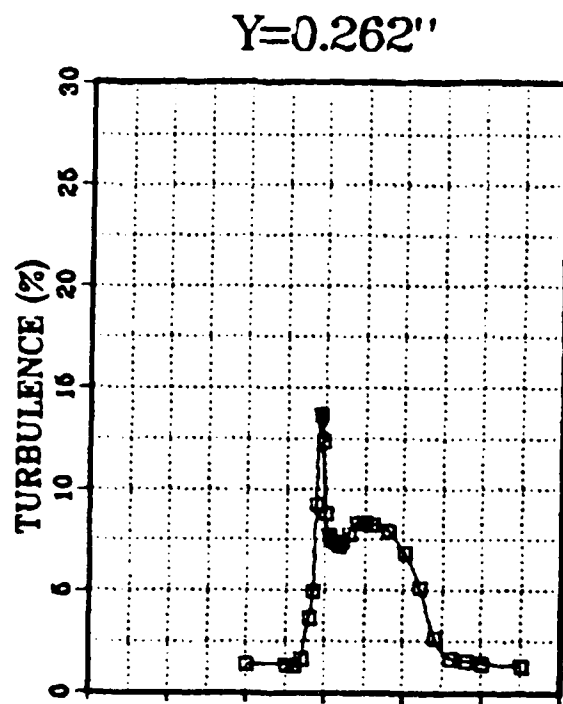


Figure 64. Wake Turbulence Level Distributions;
 $\beta_1 = 46^\circ$, $Re = 730000$.

level reached 15% in the near wake ($y = 0.262''$) and dropped to 12% at the most downstream station ($y = 1.062''$) for all three inlet angles.

- b. The suction surface side of the wake was characterized by lower turbulence levels. The peak levels were about 8%-9% at all inlet angles and positions downstream of the trailing edge.
- c. At the design angle ($\beta_1 = 40^\circ$) turbulence level distributions characteristic of the two blade trailing edge boundary layers remained defined in the near wakes ($y = 0.262'', 0.362''$). They are seen to be smeared out at the two downstream stations, and at $y = 1.062''$ the distribution was smooth and nearly symmetric.
- d. At the higher inlet angles ($\beta_1 = 43.4^\circ, 46^\circ$) the turbulence level distribution characteristic of the two boundary layers remains evident at all stations, particularly at the highest inlet angle.

A comparison of the turbulence level distribution for the three inlet angles at $y = 0.678''$ is shown in Figure 65. The pressure surface side of the wake is seen to be almost identical for all three inlet angles. On the other hand, the suction surface side shows the wake broadening, but with little change in the peak turbulence level, as inlet angle was increased.

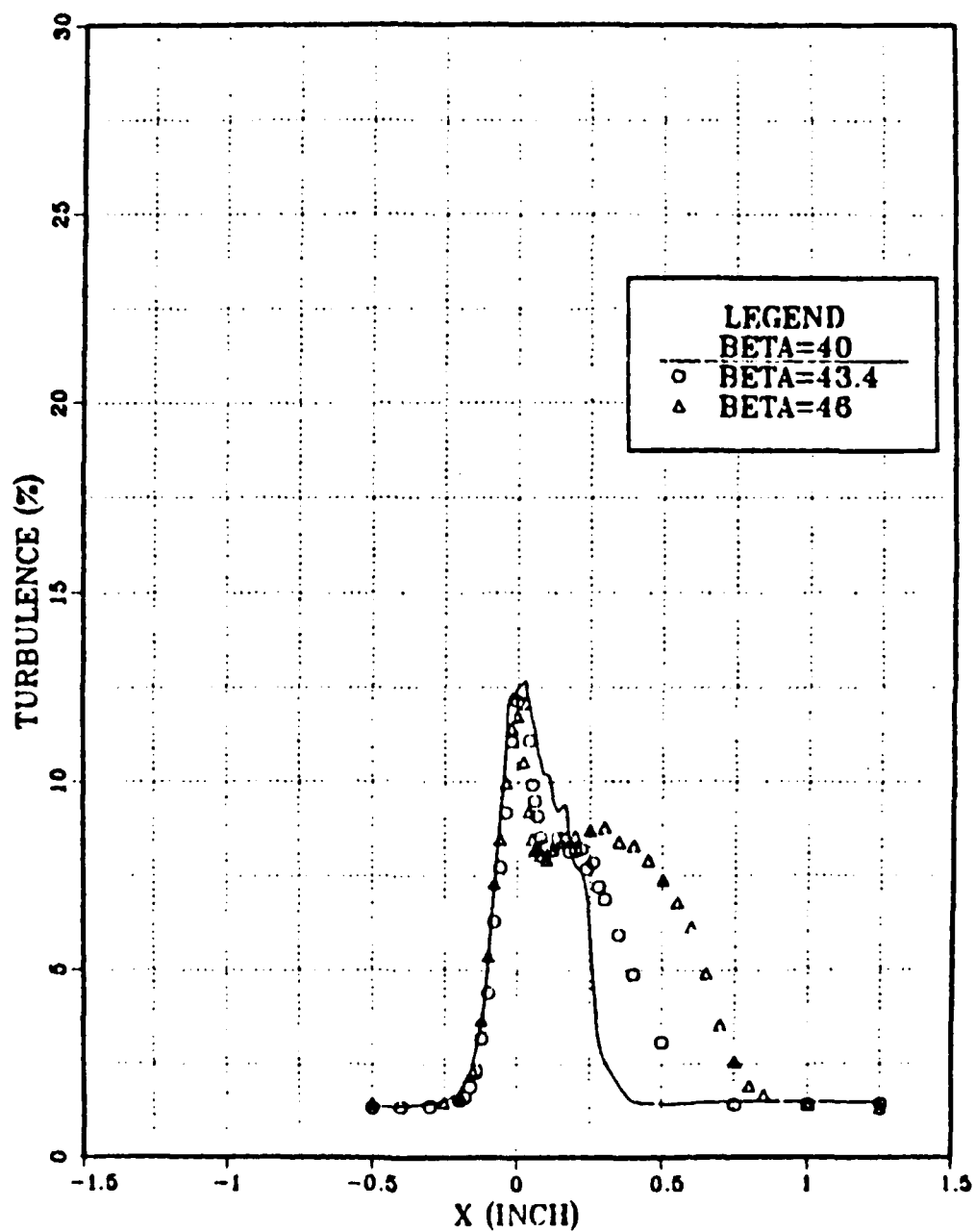


Figure 65. Turbulence Level Distributions at $y = 0.678''$ ($0.123c$ from Trailing Edge).

VI. ANALYSIS OF THE RESULTS

A. COMPARISON WITH PREVIOUS EXPERIMENTS

The following is a summary of the main parameters and physical features identified in the previous chapter in comparison with previous experience.

1. The free stream turbulence level was $1.4 \pm 0.2\%$.
2. The AVDR did not change significantly with inlet angle variation. An AVDR of 1.025 was calculated between stations 0.3 chords axially upstream and 0.24 chords downstream of the blade. This was consistent with Dreon (Ref. 41), who calculated AVDR using measurements from a five-hole probe to be 1.05 ± 0.01 between stations two chords axially upstream and 1.65 chords downstream of the blade.
3. Measurements of the edge velocity agreed quite well with the velocity calculated from measurements of the surface pressure in those regions of the flow where the surface curvature was moderate and the boundary layer was relatively thin. The edge velocity and calculated (inviscid) surface velocity would be expected to be different where the surface curvature is significant and the boundary layer not sufficiently thin.
4. A separation bubble was identified on the suction surface by the LDV measurements. A rough estimation

of the reattachment point using the LDV data was 5%-15% of chord. Sanger and Shreeve (Ref. 45) reported that flow visualization with china clay located reattachment somewhat closer to the leading edge, at 4%-7% of chord. Their results showed the same trend as did the LDV data, i.e., the reattachment point moved downstream as inlet angle was increased. Sanger and Shreeve's results were obtained at a chord Reynolds number of 340000. The lower Reynolds number may explain the quantitative difference. In both the present and previous experiments with china clay, it was concluded that transition took place in the free shear layer, above the bubble.

5. The turbulent boundary layer on the suction surface was found to be fully attached throughout the inlet angle range. Sanger and Shreeve (Ref. 45) used the china clay method to detect separation. Their findings were different. At $\beta_1 = 39^\circ$ separation was detected at 95% chord. At $\beta_1 = 43^\circ$ separation was at 90% chord and at $\beta_1 = 46^\circ$ separation was around 87% chord. Once again, the difference in Reynolds number may explain the apparent disagreement. However, an alternative explanation can be that the china clay technique gave erroneous results in this particular region of the flow field. The vertical orientation of the suction surface near the trailing edge allowed the

liquid in the china clay to creep forward against very low dynamic pressures within the suction surface boundary layer. the interpretation that the drying pattern indicated separation could be in error under these circumstances. LDV measurements at lower Reynolds number are needed to resolve the question.

6. Inlet angle variations had relatively little effect on the boundary layer distribution on the pressure surface, although increasing the inlet angle (at positive incidence angles) delayed transition and caused the turbulent boundary layer at the trailing edge to be measurably thinner. This is consistent with previous experience (Ref. 30).
7. A comparison between the LDV wake measurements in the present study and measurements obtained by Dreon (Ref. 41) can be seen in Figures 66-69. Dreon used a calibrated five-hole pneumatic probe to measure the velocity and flow angle distributions at six stations downstream of the trailing edge. The comparison is made with Dreon's data obtained at 0.123 chords downstream of the trailing edge for the design inlet angle (40°) and one positive incidence angle ($\beta_1 = 43.4^\circ$).

At the design angle shown in Figure 66, there was seen to be good agreement between the two velocity distributions. There was a good match in the location of the center of the wake, the minimum velocity, and

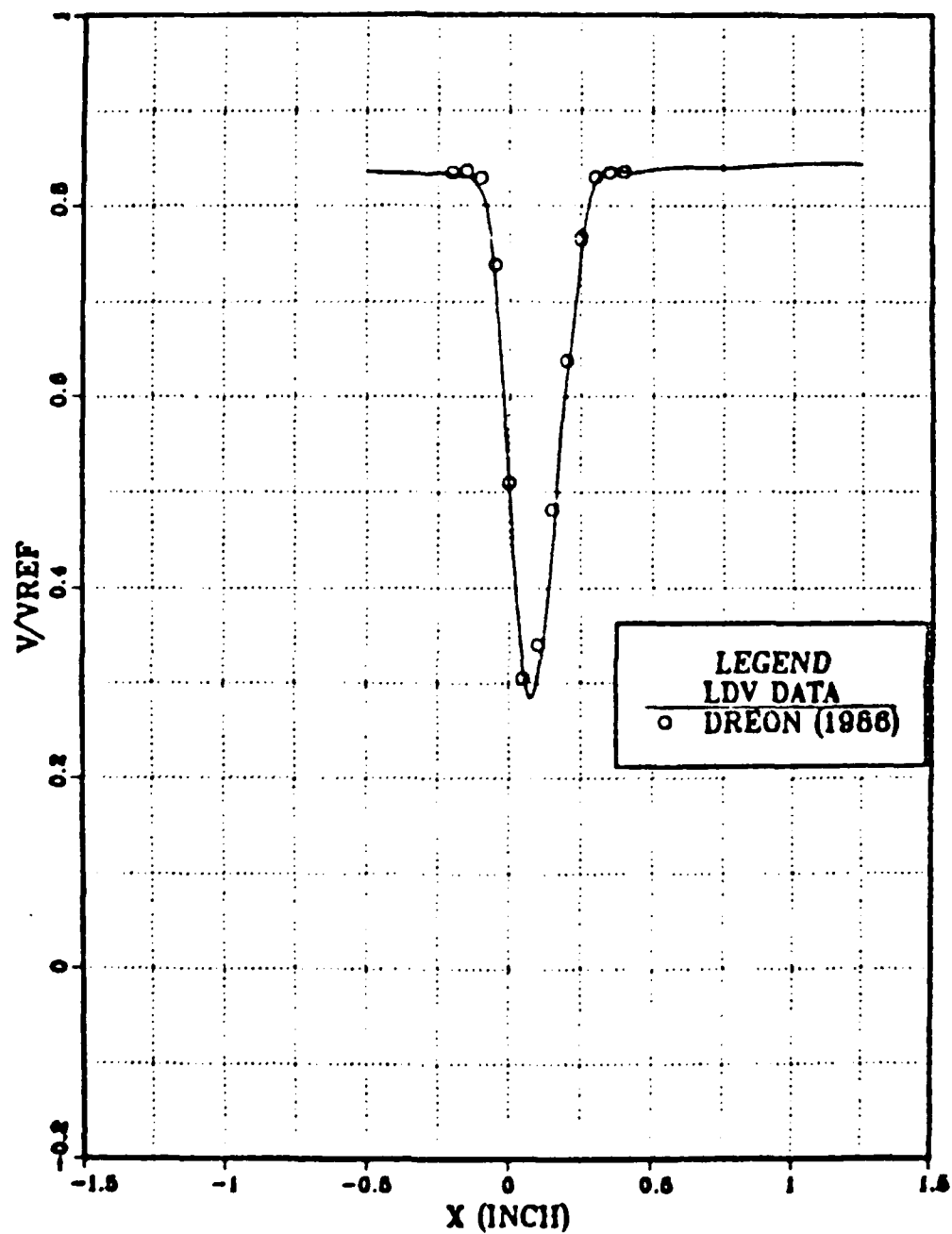


Figure 66. Wake Velocity Distribution;
 $\beta_1 = 40^\circ$.

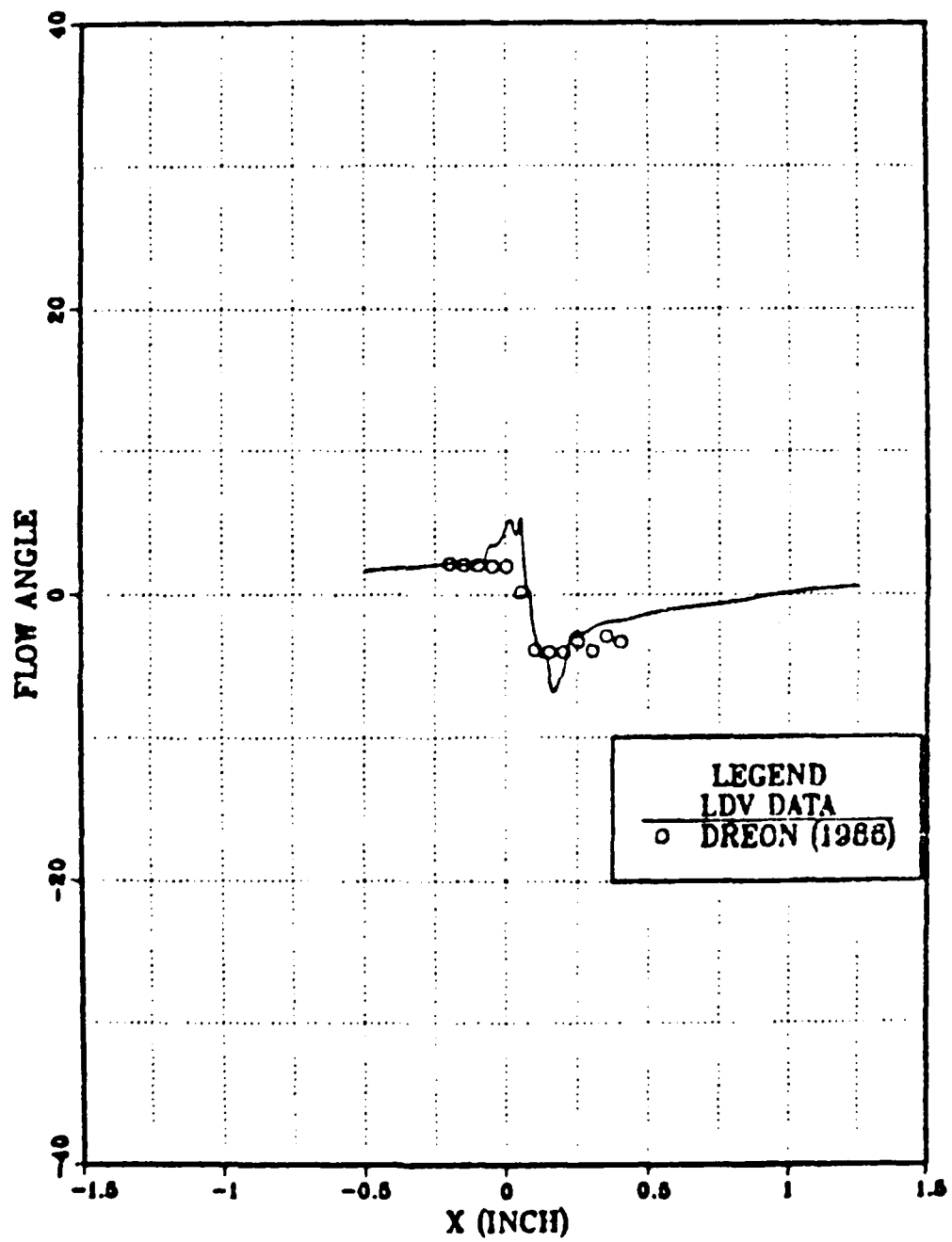


Figure 67. Wake Flow Angle Distribution;
 $\beta_1 = 40^\circ$.

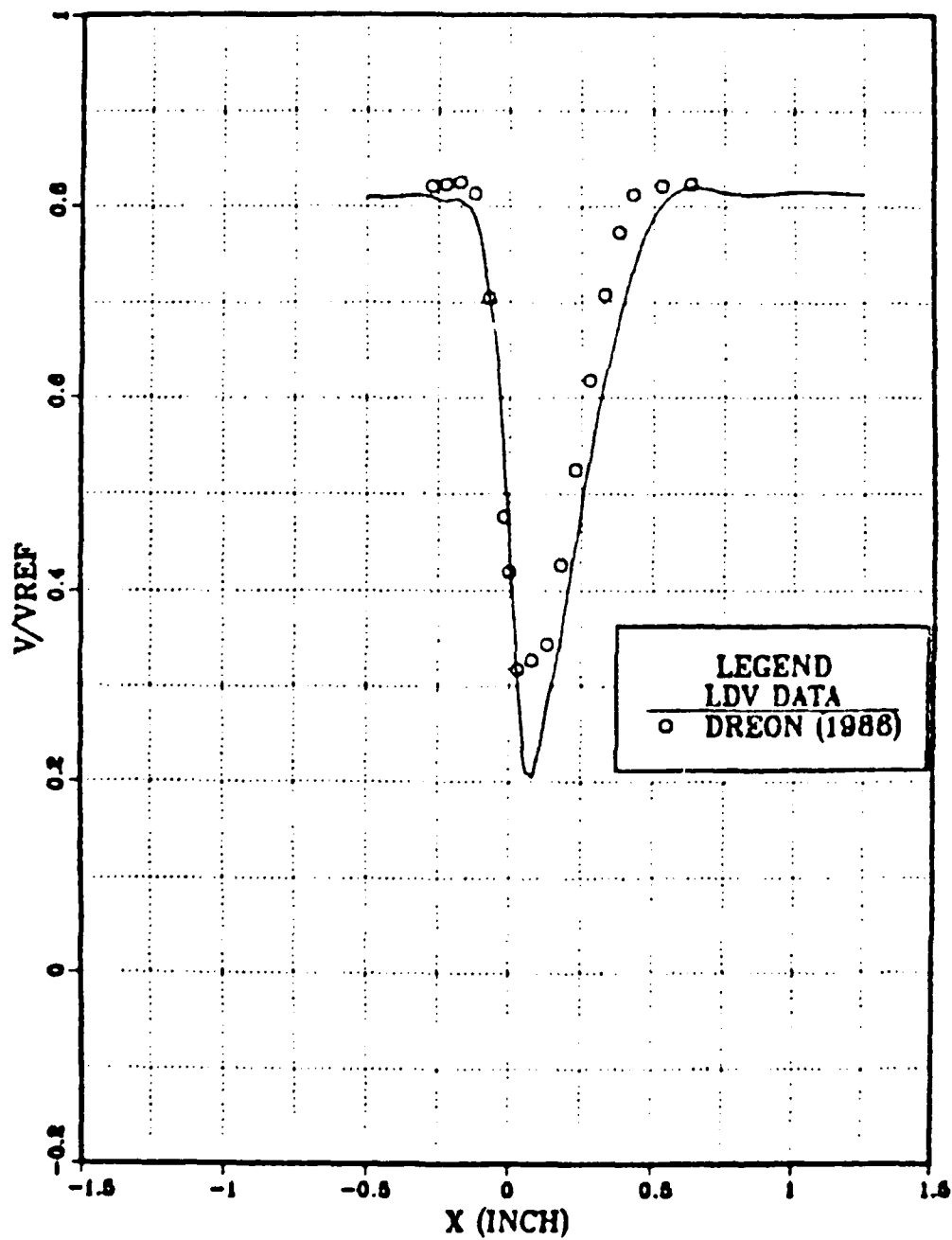


Figure 68. Wake Velocity Distribution;
 $\beta_1 = 43.4^\circ$.

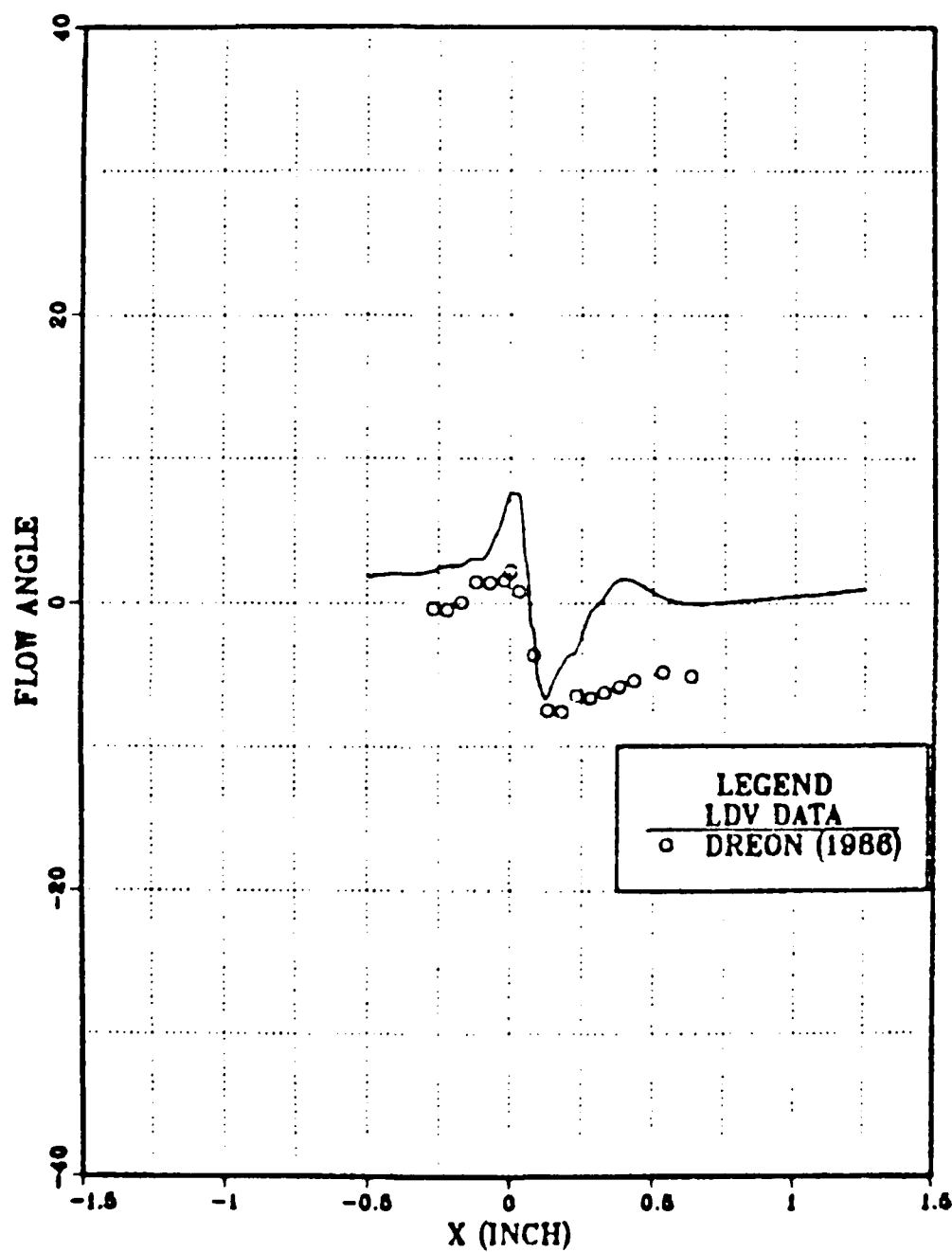


Figure 69. Wake Flow Angle Distribution;
 $\beta_1 = 43.4^\circ$.

in the velocity through the two sides of the wake. There was some difference, however, between the flow angle distributions shown in Figure 67. Larger excursions of the flow angle through the wake shear layers were detected in the LDV measurements than were indicated in Dreon's probe measurements. At the higher inlet angle shown in Figure 68, the two velocity distributions agreed well in the location of the center of the wake and in the distribution through the pressure surface side of the wake. There was disagreement in the magnitude of the minimum velocity and in the distribution through the suction surface side. The LDV system measured a lower minimum and a thicker wake. The flow angle distribution in Figure 69, showed again quite a significant disagreement although the general trends were similar. It should be noted that Dreon attempted to resolve the uncertainty in his measurements of the flow angle in the blade wakes by using a special probe designed to measure angle (only) through the shear layer. Unfortunately, no measurements were made with the angle probe at the stations where LDV data were taken in the present study. Thus, the comparisons in Figures 68 and 69 are with data from a United Sensor cone probe, with the probe shaft quite close to the blade trailing edge. Probe interference may explain the differences.

8. A comparison between some LDV wake measurements in the present study and measurements obtained by Baydar (Ref. 50) can be seen in Figures 70-71. Baydar used a single wire TSI hot-wire system to measure the velocity and turbulence level distributions at three stations in the wake. The comparison is made with Baydar's data at 0.123 and 0.2 chords downstream of the trailing edge for design inlet angle ($\beta_1 = 40^\circ$) and the highest incidence angle ($\beta_1 = 46^\circ$). The comparison shows very good agreement between the two sets of data.
9. An attempt was made to calculate the loss coefficient from the LDV data to compare with data reported by Sanger and Shreeve (Ref. 45) and Dreon (Ref. 41). The loss coefficient is defined as:

$$\omega = \frac{P_{t1} - P_{t2}}{q_1}$$

P_{t1} was mass averaged at the inlet. P_{t2} was calculated assuming that the static pressure was atmospheric and adding the mass averaged dynamic pressure derived from the measured outlet velocity profile with constant density. Unfortunately, the calculations did not give good results since the numerator was a small difference between large numbers, each of which was approximate. Thus, the uncertainty was of the same order of magnitude as the loss coefficient itself.

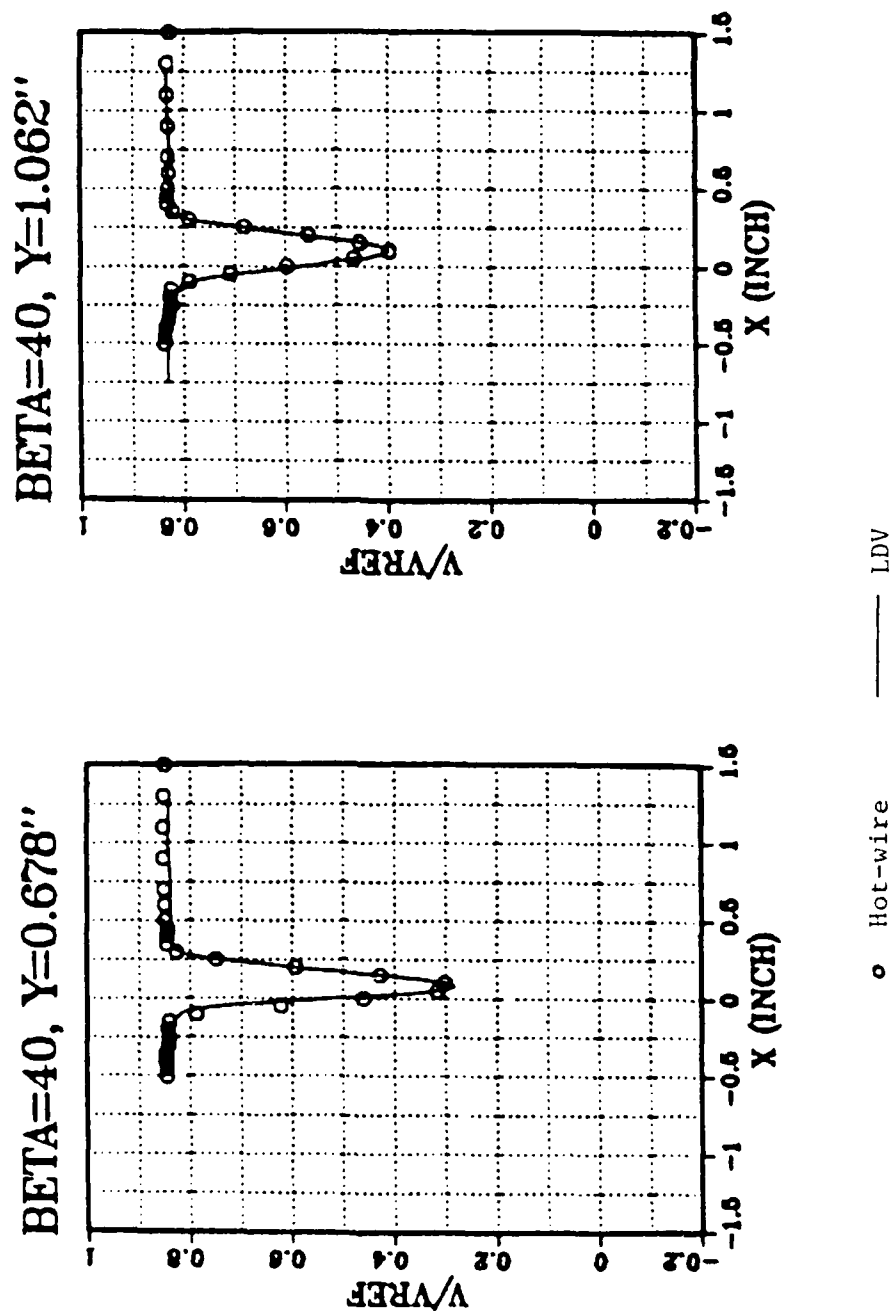


Figure 70. Comparison with Hot-Wire Measurements.

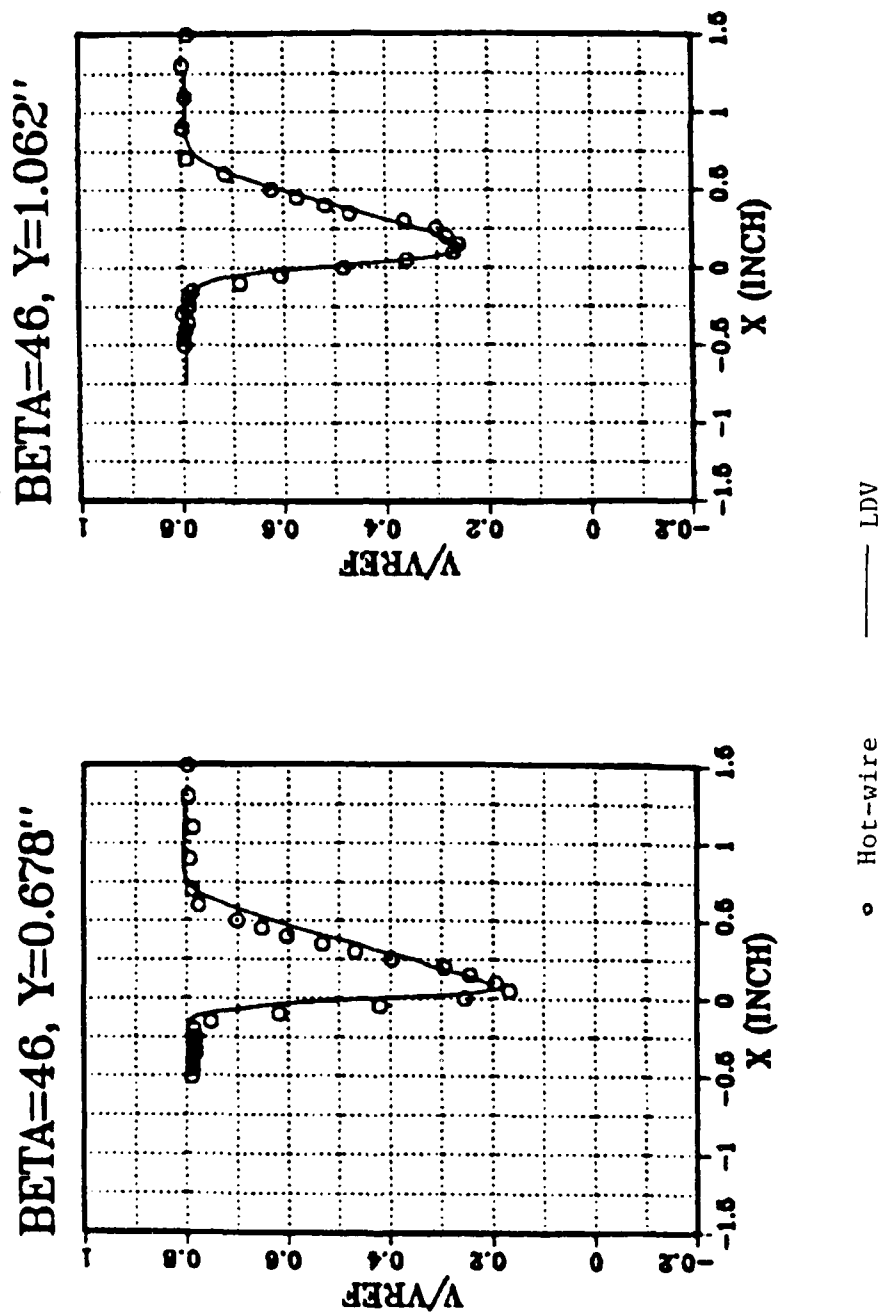


Figure 70. (cont'd) Comparison with Hot-Wire Measurements.

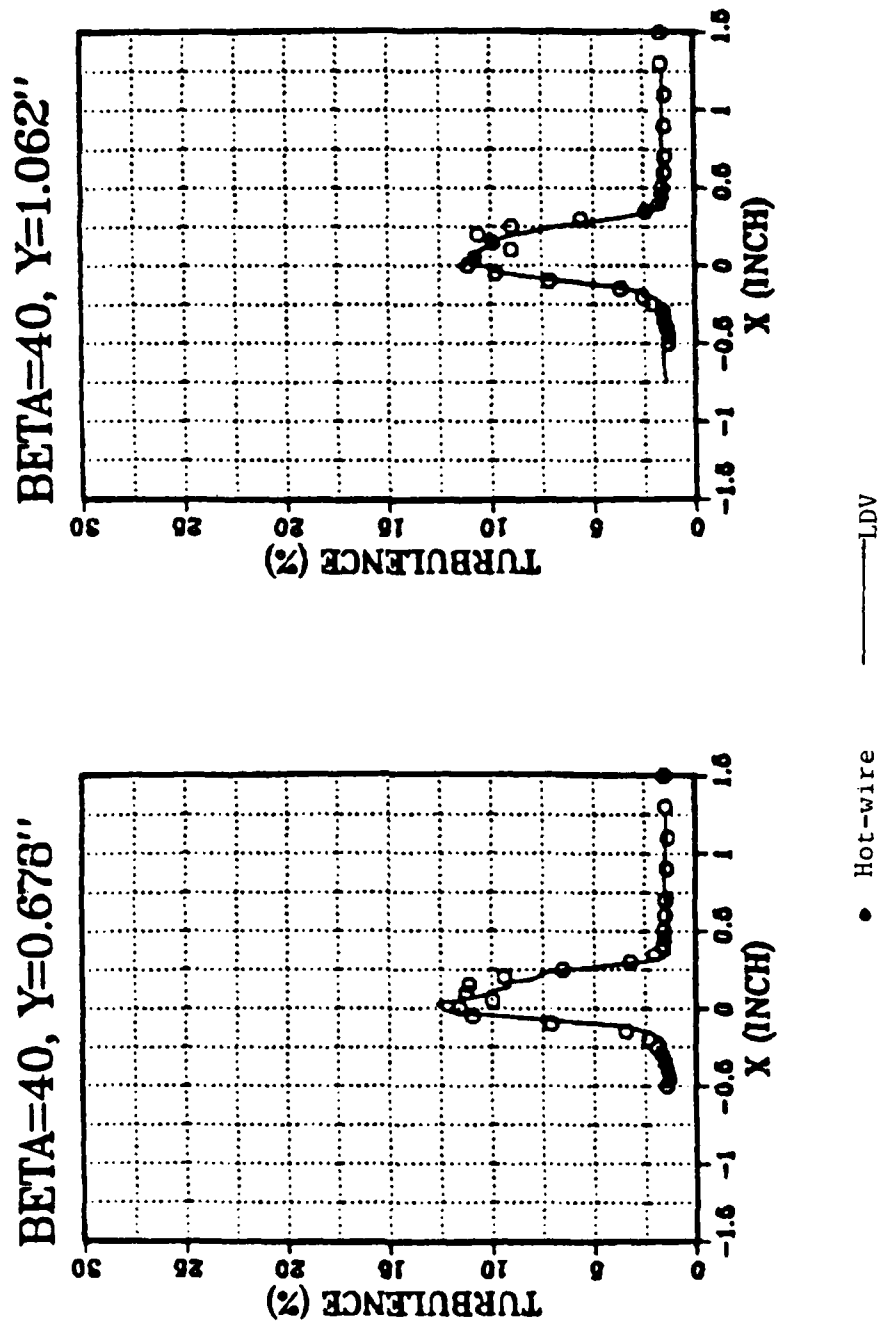


Figure 71. Comparison with Hot-Wire Measurements.

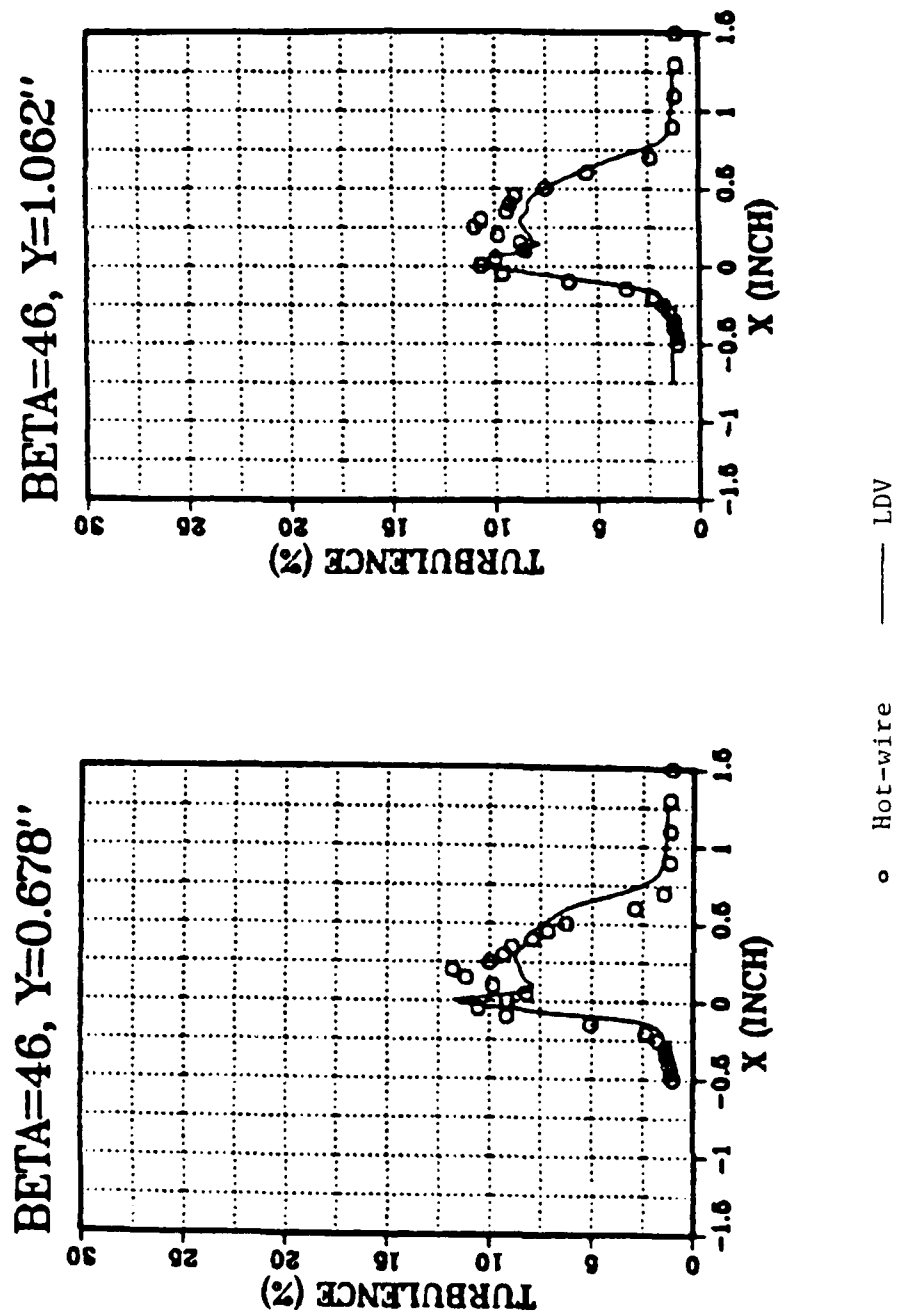


Figure 71. (cont'd) Comparison with Hot-Wire Measurements.

B. COMPARISON WITH CODE PREDICTIONS

Three codes have been used to calculate the viscous behavior through the cascade for the conditions of the experiment; namely, a non-interactive boundary layer code, a strongly interactive inviscid-viscous boundary layer code, and a Navier-Stokes code.

1. Non-Interactive Boundary Layer Code

The boundary layer growth on the suction surface at $\beta_1 = 40^\circ$ and $\beta_1 = 43.4^\circ$ was calculated using a boundary layer code developed by McNally (Ref. 7). This was the code used by Sanger (Ref. 5) in designing the blade shape. Momentum and displacement thicknesses downstream of reattachment were input together with the edge velocity distribution that was measured by the LDV.

The results are shown plotted in Figure 72. The lines represent the calculated thickness and the symbols represent the measured thickness. There was good agreement between the calculated and measured data over the forward half of the blade, but further downstream the measured data departed significantly from the calculated thickness. At the trailing edge, the measured boundary layer was twice as thick as the calculated boundary layer. The disagreement may be the result of the particular turbulence model used in the code. Figure 73 examines this suggestion by comparing the calculated boundary velocity profile with the measured profile. The differences are seen to be significant and

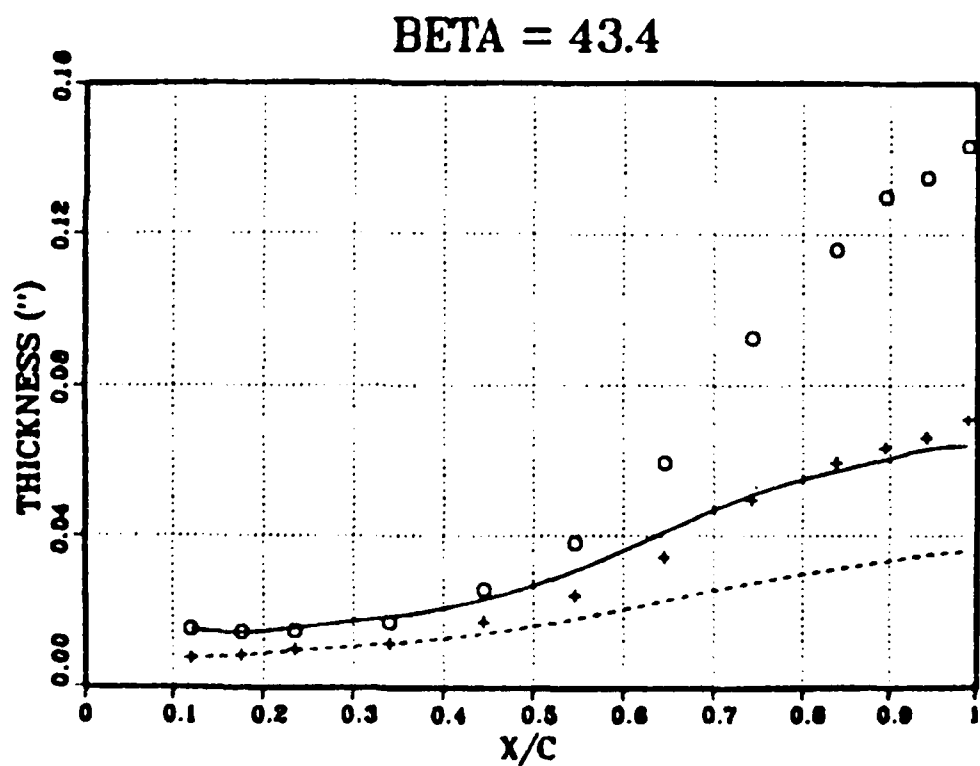
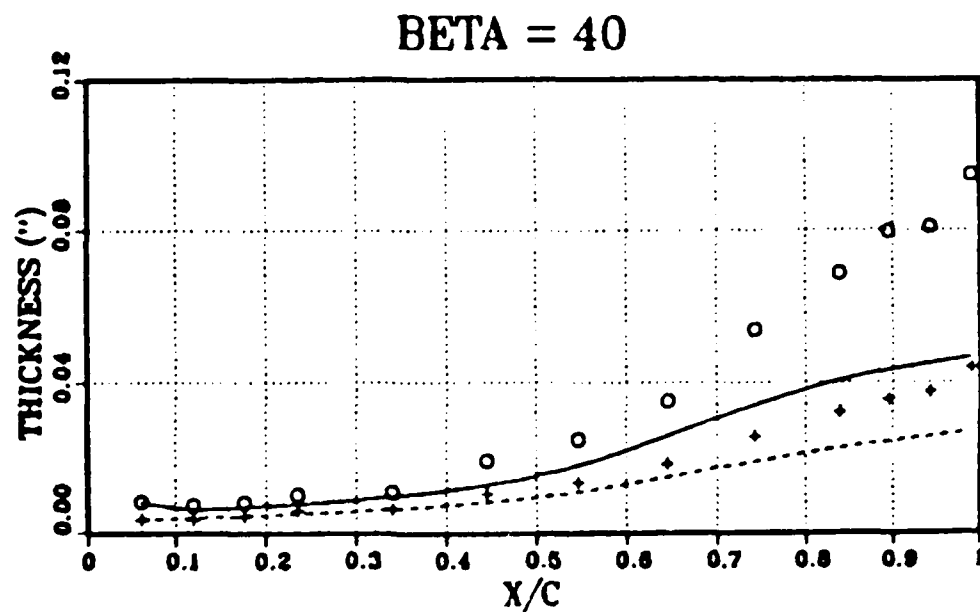


Figure 72. Comparison with Suction Surface Boundary Layer Thicknesses Calculated Using BLAYER

Displacement: — Calculated. • LDV
Momentum: - - - Calculated. + LDV

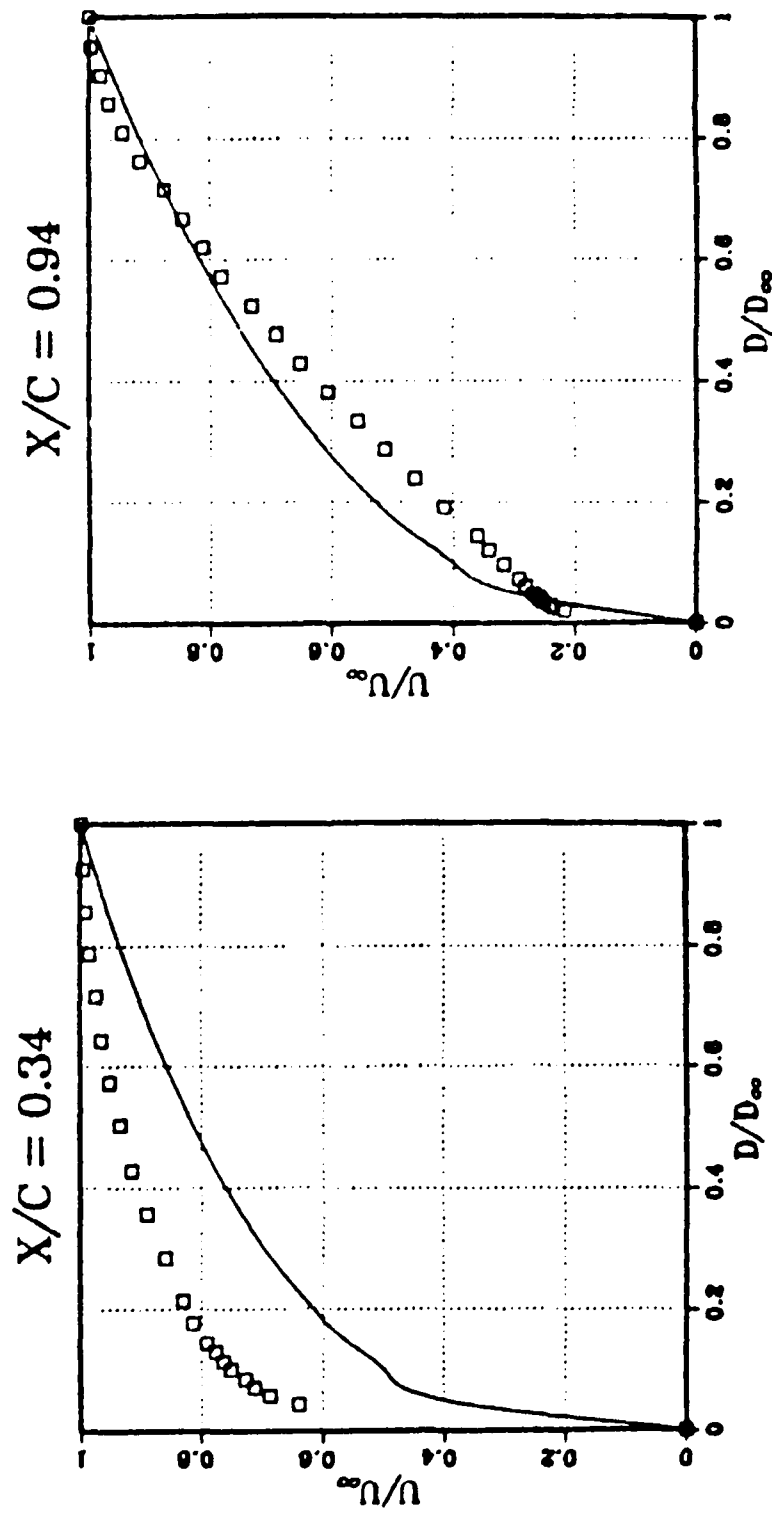


Figure 73. Comparison with Suction Surface Boundary Layer Velocity Profiles Calculated Using RLAYER; $\beta_1 = 43.4^\circ$.
 □ Calculated. — Measured with LDV

result from the assumption in McNally's code that the velocity profile follows a power law. Sanger and Shreeve (Ref. 45) used McNally's code together with an inviscid code and compared measured surface pressure distributions on the suction surface with calculated results. The calculated data deviated from the measured data as one moved downstream towards the trailing edge. The inaccuracy apparent in the viscous calculation would help explain the disagreement.

2. Interactive Inviscid-Viscous Boundary Layer Code

An incompressible viscous-inviscid strongly interactive (S.I.) code being developed by Cebeci (Ref. 16) was used by Krainer (Ref. 17) to predict boundary layer distributions on the suction and pressure surfaces of the present blade. The displacement thickness distributions calculated for each of the three inlet angles on the suction and pressure surfaces are shown in Figures 74-75, respectively. The solid lines represent the calculated thickness and the symbols represent the measurements. Also, shown on the two figures are the locations of laminar separation (LS), transition (T), reattachment (R), full turbulence (Tu), and turbulent separation (TS), as given by the code. The predictions using the code disagreed quantitatively and qualitatively with the measured data as follows.

- a. At the design inlet angle ($\beta_1 = 40^\circ$), the calculations indicated that there was no laminar separation on the suction surface. Instead, the laminar boundary layer

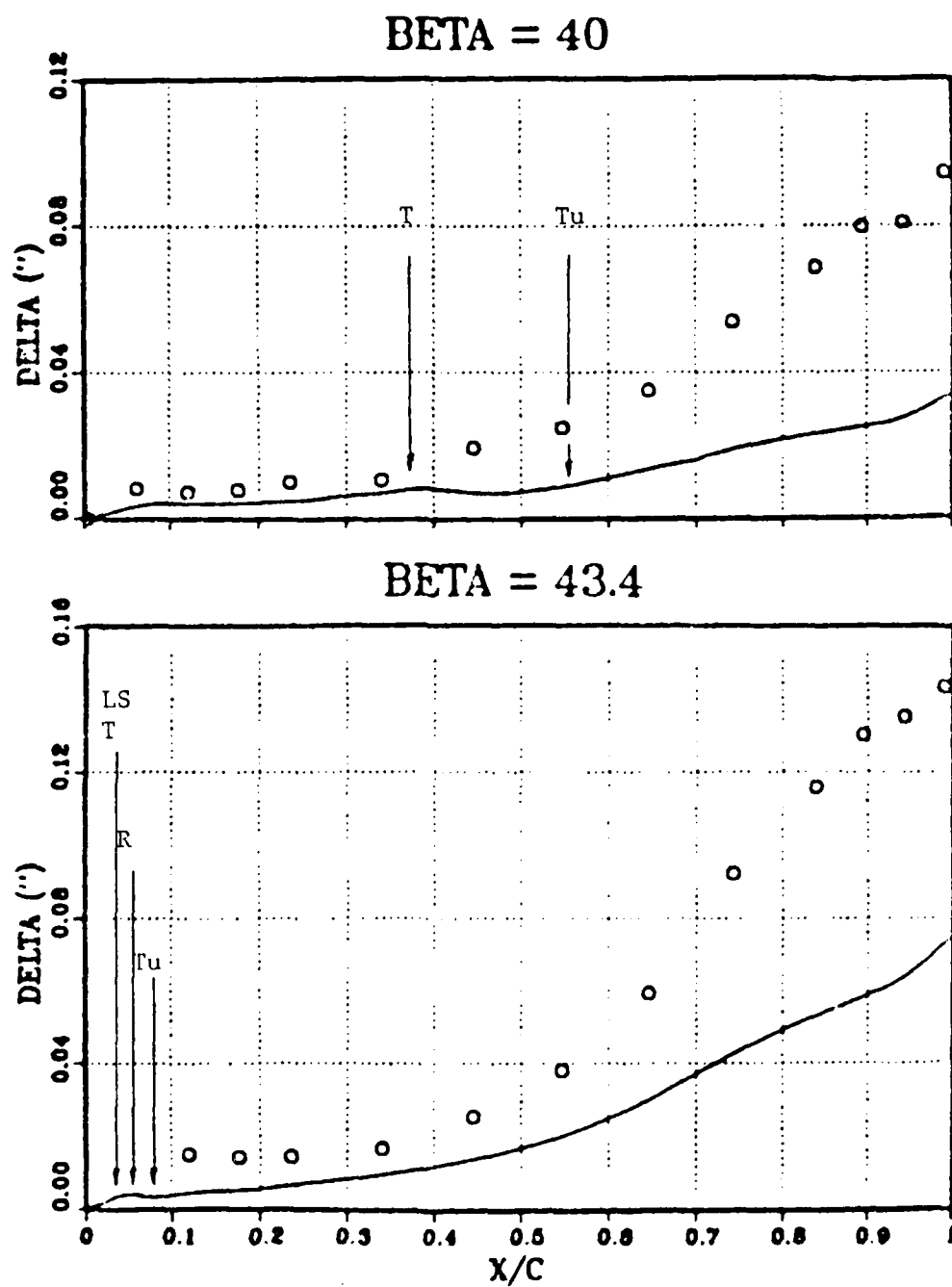


Figure 74. Comparison with Displacement Thickness on the Suction Surface Calculated Using S.I. Code.

— Calculated with Original Models.
 ○ Measured

BETA = 46

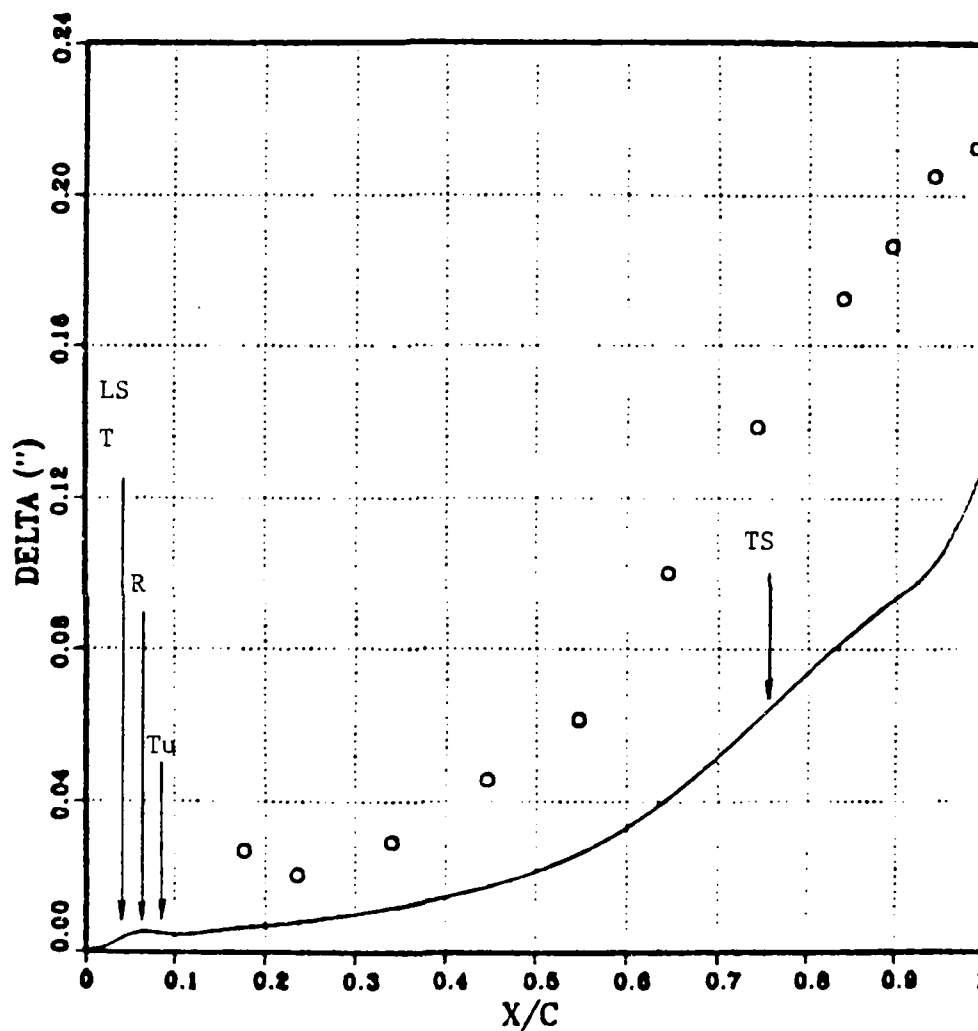


Figure 74. (cont.) Comparison with Displacement Thickness on the Suction Surface Calculated Using S.I. Code.

— Calculated with Original Models.
 • Measured

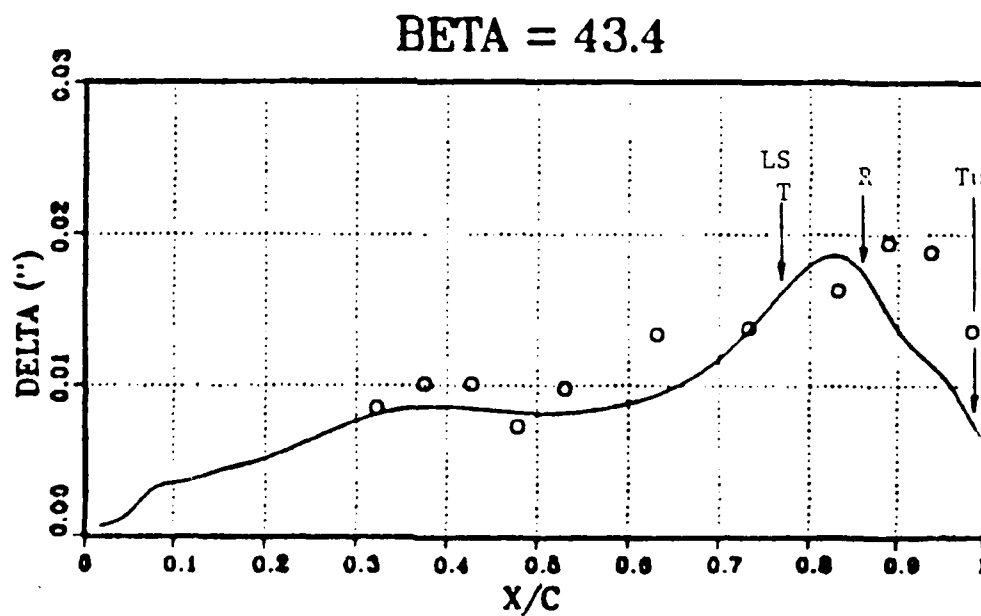
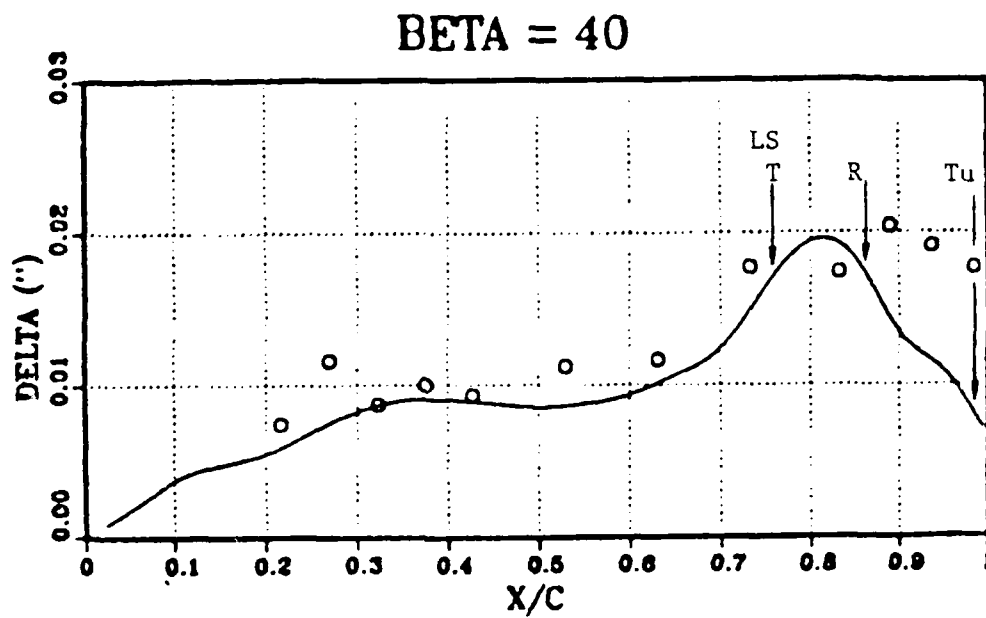


Figure 75. Comparison with Displacement Thickness on the Pressure Surface Calculated Using S.I. Code.

— Calculated with Original Models.
 ○ Measured

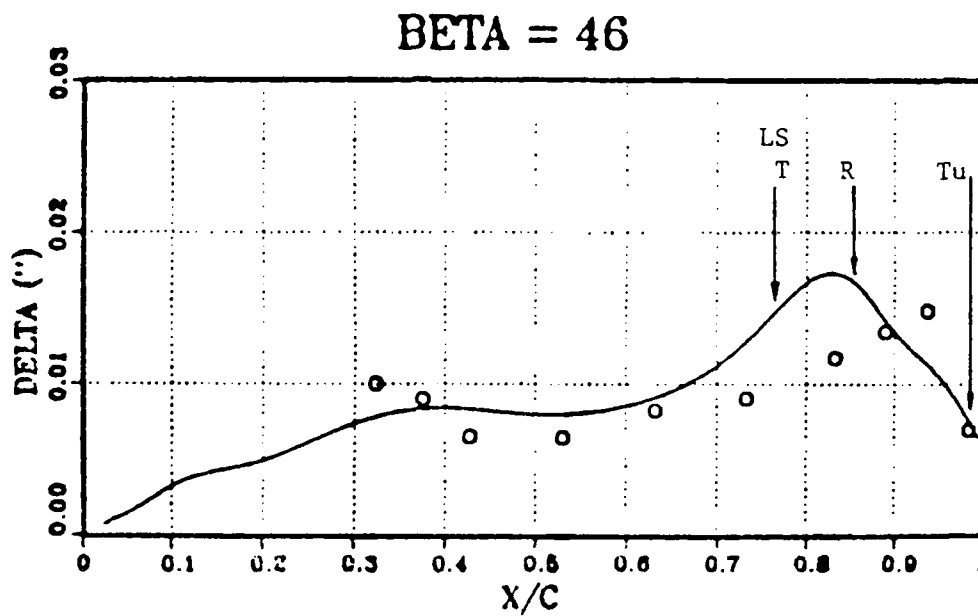


Figure 75. (cont.) Comparison with Displacement Thickness on the Pressure Surface Calculated Using S.I. Code.

— Calculated with Original Models.
 • Measured

underwent transition to turbulence through a boundary layer transition. Onset of transition was calculated to be at 37% chord. The transition extended to 55% chord, where the flow became turbulent. In contrast, the LDV data clearly indicated the presence of a separation bubble, and this was consistent with the flow visualization results reported by Sanger and Shreeve (Ref. 45).

- b. On the pressure surface, the calculations indicated that transition followed laminar separation at all three angles. At each angle, laminar separation was predicted at $76 \pm 1\%$ chord, reattachment at $85 \pm 1\%$ chord and the boundary layer to become fully turbulent at 99% chord. In contrast, the measurements showed no laminar separation on the pressure surface at the indicated inlet angles. Transition extended to no more than 60% of chord where the velocity profiles were fully turbulent.
- c. The measured boundary layer displacement thick-ness everywhere on the suction surface was significantly larger than the calculated displacement thickness at each inlet angle.
- d. On the suction surface, at the highest inlet angle ($\beta_1 = 46^\circ$), the calculations indicated that separation of the turbulent boundary layer would occur at

approximately 76% chord. In contrast, the measured data showed the flow to be fully attached at these test conditions.

Clearly, the S.I. code, as it was used for the above calculations provided an inaccurate prediction and description of transition. Therefore, to improve the calculated results, the onset of transition and the transition length were forced as inputs into the interactive calculations. The results for the boundary layer growth on the pressure surface are shown plotted in Figure 76. The location of the onset of transition and the transition length are shown in the figure. The lines represent the calculated distributions and the symbols represent the measured data. The calculated momentum and displacement thicknesses are seen to agree quite well with the measured thicknesses.

Forcing transition on the suction surface did not give equally good results. Transition through the laminar separation (separation bubble) could not be induced at the lower inlet angle ($\beta_1 = 40^\circ$). Figure 77 shows the suction surface boundary layer thicknesses for $\beta_1 = 46^\circ$ with transition modified to obtain a reasonable match to the measured data close to the bubble. The calculated boundary layers are much thinner than were measured, and the calculations predicted the absence of separation, which was consistent with the LDV observations. However, the growth was not significantly changed from that calculated with the

AD-A194 490

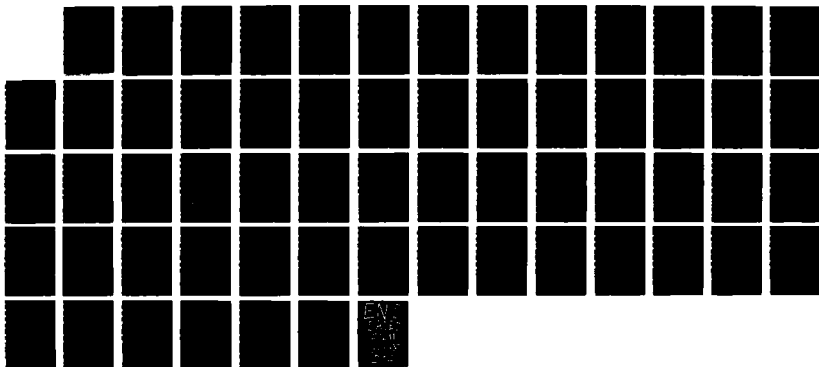
A MAPPING OF THE VISCOUS FLOW BEHAVIOR IN A CONTROLLED
DIFFUSION COMPRESS (U) NAVAL POSTGRADUATE SCHOOL
MONTEREY CA V ELAZAR MAR 88 NPS67-88-001

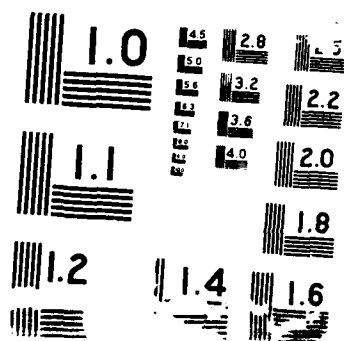
3/3

UNCLASSIFIED

F/G 28/4

NL





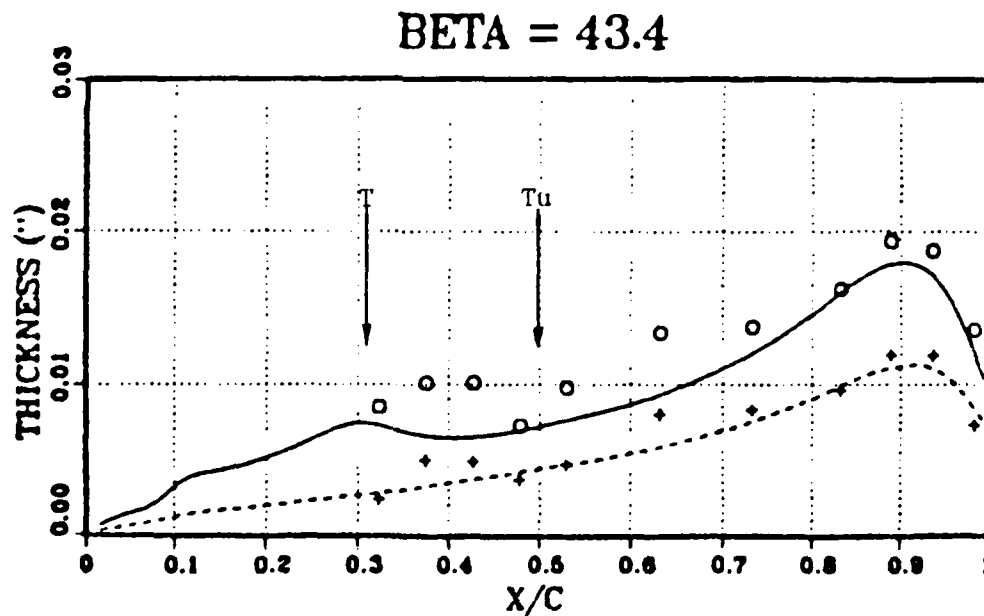
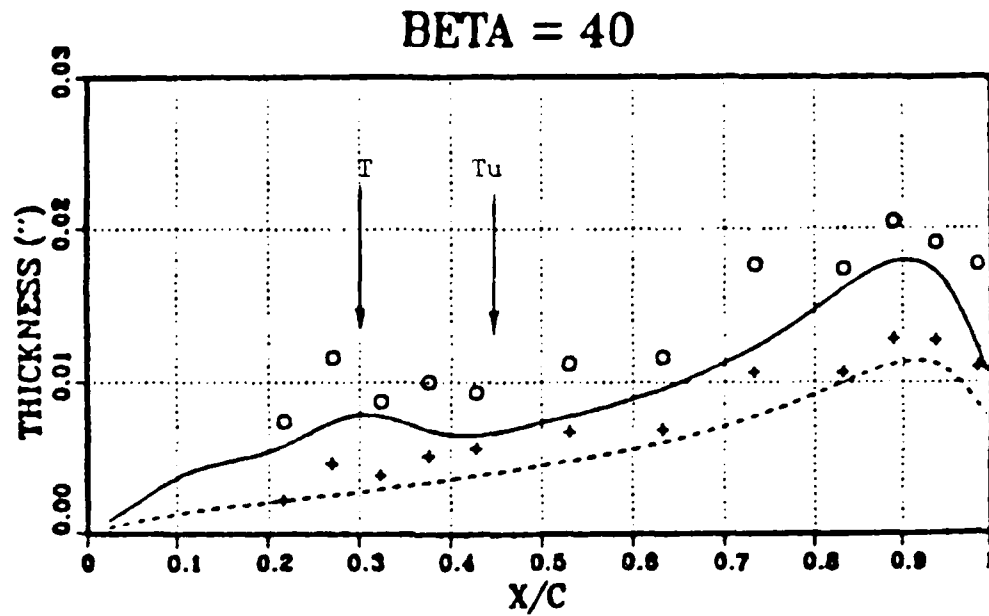


Figure 76. Comparison with Pressure Surface Boundary Layer Thicknesses Calculated Using S.I. Code with Forced Transition.

Displacement: — Calculated. • LDV.
Momentum: ---- Calculated. + LDV.

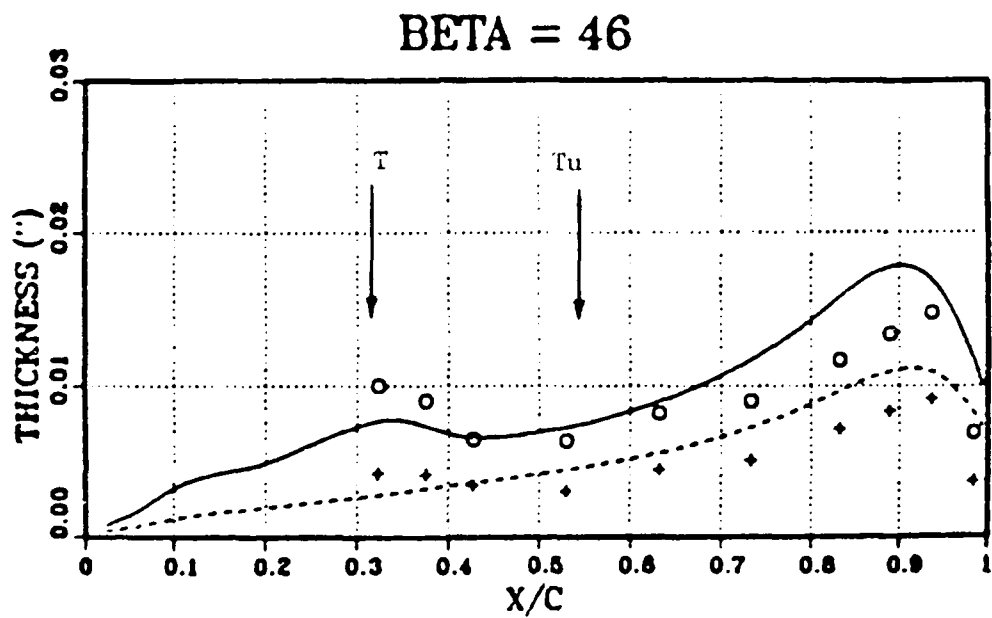


Figure 76. (cont.) Comparison with Pressure Surface Boundary Layer Thicknesses Calculated Using S.I. Code with Forced Transition.

Displacement: — Calculated. • LDV.
Momentum: ---- Calculated. + LDV.

BETA = 46

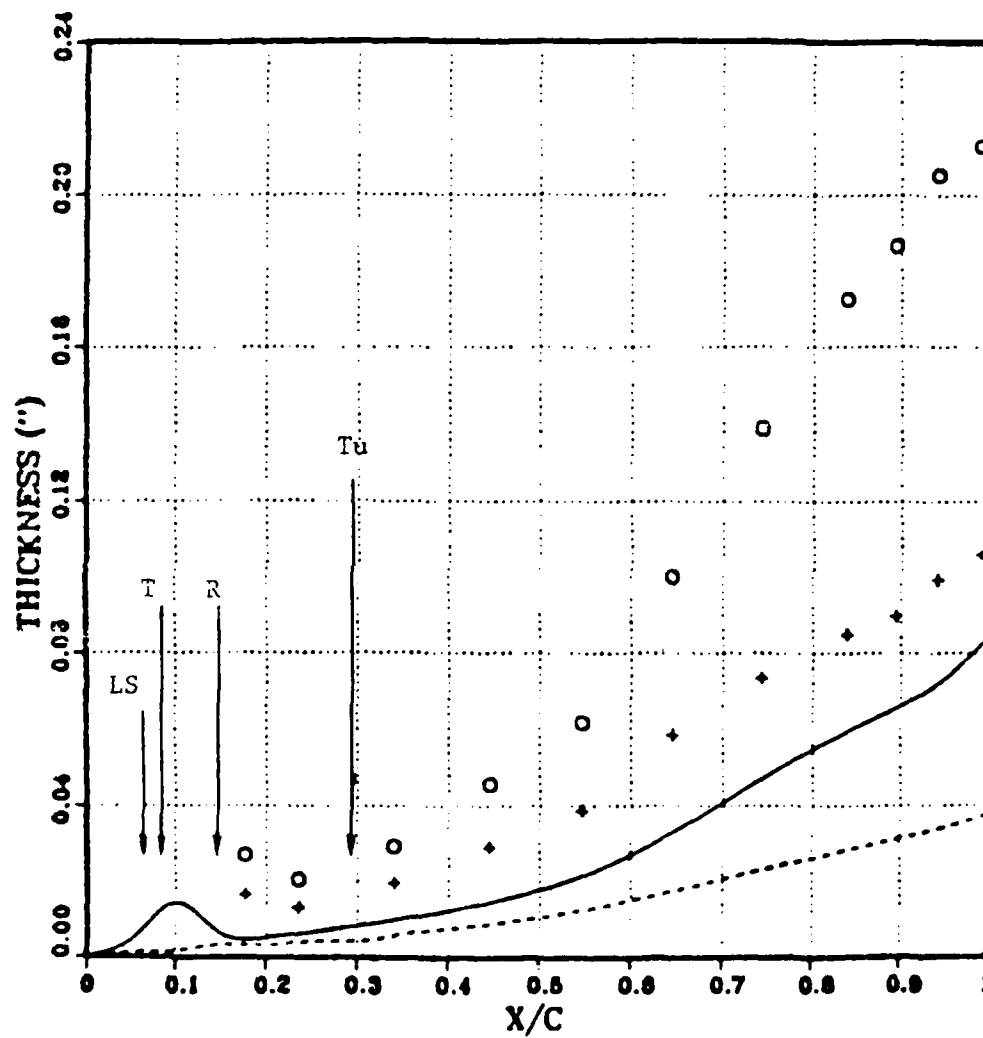


Figure 77. Calculated Suction Surface Boundary Layer Thicknesses Calculated Using S.I. Code with Forced Transition.

Displacement: — Calculated. ° LDV.
Momentum: ---- Calculated. + LDV.

modified code (Figure 74). The disagreement between calculation and measurement is seen to start immediately after reattachment. Presently, there is no procedure available within the code which could force the boundary layer to be thicker by a change in the input parameters. A modification in the model used for calculating the bubble or other improvements are required before the interactive code can describe the observed suction surface flow behavior accurately.

3. Navier-Stokes Code

A well-tested Navier-Stokes code for cascade flow (Ref. 51) was applied by Dr. Shamroth and S. K. Choi of Scientific Research Associates, Inc. to compute the flow field at each of the three inlet angles. They were supplied with the cascade geometry, inlet angles, stagnation pressure and temperature, and outlet static pressure. A free stream turbulence level of 2.5% was assumed, following the far upstream value given by Sanger and Shreeve (Ref. 45). The code was run with the choice of parameters shown in the upper part of Table 12. The code assumes transition onset on the suction surface at the laminar separation and at $Re\delta^* = 700$ for the pressure surface as shown in the table. The location of transition calculated by the code, as a result of the criteria adopted, are shown in the lower part of Table 12. A Prandtl mixing length turbulence model was used.

Preliminary comparisons of the data with the predictions of the code, run under the conditions that no information from the experiment was provided to the operators, are shown in Figure 78 and Figure 79. There was good agreement between the measured and calculated pressure coefficient as shown in Figure 78 for all three inlet angles. A mismatch is noticed at the leading and trailing edges, although the mismatch is relatively small. The calculated boundary layer velocity profile on the suction surface at 90% chord agreed very well with the measured profile as shown in Figure 79.

It is certain that an input of information from the experiment, the transition length for example, would improve the comparison shown in Figure 78, and this is planned. Davis (Ref. 52 and 53), Hah (Ref. 54), Rai (Ref. 55), and Delaney (Ref. 56) have also expressed interest in applying or modifying Navier-Stokes codes to analyze the present sent CD cascade. All codes are based on the Reynolds-averaged Navier-Stokes equations, and therefore require the inclusion of empirical models for laminar-to-turbulent transition, and for turbulent transport of momentum and energy.

TABLE 12.

DATA FOR NAVIER-STOKES CODE

INPUT SELECTED:

GRID: C Type
 113 Pseudo-Azimuthal Points
 30 Pseudo-Radial Points, with First
 Point .0003 Chords from the
 Surface.

TRANSITION DISTANCE Both Surfaces - 0.05 Chords.

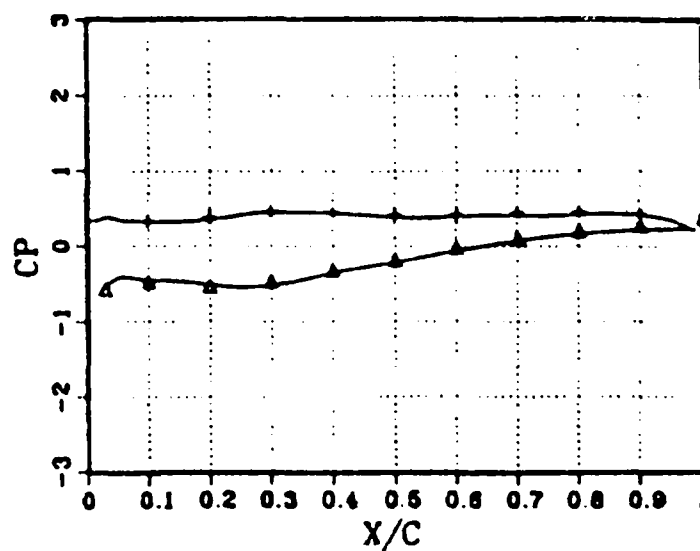
TRANSITION LOCATION

suction surface	separation bubble
pressure surface	$Re_\delta = 700$

CALCULATED BY THE CODE:

TRANSITION LOCATION	$\beta_1 = 40^\circ$	$\beta_1 = 43.4^\circ$	$\beta_1 = 46^\circ$
suction surface	.037	.025	.025
pressure surface	.212	.312	.516

BETA = 40 DEG.



BETA = 43.4 DEG.

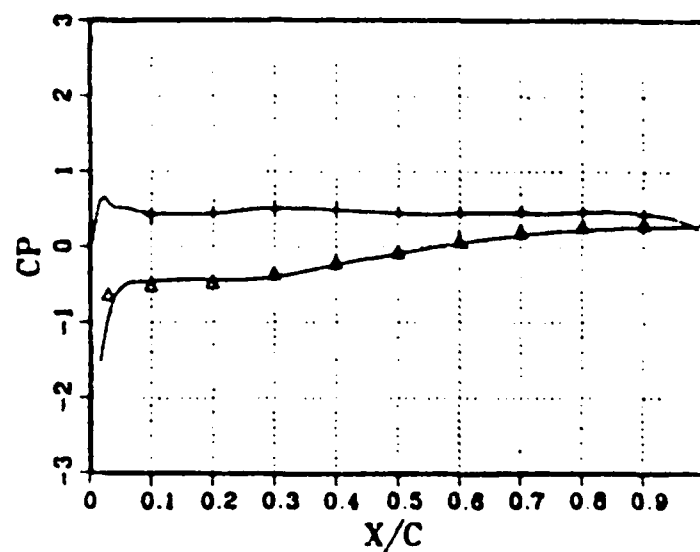


Figure 78. Comparison with Pressure Coefficient Calculated Using Navier-Stokes Code.

— Measured +, ▲ Calculated.

BETA = 46 DEG.

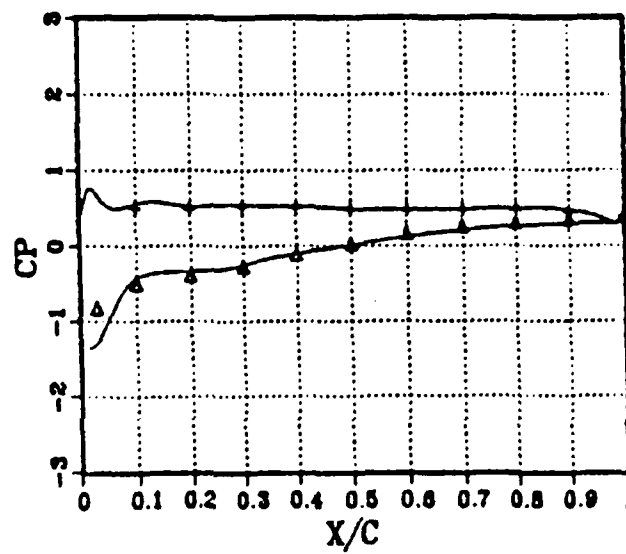


Figure 78. (cont.) Comparison with Pressure Coefficient Calculated Using Navier-Stokes Code.

— Measured +, Δ Calculated.

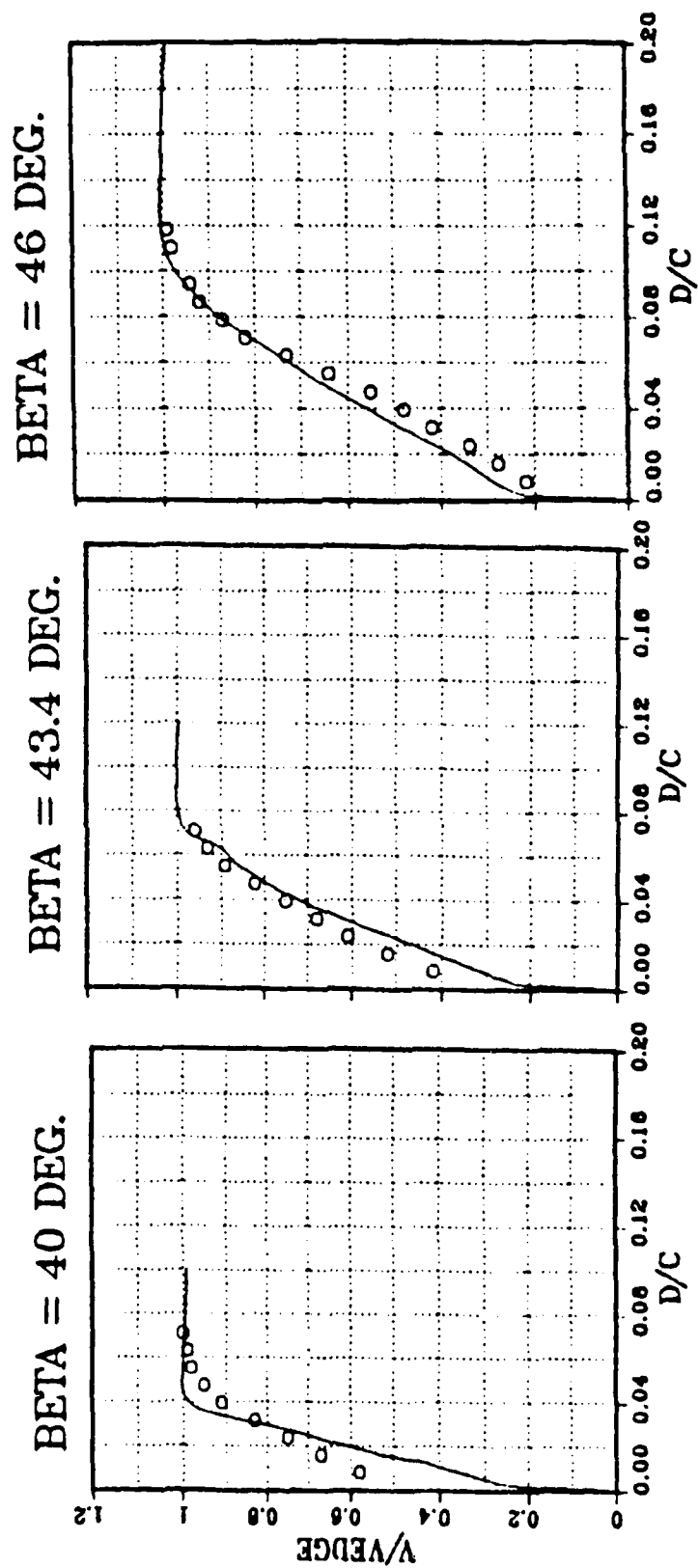


Figure 79. Comparison with Suction Surface Boundary Layer Velocity Profile Using Navier-Stokes Code.

— Measured • Calculated

C. SUMMARY ASSESSMENT

The following is a preliminary assessment of the numerical codes as cascade flow predictors:

- a. The non-interactive boundary layer code predicted boundary layer growth quite well on the forward half of the suction surface of the blade, but quite poorly on the rear half of the suction surface. The interactive boundary layer code predicted boundary layer growth on the pressure surface of the blade quite well once onset of transition and transition length were introduced as input data.
- c. The interactive boundary layer code predicted the flow field on the suction surface quite poorly.
- d. The Navier-Stokes code predicted the flow field in the cascade quite successfully.

VII. CONCLUSIONS AND RECOMMENDATIONS

LDV flow measurements were carried out to determine the passage flow field, the suction and pressure surface boundary layers and the wake flow field of a controlled diffusion compressor cascade. The measurements were performed at nominally constant Mach number (~ 0.25), constant Reynolds number (~ 700000) and at three inlet angles; namely, design condition $\beta_1 = 40^\circ$, and positive incidence inlet angles $\beta_1 = 43.4^\circ, 46^\circ$. The following were concluded:

- a. A separation bubble existed on the suction surface, close to the leading edge. The flow underwent transition in the free shear layer above the bubble. The reattachment point moved downstream as the inlet angle was increased.
- b. The turbulent boundary layer on the suction surface was fully attached throughout the inlet angle range. Separation took place on the blunt trailing edge curvature.
- c. The suction surface boundary layer thickness increased dramatically with inlet angle and reached 15% chord at the highest inlet angle ($\beta_1 = 46^\circ$).
- d. The pressure surface boundary layer changed very little with the inlet angle variations. The flow underwent natural transition at about mid-chord.

- e. Wake velocity LDV measurements compared well with previous calibrated pneumatic probe measurements. The profile of the trailing edge suction and pressure surface boundary layers remained well defined in the wake profiles. Flow reversal was measured close to the trailing edge (within 0.04 chords, or 1.6 trailing edge diameters, downstream the trailing edge), consistent with separation occurring not before the trailing edge curvature.

The LDV data were compared with the predictions of three computational codes: a non-interactive boundary layer code, a research viscous-inviscid interactive code, and a near-production Navier-Stokes code. The following were concluded:

- a. The boundary layer code predicted boundary layer growth properly at the forward half of the blade but was very inaccurate towards the trailing edge. This suggested that transition was modelled well but that assumption of a power law shape for the profile was too restrictive.
- b. The interactive code lacked accuracy in its modelling of transition. However, when the measured onset of transition and transition length were input into the code, the pressure surface boundary layer was predicted well.

- c. The interactive code did not predict transition and boundary layer growth properly on the suction surface. Parameters could not be input or easily edited into the code to correct the prediction, as was done on the pressure surface, since the bubble structure was calculated by the code without reference to empirical inputs.
- d. The Navier-Stokes code, without reference to the results of measurements, predicted the measured surface pressure distributions very well at all three incidence angles. Suction surface boundary layer growth was predicted well although some disagreement was found in the velocity profiles near to the trailing edge. The entry of experimental information into the code is thought certain to improve the degree of agreement.

What has been clearly shown, is that currently available numerical codes for viscous cascade flow depend critically on the modelling of the transition process. What was seen in the experiment was that the boundary layer transition can be followed and mapped using the LDV technique, whereas the laminar bubble, with its free shear layer transition, is invisible to the LDV unless an auxiliary seeding technique is found to seed inside the bubble.

Therefore, the following recommendations are made concerning the future of the immediate experimental and computational work:

1. A technique for seeding the bubble should be sought, and some definition of the bubble region should be attempted.
2. Data should be obtained at one higher angle, ($\sim 48^\circ$) at which separation should move forward, providing an even more difficult test case for codes.
3. The S.I. code should be re-examined in the light of the present disagreements and the transition model in the code should be revised.
4. The inputs to the Navier-Stokes code should be modified, in light of the test data, and the three cases rerun in the attempt to obtain closer agreement at each angle. Comparisons with other Navier-Stokes codes should also be pursued. The data included herein are sufficient to justify computer experimentation with transition models.

Finally, it is clear that the LDV technique can be used to provide the detailed data necessary to calibrate the empiricism inherent in viscous flow computational codes. More data of the type obtained in the present study are rather urgently required, preferably using a wide variety of cascade blade shapes. Also, in a separate experiment, a

very much larger model should be used to create a separation bubble which, with the reattachemnt and downstream viscous development, can be resolved adequately. Until proper models are proven for the transition process, the computational prediction of stall in the cascade cannot be expected to be accurate.

APPENDIX A

PARTICLE SIZE DISTRIBUTION MEASUREMENTS

A1. INTRODUCTION

The oil droplet particle size distribution produced by the seeding apparatus was measured in a preliminary experiment. Since smaller particles follow the flow better than larger ones, the average particle diameter affects the accuracy of velocity measurements and the size distribution affects the accuracy of turbulence measurements. The objectives of the experiment were to determine the optimal seeding pressure and seeder length, and to determine the particle size distribution produced by the chosen seeding probe configuration.

A2. DESCRIPTION OF THE EXPERIMENT

A2.1. Particle Generator

The particle generator which was used is shown in Figure 9. Commercial olive oil was the seeding fluid. The oil reservoir served both as a relaxing chamber for the droplets and as a sump for oil overflow from the atomizer. Oil is fed to the atomizer where the fluid is broken into fine droplets. A mixture of droplets and air flows out of the atomizer, through the relaxation chamber to the seeding probe.

A2.2. Particle Sizer

The particle sizer used in the experiment was a MALVERN 2600 series manufactured by MALVERN Instruments of Malvern, England. The principle of operation is that light is scattered by a particle at an angle which is a function of the particle's diameter. Figure A1 shows a schematic diagram of the system. A He-Ne laser beam passes through the test section where particles are introduced. The scattered light is collected by 31 concentric rings. The distribution of light intensities over the concentric rings is interpreted as particle size distribution through software that was provided by MALVERN. A detailed description of the system (used to measure the particle size distribution in the exhaust of a solid propellant rocket motor) is given by Pruitt (Ref. 57).

A2.3. Procedure and Program of Measurements

First, particle size distribution was measured with varying pressure drop across the atomizer and with various length of the exhaust tube. Data were collected as pressure was varied between 30 and 50 psi, for three different exhaust tube lengths, namely, 40, 80, and 120 inches. A vacuum cleaner constantly sucked the air from the test section to clear olive oil fumes and to prevent residual droplets from previous measurements from affecting the next one. A three-minute interval was maintained between measurements to make sure the test section was

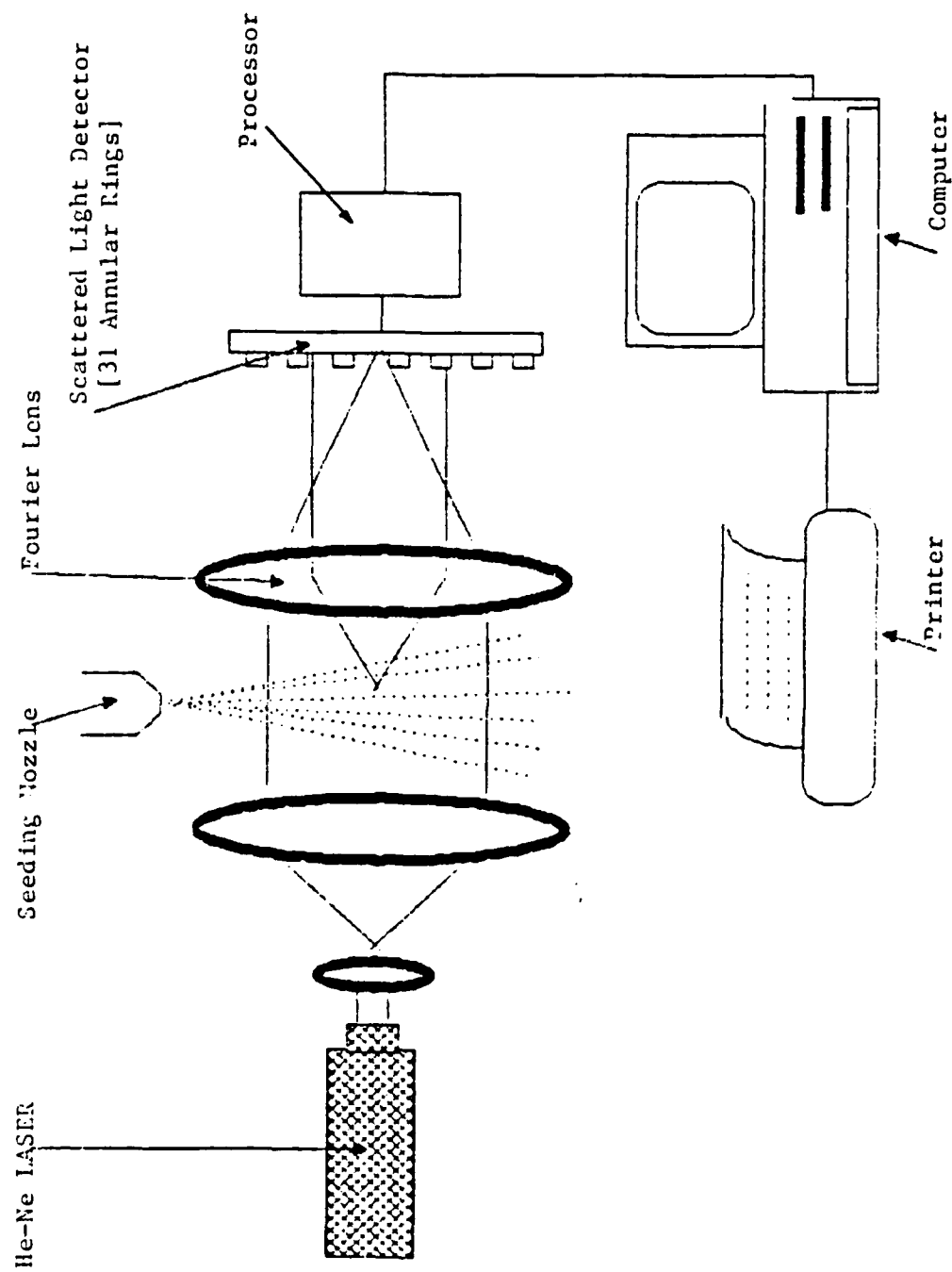


Figure A1. Particle Size Distribution Measurements.

clear and background measurements were frequently taken for the same purpose.

Second, the seeding probe was connected to the exhaust tube coming out of the particle relaxing chamber. Pressure drop across the atomizer was varied between 20 and 50 psi, and particle size distribution data were collected in the same manner as before.

A3. RESULTS AND DISCUSSION

Data from the first part of the experiment are summarized in Table A1. The data values are the percentage of particles with diameters smaller than the indicated values (in microns) for different pressures (p) and exhaust tube lengths (L). It was concluded that the best size distribution was obtained for $L = 120"$, $p = 40$ psi. Under those conditions the particle generator produced droplet diameters below 2.6 microns, with more than half below 1.2 microns in diameter. The seeding probe was, therefore, designed to have a total length less than 120".

The data from the second part of the experiment are summarized in Tables A2 and A3 and plotted in Figure A2. Table A2 contains the data output by the particle sizer data acquisition system. Table A3 shows a presentation of these data in the form of a histogram of size distribution, average droplet diameter, and standard deviation for each case. Figure A2 is a plot of the histogram using the data

TABLE A1						
<u>PARTICLE SIZE DISTRIBUTION</u>						
(Seeder Probe Not Included)						
SIZE (MIC)	UNDER (%) L= 40" P= 40	UNDER (%) L= 40" P= 50	UNDER (%) L= 80" P= 30	UNDER (%) L= 80" P= 40	UNDER (%) L= 80" P= 50	UNDER (%) L= 120" P= 40
1.2	40.3	55.5	14.2	36.7	27.3	53.9
1.4	72.4	85.5	43.6	69.7	57.3	84.4
1.6	95.9	95.8	80.1	94.6	91.4	95.2
1.9	97.6	99.1	89.0	96.9	97.7	98.7
2.2	98.6	99.9	93.6	98.1	99.6	99.9
2.6	99.1	99.9	95.4	98.8	99.6	100.0
3.0	99.5	100.0	96.7	99.4	99.7	100.0
3.4	99.0	100.0	98.3	99.7	99.9	100.0
4.0	100.0	100.0	99.7	99.9	99.9	100.0
4.6	100.0	100.0	100.0	100.0	100.0	100.0

TABLE A2

PARTICLE SIZE DISTRIBUTION

(With Seeder Probe)

PRESSURE (PSI)	Under . . . Microns											
	0.5 %	1.2 %	1.4 %	1.6 %	1.9 %	2.2 %	2.6 %	3.0 %	3.4 %	4.0 %	4.6 %	
40.0	21.8	65.7	90.2	97.7	98.8	99.5	99.8	99.9	100.	100.	100.	
40.0	21.7	66.0	90.3	97.8	98.9	99.5	99.8	99.9	100.	100.	100.	
35.0	20.7	68.1	91.0	97.7	98.5	99.2	99.8	99.9	100.	100.	100.	
35.0	20.4	68.6	91.2	97.8	98.5	99.2	99.7	99.9	100.	100.	100.	
30.0	20.7	67.8	90.7	97.5	98.2	99.0	99.6	99.9	100.	100.	100.	
30.0	20.7	67.9	90.8	97.5	98.2	99.0	99.6	99.9	100.	100.	100.	
25.0	38.7	51.3	89.5	98.0	98.6	99.0	99.5	99.8	99.9	99.9	100.	
25.0	39.9	49.0	88.7	97.7	98.4	99.0	99.4	99.8	100.	100.	100.	
25.0	39.1	50.7	89.3	97.9	98.5	99.0	99.5	99.8	100.	100.	100.	
20.0	38.8	50.8	89.1	97.6	98.2	98.6	99.1	99.6	99.9	99.9	100.	
20.0	39.5	49.6	88.8	97.5	98.2	98.7	99.2	99.6	99.8	99.9	100.	
20.0	39.6	49.3	88.6	97.5	98.1	98.7	99.2	99.6	99.8	99.9	100.	
C	NEW BACKGROUND WAS TAKEN											
40.0	24.1	59.9	87.5	96.5	98.5	99.6	100.	100.	100.	100.	100.	
40.0	23.6	61.1	88.1	96.8	98.6	99.7	100.	100.	100.	100.	100.	
40.0	23.9	60.3	87.7	96.6	98.5	99.6	100.	100.	100.	100.	100.	
45.0	23.4	61.8	88.5	97.0	98.8	99.7	100.	100.	100.	100.	100.	
45.0	23.5	61.4	88.3	96.9	98.6	99.6	99.9	100.	100.	100.	100.	
45.0	23.4	61.9	88.5	97.0	98.7	99.7	100.	100.	100.	100.	100.	
45.0	23.3	62.1	88.6	97.0	98.7	99.7	100.	100.	100.	100.	100.	
50.0	22.6	63.6	89.2	97.2	98.6	99.3	99.7	99.9	100.	100.	100.	

TABLE A3
PARTICLE SIZE DISTRIBUTION IN HISTOGRAM FORMAT

(With Seeder Probe)													
Under . . . Microns													
PRESS. (PSI)	0.3	0.8	1.3	1.5	1.8	2.0	2.4	2.8	3.2	3.7	4.3	DIAM.	STD.
	%	%	%	%	%	%	%	%	%	%	%		
40.0	21.8	43.9	24.5	7.5	1.1	0.7	0.3	0.1	0.1	0.0	0.0	0.91	0.438
40.0	21.7	44.3	24.3	7.5	1.1	0.6	0.3	0.1	0.1	0.0	0.0	0.90	0.436
35.0	20.7	47.4	22.9	6.7	0.8	0.7	0.6	0.1	0.1	0.0	0.0	0.90	0.432
35.0	20.4	48.2	22.6	6.6	0.7	0.7	0.5	0.2	0.1	0.0	0.0	0.90	0.431
30.0	20.7	47.1	22.9	6.8	0.7	0.8	0.6	0.3	0.1	0.0	0.0	0.91	0.442
30.0	20.7	47.2	22.9	6.7	0.7	0.8	0.6	0.3	0.1	0.0	0.0	0.91	0.441
25.0	38.7	12.6	38.2	8.5	0.6	0.4	0.5	0.3	0.1	0.0	0.1	0.87	0.551
25.0	39.9	9.1	39.7	9.0	0.7	0.6	0.4	0.4	0.2	0.0	0.0	0.88	0.558
25.0	39.1	11.6	38.6	8.6	0.6	0.5	0.5	0.3	0.2	0.0	0.0	0.87	0.549
20.0	38.8	12.0	38.3	8.5	0.6	0.4	0.5	0.5	0.3	0.0	0.1	0.88	0.568
20.0	39.5	10.1	39.2	8.7	0.7	0.5	0.5	0.4	0.2	0.1	0.1	0.88	0.573
20.0	39.6	9.7	39.3	8.9	0.6	0.6	0.5	0.4	0.2	0.1	0.1	0.89	0.575
40.0	24.1	35.8	27.6	9.0	2.0	1.1	0.4	0.0	0.0	0.0	0.0	0.93	0.465
40.0	23.6	37.5	27.0	8.7	1.8	1.1	0.3	0.0	0.0	0.0	0.0	0.92	0.457
40.0	23.9	36.4	27.4	8.9	1.9	1.1	0.4	0.0	0.0	0.0	0.0	0.92	0.463
45.0	23.4	38.4	26.7	8.5	1.8	0.9	0.3	0.0	0.0	0.0	0.0	0.92	0.452
45.0	23.5	37.9	26.9	8.6	1.7	1.0	0.3	0.1	0.0	0.0	0.0	0.92	0.458
45.0	23.4	38.5	26.6	8.5	1.7	1.0	0.3	0.0	0.0	0.0	0.0	0.92	0.453
45.0	23.3	38.8	26.5	8.4	1.7	1.0	0.3	0.0	0.0	0.0	0.0	0.92	0.452
50.0	22.6	41.0	25.6	8.0	1.4	0.7	0.4	0.2	0.1	0.0	0.0	0.92	0.455

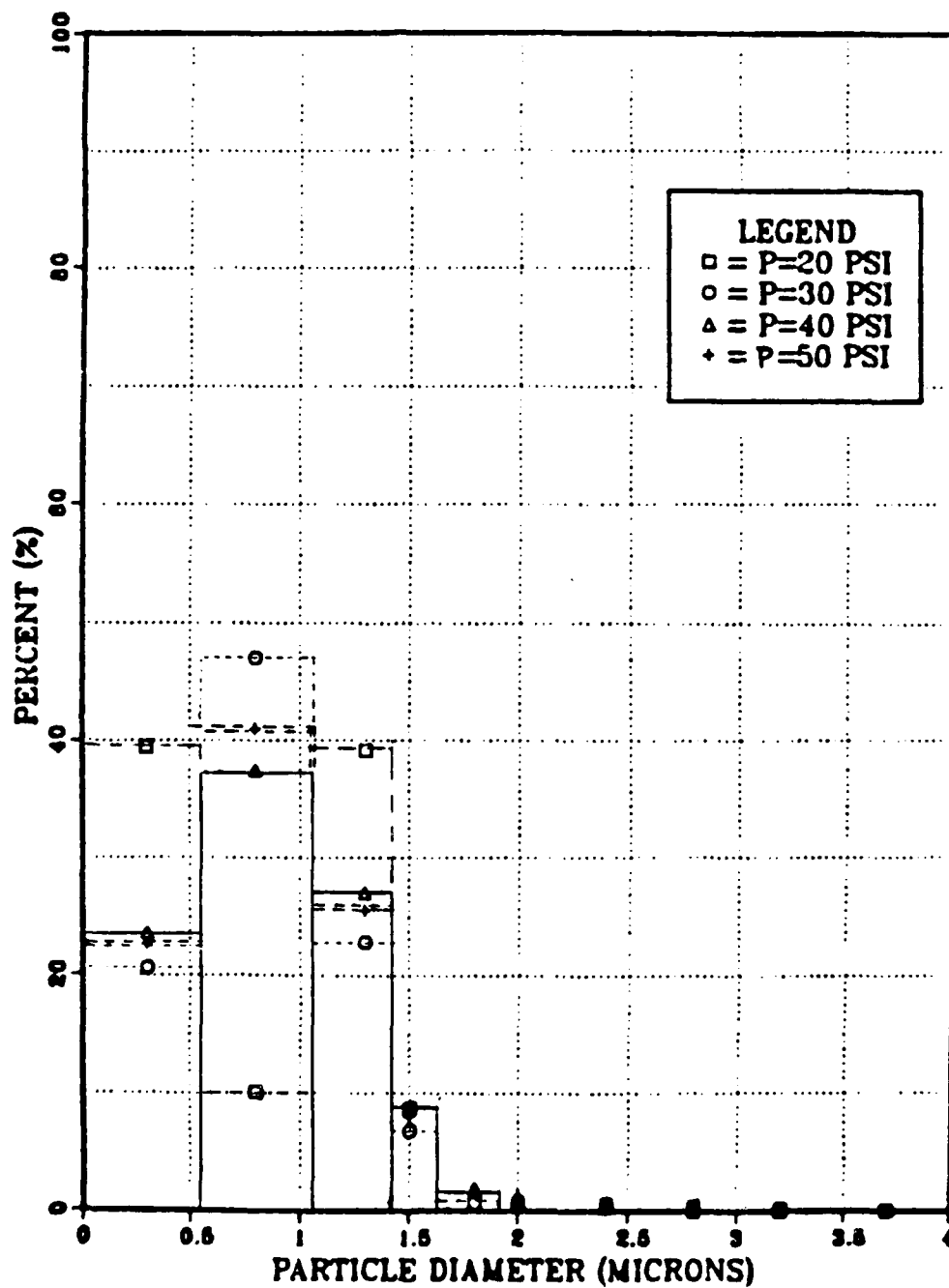


Figure A2. Particle Size Distribution.

in Table A3. The average particle diameter varied between 0.88 and 0.93 microns. The standard deviation varied between 0.43 and 0.58. The smallest average particle diameter was achieved with low pressures (20-25 psi) but the distribution was not favorable since there was a large number of larger particles. Forty percent of the particles were larger than 1.2 microns. The average diameter was favorable at these pressures, but the standard deviation was unfavorable. In contrast, for pressures between 30-50 psi, little change in the average diameter and standard deviation was noted.

A4. CONCLUSIONS

- a. The average particle diameter for an atomizer pressure drop of 30-50 psi was 0.9 - 0.95 microns.
- b. The standard deviation in the size at those conditions was 0.44 - 0.47 microns.
- c. Ninety percent of the droplets were smaller than 1.5 microns.
- d. The data agreed with the atomizer manufacturer's manual which specified an average particle diameter of 0.8 - 0.9 microns for most mineral and vegetable oils at 30-50 psi pressure drop.

APPENDIX B

PRELIMINARY MEASUREMENTS OF THE BOUNDARY LAYER ON A FLAT PLATE

B1. INTRODUCTION

Measurements were made of the distribution of velocity and turbulence in the boundary layer on a flat plate. Results were compared with the Blasius solution for a laminar boundary layer on a flat plate and with published experimental results. The experiment served to verify the use of the LDV system for boundary layer measurements in the compressor cascade wind tunnel.

B2. DESCRIPTION OF THE EXPERIMENT

B2.1. Wind Tunnel and Model

The arrangement of the test section and model are shown in Figure B1. The wind tunnel's adjustable walls were set to 40 degrees and the test blades were removed from the test section. A specially designed flat plate model was installed at the 7th blade station ($1/3$ tunnel width). A cross-section of the flat plate is shown in Figure B2. The section had a sharp edge and a blunt edge as shown in the figure. The model was black anodized to reduce light reflections from the surface which allowed flow measurements closer to the wall. The flat plate was installed with the sharp leading edge forward, with the flat test surface set

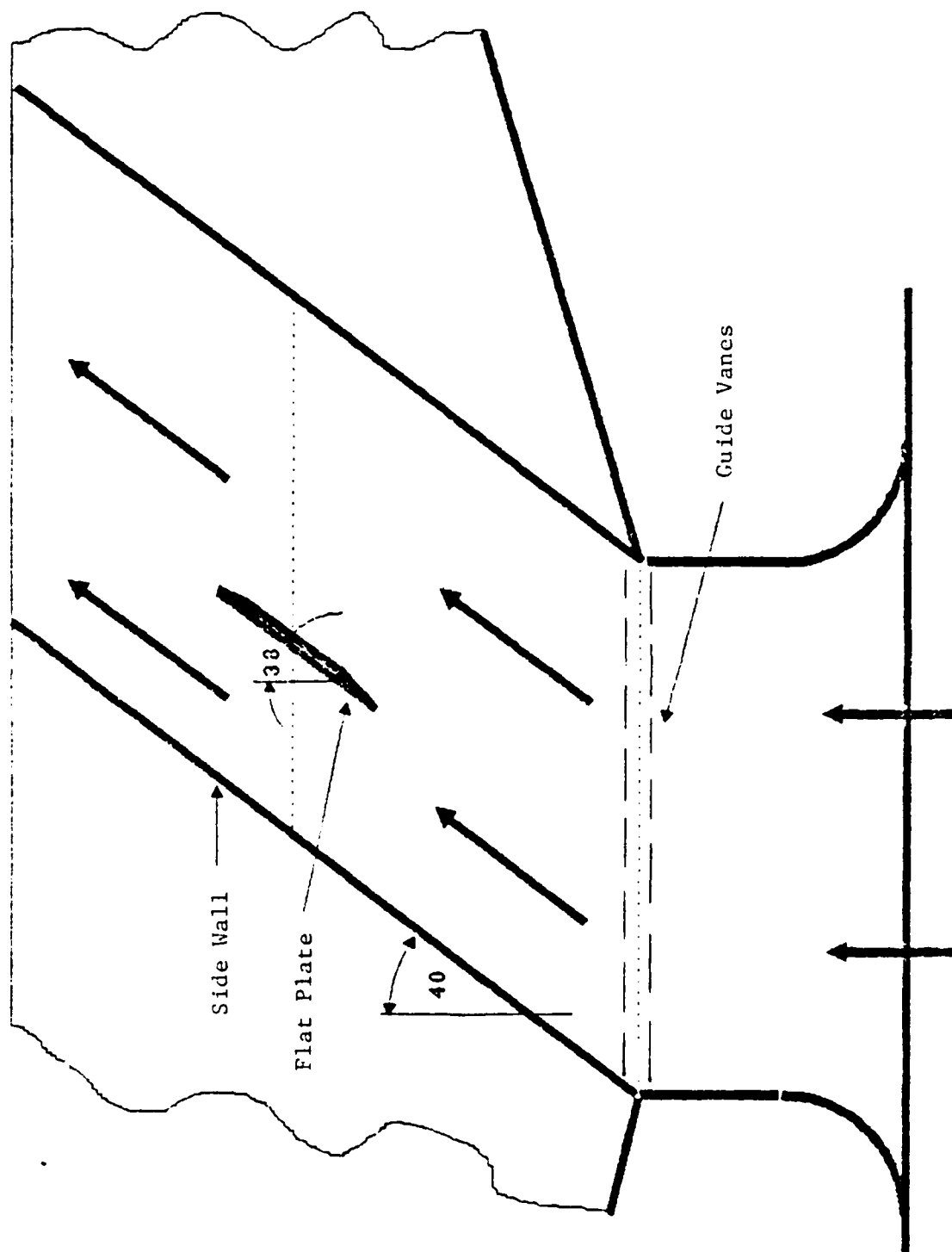


Figure B1. Flat Plate Installed in the Cascade Wind Tunnel.

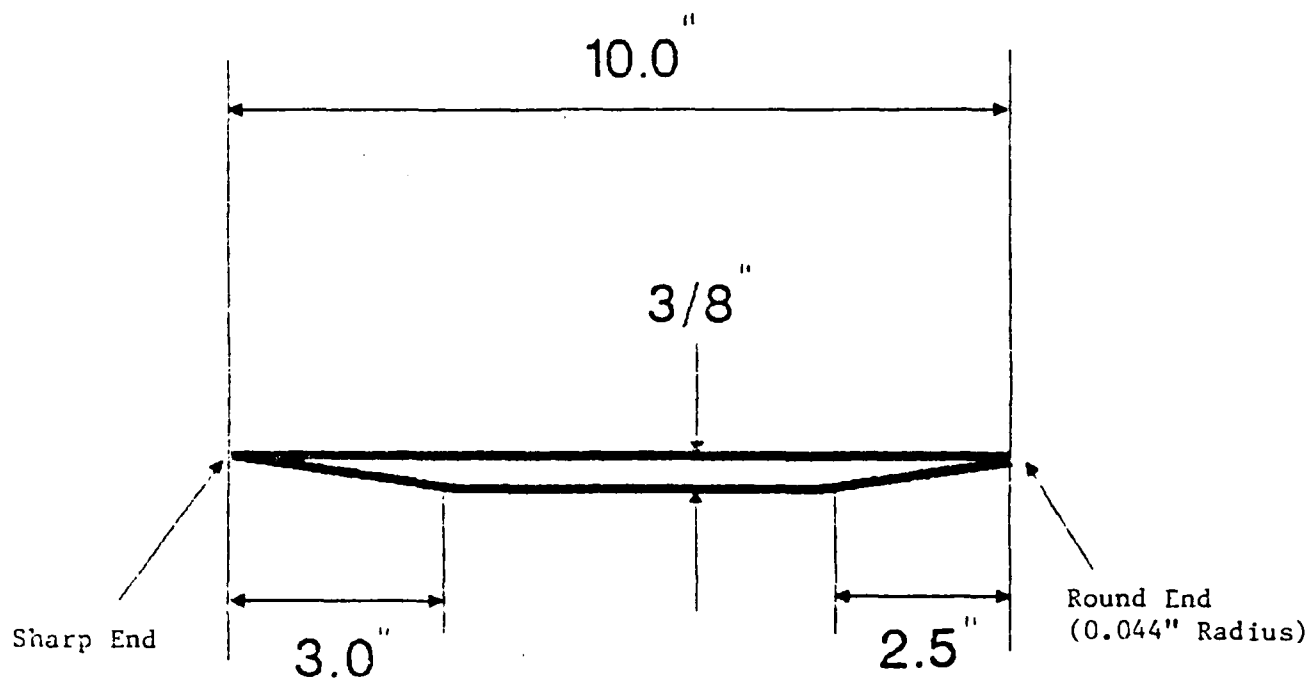


Figure B2. Flat Plate Model.

at an angle of 38 degrees. (The flat plate surface was thus at a negative angle of attack of 2 degrees with respect to the inlet walls as shown in Figure B1.) This prevented a leading edge flow separation that could cause transition to turbulent flow as was found by McGuire (Ref. 43).

B2.3 LDV System

The LDV system was as shown in Figure 8 except that the Bragg cells and the frequency shifters were removed.

B2.3 Procedure and Program of Measurements

Data were obtained for a range of Reynolds numbers by setting the wind tunnel blower to different speeds. At each speed, the LDV system was moved to the desired position downstream of the plate leading edge. The LDV traverse was adjusted to position the measuring volume at the surface, and the coordinates were recorded. LDV data were then acquired as the measuring volume was manually traversed to select displacements along a line normal to the plate surface. Five (5) different boundary layer distributions were measured, corresponding to different blower speeds and (x) position downstream of the leading edge; namely,

Boundary layer #1	x = 1.0"	Rex = 37500
Boundary layer #2	x = 1.0"	Rex = 65700
Boundary layer #3	x = 2.0"	Rex = 79000
Boundary layer #4	x = 3.5"	Rex = 152500
Boundary layer #5	x = 9.0"	Rex = 530000

The two components of the velocity and the turbulence level were measured with the LDV system. Plenum pressure was measured using a water manometer. Data were then corrected and normalized to the free stream velocity using the plenum pressure.

B3. RESULTS AND DISCUSSION

Free stream turbulence was measured to be $1.4 \pm 0.2\%$. Results are shown plotted in Figures B3 and B4. The velocity component parallel to the flat plate, normalized by the edge velocity is shown plotted as a function of the distance away from the wall in Figure B3. The lines represent the theoretical Blasius solution for a laminar boundary layer and the symbols represent the measured values. The data are shown plotted in linear coordinates (not in semi-log coordinates) so that differences between the measured velocities and the theoretical distribution are clear.

It can be seen that at lower Reynolds numbers (37500, 65700, 79000) there was good agreement between the measurements and the theoretical analysis. At higher Reynolds numbers (152500, 530000) there was good agreement close to the wall (below 0.5 mm) but as the measuring volume was traversed away from the wall a departure occurred. At a Reynolds number of 152500 the flow was apparently in transition. Wang et al (Ref. 27) showed similar results obtained with a hot-wire anemometer. They observed that

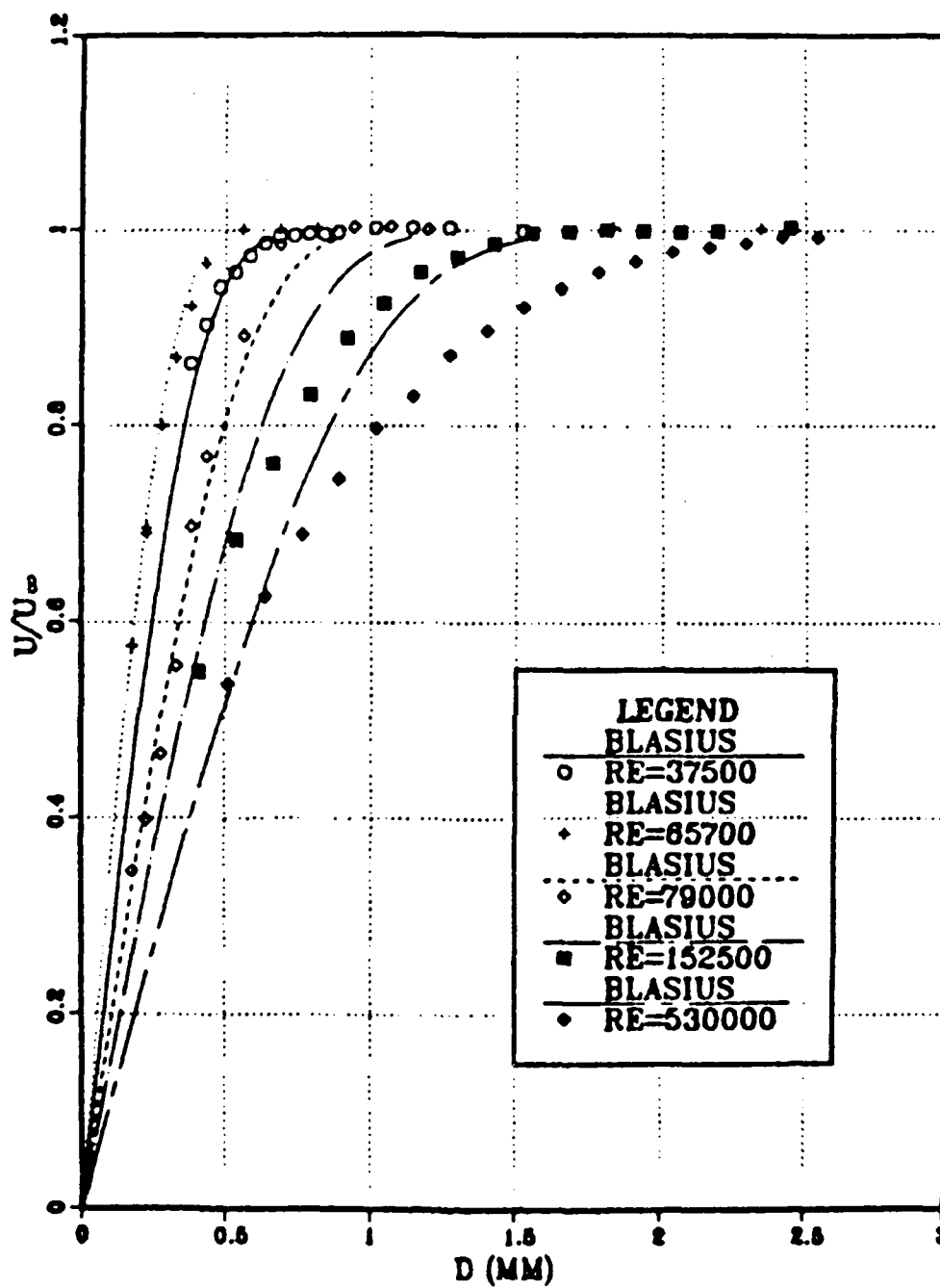


Figure B3. Boundary Layer on a Flat Plate.

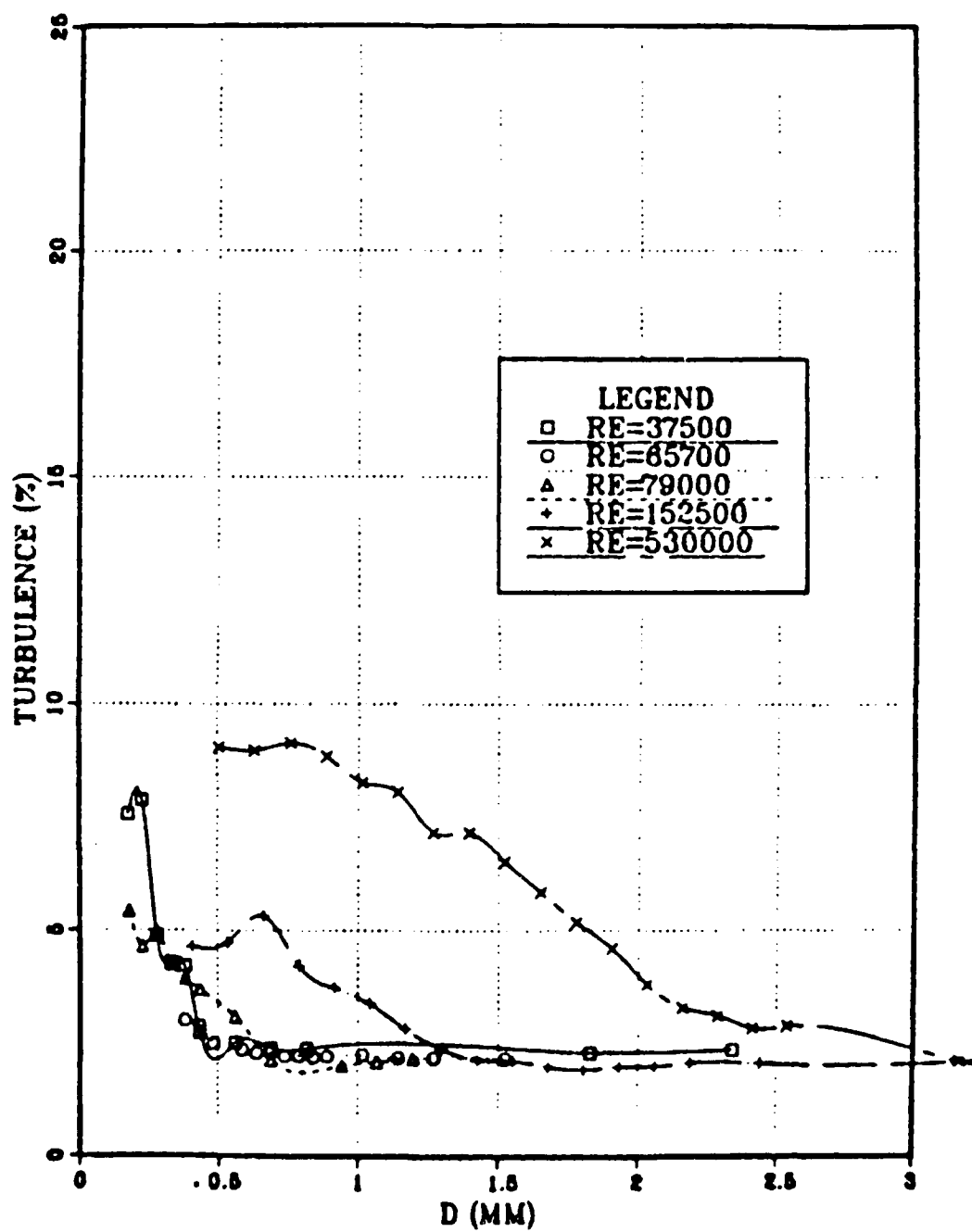


Figure B4. Boundary Layer on a Flat Plate.

with a free stream turbulence level of 2%, transition began at Reynolds numbers of 100000 to 200000. In particular, at $REX = 107000$, a lack of agreement with the Blasius profile was observed at the edge of the boundary layer. Blair (Ref. 26) showed that at a free stream turbulence level of 2%, the flow transitioned at a displacement thickness Reynolds number of 800. The displacement thickness Reynolds number of Curve #4 in Figure B3 is 766.

The measured turbulence level distributions are shown in Figure A4. The data by Wang et al (Ref 27) showed similar trends. The measured laminar boundary layer turbulence levels ranged from 5% close to the wall to 1.4% at the edge of the boundary layer, whereas for the high Reynolds number (530000) the measured turbulence was somewhat higher (9%). Even higher levels of turbulence (11%) were reported by Wang et al (Ref. 27) for the laminar layer when measurements were made closer to the wall.

B4. CONCLUSIONS

- a. Measurements of purely laminar boundary layers with the LDV system showed good agreement with the theoretical Blasius profiles.
- b. Transition of the flow was detected at Reynolds numbers which were consistent with previously reported results.

- c. In view of the observed agreement, it was concluded that the seeding particles followed the flow. Using the Blasius analysis, particles in the flow were found to follow an acceleration of $a = 6200 \text{ m/sec}^2$.
- d. Turbulence measurements were in agreement with similar previously reported measurements obtained with a hot-wire anemometer.

APPENDIX C

CALCULATION OF THE INLET FLOW REFERENCE VELOCITY USING PLENUM PRESSURE AND TEMPERATURE MEASUREMENTS

C1. INTRODUCTION

Each measurement of velocity was divided by a reference velocity to give dimensionless velocity data. The reference velocity was the free stream inlet velocity to the test section at the time the LDV measurement was made, calculated using plenum pressure and temperature measurements. The following is a description of the method used for calculating the reference velocity.

C2. METHOD

The relationship between the upstream stagnation (p_{t1}) and static pressure (p_1), and the dimensionless velocity, $x = (V/\sqrt{2C_p T_{t1}})$, assuming isentropic perfect gas flow, is given by

$$\frac{p_{t1} - p_1}{p_{t1}} = 1 - \frac{p_1}{p_{t1}} = v(x) \quad C(1)$$

where

$$v(x) = \frac{\gamma}{\gamma-1} \cdot x^2 (1-x^2) \frac{1}{\gamma-1}$$

Losses in the guide vanes are represented using the loss coefficient ω_g defined as

$$\omega_g = \frac{p_{t0} - p_{t1}}{q_0}$$

so that Equation C(1) becomes, assuming no density change across the vanes,

$$p_{t1} = p_{t0} - \rho_0 \omega_g = p_{t0} - \rho_1 \cos^2 \beta_1 \cdot \omega_g \quad C(2)$$

Losses in the test section are represented similarly as

$$\omega_b = \frac{p_{t1} - p_{t2}}{\rho_1}$$

Therefore, assuming no density change across the test blades,

$$p_{t1} = p_{t2} + \rho_1 \omega_b = p_2 + \rho_1 \frac{\cos^2 \beta_1}{\cos^2 \beta_2} + \rho_1 \omega_b = p_1 + \rho_1$$

giving

$$p_1 = p_2 + \rho_1 \left(\frac{\cos^2 \beta_1}{\cos^2 \beta_2} + \omega_b - 1 \right) \quad C(3)$$

Using Equation C(2), Equation C(3) and Equation C(1)

$$1 - \frac{p_2 + \rho_1 \left(\frac{\cos^2 \beta_1}{\cos^2 \beta_2} + \omega_b - 1 \right)}{p_{t0} - \rho_1 \cos^2 \beta_1 \cdot \omega_g} = v(X) \quad C(4)$$

Since p_2 is approximately atmospheric pressure, ω_b and ω_g are less than 0.1, and the velocities to the test section are less than 100 m/sec ($X < 0.1$), Equation C(4) can be simplified to obtain

$$1 - \frac{p_2}{p_{t0}} \approx \frac{p_{t0} - p_{atm}}{p_{atm}} = C_0 v(X) \quad C(5)$$

in which C_0 is a constant for small variations in X .

Equation C(5) relates the dimensionless upstream velocity in the test section to the difference between plenum and atmospheric pressures, and the absolute level of atmospheric pressure, through an unknown constant C_0 . C_0 depended on the geometrical configuration of the tunnel, and was established by calibration for each new setting of the inlet angle. The calibration involved measuring v_1 using the LDV system while recording $(p_{t0} - p_a)$, p_a and T_{t0} . The dimensionless velocity was calculated using

$$X = v / \sqrt{2C_p T_{t0}} \quad C(6)$$

and C_0 was calculated using Equation C(5).

With C_0 established, for each LDV measurement of velocity within the test section, the reference inlet velocity was calculated using Equation C(6) and Equation C(5), using plenum and atmospheric conditions at the time of the measurement.

APPENDIX D

LISTING OF SOFTWARE

CASCADE FORTRAN

```

*****
**   THIS FILE CONTAINS A PROGRAM THAT READS THE LDV DATA CORRECTS
**   THE VELOCITIES, CALCULATES THE TURBULENCE AND CALCULATES THE
**   STREAM FUNCTION FIELD FOR STREAMLINES PLOTS. STREAMLINES ARE
**   CALCULATED BY           $D(P_{SII}) = V \cdot DX$           ASSUMING  $P_{SII} = 0$  AT THE
**   LEFT BOUNDARY.
*****
*
* ALFA ..... FLOW ANGLE
* CP12 ..... COEFFICIENT.
* PAMB ..... STATIC PRESSURE.
* PSIE ..... NORMALIZED STREAM FUNCTION.
* PSII ..... STREAM FUNCTION.
* PT ..... PLENUM PRESSURE.
* ROLL ..... LDV OPTICS ROLL ANGLE.
* TT ..... PLENUM TEMPERATURE.
* TURB ..... TURBULENCE LEVEL.
* TURBU ..... U COMPONENT TURBULENCE.
* TURBV ..... V COMPONENT TURBULENCE.
* U .....VELOCITY.
* V .....VELOCITY.
* X ..... COORDINATE.
* Y ..... COORDINATE.
* YAW ..... LDV OPTICS YAW ANGLE.
C
  REAL C(1000),PSII(100,100),VC(100),X(100,100),X1(100),Y(100)
  REAL C0(100,20),C1(100,20),C2(100,20),C3(100,20),PSIE(100,100)
  INTEGER N(100)

```

```

      READ (11,*) M,CP12
      WRITE (21,*) '      BLADE TO BLADE FLOW FIELD '
      WRITE (21,*) '      ===== '
      WRITE (21,40)
      WRITE (21,30) M
      WRITE (21,40)
      WRITE (21,*) '      Y(INCH)      X(INCH)      U(M/SEC)      V(M/SEC)      VEL(M/S)
1ALFA(DEG)  TURB(%)'
      WRITE (21,*) '      _____      _____      _____      _____      _____
1 _____      '
C  MAIN LOOP
      DO 10 J = 1,M
        PSII(1,J) = 0.0
        READ (11,*) Y(J),N(J),PAMB,ROLL
        ROLL = ROLL*3.1416/180.
        PAMB = PAMB*13.596
        DO 11 I = 1,N(J)
          READ (11,*) X(I,J),U,TURBU,V,TURBV,PT,TT,YAW
          YAW = YAW*3.1416/180.
C  CORRECT FOR U,V ..... UC,VC(I)
          BETA = PT/(PAMB+PT)
          CALL SOLVE (BETA,CP12,XX)
          VELMES = XX*SQRT(1115.5*(TT+460.))
          TURB = SQRT(((TURBU*U)**2+(TURBV*V)**2)/2.)
          TURB = TURB/VELMES
          UC = (U*COS(ROLL)-V*SIN(ROLL))/VELMES
          UC = UC*COS(YAW)
          VC(I) = (U*SIN(ROLL)+V*COS(ROLL))/VELMES

          VEL = SQRT(UC**2+VC(I)**2)
          ALFA = ATAN(UC/VC(I))
          ALFA = ALFA * 180./3.14159
          X1(I) = X(I,J)
          IF (I.GE.2) GOTO 15
          WRITE (21,31) Y(J),X1(I),UC,VC(I),VEL,ALFA,TURB
          GOTO 11
15          WRITE (21,32) X1(I),UC,VC(I),VEL,ALFA,TURB
11          CONTINUE

          NX = N(J)
          IC = NX - 1
          CALL ICSCCU (X1,VC,NX,C,IC,IER)
          DO 12 I = 1,IC
            D = X1(I+1)-X1(I)
            II = IC + I

            III = IC + II
            PSII(I+1,J) = C(III)*D**4/4.+C(II)*D**3/3.+C(I)*D**2/2.
1              +VC(I)*D+PSII(I,J)

```



```

        C3(I,J) = C(III)
        C2(I,J) = C(II)
        C1(I,J) = C(I)
        C0(I,J) = VC(I)
12      CONTINUE
10      CONTINUE
      WRITE (21,40)
      WRITE (21,*) '          STREAM FUNCTION PRINTOUTS '
      WRITE (21,*) '          _____ '
      WRITE (21,40)
      WRITE (21,*) '  Y(INCH)    X(INCH)    PSII '
      WRITE (21,*) '  _____    _____    _____ '
      WRITE (21,40)
      ICOUNT = 0
      DO 13 J = 1,M
        DO 14 I = 1,N(J)
          ICOUNT = ICOUNT + 1
          PSIE(I,J) = PSII(I,J)/PSII(N(J),J)
C          IF (I.GE.2) GOTO 16
          WRITE (21,34) Y(J),X(I,J),PSII(I,J)
C          GOTO 14
C 16      WRITE (21,33) X(I,J),PSII(I,J)
14      CONTINUE
13      CONTINUE
      WRITE (21,35) ICOUNT
C
      WRITE (97,50) M
      DO 20 J = 1,M
        NJM1= N(J)-1
        WRITE (97,51) NJM1,Y(J)
        DO 21 I = 1,NJM1
          WRITE (97,52) X(I,J),PSIE(I,J),C0(I,J),C1(I,J),C2(I,J),
1          C3(I,J)
21      CONTINUE
20      CONTINUE
30      FORMAT (6X,I3,' DATA ROWS')
31      FORMAT (3X,F6.3,4X,F6.3,4X,F6.3,4X,F6.3,4X,F6.3,4X,F6.2,5X,F5.2)
32      FORMAT (13X,F6.3,4X,F6.3,4X,F6.3,4X,F6.3,4X,F6.2,5X,F5.2)
33      FORMAT (13X,F6.3,4X,F6.4)
34      FORMAT (3X,F6.3,4X,F6.3,4X,F6.4)
35      FORMAT (2X,'# OF DATA POINTS =',I4)
40      FORMAT (//)
50      FORMAT (2X,I2)
51      FORMAT (2X,I3,2X,F6.3)
52      FORMAT (2(2X,F7.4),4(2X,E11.4))
      STOP
      END

```

BLAYER1 FORTRAN

```

*****
**      THIS PROGRAM READS THE BOUNDARY LAYER LDV DATA NORMALIZES IT
**      WITH THE FREE STREAM VELOCITY AND TRANSFORMS THE DATA TO COORD.
**      PARALEL AND VERTICAL TO THE SURFACE. IT ALSO CALCULATES THE
**      DISPLACEMENT AND MOMENTUM THICKNESS AND THE SHAPE FACTOR.
*****
*
* ALFA .... FLOW ANGLE.
* CP12 .... COEFFICIENT.
* D ..... DISTANCE FROM BLADE SURFACE.
* DC ..... DISTANCE FROM BLADE SURFACE NORMALIZED BY CHORD.
* DELTA ... DISPLACEMENT THICKNESS.
* H ..... SHAPE FACTOR.
* PAMB .... STATIC PRESSURE.
* PT ..... PLENUM PRESSURE.
* ROLL .... LDV OPTICS ROLL ANGLE.
* THETA ... MOMENTUM THICKNESS.
* TT ..... PLENUM TEMPERATURE.
* TURB .... TURBULENCE LEVEL.
* TURBU ... U COMPONENT TURBULENCE.
* TURBV ... V COMPONENT TURBULENCE.
* U ..... VELOCITY
* UPAR .... VELOCITY PARALLEL TO BLADE SURFACE.
* UPARN ... UPAR NORMALIZED BY REFERENCE VELOCITY.
* V ..... VELOCITY
* VVER .... VELOCITY NORMAL TO BLADE SURFACE.
* VVERN ... VVER NORMALIZED BY REFERENCE VELOCITY.
* X ..... COORDINATE.
* Y ..... COORDINATE.
* YAW .... LDV OPTICS YAW ANGLE.
C
      REAL D(100),DC(100),TURB(100),UPAR(100),UPARN(100),VVER(100),
1      VVERN(100)
C
      CHARACTER*8 SURFCE
      YAW = 3.5*3.1416/180.
C
C READ LDV DATA
C
      READ (31,*) YB,K,N,PAMB,CP12,ROLL,ALFA
      READ (31,*) N1
      PAMB = PAMB*13.596
      ROLL = ROLL*3.1416/180.
      ALFA = ALFA*3.1416/180.

```

```

SURFCE= 'SUCTION '
IF (K.LT.0) SURFCE = 'PRESSURE'
DO 10 I = 1,N
    READ (31,*) X,Y,U,TURBU,V,TURBV,PT,TT
C
C CORRECT FOR U,V
C
    BETA = PT/(PAMB+PT)
    CALL SOLVE (BETA,CP12,XX)
    VELMES = XX*SQRT(1115.5*(TT+460.))
    TURB(I) = SQRT(((TURBU*U)**2+(TURBV*V)**2)/2.)/VELMES
    UN = U/VELMES
    VN = V/VELMES

    UNHOR = (UN*COS(ROLL)-VN*SIN(ROLL))*COS(YAW)
    UNVER = UN*SIN(ROLL) + VN*COS(ROLL)
    UPAR(I) = UNHOR*SIN(ALFA)+UNVER*COS(ALFA)
    VVER(I) = UNHOR*COS(ALFA)-UNVER*SIN(ALFA)
    IF (K.LT.0) VVER(I) = -VVER(I)
    D(I) = SQRT(X**2+Y**2)
    DC(I) = D(I)/5.01
10 CONTINUE
C
C NORMALIZE WITH LOCAL FREE STREAM DATA.
C
    FACTOR = UPAR(N1)
    DO 11 I = 1,N
        UPARN(I) = UPAR(I)/FACTOR
        VVERN(I) = VVER(I)/FACTOR
11 CONTINUE
C
C DISPLACEMENT & MOMENTUM THICKNESS, SHAPE FACTOR
C
    DELTA = 0.
    THETA = 0.
    DO 12 I = 1,N1-1
        DELTA = DELTA + (1.-(UPARN(I)+UPARN(I+1))/2.)*(D(I+1)-D(I))
        THETA = THETA + ((1.-UPARN(I))*UPARN(I)+(1.-UPARN(I+1))*UPAR
1      +1))*(D(I+1)-D(I))/2.
12 CONTINUE
    H = DELTA/THETA
C
C PRINTOUTS
C
    WRITE (32,*) '          BOUNDARY LAYER OUTPUT'
    WRITE (32,*) '          ====='
    WRITE (32,40)
    WRITE (32,30) YB,SURFCE

```



```
      RETURN
15      C(1) = C1
        C(2) = C2
        C(3) = C3
        C(4) = C4
14      CONTINUE
      RETURN
END
```

WAKE1 FORTRAN

```
*****
**      THIS PROGRAM READS THE WAKE LDV DATA AND NORMALIZES IT WITH
**      THE INLET VELOCITY WHICH IS CALCULATED USING PLENUM PRESSURE AND
**      TEMPERATURE. FOR THE CASE OF BEAMS ROTATED BY SOME ROT ANGLE.
*****
```

C

C

NOMENCLATURE

C

```
*      A..... HORIZONTAL COMPONENT OF THE MEASURED VELOCITY.
*      ALFA(I,J) .... ANGLE OF VELOCITY VECTOR
*      B..... VERTICAL COMPONENT OF THE MEASURED VELOCITY.
*      CP12..... COEFFICIENT
*      M ..... # OF ROWS
*      N(J) ..... # OF DATA POINTS PER ROW
*      PAMB ..... AMBIENT PRESSURE ("H2O)
*      PT(I,J) ..... PLENUM PRESSURE ("H2O)
*      ROT..... ANGLE OF ROTATION OF THE BEAMS.
*      TT(I,J) ..... MEASURED STAGNATION TEMPERATURE.
*      TURB(I,J) .... CALCULATED TURBULENCE.
*      TURBU(I,J) ... TURBULENCE MEASURED IN THE HORIZONTAL COMPONENT.
*      TURBV(I,J) ... TURBULENCE MEASURED IN THE VERTICAL COMPONENT.
*      U(I,J) ..... MEASURED HORIZONTAL COMPONENT OF VELOCITY
*      UNORM(I,J) ... U(I,J) NORMALIZED BY THE INLET VELOCITY.
*      V(I,J) ..... MEASURED VERTICAL COMPONENT OF VELOCITY
*      VEL(I,J) ..... MEASURED VELOCITY
*      VELN(I,J) .... VEL(I,J) NORMALIZED BY INLET VELOCITY.
*      VELMES(I,J) .. FREE STREAM VELOCITY
*      VNORM(I,J) ... V(I,J) NORMALIZED BY THE INLET VELOCITY.
*      X(I,J) ..... HORIZONTAL COORDINATE.
*      XX..... V/VT
*      Y(I,J) ..... VERTICAL COORDINATE.
*      YAW(I,J)..... YAW ANGLE OF LDV SYSTEM.
```

C

C

```
      REAL ALFA(150,10),PT(150,10),TT(150,10),TURB(150,10),
1      TURBU(150,10),TURBV(150,10),U(150,10),UNORM(150,10),V(150,10)
2      VEL(150,10),VELN(150,10),VELMES(150,10),VNORM(150,10),
3      X(150,10),Y(10),YAW(150,10)
```

C

```
      INTEGER N(10)
```

C

C

```
      READ AMBIENT PRESSURE & PRESSURE COEFFICIENT
```

C

```

      READ (12,*) PAMB,CP12,ROT
      ROT = ROT*3.1416/180.
      PAMB = PAMB*13.596
C
C  READ LDV DATA
C
      READ (12,*) M
      DO 10 J = 1,M
        READ (12,*) N(J),Y(J)
        DO 11 I = 1,N(J)
          READ (12,*) X(I,J),U(I,J),TURBU(I,J),V(I,J),TURBV(I,J),
1            PT(I,J),TT(I,J),YAW(I,J)
          YAW(I,J) = YAW(I,J)*3.1416/180.
11        CONTINUE
10      CONTINUE
C
C  NORMALIZE AND LDV DATA
C
      DO 12 J = 1,M
        DO 13 I = 1,N(J)
          BETA = PT(I,J)/(PAMB+PT(I,J))
          CALL SOLVE (BETA,CP12,XX)
          VELMES(I,J) = XX*SQRT(1115.5*(TT(I,J)+460.))
          A = U(I,J)*COS(ROT) - V(I,J)*SIN(ROT)
          B = U(I,J)*SIN(ROT) + V(I,J)*COS(ROT)
          A = A*COS(YAW(I,J))
          UNORM(I,J) = A/VELMES(I,J)
          VNORM(I,J) = B/VELMES(I,J)
          VEL(I,J) = SQRT(A**2+B**2)
          VELN(I,J) = VEL(I,J)/VELMES(I,J)
          ALFA(I,J) = ATAN(A/B)*180./3.1416
          TURB(I,J) = SQRT((TURBU(I,J)*U(I,J))**2+(TURBV(I,J)*V(I,J)
1            )**2)/VELMES(I,J)
          TURB(I,J) = TURB(I,J)/SQRT(2.)
13        CONTINUE
12      CONTINUE
C
C  PRINTOUTS OF LDV DATA
C
      WRITE (22,*) '                WAKE OUTPUT'
      WRITE (22,*) '                ====='
      WRITE (22,*) '                (LASER BEAMS ROTATED BY 45 DEG)'
C
      WRITE (22,*) '      Y      X      VELMES U-NORM V-NORM  VELN      ALFA      TUR
1B'
```

```

WRITE (22,*)' (IN) (IN) (M/SEC) -- -- -- (DEG) (%)
1 '
WRITE (22,*)' _____
1 '
DO 14 J = 1,M
  WRITE (22,30) Y(J),X(1,J),VELMES(1,J),UNORM(1,J),VNORM(1,J),
1 VELN(1,J),ALFA(1,J),TURB(1,J)
  DO 15 I = 2,N(J)
    WRITE (22,31) X(I,J),VELMES(I,J),UNORM(I,J),VNORM(I,J),
1 VELN(I,J),ALFA(I,J),TURB(I,J)
15 CONTINUE
14 CONTINUE
30 FORMAT (/2(1X,F6.3),1X,F6.1,3(1X,F6.3),1X,F6.1,1X,F6.2)
31 FORMAT (7X,1X,F6.3,1X,F6.1,3(1X,F6.3),1X,F6.1,1X,F6.2)
32 FORMAT (/6(2X,F6.1))
33 FORMAT (F9.1,4X,F6.2)
40 FORMAT (////)
STOP
END

```


APPENDIX E

ESTIMATION OF THE UNCERTAINTY IN THE MEASUREMENTS OF BOUNDARY LAYER THICKNESS AND SHAPE FACTOR

Displacement thickness is defined incompressibly as

$$\delta^* = \int_0^{\delta} \left(1 - \frac{u}{u_{\infty}}\right) dy \quad E(1)$$

Momentum thickness is defined incompressibly as

$$\theta = \int_0^{\delta} \left(1 - \frac{u}{u_{\infty}}\right) \frac{u}{u_{\infty}} dy \quad E(2)$$

It was assumed that the uncertainty was due mainly to an uncertainty of 0.002" in positioning the measuring volume on the blade surface. Therefore, we write

$$\delta^* = \int_0^{y_1} \left(1 - \frac{u}{u_{\infty}}\right) dy + \int_{y_1}^{\delta} \left(1 - \frac{u}{u_{\infty}}\right) dy = \delta^*_1 + \delta^*_2 \quad E(3)$$

and

$$\theta = \int_0^{y_1} \left(1 - \frac{u}{u_{\infty}}\right) \frac{u}{u_{\infty}} dy + \int_{y_1}^{\delta} \left(1 - \frac{u}{u_{\infty}}\right) \frac{u}{u_{\infty}} dy = \theta_1 + \theta_2 \quad E(4)$$

where subscript 1 denotes the data point closest to the surface.

The second integrals in Equations E(3) and E(4) are not changed in value by a shift in the y axis. Therefore, they cannot contribute to the uncertainty in either the displacement or the momentum thicknesses. In order to calculate the first term of each thickness, a linear interpolation was assumed for the integration. Thus,

$$\delta_1^* = \int_0^{y_1} \left(1 - \frac{u_1}{u_\infty}\right) dy = \left(1 - \frac{u_1}{2u_\infty}\right) y_1$$

and the uncertainty

E(5)

$$\Delta \delta^* = \Delta \delta_1^* = \left(1 - \frac{u_1}{2u_\infty}\right) \Delta y_1 = \left(1 - \frac{u_1}{2u_\infty}\right) 0.002''$$

Similarly,

$$\theta_1 = \int_0^{y_1} \left(1 - \frac{u}{u_\infty}\right) \frac{u}{u_\infty} dy = \left(\frac{1}{2} - \frac{u_1}{3u_\infty}\right) \frac{u_1}{u_\infty} \cdot y_1$$

and the uncertainty

E(6)

$$\Delta \theta = \Delta \theta_1 = \left(\frac{1}{2} - \frac{u_1}{3u_\infty}\right) \frac{u_1}{u_\infty} \Delta y_1 = \left(\frac{1}{2} - \frac{u_1}{3u_\infty}\right) \frac{u_1}{u_\infty} \cdot 0.002''$$

The shape factor is defined as

$$H = \frac{\delta^*}{\theta}$$

E(7)

The maximum uncertainty in the shape factor is therefore given by

$$\delta H = H \cdot \left(\frac{\Delta \delta^*}{\delta^*} + \frac{\Delta \theta}{\theta} \right)$$

E(8)

LIST OF REFERENCES

1. Dunker, R., Rechter, H., Starken, H., and Weyer, H., Redesign and Performance Analysis of a Transonic Axial Compressor Stator and Equivalent Plane Cascades with Subsonic Controlled Diffusion Blades, Journal of Engineering for Gas Turbines and Power, Vol. 106, pp. 279-287, April 1984.
2. Hobbs, D. E. and Weingold, H. D., Development of Controlled Diffusion Airfoil for Multistage Compressor Applications, Journal of Engineering for Gas Turbines and Power, Vol. 106, pp. 271-278, April 1984.
3. Dunham, J., Prediction of Boundary Layer Transition on Turbomachinery Blades, AGARD-AG-164, December 1972.
4. Roberts, W. B., Calculation of Laminar Separation Bubbles and Their Effect on Airfoil Performance, AIAA 79-0825, January 1979.
5. Sanger, Nelson L., The Use of Optimization Techniques to Design Controlled Diffusion Compressor Blading, NASA Technical Memorandum 82763, Lewis Research Center, Cleveland, Ohio, 1982.
6. Katsanis, T., Fortran Program for Calculating Transonic Velocities on a Blade to Blade Stream Surface of Turbomachinery, NASA TN D-5427, 1969.
7. McNally, W. D., Fortran Program for Calculating Compressible and Turbulent Boundary Layer in Arbitrary Pressure Gradients, NASA TN D-5681, 1970.
8. Walker, G. J., Observation of Separated Laminar Flow on Axial Compressor Blading, ASME Paper No. 75-GT-63.
9. Schlichting, H., Boundary Layer Theory, Seventh Ed., p 557, McGraw Hill Book Company, Inc., 1978.
10. Beam, R. H. and Warming, R. F., An Implicit Forced Scheme for the Compressible Navier-Stokes Equations, AIAA Journal, Vol. 16, No. 4, pp. 393-402, April 1978.
11. Steger, J. L., Implicit Finite Difference Simulation of Flow about Arbitrary Two-Dimensional Geometries, AIAA Journal, Vol. 16, pp. 679-686, 1978.

12. Rubin, S. G. and Koshla, P. K., Navier-Stokes Calculations with a Coupled Strongly Implicit Method, AIAA 79-0011, January 1979.
13. Shamroth, S. J., McDonald, H., and Briley, W. R., Prediction of Cascade Flow Fields Using the Averaged Navier-Stokes Equations, Journal of Engineering for Gas Turbines and Power, Vol. 106, pp. 383-390, April 1984.
14. Schafer, O., Fruhauf, H. H., Bauer, B., and Guggolz, M., Application of Navier-Stokes Analysis to Flows Through Plane Cascades, Journal of Engineering for Gas Turbines and Power, Vol. 108, pp. 103-111, January 1986.
15. Johnston, W. and Sockol, P., Viscous Inviscid Interactive Procedure for Rotational Flow in Cascades of Airfoils, AIAA, Vol. 9, pp. 1281-1282, September 1984.
16. Cebeci, T., Hess, J. L., and Lee, K. H., An Interactive Procedure for Cascade Flows, NAVAIR Report, Contract No. N00014-84-K-0740, 1986.
17. Krainer, A., Viscous-Inviscid Interaction Analysis of Incompressible Cascade Flows, Naval Postgraduate School Contractor Report, No. NPS-67-86-005CR, December 1986.
18. Bradshaw, P., The Understanding and Prediction of Turbulent Flow, Aeronautical Journal 76, pp. 403-418, 1972.
19. Launder, B. E. and Spalding, D. B., Mathematical Models of Turbulence, Academic Press, London, 1972.
20. Rotta, J. C., Turbulent Shear Layer Prediction on the Basis of the Transport Equations for the Reynolds Stresses, Proc. 13th Int. Congr. Theor. Appl. Mech., Moscow 1972, pp. 295-308.
21. Mellor, G. L. and Herring, H. J., A Survey of the Mean Turbulent Field Closure Models, AIAA Journal, Vol. 19, No. 2, pp. 590-599, 1973.
22. Launder, B. E., Reece, G. E., and Rodi, W., Progress in Development of a Reynolds-Stress Turbulence Closure, Journal of Fluid Mechanics, Vol. 68, Part 3, pp. 537-566, 1975.
23. McDonald, H. and Fish, R. W., Practical Calculations of Transitional Boundary Layers, Int. Journal of Heat and Mass Transfer, Vol. 16, pp. 1729-1744, 1973.

24. Forest, A. E., Engineering Predictions of Transitional Boundary Layers, AGARD Conference Proceedings No. 22, pp. 22-1 - 22-19, 1977.
25. Abu-Ghannam, B. J. and Shaw, R., Natural Transition of Boundary Layers - The Effects of Turbulence, Pressure Gradients, and Flow History, J. of Mechanical Engineering Science, Vol. 22, No. 5, pp. 213-228, 1980.
26. Blair, M. F., Influence of Free Stream Turbulence on Boundary Layer Transition in Favorable Pressure Gradients, J. of Engineering for Power, Vol. 104, pp. 743-750, 1982.
27. Wang, T., Simon, T. W., and Buddhavarapu, J., Heat Transfer and Fluid Mechanics Measurements in Transitional Boundary Layer Flows, J. of Engineering for Gas Turbines and Power, Vol. 107, pp 1007-1015, 1985.
28. Horton, H. P., A Semi-Empirical Theory for the Growth and Bursting of Laminar Separation Bubbles, U.K. Aeronautical Research Council, Current Paper No. 1073, 1979.
29. Walker, G. J., Transitional Flow on Axial Turbomachine Blading, AIAA Paper No. 87-0010.
30. NASA Special Publication SP-36, Aerodynamic Design of Axial Flow Compressors, edited by Irving A. Johnson and Robert A. Bullock, 1965.
31. Erwin, J. R. and Emery, J. C., Effect of Tunnel Configuration and Testing Technique on Cascade NASA Report 1016, 1951.
32. Starken, H., Bruegelmans, F. A. E., and Schimming, P., Investigation of Axial Velocity Density Ratio on a High Turning Cascade, ASME Paper No. 75-GT-25, 1975.
33. Evans, R. L., Boundary Layer Development on Axial Compressor Stator Blade, J. of Engineering for Power, Vol. 100, pp. 287-293, April 1978.
34. Shama, O. P., Wells, R. A., Schlinker, R. H., and Baily, D. A., Boundary Layer Development on Turbine Airfoil Suction Surface, J. of Engineering for Power, Vol. 104, pp. 698-706, July 1982.

35. Walker, G. J., The Turbulent Boundary Layer on an Axial Compressor Blade, ASME Paper No. 82-GT-52.
36. Deutsch, S. and Zierke, W. C., The Measurements of Boundary Layers on a Compressor Blade in Cascade (Parts 1, 2, and 3), ASME Paper No. 87-GT-248, 249, 250.
37. Lakshminarayana, B. and Davino, R., Mean Velocity and Decay Characteristics of the Guidevane and Stator Blade Wake of an Axial Flow Compressor, J. of Engineering for Power, Vol. 102, pp. 50-60, January 1980.
38. Ravindranath, A. and Lakshminarayana, B., Mean Velocity and Decay Characteristics of the Near and Far Wake of a Rotor Blade of Moderate Loading, J. of Engineering for Power, Vol. 102, pp. 535-548, July 1980.
39. Hobbs, D. E., Wagner, J. H., Dannenhoffer, J. F., and Dring, R. P., Experimental Investigation of Compressor Cascade Wakes, ASME Paper No. 82-GT-299.
40. McCormick, D. C., Paterson, R. W., and Weingold, H.D., Experimental Investigation of Loading Effects on Simulated Compressor Airfoil Trailing-Edge Flow Fields, AIAA 88-0365.
41. Dreon, J. W., Controlled Diffusion Compressor Blade Wake Measurements, M.S. Thesis, Naval Postgraduate School, Monterey, California, September 1986.
42. Himes, S. J., Report of Tests of a Compressor Configuration of DCA Blading, M.S. Thesis, Naval Postgraduate School, Monterey, California, June 1983.
43. McGuire, A. G., Determination of Boundary Layer Transition and Separation on Double Circular Arc Compressor Blade in a Large Subsonic Cascade, M.S. Thesis, Naval Postgraduate School, Monterey, California, September 1983.
44. Koyuncu, Y., Report of Tests of a Compressor Configuration of CD Blading, M.S. Thesis, Naval Postgraduate School, Monterey, California, March 1984.
45. Sanger, N. L. and Shreeve, R. P., Comparison of Calculated and Experimental Cascade Performance for Controlled Diffusion Compressor Stator Blading, J. of Turbomachinery, Vol. 108, No. 1, pp. 42-50, 1986.

46. Rose, C. C. and Guttormson, D. L., Installation and Test of a Rectilinear Cascade, M.S. Thesis, Naval Postgraduate School, Monterey, California, 1964.
47. Durst, F., Melling, A., and Whitelaw, J. H., Principles and Practice of Laser Doppler Anemometry, Academic Press, 1976.
48. Dring, R. P., Sizing Criteria for Laser Anemometry Particles, J. of Fluid Engineering, Vol. 104, pp. 15-17, 1982.
49. Kuethe, A. M. and Chow, C. Y., Foundation of Aerodynamics, Third Edition, John Wiley and Sons Books, Inc., 1976.
50. Baydar, A., Hot-Wire Measurements of Compressor Blade Wakes in a Cascade Wind Tunnel, M.S. Thesis, Naval Postgraduate School, Monterey, California, March 1988.
51. Shamroth, S. G., Scientific Research Associates Inc. (Private Communication), Glastonbury, Connecticut, December 1987.
52. Davis, R. L., Ni, R.-H., and Carter, J. E., Cascade Viscous Flow Analysis Using the Navier-Stokes Equations, AIAA J. of Propulsion and Power, Vol. 3, No. 5, Sept-Oct. 1987, pp. 406-414.
53. Davis, R. L., United Technologies Research Center (Private Communication), East Hartford, Connecticut, January 1988.
54. Hah, C., General Electric Research Laboratories (Private Communication), Schenectady, New York, December 1987.
55. Rai, M. M., NASA Ames Research Center (Private Communication), Moffett Field, California, DEcember 1987.
56. Delaney, R. A., Alison Division, General Motors Corporation (Private Communication), Indianapolis, Indiana, February 1988.
57. Pruitt, T., Measurements of Particle Size Distribution in a Solid Propellant Rocket Motor Using Light Scattering, M.S. Thesis, Naval Postgraduate School, Monterey, California, June 1987.

INITIAL DISTRIBUTION LIST

1. COMMANDER
Naval Air Systems Command
Washington, D.C. 20361
Attention: Code AIR 931 1
Code AIR 931E 1
Code AIR 530 1
Code AIR 536 1
Code AIR 5004 4
Code AIR 93D 1
2. Office of Naval Research
800 N. Quincy Street
Arlington, Virginia 22217
Attention: Dr. Jack Hansen 1
Dr. R. Whitehead 1
3. Commanding Officer
Naval Air Propulsion Center
Trenton, NJ 08628
Attention: G. Mangano, PE-31 1
4. Commanding Officer 1
Naval Air Development Center
Warminster, PA 19112
Attention: AVTD
5. Library 1
Army Aviation Material Laboratories
Department of the Army
Fort Eustis, Virginia 23604
6. Dr. Arthur J. Wennerstrom 1
AFWAL/POTX
Wright-Patterson AFB
Dayton, Ohio 45433
7. Air Force Office of Scientific Research 1
AFOSR/NA
Bolling Air Force Base
Washington, D.C. 20322
Attention: Dr. James Wilson

8. National Aeronautics & Space Administration
Lewis Research Center
21000 Brookpark Road
Cleveland, Ohio 44135
Attnetion: Chief, Internal Fluid Mechanics Div. ... 1
Library 1
N. Sanger (MS: 5-11) 1
R. Chima (MS: 5-11) 1
9. Library 1
General Electric Company
Aircraft Engine Technology Division
DTO Mail Drop H43
Cincinnati, Ohio 45215
10. Library 1
Pratt & Whitney Aircraft Group
Post Office Box 2691
West Palm Beach, Florida 33402
11. Library 1
Pratt-Whitney Aircraft Group
East Hartford, Connecticut 06108
12. Library 1
Curtis Wright Corporation
Woodridge, New Jersey 07075
13. Library 1
AVCO/Lycoming
550 S. Main Street
Stratford, Connecticut 06497
14. Library 1
Teledyne CAE, Turbine Engines
1330 Laskey Road
Toledo, Ohio 43612
15. Library 1
Williams International
P. O. Box 200
Walled Lake, Michigan 48088
16. Library 1
Detroit Diesel Allison Division G.M.C.
P. O. Box 894
Indianapolis, Indiana 46202

17. Library 1
Garrett Turbine Engine Company
111 S. 34th Street
P. O. Box 5217
Phoenix, Arizona 85010
18. Professor J. P. Gostelow 1
School of Mechanical Engineering
The New South Wales Institute of Technology
New South Wales
AUSTRALIA
19. Dr. G. J. Walker 1
Civil and Mechanical Engineering Department
The University of Tasmania
Box 252C
GPO Hobart, Tasmania 7110
AUSTRALIA
20. Professor F. A. E. Breugelmans 1
Institut von Karman de la Dynamique des Fluides
72 Chaussee de Waterloo
1640 Rhode-St. Genese
BELGIUM
21. Professor Charles Hirsch 1
Vrije Universiteit Brussel
Pleinlaan 2
1050 Brussels
BELGIUM
22. Director 1
Gas Turbine Establishment
P. O. Box 305
Jiangyou County
Sichuan Province
CHINA
23. Professor C. H. Wu 1
P. O. Box 2706
Beijing 100080
CHINA
24. Director 1
Whittle Laboratory
Department of Engineering
Cambridge University
ENGLAND

25. Library 1
ONERA
29, Ave. de la Division Leclerc
92 Chatillon
FRANCE

26. Professor D. Adler 1
Technion Israel Institute of Technology
Department of Mechanical Engineering
Haifa 32000
ISRAEL

27. Dr. P. A. Paranjpe 1
Head, Propulsion Division
National Aeronautics Laboratory
Post Bag 1700
Bangalore - 17
INDIA

28. Dr. W. Schlachter 1
Brown, Boveri Company Ltd.
Dept. T-T
P. O. Box CH-5401 Baden
SWITZERLAND

29. Professor Leonhard Fottner 1
Department of Aeronautics and Astronautics
German Armed Forces University
Hochschule des Bundeswehr
Werner Heisenbergweg 39
8014 Neubiberg near Munich
WEST GERMANY

30. Professor Dr. Ing. Heinz E. Gallus 1
Lehrstuhl und Institut fuer Strahlantriebe
und Turbourbeitsmashinen
Rhein.-Westf. Techn. Hochschule Aachen
Templergraben 55
5100 Aachen
WEST GERMANY

31. Dr. Ing. Hans-J. Heinemann 1
DFVLR-AVA
Bunsenstrasse 10
3400 Geottingen
WEST GERMANY

32. Dr. H. Weyer 1
 DFVLR
 Linder Hohe
 505 Porz-Wahn
 WEST GERMANY

33. United Technologies Research Center
 East Hartford, Connecticut 06108
 Attention: Dr. R. P. Dring 1
 Dr. J. Verdon 1
 Dr. R. L. Davis 1

34. Director 1
 Gas Turbine Laboratory
 Massachusetts Institute of Technology
 Cambridge, Massachusetts 02139

35. Dr. B. Lakshminarayana 1
 Professor of Aerospace Engineering
 The Pennsylvania State University
 233 Hammond Building
 University Park, Pennsylvania 16802

36. Mr. R. A. Langworthy 1
 Army Aviation Material Laboratories
 Department of the Army
 Fort Eustis, Virginia 23604

37. Mechanical Engineering Department
 Virginia Polytechnic Institute and
 State University
 Blackburg, VA 24061
 Attention: Professor W. O'Brian 1
 Professor H. Moses 1
 Professor J. Moore 1

38. Professor T. H. Okiishi 1
 Professor of Mechanical Engineering
 208 Mechanical Engineering Building
 Iowa State University
 Ames, Iowa 50011

39. Dr. Fernando Sisto 1
 Professor and Head of Mechanical
 Engineering Department
 Stevens Institute of Technology
 Castle Point
 Hoboken, New Jersey 07030

40. Dr. Leroy H. Smith, Jr. 1
 Manager, Compressor and Fan
 Technology Operation
 General Electric Company
 Aircraft Engine Technology Division
 DTO Mail Drop H43
 Cincinnati, Ohio 45215

41. Dr. W. Tabakoff 1
 Professor, Department of Aerospace Engineering
 University of Cincinnati
 Cincinnati, Ohio 45221

42. Mr. P. Tramm 1
 Manager, Research Labs
 Detroit Diesel Allison Division
 General Motors
 P. O. Box 894
 Indianapolis, Indiana 46206

43. Mr. P. F. Yaggy 1
 Director
 U.S. Army Aeronautical Research Laboratory
 AMES Research Center
 Moffett Field, California 94035

44. Defense Technical Information Center 2
 Cameron Station
 Alexandria, Virginia 22314

45. Naval Postgraduate School
 Monterey, California 93943-5000
 Attention: Superintendent, Code 00 1
 Professor M.F. Platzter (67Pl) 1
 Professor S. K. Hebbar (67Hb) 1
 Professor A. L. Schoenstadt (53Zh) 1
 Professor P. H. Nunn (69Nn) 1
 Turbopropulsion Laboratory (67Sf) 15
 Library (0142) 2
 Research Administration (012) 1

46. Dr. M. M. Ral 1
 NASA Ames Research Center
 Moffett Field, California 94035

47. Dr. Chunill Hah 1
 General Electric Company
 CR & D K-1
 Schenectady, New York 12345

48. Dr. Tuncer Cebeci 1
 AFMI, Inc.
 212138 Hawthorne Blvd, Suite 5388
 Torrance, California 90509-2881

49. Professor E. M. Greitzer, Director 1
 Gas Turbine Laboratory
 Massachusetts Institute of Technology
 Cambridge, Massachusetts 02139

50. Dr. Stephen J. Shamroth 1
 Scientific Research Associates
 P. O. Box 498
 Galstonbury, Connecticut 06033

51. Dr. Kyriacos D. Papailiou 1
 National Technical University of Athens
 Department of Mechanical Engineering
 Patission 42
 106 82 Athens
 GREECE

52. Dr. Yekuti'el Elazar20
 1 Haoranim Street
 Yokneam Ilit, 20692
 ISRAEL

53. Marie Hashimoto 1
 Department of Aeronautics & Astronautics
 Code 67mbh
 Naval Postgraduate School
 Monterey, California 93943-5000

END

DATED

FILM

8-88

Dtic